

Atomistic Simulations of Thermodynamics and Kinetics Related to Advanced Alloy Processing

by

Mingfei Zhang

A dissertation submitted in partial fulfillment
of the requirements for the degree of
Doctor of Philosophy
(Materials Science and Engineering and Scientific Computing)
in The University of Michigan
2020

Doctoral Committee:

Assistant Professor Liang Qi, Chair
Professor Fei Gao
Associate Professor Emmanouil Kioupakis
Professor Amit Misra

Mingfei Zhang
mingfei@umich.edu
ORCID iD: 0000-0002-4865-6274

©Mingfei Zhang 2020

To my family
For their love, support, and dedication

ACKNOWLEDGEMENTS

First and foremost, I would like to express my deepest gratitude to my advisor Prof. Liang Qi for his continuous guidance of my study, great patience, and immense knowledge. It is my honor to be the first student to join his research group. I am grateful for the open and inclusive collaboration culture he created across the group. I am fortunate to have Prof. Qi not only as a good mentor in academic research but also as a good mentor in my life. Prof. Qi inspired me with his enthusiasm for science. The problem-solving skills and attitude to others which I learned from him will guide me, no matter what I do in the future. I sincerely appreciate all he has done for me.

Besides, I would like to express my sincere thanks to Prof. Amit Misra, Prof. Emmanouil Kioupakis, and Prof. Fei Gao for serving on my thesis committee. The path to a Ph.D. is long, rocky and confusing. Without their insightful suggestions, unlimited help, and generous encouragement, I could not have gone that far.

I also would like to thank my group mates: Chaoming Yang, Dr. Yong-Jie Hu, Aditya Sundar, Zhucong Xi, and Bin Bin for your help, your support, and many memorable moments. You guys are the best! I would like to thank other colleagues from U-M: Nocona Sanders, Dr. Erica Chen, and Dr. Cheng Zhang for their collaboration and discussion. I am also grateful to the MSE Department for all the support. I also want to thank Dr. Louis Hector, Jr., Prof. L. Jay Guo, Dr. Jing-Yu Lao for their great collaboration.

I am also grateful and feel lucky for funding supports provided by Materials

Science and Engineering Department, Guardian Industry, General Motors, and National Science Foundation Grant Opportunities for Academic Liaison with Industry (GOALI) program. I thank computational resources provided by the University of Michigan HPC Great Lakes, Extreme Science and Engineering Discovery Environment (XSEDE), National Energy Research Scientific Computing Center (NERSC).

I would like to thank my dearest friends: Ruiming Lu, Dandan Wang, Patrick (Peng) Sun, and Judy (Xin-Yi) Song.

At last, I would like to thank my family. I would like to thank my parents for their support, understanding, and love. And I would like to thank my beautiful wife Yan Zhang for her love, company, and tolerance. I love you all.

TABLE OF CONTENTS

| | |
|--|------|
| DEDICATION | ii |
| ACKNOWLEDGEMENTS | iii |
| LIST OF FIGURES | viii |
| LIST OF TABLES | xiii |
| LIST OF ABBREVIATIONS | xiv |
| ABSTRACT | xvii |
| CHAPTER | |
| I. Introduction | 1 |
| 1.1 Background | 1 |
| 1.2 Outline | 3 |
| II. Computational Material Science Methodologies | 7 |
| 2.1 Density Functional Theory | 7 |
| 2.2 Grand Canonical Monte Carlo Simulation | 10 |
| 2.2.1 Grand Canonical Ensemble | 10 |
| 2.2.2 Monte Carlo Methods | 10 |
| 2.2.3 Grand Canonical Monte Carlo Simulation | 11 |
| 2.3 Deep Learning and Neural Network | 12 |
| 2.4 Kinetic Monte Carlo Simulation | 13 |
| III. Electronic Mechanism of H Adsorptions on ZnO Surfaces . . | 15 |
| 3.1 Introduction | 16 |
| 3.2 Coverage-dependent Hydrogen Adsorption Energies on ZnO (000 $\bar{1}$) Surface | 18 |
| 3.3 Electronic Structure Analyses and Electron Counting Model . | 23 |

| | | |
|--|--|------------|
| 3.4 | Hydrogen Adsorption on (000 $\bar{1}$) Surface of ZnO with Dopants | 27 |
| 3.5 | Model Generalization for Other Polar Surfaces | 32 |
| 3.6 | Conclusions | 35 |
| IV. Grand Canonical Monte Carlo Simulations of Ag Thin Film Depositions | | 38 |
| 4.1 | Introduction | 39 |
| 4.2 | Customized Empirical Potential and GCMC Simulation Setup for Deposition | 41 |
| 4.3 | ZnO Substrate Yields the Best Ag Thin Film | 44 |
| 4.4 | Substrate “Anchor” Sites for Continuous Thin Film Morphology | 52 |
| 4.5 | Alloy Segregation at Grain Boundary to Stabilize Polycrystalline Thin Film | 60 |
| 4.6 | Conclusions | 66 |
| V. Using Alloy to Enhance Corrosion Resistance of Mg Alloy with Transition Metal Impurities | | 67 |
| 5.1 | Introduction | 68 |
| 5.2 | Criteria to determine candidate elements to inhibit Mg corrosion | 75 |
| 5.3 | High Throughput Screening Results | 86 |
| 5.4 | Electronic Mechanism of Mg Corrosion Inhibition | 91 |
| 5.5 | Sensitivity Analysis for H Adsorption Energy on Surface Alloying Coverage | 96 |
| 5.6 | Model Generalization on Other Precipitates | 98 |
| 5.7 | Conclusions | 100 |
| VI. Kinetic Monte Carlo Simulations of Solute Clustering in Multi-component Al Alloys | | 105 |
| 6.1 | Introduction | 106 |
| 6.2 | Fitting Vacancy Migration Barriers using Neural Network . . | 111 |
| 6.3 | Kinetic Monte Carlo Setup | 121 |
| 6.3.1 | kinetic Monte Carlo (kMC) Algorithm | 121 |
| 6.3.2 | Local Super-basin Kinetic Monte Carlo (LSKMC) . | 124 |
| 6.3.3 | least recently used (LRU) Cache | 125 |
| 6.4 | Results and Discussion | 129 |
| 6.4.1 | Cluster Searching Algorithm | 129 |
| 6.4.2 | Benchmark of Al-Mg-Zn Clusters | 131 |
| 6.4.3 | Searching for Potential Elements that Can Slow Down Precipitate Hardening | 136 |
| 6.5 | Conclusion | 146 |
| VII. Summary and Future Work | | 148 |

| | | |
|-------------------------------|-----------------------|------------|
| 7.1 | Summary | 148 |
| 7.2 | Future Work | 151 |
| BIBLIOGRAPHY | | 156 |

LIST OF FIGURES

Figure

| | | |
|-----|---|----|
| 2.1 | Illustration plot of grand canonical ensemble. | 10 |
| 2.2 | Illustration plot of a neural network. | 13 |
| 3.1 | Schematic of (2×2) supercell used to model $(000\bar{1})$ wurtzite ZnO surface with H adsorption. | 19 |
| 3.2 | H adsorption energies on ZnO surfaces with different H coverage . . | 23 |
| 3.3 | projected density of states (PDOS) for all the surface atoms on pure ZnO (2×2) $(000\bar{1})$ surface under different H coverage. | 25 |
| 3.4 | Top views of the charge density difference isosurfaces before and after H adsorption. | 26 |
| 3.5 | H adsorptions on ZnO surfaces with subsurface doping element: Al, Ti, V. | 28 |
| 3.6 | H adsorptions on ZnO surfaces with subsurface doping element: Na, Mg, Be, Fe, Sn, Pb. | 29 |
| 3.7 | E_{ad}^H on (2×3) ZnO $(000\bar{1})$ surface with the co-existence of 1 Al substitutional dopant atom and 1 Ti substitutional dopant atom at bulk Zn sites. | 34 |
| 4.1 | Illustration of multi-layer structures of architecture glass. | 40 |
| 4.2 | Lennard-Jones potential used to describe different bonding strength and bond length, and atomistic pictures of Ag adsorbed on ZnO surface with $\frac{1}{2}$ ML coverage. | 41 |

| | | |
|------|---|----|
| 4.3 | Four different substrate types for Grand Canonical Monte Carlo (GCMC) simulation. | 43 |
| 4.4 | Simulated XRD plots of FCC and HCP Ag. | 44 |
| 4.5 | GCMC simulated Ag thin film morphology on hexagonal substrates with bond length. | 45 |
| 4.6 | Simulated X-ray diffraction (XRD) results of Ag thin film on hexagonal substrates with different bond length. | 46 |
| 4.7 | common neighbor analysis (CNA) plots of Ag thin film on hexagonal substrates with different bond length. | 48 |
| 4.8 | GCMC simulation results of Ag thin film morphology on rectangular substrates. | 49 |
| 4.9 | Simulated XRD results of Ag thin film morphology on rectangular substrates. | 50 |
| 4.10 | CNA and centro-symmetry analysis for Ag thin film quality on rectangular substrates. | 51 |
| 4.11 | GCMC simulation results of Ag thin film morphology on square substrates. | 52 |
| 4.12 | Simulated XRD results of Ag thin film morphology on square substrates. | 53 |
| 4.13 | Side-view of GCMC simulated Ag thin film morphology on square substrates. | 54 |
| 4.14 | CNA and Simulated XRD results of Ag thin film morphology on an amorphous substrate. | 55 |
| 4.15 | Possible water and H ₂ dissociation reactions on ZnO substrate with one “anchor” site. | 56 |
| 4.16 | Water and H ₂ dissociation reactions energies on ZnO substrate with “anchor” sites. | 57 |
| 4.17 | GCMC simulation results for 10monolayer (ML) Ag deposition on ZnO with and without 0.05ML surface “anchor” sites. | 59 |
| 4.18 | Illustration of grain boundary grooving between two grains. | 60 |

| | | |
|------|--|-----|
| 4.19 | Atomistic structure of $\Sigma 5$ (310) Ag grain boundary. | 61 |
| 4.20 | Segregation energies of different elements at $\Sigma 5$ (310) grain boundary. | 62 |
| 4.21 | Segregation energies of different elements at $\Sigma 3$ (112) grain boundary. | 63 |
| 4.22 | Segregation energies of different elements at $\Sigma 3$ (111) grain boundary. | 64 |
| 4.23 | Atomistic structure of $\Sigma 29$ (520) Ag grain boundary. | 65 |
| 5.1 | Illustration of corrosion reaction mechanism on Mg and the alloying strategy to inhibit hydrogen evolution reaction (HER). | 68 |
| 5.2 | Perspective and side views of a generic alloying element in the simulation. | 72 |
| 5.3 | Top-down views of Fe surfaces with substitutional alloying elements and adsorbed H atoms. | 74 |
| 5.4 | Summary of the high-throughput search for alloying elements that can inhibit HER on surfaces of Fe second-phase particles in Mg matrix. | 76 |
| 5.5 | Segregation energies to bulk second-phase particles $E_{particlessig}$ defined in Equation 5.4 for the 68 potential alloying elements. | 78 |
| 5.6 | Segregation energies $E_{surfseg}$ defined in Equation 5.5 for Fe (100) of 24 alloying elements narrowed from the first screening round. | 81 |
| 5.7 | Segregation energies $E_{surfseg}$ defined in Equation 5.5 for Fe (110) of 24 alloying elements narrowed from the first screening round. | 83 |
| 5.8 | H adsorption energies E_{ad}^H defined in Equation 5.6 on Fe (100) and Fe (110) with the 13 alloying elements that pass the second screening round. | 85 |
| 5.9 | Top-down views of isosurfaces of electron density difference ($\Delta\rho$ defined in Equation 5.8) for (2 \times 2) Fe (110) with one substitutional alloying atom in top surface layer. | 91 |
| 5.10 | Top-down views of isosurfaces of electron density difference ($\Delta\rho$ defined in Equation 5.8) for (2 \times 2) Fe (100) with one substitutional alloying atom in top surface layer. | 93 |
| 5.11 | Effects of 6 p-block elements on higher surface alloying coverage. . . | 103 |

| | | |
|------|--|-----|
| 5.12 | Effects of 6 p-block elements on other precipitates(Cu and Ni). | 104 |
| 6.1 | Schematics of the fabrication process of 7000 series Al sheet alloy parts in the automobile industry. | 106 |
| 6.2 | Illustration of a vacancy migration in a 2D lattice of a multicomponent system. | 108 |
| 6.3 | Correlation between migration barriers (E_a) and energy differences (ΔE) for many vacancy migration events in Al-Mg-Zn systems obtained from our DFT + climbing image nudged elastic band (CI-NEB) calculations. | 110 |
| 6.4 | Plot of k-point grids convergence and efficiency test on vacancy migration barrier. | 112 |
| 6.5 | Atomistic pictures of $(4 \times 4 \times 4)$ supercells containing 256 atoms. | 114 |
| 6.6 | Illustration of atomic structures of the 1 st and 2 nd nearest neighbors surrounding the jumping pairs (the lattice sites of the vacancy before and after a migration event). | 115 |
| 6.7 | Predictions accuracy of vacancy migration barriers from neural network surrogate model, compared with DFT calculated results. | 119 |
| 6.8 | Predictions accuracy of vacancy migration barriers from neural network model using custom loss function, compared with DFT calculated results. | 120 |
| 6.9 | Scalability of KNN2 code for 108,000 atoms on Great Lakes HPC from the University of Michigan with 2x 3.0 GHz Intel Xeon Gold 6154 processors and InfiniBand HDR100 networking, capable of 100 Gb/s throughput. | 123 |
| 6.10 | Comparison of different LSKMC parameters setup. | 126 |
| 6.11 | Comparison of LRU cache size effects on simulation speed for a 108,000-atom supercell system running 10,000,000 steps on TACC Stampede2 cluster. | 127 |
| 6.12 | Number of calls of LRU cached results as time increases. | 128 |
| 6.13 | Atomistic pictures of the top 10 largest clusters by size via cluster searching algorithm from a snapshot during a kMC simulation. | 130 |

| | | |
|------|--|-----|
| 6.14 | Size changes and ratio changes vs. time for ~ 5.5 seconds. | 132 |
| 6.15 | Vacancy migration barrier changes vs. different local environment concentrations. | 133 |
| 6.16 | Atomistic pictures of 108,000 atoms for control group, corresponding to setup #0 in Table 6.3. | 135 |
| 6.17 | Size distribution of identified clusters at 5 and 22 seconds. | 136 |
| 6.18 | Cluster size and Mg-Zn bonds change for the first 22 seconds. | 137 |
| 6.19 | Atomistic pictures of 108,000 atoms for ε_{Al-X} sensitivity test using $size_{critical}$ of 3 and $bond_{critical}$ of 3. | 140 |
| 6.20 | Atomistic pictures of 108,000 atoms for ε_{Mg-X} sensitivity test using $size_{critical}$ of 3 and $bond_{critical}$ of 3. | 141 |
| 6.21 | Atomistic pictures of 108,000 atoms for ε_{Zn-X} sensitivity test using $size_{critical}$ of 3 and $bond_{critical}$ of 3. | 142 |
| 6.22 | Size changes of different clusters vs. time using $size_{critical}$ of 3 and $bond_{critical}$ of 3. | 143 |
| 6.23 | Ratio changes of different clusters vs. time using $size_{critical}$ of 3 and $bond_{critical}$ of 3. | 144 |
| 6.24 | Bonds between different species vs. time using $size_{critical}$ of 3 and $bond_{critical}$ of 3. | 145 |

LIST OF TABLES

Table

| | | |
|-----|---|-----|
| 3.1 | The coverage-dependent adsorption energy of H atom E_{ad}^{H} in unit of eV on (2×2) O-terminated (0001) ZnO surface with different mechanisms to passivate the Zn-terminated (0001) surface, including a clean Zn-terminated surface, a $\frac{1}{4}$ ML Zn vacancy (V_{Zn}) on the Zn-terminated surface and pseudo-hydrogen atoms with different numbers of valence charges (1.5, 1.0 and 0.5 electron, respectively) at each Zn site on the Zn-terminated surface ($H_{1.5}$, $H_{1.0}$ and $H_{0.5}$). | 21 |
| 3.2 | The coverage-dependent adsorption energy of H atom E_{ad}^{H} (unit: eV/atom) on O-terminated (0001) ZnO surface with substitutional Be dopant atom at different locations to the top surface layer. | 30 |
| 4.1 | “Anchor” elements diffusion barriers on ZnO saturated with $\frac{1}{2}$ ML H. | 57 |
| 4.2 | Ag adsorption on saturated ZnO substrate with “anchor” sites. | 58 |
| 4.3 | Tungsten segregation energy E_{seg} at different sites of Σ29 (520) Ag grain boundary. | 65 |
| 5.1 | Summary of H adsorption energies (eV/atom) defined at Equation 5.6 at selected sites on (2×2) Fe (100) and Fe (110) surface slabs without/with one substitutional atom from one of the 13 alloying elements that pass the second screening round. | 87 |
| 6.1 | Atom species encoding map for the neural network (NN) input layer. | 115 |
| 6.2 | Neural network architecture with activation functions and dropout probability of each layer. | 118 |
| 6.3 | Sensitivity analyses of different ε_{i-X} in Equation 6.6b. | 139 |

LIST OF ABBREVIATIONS

MC Monte Carlo

MD molecular dynamics

GCMC Grand Canonical Monte Carlo

kMC kinetic Monte Carlo

LSKMC Local Super-basin Kinetic Monte Carlo

NN neural network

RBM restricted Boltzmann machine

ReLU Rectified Linear Unit

MSE mean squared error

RMSE root mean squared error

SQS special quasi-random structure

MPI message passing interface

LRU least recently used

DFS depth-first search

BFS breadth-first search

NEB nudged elastic band

CI-NEB climbing image nudged elastic band

XRD X-ray diffraction

CNA common neighbor analysis

CE cluster expansion

ML monolayer

UHV ultrahigh vacuum

HV high vacuum

DFT density functional theory

LDA local density approximation

VASP Vienna Ab-Initio Simulation Package

PAW projector augmented wave

PBE Perdew-Burke-Ernzerhof

GGA generalized gradient approximation

EAM embedded-atom

L-J Lennard-Jones

PDOS projected density of states

FCC face-centered cubic

HCP hexagonal close-packed

BCC body-centered cubic

GB grain boundary

HER hydrogen evolution reaction

SHE standard hydrogen electrode

NDE negative difference effect

GP Guinier-Preston

BEP Bell-Evans-Polanyi

VRC vacancy-rich clusters

ABSTRACT

In my dissertation, thermodynamic driving forces and kinetics of critical reaction steps during advanced alloy processing are studied systematically by theoretical models and simulation tools at the atomistic scale. These efforts include improving the Ag thin-film quality during sputtering, discovering a build-in corrosion-resistant mechanism for cast Mg alloys, and slowing down cluster nucleation and growth in Al solid solution alloys during natural aging to avoid costly hot stamping procedures. First, the thermodynamic driving force of H adsorption on anion-terminated ($(000\bar{1})$) surfaces of pure and doped wurtzite ZnO as dielectric substrates are investigated under varying H surface coverage conditions. Understanding of these H adsorption mechanisms provides a general way to design substrate surfaces with desired binding strengths for the Ag thin-film. Second, Grand Canonical Monte Carlo (GCMC) simulations are conducted to simulate the deposition “kinetics” of Ag thin film on substrates, which can be constructed based on the structures and properties of H-adsorbed ZnO ($(000\bar{1})$) surfaces. The results demonstrate the reason why ZnO is the most suitable substrate for Ag thin film deposition and the mechanism to achieve thinner continuous Ag films by adding “anchor” sites on the substrate surface. We use first-principles calculations to search for potential dopant elements as good “anchor” sites on ZnO substrates and other dopants to stabilize the Ag grain boundaries to improve the polycrystalline Ag thin-film during heat treatment. Third, the hydrogen evolution reaction (HER) as the cathodic reaction on surfaces of the second-phase transition-metal (Fe) particles

can speed up the corrosion of cast Mg metals and alloy. Thus, thermodynamic criteria to slow down the HER are used for high-throughput first-principles computations to search alloying elements that can reduce HER rate to achieve build-in corrosion resistance for cast Mg alloys. Our first-principles search goes across the periodic table and discovers six p-block elements that can increase the corrosion resistance for Mg, consistent with the available experimental results. Fourth, kinetic Monte Carlo (kMC) simulations are performed to study the early transition behavior from a supersaturated solid solution to Guinier-Preston (GP) zone of Al 7000 series alloys at room temperature (so-called natural aging), which is critical for their thermal-mechanical processing in automobile manufacturing. Our kMC method includes a neural network (NN) model trained by thousands of density functional theory (DFT) calculations to accurately predict vacancy migration barriers in Al-Mg-Zn-based alloys. Besides, advanced modeling approaches like least recently used (LRU) cache and Local Super-basin Kinetic Monte Carlo (LSKMC) are also implemented to speed up the kMC simulations in order to directly study the natural aging of Al alloys in the realistic time scales.

CHAPTER I

Introduction

1.1 Background

Humans in all times have never stopped the discovery of innovative metallic alloys with unique properties. These targets can only be achieved by tuning the alloying compositions and by optimizing the corresponding processing procedures. In fact, the history of alloy processing is a history of humankind itself. Metallurgists have been making every effort to invent new desired alloys with appropriate processing methods. As the requirements of the quality and combination of different properties of materials become more demanding, more costly and complicated processing techniques have to be used. The development of materials has always been strongly guided by economic factors. Those techniques and facilities are suitable for high-profit industries, like semiconductor and aviation manufactures. However, many of those techniques are not affordable to transfer to low-profit industry products, like architecture glasses, automobile frames, and so on.

For example, thin-film deposition manufacturing is essential for solar panels, electronic, and optical devices manufacturers today. Basically, a very thin layer of materials with \sim nanometers to \sim micrometers in thickness is deposited onto a surface to be coated. In order to put billions of transistors into a small CPU or build multiple-layer photodiodes, advanced deposition methods, like chemical vapor deposition (CVD),

physical vapor deposition (PVD) or atomic layer deposition (ALD), is used. In these methods, ultra-high vacuum status will be reached in the chamber to achieve the highest thin film quality. However, it is impossible to apply those techniques to large scale coating on architectural glasses for low-emissivity or anti-glaring purposes. If a similar thin-film quality could be achieved during sputtering, it will largely reduce the cost.

Not only 2D materials, but bulk materials also need some expensive “magic” to make materials to be easily manufactured. For example, structural alloys need high specific strength and long product life cycles. They are also required to have good ductility and formability to be mechanically processed into a special shape to function properly. The ability to create materials of high yield strength and yet high ductility has been very challenging for a long time. Some high-strength aluminum alloys can be subjected to costly procedures, such as controlled hot-working, warm stamping, and coupled solutioning-quenching-stamping operations in a narrow time window, followed by artificial aging to achieve precipitate hardening. The procedures described above are widely used in the aerospace industry but not suitable for the automobile industry or other civilian-sector industries that need high strength-weight-ratio. If the costly hot-working, warm stamping could be finished at room temperature, the automobile industry can be benefited from using low weight Mg alloys, thus increasing fuel efficiency.

On the other hand, corrosion resistance is another important property for alloys. Usually, the corrosion-resistant coating is used in automobile industries. However, the ability to resist corrosion decreases during the service, especially if small scratches appear. This traditional coating protection also increases the cost of maintenance and lowers sustainability. It is necessary to increase the build-in corrosion resistance of alloys, such as lightweight Mg alloys, that lack no effective passive oxide layers to impede corrosion reactions. In addition, the casting process of Mg alloys inevitably

introduces the Fe and other transition-metal impurities from the containers. These impurities exist as the second-phase particles and serve as the active reaction sites for the cathodic reactions to speed up the galvanic corrosion reaction significantly. Thus, one research target in this thesis is how to reduce this type of corrosion reaction for Mg alloys due to the transition-metal impurities induced from the casting processing.

1.2 Outline

In this work, efforts were made to solve problems related to alloy processing mentioned above. The target is to combine adding a trace amount of element and affordable processing techniques to make materials with relatively high-quality for large-scale commercial applications. Attentions are paid to achieve ultra-thin Ag films under regular vacuum conditions, to increase Mg alloy corrosion resistance, and to increase formability for high strength Al alloys. To achieve these targets, the trace amount of element added to the alloy will either change the thermodynamic driving force or the activation barriers related to kinetics during the processing procedures. Because the amount of alloying elements added is minimal, it is expected that such alloying would not affect the original properties of alloys significantly. The rest of this dissertation is organized as the following.

In Chapter II, the fundamental principles of the computational methods applied in the present dissertation are discussed in detail, including 1) the background and details for first-principles calculations, 2) the Grand Canonical Monte Carlo (GCMC) simulations, 3) the Monte Carlo (MC) simulations, and 4) deep learning and neural network methods trained by first-principles calculation results to predict the activation barriers of vacancies in multicomponent alloys.

In Chapter III, the effects of alloying elements on the hydrogen (H) equilibrium coverage on zinc oxide (ZnO) and other similar semiconductor surfaces are investigated systematically. This study can enhance our understanding of the semiconductor

substrate conditions for silver (Ag) thin film deposition. The electronic mechanism of H equilibrium coverage on pure ZnO surfaces and those with alloying elements (Na, Mg, Al, Ti, Fe, Pb, Sn, and V) are studied. The simple bond-counting mechanism is proposed to determine and manipulate the equilibrium H adsorption configurations for different alloying surfaces. Besides, the generalization of this mechanism on other different semiconductor polar surfaces with chemical dopant elements are also discussed. This work has been published in *Journal of Applied Physics* in 2018. [1]

Follow the previous study of H equilibrium coverage on ZnO surfaces, in Chapter IV, atomistic Grand Canonical Monte Carlo (GCMC) simulations of Ag deposition on ZnO surfaces are performed to investigate the key parameters that control the quality of Ag thin films. First, the possible reasons why the ZnO substrate is appropriate for high-quality (continuous and crystalline states) Ag thin films are proposed. Then, pseudo-atoms are added on the ZnO surfaces as “anchor” sites in GCMC simulations to achieve ultra-thin Ag film under regular low vacuum conditions. Following this, first-principles high-throughput calculations are conducted to search suitable “anchor” site choices that match the requirements from the above GCMC simulations. Last but not least, efforts are made to search elements that can segregate to Ag grain boundaries (GBs) to stabilize GBs and the thin-film quality during the high-temperature heat treatment processing. So far, first-principles calculation results on GB separations have some discrepancies with the experimental observations, but possible reasons are explained, and a new methodology to resolve this inconsistency is proposed. The methodology will be published in *Computational Materials Science* in 2020 as a co-authored paper. [2]

In Chapter V, because the hydrogen evolution reaction (HER) on second-phase transition metal particles is the cathodic reactions of the Galvanic corrosion in Mg alloy, thermodynamic criteria are proposed to slow down the HER rate on surfaces of these particles. Based on these criteria, we perform high-throughput first-principles

calculations to search for possible alloy elements that can slow down HER to achieve build-in corrosion resistance for Mg alloys. Our first-principles computational procedure goes across all metal and semi-metal elements in the periodic table. The results suggest that six promising p-block elements slow down the HER on the surfaces of common Fe impurities from the casting processing. The most effective two elements of them (As and Ge) are in accord with recent experiments. The electronic mechanism to reduce the HER rate on these surfaces is also discussed. Moreover, the generalization ability of this high-throughput computation paradigm is also tested on other precipitates as potential active sites for the cathodic corrosion reaction. This work has been published in *Computational Materials Science* in 2019. [3]

Chapter VI focuses on the methodology development on simulating the solute clustering kinetics in multicomponent Al alloys quantitatively. To slow down solute clustering at room temperatures (so-called natural aging) after the high-temperature solid-solution treatment is crucial to expand the time window for the mechanical forming of certain high-strength multicomponent Al alloys, such as 7000 series Al-Mg-Zn alloys. Since the clustering is achieved by solute diffusion based on vacancy migration, we first discuss the relationship between vacancy migration barriers and local lattice occupation environments. It is found that the traditional bond counting method fails to predict vacancy migration barriers for the multicomponent systems. Second, a neural network (NN) surrogate model based on the first-principles training data set is introduced to predict the vacancy migration barrier accurately. Third, a kinetic Monte Carlo (kMC) simulation package based on NN model with advanced acceleration methods, such as parallel schema, least recently used (LRU) cache, Local Super-basin Kinetic Monte Carlo (LSKMC) is introduced to simulate the solute clustering kinetics in multicomponent Al alloys. Last but not least, the visualization and characterization methods of solute clusters in the kMC simulation results are investigated. The information on cluster compositions and structures lays the

foundation for the studies of the clustering effects on the strengths and formability of multicomponent Al alloys in the future. The manuscript for this work is still under preparation.

All of the above studies are related to the thermodynamics and kinetics of alloy processing at the atomistic scale. These studies can be understood in an integrated way described as the following. For complex kinetics related to alloy processing, it is more convenient to divide a complicated full reaction path into many elementary reaction steps. Then the efforts are made to investigate the elementary steps, especially those critical rate-determining ones. There are two general types of investigation approaches for these elementary steps. The studies from Chapter III to Chapter V are performed under the “quasi-equilibrium” kinetic approximation, which is based on the assumption that the thermodynamic equilibrium is achieved for most elementary steps except the rate-determining ones. In addition, to further simplify the first-principles calculations, the kinetic barrier of each elementary step is assumed to be not significantly deviated from the maximum thermodynamic driving force. Therefore, only the energy differences (ΔE) between initial and final states of the critical elementary steps will be investigated, and the kinetics of elementary steps will be derived or simulated based on these energy differences (the kinetic barrier $E_a = 0$ if the energy driving force $\Delta E < 0$, otherwise $E_a \sim \Delta E$). On the other hand, only studies in Chapter VI are conducted based on the prediction of the accurate activation barrier and kinetics in every single elementary step. This direct approach is critical for the accurate prediction of kinetics in multicomponent alloy systems, where the shapes of the potential energy landscape are so complex that the simple assumptions on the relations between thermodynamics and kinetics may fail. Thus, the studies in this thesis provide a comprehensive portrayal to future researchers to choose appropriate methods to investigate the alloying processing at the atomistic scale.

Chapter VII concludes the thesis and provides some thoughts on future works.

CHAPTER II

Computational Material Science Methodologies

2.1 Density Functional Theory

In order to investigate interactions between hydrogen atoms and free surfaces of metals or oxides, we need to study their electronic structures. On the other hand, an accurate diffusion barrier energy also relies on a accurate reaction pathway. These can be achieved by first-principles methods. The calculation of interactions between the positively charged nuclei and negatively charged electrons is considered to be a many-body problem combining kinetic energy, interactions between nuclei and electrons, and electron-electron interactions. In principle, a quantum mechanical solution to this many-body problem with N electrons in an external potential $V_{ext}(r)$ generated by the nuclei can be obtained by solving the Schrödinger's equation. Based on the Born-Oppenheimer approximation, the motion of nuclei and electrons can be considered separately. Besides, $V_{ext}(r)$ can be obtained by calculating the Coulomb interactions between the atomic nuclei and electrons. The time-independent, non-relativistic Schrödinger's equation for an N-electrons system can be written as,

$$\hat{H}\Psi = E\Psi \quad (2.1a)$$

$$(-\sum_i^N \frac{\hbar^2}{2m} \nabla_i^2 + \sum_i^N V_{ext}(r) + \frac{1}{2} \sum_{i \neq j}^N \frac{1}{|r_i - r_j|})\Psi = E\Psi \quad (2.1b)$$

where E denotes the system energy, Ψ is the many-body wave function of electrons in the system, \hat{H} is the Hamiltonian operator, N is the total number of electrons in the system, m is the mass of a single electron, r_i denotes the position of electron i .

The many-body system will result in many variables in the wave function ($3N$ degrees of freedom), hence making it very difficult to solve. Due to the complexity and costly computation of directly solving Equation 2.1b, density functional theory (DFT) provides a simpler method to transfer the many-body electron problem to a single-body problem based on the density functional of electrons. [4, 5] First, Hohenberg and Kohn proved that for any system of interacting electrons in an external potential $V_{ext}(r)$, the potential $V_{ext}(r)$ is determined uniquely by the ground state electron density $\rho_0(r)$, which means the Hamiltonian in Equation 2.1a is solely determined by the ground state electron density $\rho_0(r)$. Second, the ground state energy of the system may be obtained variationally, such that the electron density $\rho(r)$ that can minimizes the total energy is the ground state density $\rho_0(r)$ exactly. In the Kohn-Sham system, the electron density $\rho(r)$ of N electrons [5] is expressed as,

$$\rho(r) = \sum_i^N |\phi_i(r)|^2 \quad (2.2a)$$

where $\phi_i(r)$ is the Kohn-Sham orbital which is solved by using the Kohn-Sham Schrödinger-like equation:

$$(H_{KS} - \epsilon_i)\Psi_i(r) = 0 \quad (2.3a)$$

where $\Psi_i(r)$ is the eigenvector and ϵ_i is the corresponding eigenvalue or orbital energy for a non-interacting electron. H_{KS} is the effective Kohn-Sham Hamiltonian defined

as,

$$H_{KS} = -\frac{\hbar^2}{2m}\nabla_i^2 + V_{ext}(r) + V_{Hartree}(r) + V_{xc}(r) \quad (2.4a)$$

$$V_{Hartree}(r) = e^2 \int \frac{\rho(r)}{|r - r'|} d^3r \quad (2.4b)$$

$$V_{xc}(r) = \frac{\partial E_{xc}(\rho(r))}{\partial \rho(r)} \quad (2.4c)$$

In Equation 2.4a, $V_{ext}(r)$ is still the potential accounting for the electron-nuclei interaction as Equation 2.1b, $V_{Hartree}(r)$ is the Coulomb electron-electron interaction as defined in Equation 2.4b, $V_{xc}(r)$ is the exchange-correlation potential as obtained by Equation 2.4c, which accounts for the nonphysical self-interaction error, alongside with other effects. This term is unknown in the Kohn-Sham equation which is the reason why it is the derivative to its energy expression. However, approximation exists and depends only on the value of $\rho(r)$ at a coordinate in space where the functional is evaluated. This method is also known as the local density approximation (LDA). [6] DFT results from LDA approximations usually yield a good estimation of atomic geometries of studied system, but may overestimate the binding energies between different species. A better solution comes from generalized gradient approximation (GGA). [7] The GGA method is local but it also incorporates the effects of inhomogeneity by including the gradient of electron density at the same coordinate. [8] And GGA method usually gives good estimations of the ground state energies, so it is widely used in surface calculations and transition states calculations. There are many different implementations of GGA have been developed: for examples, 1) PW91-GGA from Perdew and Wang (PW91-GGA) [9], 2) PBE-GGA from Perdew, Burke and Ernzerhof (PBE) [10], and 3) revised PBE-GGA for solids (PBEsol) [11]. Based on these approximate functionals for exchange-correlations, the Kohn-Sham Equation 2.3a can be solved based on iterative methods.

2.2 Grand Canonical Monte Carlo Simulation

2.2.1 Grand Canonical Ensemble

The canonical ensemble is a statistical ensemble that consists of N atoms and is in thermodynamic equilibrium with a big reservoir. Energy transfer is allowed between the system and the big reservoir, but particle transfer is impermissible. The big reservoir can be described as a system with relatively large heat capacity, and its temperature T remains constant in spite of any energy transfer. Grand canonical ensemble is a statistical ensemble that can exchange particles with a reservoir as an open system. Besides, the big reservoir can also act as an infinite heat resource allowing heat transfer as shown in Figure 2.1. [12] Therefore in the grand canonical ensemble, the number of atoms N in the system can be changed and chemical potential of each element μ_i , the volume of the system V and temperature T are fixed, hence this system is known as μVT system.

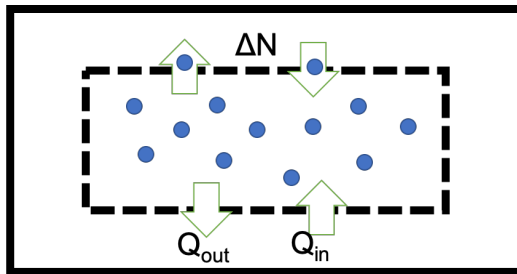


Figure 2.1: Illustration plot of grand canonical ensemble. Black line shows the universe. Black dashed line confines the ensemble. Blue solid circles are atoms in the system.

2.2.2 Monte Carlo Methods

MC methods are a broad class of computational algorithms that rely on repeated random sampling to obtain numerical results for a problem that is difficult to solve in principle. The physics behind is to use randomness to solve problems that might be deterministic. They are often used in mathematical [13] and physical [14] problems. In

this thesis, MC methods are used to do optimization for complex grain boundary (GB) structures in Chapter 4.5, thin-film morphology in Chapter IV and solving stochastic time evolution in Chapter VI. A general MC algorithm involves: i) drawing a random number $u \in (0, 1]$ and ii) accepting/rejecting event base on Boltzmann probability.

2.2.3 Grand Canonical Monte Carlo Simulation

GCMC simulation combines the grand canonical ensemble with MC simulations. Following grand canonical(μVT) ensemble discussed above, the number of atoms N in the ensemble can be changed, thus grants two types of events, inserting a new atom and deleting an existing atom. In addition to these two events, moving an atom to a different location is also considered in the event list. Therefore, the probability of accepting moving an existing atom is via [12]:

$$acc(s \rightarrow s') = \min(1, \exp(-\beta(U(s'^N) - U(s^N))) \quad (2.5)$$

inserting a new atom:

$$acc(N \rightarrow N + 1) = \min(1, \frac{V}{\wedge^3(N + 1)} \exp(\beta(\mu - U(N + 1) + U(N)))) \quad (2.6)$$

and removing an existing atom:

$$acc(N \rightarrow N - 1) = \min(1, \frac{\wedge^3(N)}{V} \exp(-\beta(\mu + U(N - 1) - U(N)))) \quad (2.7)$$

where, β is the thermodynamic beta and \wedge is the de Broglie wavelength. Additionally, molecular dynamics (MD) steps are usually combined together with GCMC simulations to reduce the thermal instability or stress introduced by randomly inserting and moving atoms, as know as the hybird MC/MD method in Chap. 4.4 of Frenkel 2001 [12]. Atomic structures in my thesis are generated by Atomeye, a high efficient

visualization tool for millions of atoms. [15]

2.3 Deep Learning and Neural Network

As previously mentioned in Chapter 2.1, DFT calculations are accurate but also computationally costly. In order to solve the short time span of DFT simulations, researchers fit DFT results to classical force fields or empirical interatomic potentials, which are simpler analytical formulas or functional. Classical force fields or empirical interatomic potentials simplify the description of inter-atomic interactions by summing components of the short-ranged bonding[16], angular[17], dihedral[18], and long-ranged Coulomb interaction[19]. Empirical potentials can be used in large-scale atomistic simulations with a reduced computational cost. Scientists and researchers have been constantly working on fitting more accurate empirical potentials to improve statistical sampling and accuracy of MD and MC simulations for the longer time domain. Due to the simplicity of analytical formulas and costly DFT calculations, empirical potentials can only focus on a limited number of material properties of the fitted system. As the number of species included in the system increases, it is also more difficult to fit the desired empirical potential. Besides, empirical potentials are, in general, good at describing the interactions close to the equilibrium, but not very well at intermediate or transitional states. Therefore, to study the early nucleation stage of multi-component systems via vacancy diffusion, a more complex functional need to be used, which could be machine learning or neural network (NN) methods.

Recently, machine learning methods have been widely used in materials science to construct the interatomic force fields in complex multi-component systems[20], predict material properties[21, 22]. Deep learning (or NN) is a special category of machine learning models that uses a network of neurons, which are arranged in (fully/partially) interconnected layers. A NN works similarly to the human brain's neural connec-

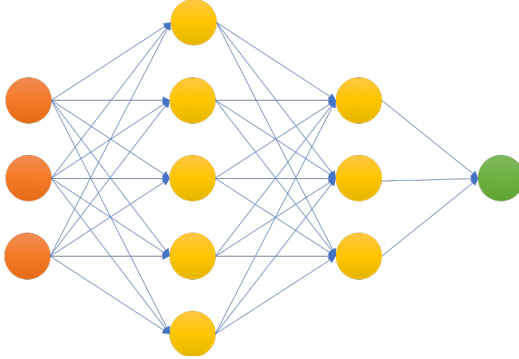


Figure 2.2: Illustration plot of a neural network. Orange, yellow, and green nodes indicate the input layer, hidden layers, and output, respectively.

tivity, which will be activated under certain circumstances using various activation functions. NNs are non-linear functions with parameters in different layers, called weights. Weights are optimizable through the back-propagation method of a cost function with respect to each weight. The input layer collects input patterns. The output layer has classifications or regression values to which input patterns are related. Hidden layers fine-tune the input weighting parameters until the NN’s cost function is minimal. It is hypothesized that hidden layers extrapolate features in the input data that have predictive power about the outputs. In Figure 2.2, a two-layer NN is shown. Three orange nodes on the left indicate input nodes, which can be atom species encoding in the on-lattice bulk diffusion model. Yellow nodes in the middle are two layers of fully connected hidden layers. The green node on the right is the output layer, which can be the diffusion barrier. In practice, the neural network architecture will be much more complicated. Details of fitting diffusion barriers will be discussed in Chapter VI.

2.4 Kinetic Monte Carlo Simulation

Many real reactions will take a long time, for example, hours, to happen, so the reaction kinetics are difficult to observe by only using DFT calculations or MD. As

discussed in Section 2.2.2, MC method is used here to help to solve stochastic time evolution in a much longer time scale. Much previous research used this method to simulate vacancy bulk diffusion, surface diffusion, and surface growth. [12, 23] A typical kMC method is shown in Algorithm 1.

Algorithm 1 Kinetic Monte Carlo Algorithm

- 1: Start the simulation at time $t = 0$.
- 2: **while** $t < t_{Max}$ Or $epoch < epoch_{Max}$ **do**
- 3: Build or update an event list for all the possible event i with rate r_i in the system.
- 4: Calculate the cumulative rate $R = \sum_{j=1}^N r_j$, where N is the total number of events.
- 5: Calculate probability, p_i , of event i by normalizing r_i by R .
- 6: Generate two uniform random number $u, v \in (0, 1]$.
- 7: Choose the event i based on, $\sum_{k=1}^{i-1} p_k < u < \sum_{k=1}^i p_k$.
- 8: Carry out the event i .
- 9: Update the time with $t = t + \Delta t$, where Δt is obtained via

$$\Delta t = -\frac{\log v}{R_N} \quad (2.8)$$

-
- 10: **end while**
-

For a system of vacancy on-lattice diffusion in bulk materials, each event rate can be calculated from DFT with nudged elastic band (NEB) method in principle. However, NEB calculations are extremely time-consuming for simulating billions of steps for kMC. And the relationship between diffusion barriers and energy differences are not linear for multi-component systems. Therefore, the NN functional is trained based on DFT calculations to predict diffusion barriers. Thus, we can build a multi-scale methodology, which combines DFT, NN, and kMC, to study the thermodynamics and kinetics of the early nucleation stage of GP zone in Al alloys.

CHAPTER III

Electronic Mechanism of H Adsorptions on ZnO Surfaces

In this chapter, the thermodynamic driving force of H adsorption on anion-terminated ($000\bar{1}$) surfaces of pure and doped wurtzite ZnO, which is the dielectric substrate for Ag thin film deposition by sputtering, are investigated under varying H surface coverage conditions. A $\frac{1}{2}$ ML of adsorbed H changes the electronic structure of pure ZnO ($000\bar{1}$) surface from metallic to semiconductor state by saturating unpaired electrons of surface oxygen atoms. This closed-shell electron configuration of ZnO ($000\bar{1}$) surface significantly reduces the adsorption strengths of subsequent H atoms, making the dissociative adsorption of a hydrogen molecule endothermic. A simple electron counting model is applied to predict and tune the coverage-dependent H adsorption strengths on doped ZnO surfaces. The equilibrium H coverage, above which the dissociative adsorption of a hydrogen molecule is endothermic, will decrease when doping elements (such as Al, Ti, and V) have more valence electrons than Zn. We also expand the method of tuning H equilibrium coverage to other similar polar semiconductors, such as wurtzite GaN ($000\bar{1}$), and zincblende ZnS ($\overline{1}\overline{1}\overline{1}$) surfaces. This method provides a general way to generate desired surface configurations of dielectric substrates before sputtering. The results will be used in the following chapter, Chapter IV, where multiscale simulation efforts are made to improving the Ag thin-film

quality during sputtering by changing substrate structures and chemistry.

3.1 Introduction

H adsorption on solid surfaces is critical to determine the electronic [24, 25], optical [26, 27], catalytic [28, 29, 30] and many other material applications based on surface physical and chemical properties. For example, the catalytic activities of noble metal catalysts depend on the adsorption strength of critical reaction intermediates on noble metal surfaces at steady states[31]. The surface electronic structures of oxides, such as ZnO, can change significantly with a different surface coverage of H atoms, and there are still debates on whether the origin of the n-type ZnO conductivity results from adsorbed H on ZnO surfaces[32]. In addition, semiconductor oxides are used as the substrate materials for the metallic thin films, whose adhesion strengths on these substrates can be reduced significantly because of adsorbed H on substrate surfaces, resulting in thin-film dewetting and the formation of the undesired discontinued islands[33, 34].

There have been many theoretical studies based on first-principles calculations to investigate H adsorption on both metal and oxide surfaces. The adsorption strengths of H and other adsorbates on surfaces depend not only on the interaction between the surface and a single adsorbed atom/molecule but also on the lateral interactions between adsorbates. Usually, the lateral interactions are relatively strong for adsorbates with relatively large atomic sizes, such as oxygen (O), hydroxyl (OH) and carbon monoxide (CO)[35, 31]. It is expected that H atoms have relatively weak lateral interactions. First-principles calculations confirmed that H adsorption strength increases slightly and continuously when H surface coverage θ_H increases from 0 ML to 1 ML on metal surfaces [36]. Thus, H coverage on metal surfaces at equilibrium conditions changes smoothly with H chemical potential in the reservoir, and the Langmuir model can be used to describe the adsorption isotherm of H atoms in many circumstances

[37].

On semiconductor surfaces, the coverage-dependent H adsorption strengths may show different characteristics compared to those on metal surfaces. H coverage on these semiconductor surfaces at equilibrium conditions can change discontinuously by varying H chemical potential in the reservoir. Surface phase diagrams of H adsorption are applied to describe the stable surface structure with different H coverage [38, 39, 40]. Clean semiconductor surfaces contain unpaired electrons in dangling chemical bonds and can be energetically unstable [41, 42, 43, 44, 45]. These surfaces can be stabilized by either surface reconstructions or adsorptions under different environmental conditions [46, 47, 40, 48, 49, 50], and the electron counting rule [51] plays an important role. Recently, a simple electron counting model is developed to predict and study the half-Heusler surfaces of CoTiSb [52]. Similarly, the electron counting rule can also be applied to H adsorptions on semiconductor surfaces. So far many surface phase diagrams were obtained case-by-case using first-principles calculations. Most of the reported unreconstructed surfaces with lowest energies [47, 49, 50] still follow the electron counting rule. Based on the understanding of the electron counting rule, it is easy to predict equilibrium H coverage on a given surface construction. However, a general method to manipulate H surface coverage is still missing.

Many efforts have been made to study H adsorption on surfaces of ZnO [53, 47, 39, 49, 40, 48, 50], a wide-band-gap semiconductor widely used in the fields of catalysis, gas sensing, and optoelectronics [54, 55]. There are also a few studies on surfaces of ZnO with dopant elements, like Al and Mg [56, 57]. Since there are increasing applications of doped ZnO and other semiconductors depending on their surface structures and electronic properties [58, 59, 56, 60, 61, 62, 63, 64], it is necessary to explore the general principles that guide H adsorption strengths on a wide range of pure and doped ZnO and similar semiconductor surfaces. Especially, it will be interesting to verify for these general cases the accuracy of the electron counting model, which was

recently applied to determine the atomic and electronic structures of (001) surface of CoTiSb, a prototypical semiconducting half-Heusler compound[52].

When ZnO bulk structure is chopped into slabs along [0001] directions, two types of surfaces, O-terminated ($(000\bar{1})$) surface, and Zn-terminated ((0001)) surface are exposed as shown in Figure 3.2. These two surfaces were found to have different stabilization principles[40]: the Zn-terminated ((0001)) surface usually has corrugated morphology and complex surface reconstructions because the transition-metal element Zn is more flexible with respect to bonding orientation [42, 65]; the O-terminated ($(000\bar{1})$) surface is usually flat on the top layer with different coverage and occupation sites for O and H atoms depending on their chemical potentials because O prefers the bonding configurations with certain bond angles and nearest neighbors [47, 40]. In addition, many functional applications of ZnO surfaces are used in oxygen-rich environments, where there are few oxygen vacancies on ZnO ($(000\bar{1})$) surface [47, 40, 48]. For these reasons, we use the simple O-terminated ($(000\bar{1})$) wurtzite ZnO by its bulk-terminated ideal form (the top surface in Figure 3.2) as the model system to investigate the effects of electronic structures and dopant elements on the coverage-dependent H adsorption strength in this study.

3.2 Coverage-dependent Hydrogen Adsorption Energies on ZnO ($(000\bar{1})$) Surface

We performed first-principles calculations based on DFT by using Vienna Ab-Initio Simulation Package (VASP) [66, 67]. Projector augmented wave (PAW) [68] potentials with Perdew-Burke-Ernzerhof (PBE) [10] exchange-correlation functional and the Hubbard U correction [69] were used. We applied GGA+U with $U_{\text{eff}} = U - J = 5.0\text{eV}$ on Zn d orbitals as reported in literature[70, 71]. Several other Hubbard U correction parameters ($U_{\text{eff}} = 3.0$ or 7.5 eV) were also tested and showed

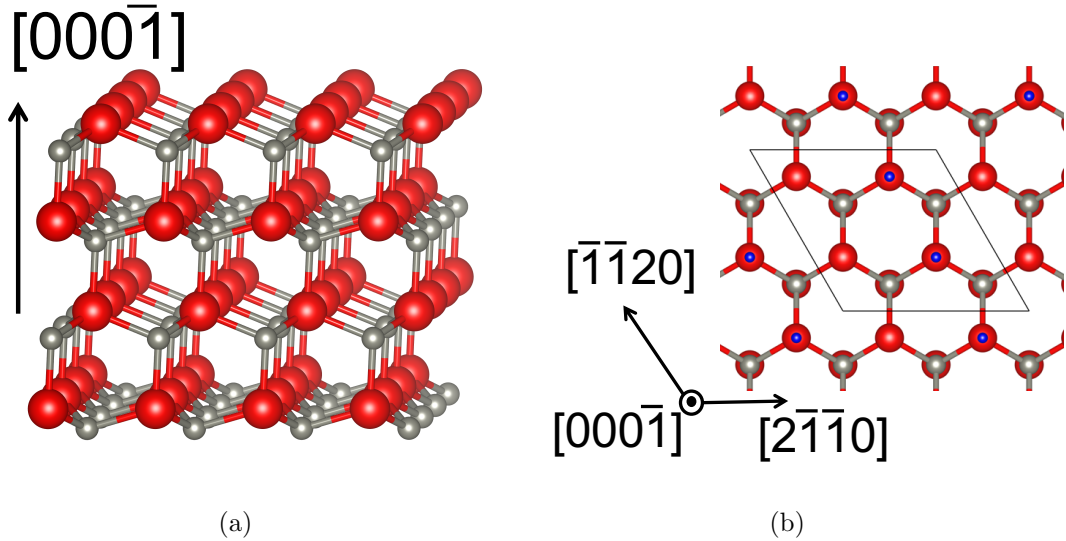


Figure 3.1: Schematic of (2×2) supercell used to model $(000\bar{1})$ wurtzite ZnO surface with H adsorption. (a) and (b): Schematic of (2×2) supercell used to model $(000\bar{1})$ wurtzite ZnO surface with H adsorption. Large red, small grey and small blue atoms are O, Zn and H atoms, respectively. (a) is the side view projection of ZnO $(000\bar{1})$ slabs, (b) is the top view of (2×2) O-terminated $(000\bar{1})$ ZnO surface with $\frac{1}{2}$ ML adsorbed H.

no significant effects on H adsorption energies. K-points sampling for Brillouin zone integration was performed on a grid of $6 \times 6 \times 1$, $6 \times 4 \times 1$ with Monkhorst-Pack meshing scheme for (2×2) and (2×3) surface, respectively[72]. An energy cut-off of 450.0 eV was used in the calculation. The electronic convergence threshold was set as 10^{-4} eV. The wurtzite ZnO $(000\bar{1})$ surfaces were constructed by periodic supercell slab models. (2×2) supercells with a vacuum layer of 18 Å in the directions perpendicular to the surfaces were applied as shown in Figure 3.2 and 3.2. Each slab contains eight layers of Zn-O repeating units along $[0001]$ direction. Since the ZnO surface slab supercell is not symmetric along $[0001]$ direction, we tested the dipole effects on H adsorption energies and found the dipole effects are minimal if the passivation of the Zn-terminated surface eliminates the artificial electron transfer described as the following. So only the results corresponding to no dipole corrections are reported in this study.

As shown in Figure 3.2, two types of surfaces are exposed, O-terminated ($(000\bar{1})$) surfaces and Zn-terminated ((0001)) surfaces, are presented in ZnO slab by its bulk-terminated ideal form. In theoretical modeling, if both sides of a surface slab layer are exposed without modifications, there will be an unbalanced electron transfer from the Zn-terminated surface to O-terminated surface[53]. In reality, if the O-terminated surface is exposed to the external environment, the Zn-terminated surface usually is connected to a substrate, which can act as an electron reservoir and compensate unsaturated electrons on the Zn-terminated surface. Many methods have been applied to reduce this artificial electron transfer, such as the introduction of pseudo-hydrogen passivation atoms, Zn vacancies and other adsorbates on Zn-terminated surfaces[45, 73, 57].

In this work, we focused on O-terminated ($(000\bar{1})$) ZnO surface, where H atoms are adsorbed on the top of each surface O atoms as shown in Figure 3.2. Zn-terminated ((0001)) surface on the other side of the slab model was passivated by two different methods to examine their effect on long-distance surface-to-surface electron transfer in the same supercell[1]. First, $\frac{1}{4}$ ML of Zn vacancy was introduced on the top layer of the Zn-terminated surface in a (2×2) supercell. Second, pseudo-hydrogen atoms with different numbers of valence electrons were introduced on the top layer of the Zn-terminated surface. Each Zn atom on the top layer of the Zn-terminated surface was bonded with one pseudo-hydrogen atom, which can have 1.5, 1.0 or 0.5 electrons (denoted as $H_{1.5}$, $H_{1.0}$ and $H_{0.5}$, respectively). In this paper, all the adsorption energy calculations and electronic structure analyses were conducted on the supercells with $H_{1.5}$ -passivated Zn-terminated surfaces unless otherwise specified.

As mentioned in Section 3.2, the above coverage-dependent H adsorption strengths E_{ad}^H on O-terminated ($(000\bar{1})$) ZnO surface may change due to different passivation methods on the Zn-terminated ((0001)) surface, where each Zn atom has a dangling bond with 0.5 unpaired electron in its bulk-terminated ideal form. The dangling

bond of each surface Zn atom should be emptied to reach the passivated structure and eliminate the artificial charge transfer from (0001) to (000 $\bar{1}$) surface according to the classical electron counting model[51]. It can be achieved by generating a $\frac{1}{4}$ ML Zn vacancy on (0001) surface layer (one Zn vacancy in the (2×2) supercell) because the 0.5 unpaired electrons from each of 3 remaining Zn atoms on (0001) surface can transfer to each of 3 O atoms that are the first-nearest neighbors of the Zn vacancy to form the stable closed-shell electron configurations. In addition, the passivated (0001) surface can also be achieved by adding one atom, such as a pseudo-hydrogen atom with 1.5 electrons ($H_{1.5}$), to each Zn atom on (0001) surface to fill the dangling bond.

Table 3.1: The coverage-dependent adsorption energy of H atom E_{ad}^H in unit of eV on (2×2) O-terminated (000 $\bar{1}$) ZnO surface with different mechanisms to passivate the Zn-terminated (0001) surface, including a clean Zn-terminated surface, a $\frac{1}{4}$ ML Zn vacancy (V_{Zn}) on the Zn-terminated surface and pseudo-hydrogen atoms with different numbers of valence charges (1.5, 1.0 and 0.5 electron, respectively) at each Zn site on the Zn-terminated surface ($H_{1.5}$, $H_{1.0}$ and $H_{0.5}$).

| (eV/Atom) | 0.25ML | 0.5ML | 0.75ML | 1ML |
|---------------------|--------|-------|--------|------|
| V_{Zn} | -2.43 | -2.18 | 0.43 | 0.95 |
| $H_{1.5}$ | -2.45 | -2.28 | 0.42 | 0.96 |
| $H_{1.0}$ | -2.45 | -2.27 | 0.11 | 0.95 |
| $H_{0.5}$ | -2.38 | -1.82 | 0.43 | 0.98 |
| Clean Zn-terminated | -2.34 | -1.49 | 0.52 | 0.95 |

Table 3.1 lists the H adsorption energies on (2×2) (000 $\bar{1}$) ZnO calculated using different passivation methods: the addition of Zn vacancies or (pseudo-)hydrogen atoms with different numbers of valence charges ($H_{1.5}$, $H_{1.0}$, and $H_{0.5}$) on (0001) surface. $\frac{1}{4}$ ML Zn vacancy (V_{Zn}) and $H_{1.5}$ generate almost the same E_{ad}^H on (000 $\bar{1}$) for all investigated H surface coverages θ_H . These results confirm that both methods can fully passivate the Zn-terminated surface and eliminate the artificial electron transfer in the supercell. Meanwhile, an obvious difference between $H_{1.0}$ and $H_{1.5}$ cases can be observed for the adsorption of the third H atom in the (2×2) supercell ($\theta_H = 0.75$

ML), where E_{ad} of $\text{H}_{1.0}$ case is 0.11 eV, ~ 0.3 eV lower than the values for V_{Zn} and $\text{H}_{1.5}$ cases. This is because one $\text{H}_{1.0}$ atom cannot completely fill the dangling bond of each Zn atom on (0001). For the cases of Zn-terminated surfaces without pseudo-hydrogen atoms (Clean Zn-terminated in Table 3.1) and the cases of $\text{H}_{0.5}$, because there are large amounts of electron transfers from Zn-terminated to O-terminated surfaces, H adsorption energies on the O-terminated surfaces are much weaker than those of V_{Zn} and $\text{H}_{1.5}$ cases for $\theta_{\text{H}} = 0.5$ and 0.75 ML. Here, only the results corresponding to $\text{H}_{1.5}$ cases (fully passivated Zn-terminated surfaces) are reported.

Hydrogen adsorption energy E_{ad}^{H} with H surface coverage θ_{H} equal to $\frac{n}{m}$ ML is calculated as:

$$E_{\text{ad}}^{\text{H}}(\theta_{\text{H}} = \frac{n}{m} \text{ML}) = E_{\text{slab}+n\text{H}} - E_{\text{slab}+(n-1)\text{H}} - \frac{1}{2}E_{\text{H}_2} \quad (3.1)$$

Here $E_{\text{slab}+n\text{H}}$ and $E_{\text{slab}+(n-1)\text{H}}$ is the total energy of surface slab supercell containing n and $n - 1$ adsorbed H atoms, respectively, and E_{H_2} is the energy of an isolated H_2 molecule. The $(x \times y)$ surface slab supercell itself contains $m = x \cdot y$ duplicates of (1×1) unit cell of 2D surface lattice, so $m = 4$ and $m = 6$ for (2×2) and (2×3) slab supercells, respectively. As shown in Figure 3.2, E_{ad}^{H} on platinum (Pt) (111) surface only increases slightly with a rising surface H coverage θ_{H} ($\delta E_{\text{ad}}^{\text{H}} \sim 0.1$ eV when θ_{H} increases from $\frac{1}{4}$ ML to 1 ML). On the contrary, E_{ad}^{H} is highly negative and increases slightly on (2×2) slab supercell of $(000\bar{1})$ ZnO when $\theta_{\text{H}} = \frac{1}{4}$ and $\frac{1}{2}$ ML, then E_{ad}^{H} jumps up suddenly after θ_{H} above $\frac{1}{2}$ ML.

In order to confirm the critical transition, E_{ad}^{H} for a larger wurtzite ZnO $(000\bar{1})$ slab supercell with (2×3) in-plane periodicity was also studied. The abrupt increase of E_{ad}^{H} , again, happens when θ_{H} is higher than $\frac{1}{2}$ ML, as shown in Figure 3.2. It can be concluded that there is a large driving force ($E_{\text{ad}}^{\text{H}} < -2$ eV per H atom) for an isolated H_2 molecule to dissociate into two H atoms adsorbed on ZnO $(000\bar{1})$ surface

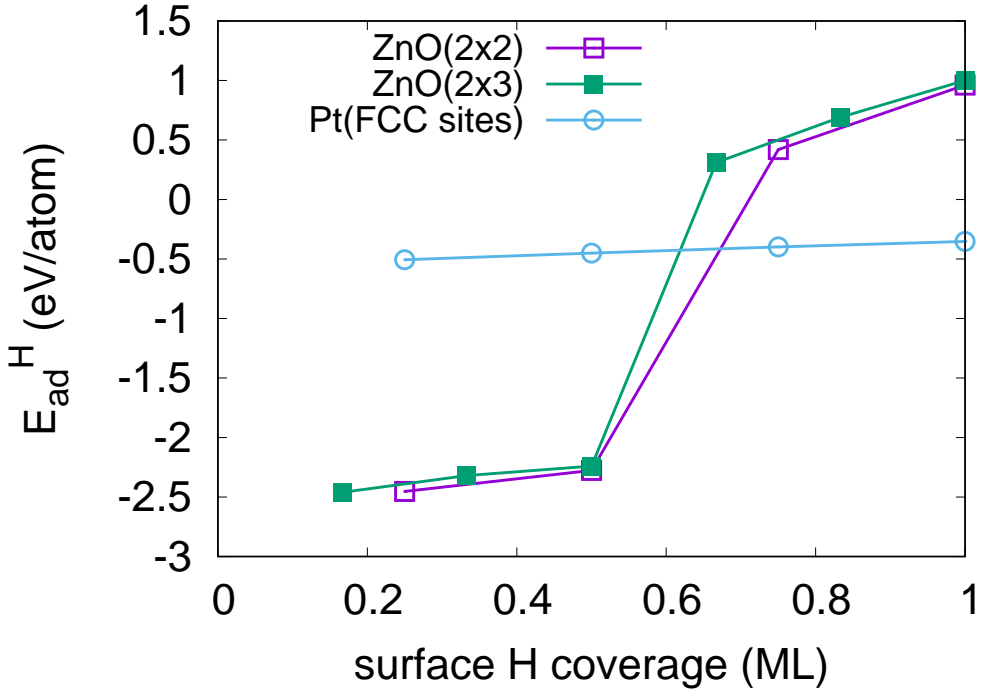


Figure 3.2: H adsorption energies E_{ad}^H defined by Equation 3.1 on ZnO (000 $\bar{1}$) and Pt (111) surfaces with different H coverage

if θ_H smaller than $\frac{1}{2}$ ML, above which such adsorption-dissociation reaction becomes highly endothermic and difficult to occur ($E_{ad}^H > 0$). These results are consistent with previous theoretical calculations and experimental characterizations that $\frac{1}{2}$ ML of adsorbed H were often observed on ZnO (000 $\bar{1}$) surface[33, 47, 40].

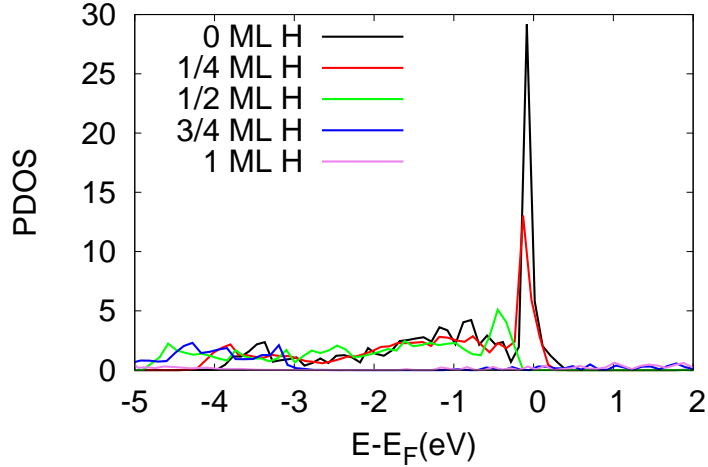
3.3 Electronic Structure Analyses and Electron Counting Model

Electronic structures of surface oxygen atoms before and after H adsorption are analyzed in order to understand the mechanism to determine the critical transition of E_{ad}^H on ZnO (000 $\bar{1}$) surface. We plot PDOS of all four surface O atoms on the top layer of (2 \times 2) ZnO (000 $\bar{1}$) surface with different H coverage in Figure 3.3. PDOS of O atoms for $\theta_H = 0$ ML and $\frac{1}{4}$ ML cases have strong peaks at the Fermi level, so these ZnO surfaces are in metallic states. When ZnO surface is covered by $\frac{1}{2}$ ML of H atoms, the Fermi level is 0.1 eV above valence band maximum, making these ZnO surfaces in

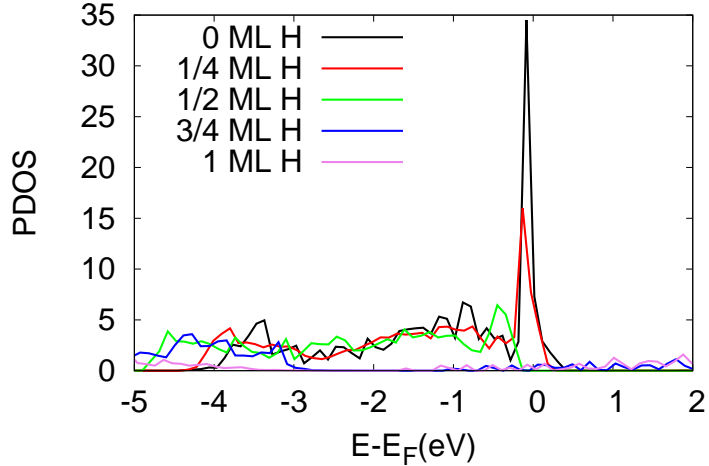
semiconductor states. The cases of $\theta_H = \frac{3}{4}$ and 1 ML keep in semiconductor states by further decreasing the valence band maximum to the positions much lower than the Fermi level. PDOS of all surface atoms, including all O, Zn and adsorbed H atoms on the top layer of ZnO (000 $\bar{1}$) surface, are plotted in Figure 3.3 to confirm the above analyses. Similar to Figure 3.3, PDOS of all surface atoms for the cases of $\theta_H = 0$ ML and $\frac{1}{4}$ ML show strong peaks in the Fermi level, while the PDOS of all surface atoms for the cases of $\theta_H = \frac{1}{2}$ ML and above exhibit semiconductor characteristics. Thus, $\frac{1}{2}$ ML is the critical θ_H to transform ZnO (000 $\bar{1}$) surface from metallic into semiconductor states.

The coincidence ($\frac{1}{2}$ ML) of the critical θ_H for the abrupt change of E_{ad}^H and the critical θ_H for the metal-semiconductor transition indicates that E_{ad}^H is controlled by surface electronic structures. This coincidence can be explained by the electron counting model[51]. Each Zn has 2 valence electrons, and each O has 6 valence electrons. In bulk wurtzite lattice, each Zn/O atom connects to 4 nearby O/Zn atoms so that every Zn-O bond has 2 valence electrons, in which 1.5 electrons are contributed from O and 0.5 electron is from Zn. After bulk ZnO is chopped into two slabs with two surfaces in [0001] direction, each surface O and Zn atom has one broken Zn-O bond, as shown in Figure 3.2. For Zn-terminated (0001) surface, we applied appropriate methods to passivate the dangling bonds as explained above. For O-terminated (000 $\bar{1}$) surface, each O atom requires 0.5 more electrons to fill its dangling bond and reach the closed-shell electron configuration. Thus, the electrons of clean O-terminated (000 $\bar{1}$) surface are in open-shell configurations.

The unpaired electrons from surface O atoms are delocalized, making the ZnO surface in metallic states. There is a large energetic driving force for surface O atoms to reach closed-shell configurations, meaning ZnO surface has a strong adsorption strength to any atoms/molecules that can contribute electrons to surface O atoms, such as H. In a simple picture, each H atom can contribute one electron to make 2



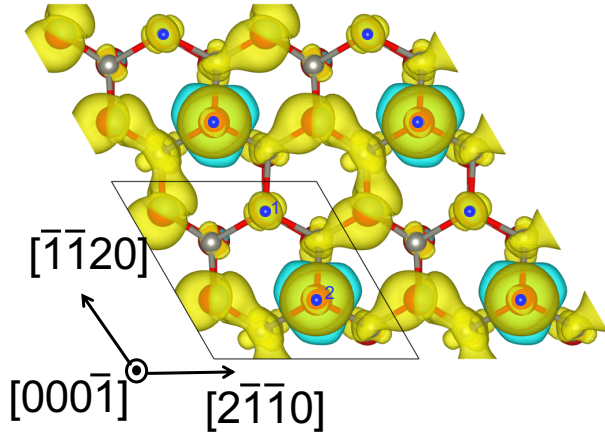
(a)



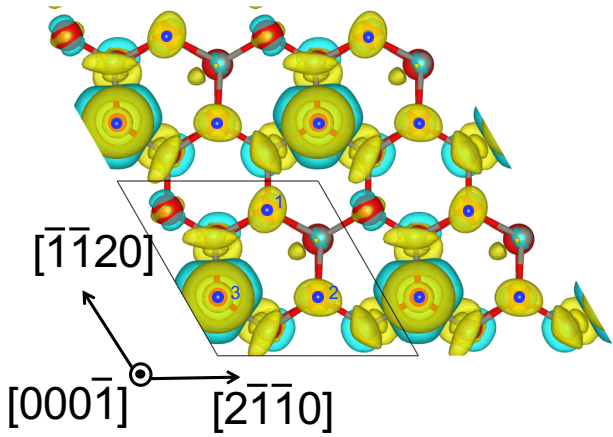
(b)

Figure 3.3: PDOS for all the surface atoms on pure ZnO (2×2) (000\bar{1}) surface under different H coverage. (a) PDOS for all the surface O atoms on pure ZnO (2×2) (000\bar{1}) surface under different H coverage. (b) PDOS of all O, Zn and adsorbed H atoms on the topmost layer of ZnO (000\bar{1}) surface under different H coverage.

surface O atoms on (000\bar{1}) ZnO surface transform into electron closed-shell configurations. Thus, once θ_H reaches $\frac{1}{2}$ ML, there are no unpaired electrons in delocalized states on (000\bar{1}) ZnO surface. Correspondingly, the surface transforms into a semiconductor state and has much weaker adsorption strength for the consecutive H atoms.



(a)



(b)

Figure 3.4: Top views of the charge density difference isosurfaces before and after H adsorption. Top views of the charge density difference isosurfaces before and after (a) the second H and (b) the third adsorption on ZnO ($000\bar{1}$) surface in (2×2) supercells, corresponding to $\Delta\rho(\theta_H = \frac{1}{2} \text{ ML})$ and $\Delta\rho(\theta_H = \frac{3}{4} \text{ ML})$ defined in Equation 3.2, respectively. Large red, small grey and small blue atoms are O, Zn and H atoms, respectively. Label 1, 2 and 3 in the plots denote the adsorption site for the first, second, and third H atom, respectively. The yellow and blue color indicate electron accumulation and annihilation with the isosurface of $0.001e/\text{\AA}^3$.

Such electron counting rule and the corresponding PDOS analyses can be further confirmed by the analyses of charge density difference on ZnO ($000\bar{1}$) surface due to

H adsorption. Here we define the charge density difference $\Delta\rho$ at different θ_H as the following

$$\Delta\rho(\theta_H = \frac{n}{m}\text{ML}) = \rho(\text{slab}+n\text{H}) - \rho(\text{slab}+(n-1)\text{H}) \quad (3.2)$$

Here $\rho(\text{slab}+n\text{H})$ and $\rho(\text{slab}+(n-1)\text{H})$ is the charge density of ZnO (000 $\bar{1}$) surface slab with n and $(n-1)$ adsorbed H atoms, respectively. For (2×2) supercell, $\Delta\rho(\theta_H = \frac{1}{2}\text{ ML})$ and $\Delta\rho(\theta_H = \frac{3}{4}\text{ ML})$ corresponds to the charge density difference induced by the adsorption of the second and third H atom in the supercell, as shown in Figure 3.3 and 3.3, respectively.

In Figure 3.3, the second H added on (2×2) ZnO (000 $\bar{1}$) surface induces charge density accumulation not only near this H atom itself but also other surface sites without H. Such delocalized $\Delta\rho$ is consistent with the metallic state of ZnO (000 $\bar{1}$) surface with $\theta_H < \frac{1}{2}\text{ ML}$. The increase of charge density at multiple surface sites indicates that the electron from the second H atom intends to saturate the unpaired electrons on the whole surface and induce the metal-semiconductor transition. In Figure 3.3, the third H added on (2×2) ZnO (000 $\bar{1}$) surface results in charge density accumulation mostly located near the third H atom itself, with a localized s-orbital-like isosurface of $\Delta\rho$ shown in Figure 3.3. Such localized $\Delta\rho$ is consistent with the semiconductor electronic structure of ZnO (000 $\bar{1}$) surface with $\theta_H \geq \frac{1}{2}\text{ ML}$.

3.4 Hydrogen Adsorption on (000 $\bar{1}$) Surface of ZnO with Dopants

In this study, we find that the electron counting model can also be applied to explain the variation of E_{ad}^{H} with θ_H on (000 $\bar{1}$) surfaces of doped ZnO[51]. Different metallic elements are added as substitutional dopants on Zn lattice sites. Because these dopant elements can have different numbers of valence electrons than Zn, it can change the required number of adsorbed H atoms to saturate all surface O atoms

and induce the metal-semiconductor transition on the surface. Correspondingly, the critical θ_H for the transition of E_{ad}^H can also be varied. Based on this mechanism, one Zn atom in ZnO bulk lattice is replaced by various types of dopant atoms.

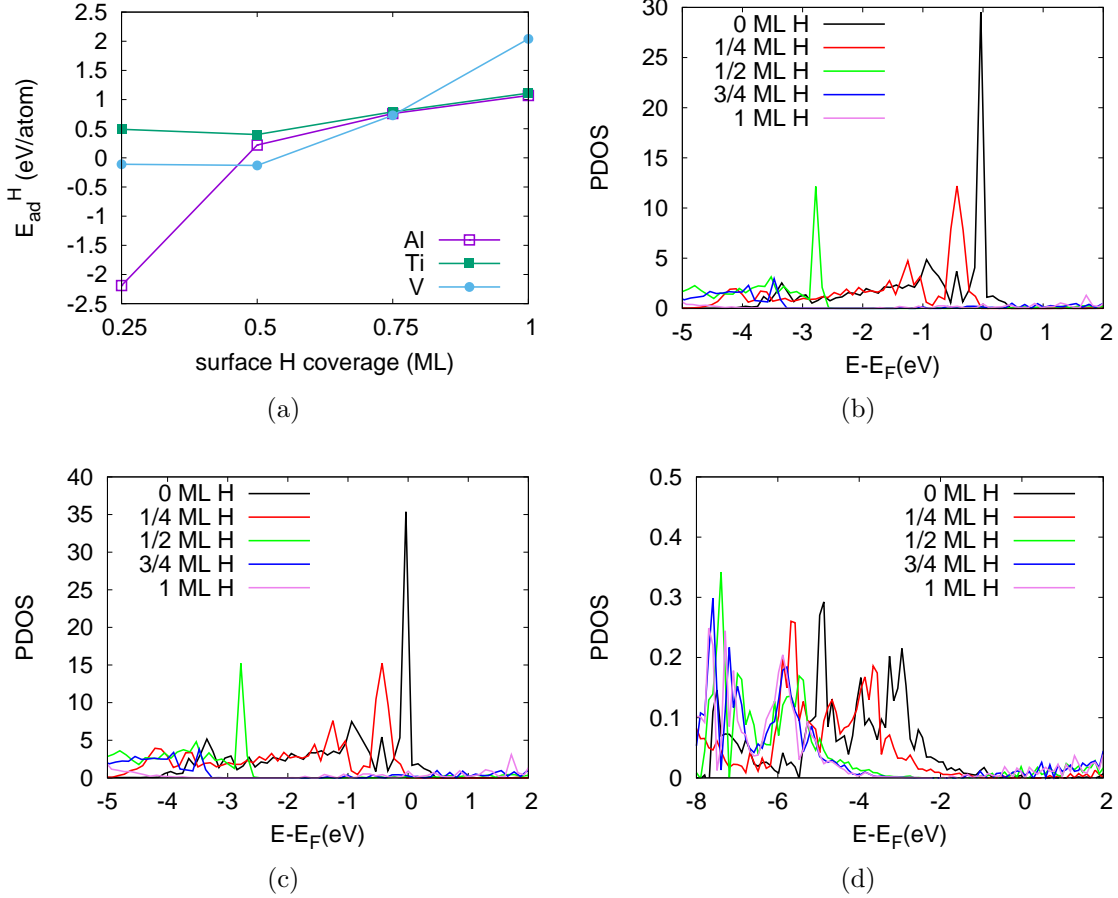
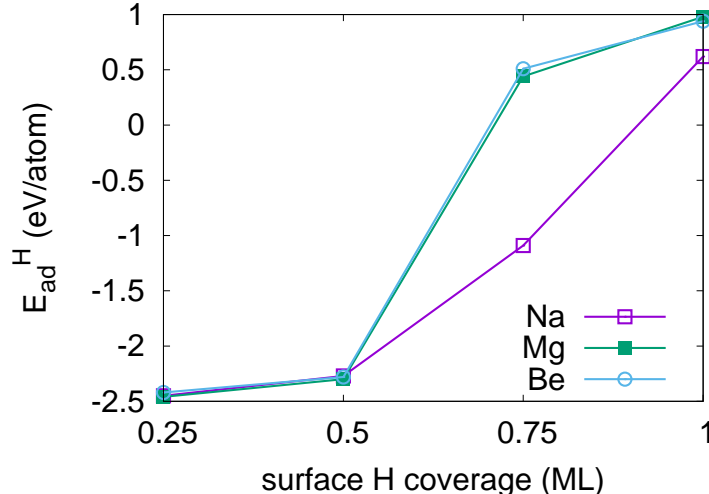
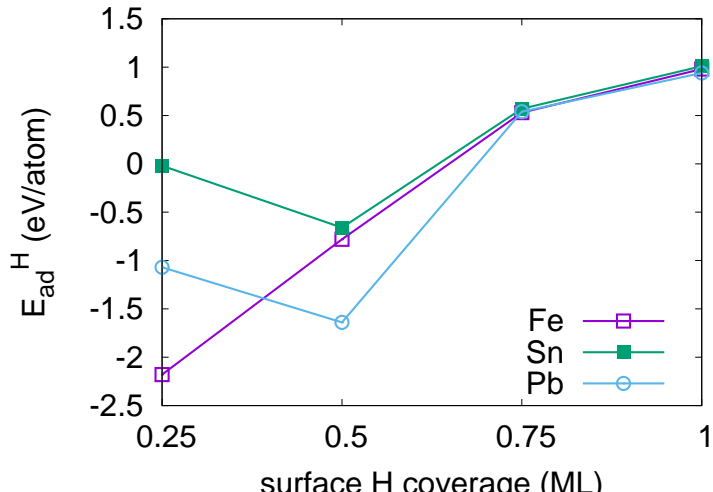


Figure 3.5: H adsorptions on ZnO surfaces with subsurface doping element: Al, Ti, V. (a) E_{ad}^H on (2×2) ZnO (0001) surface with one substitutional dopant atom at Zn site. Each dopant atom has more valence electrons than Zn. (b) PDOS for all the O atoms on top surface layer of Al-doped ZnO (0001) under different θ_H . (c) PDOS of all O, Zn and adsorbed H atoms on the topmost layer of Al-doped ZnO (0001) under different θ_H . (d) PDOS for Al atom in the bulk layer of Al-doped ZnO (0001) under different θ_H .



(a)



(b)

Figure 3.6: H adsorptions on ZnO surfaces with subsurface doping element: Na, Mg, Be, Fe, Sn, Pb. (a) E_{ad}^H on (2×2) $\text{ZnO}(000\bar{1})$ surface with one substitutional dopant atom at bulk Zn sites. Each dopant atom has equal or less valence electrons than Zn. (b) E_{ad}^H on (2×2) $\text{ZnO}(000\bar{1})$ surface with one substitutional dopant atom at bulk Zn sites. Each dopant atom has multiple common charge states.

The dopant atoms located at slab layers with different distances to the top $(000\bar{1})$ surface layer are investigated, and our results show that the location of such dopant atom does not have a significant effect on H adsorption energetics and the critical θ_H . As illustrated in Table 3.2, H adsorption energies with the substitutional dopant

elements on Zn lattice sites at different layers away from the O-terminated ($(000\bar{1})$) surfaces are listed. H adsorption energies do not show significant variations for the dopant atom at varying distances to the top layer of ($000\bar{1}$) surfaces. Thus, the results for one dopant atom (Al, Ti, V, Na, Mg, Be, Fe, Sn, and Pb) at bulk Zn site far away from the top surface layer in (2×2) ZnO ($000\bar{1}$) supercells are summarized in Figure 3.6.

Table 3.2: The coverage-dependent adsorption energy of H atom E_{ad}^{H} (unit: eV/atom) on O-terminated ($000\bar{1}$) ZnO surface with substitutional Be dopant atom at different locations to the top surface layer. Layer 1 is at the Zn lattice site nearest to the top surface layer.

| eV/atom | 0.25ML | 0.5ML | 0.75ML | 1ML |
|---------|--------|-------|--------|------|
| Layer 1 | -2.71 | -2.39 | 0.52 | 0.97 |
| Layer 2 | -2.38 | -2.23 | 0.43 | 0.97 |
| Layer 3 | -2.42 | -2.28 | 0.51 | 0.94 |
| Layer 4 | -2.39 | -2.32 | 0.46 | 0.98 |

In Figure 3.4, all dopant atoms (Al, Ti, and V) have more valence electrons than Zn. For Al-doped ZnO surface, if the one extra valence electron from Al already transfers to O atoms on the top surface layer, only one H atom is required to saturate all 4 O atoms in a (2×2) supercell and induce the metal-semiconductor transition according to the electron counting model. Consistent with this interpretation, the H adsorption strength for the Al-doped ZnO surface in Figure 3.4 is as strong as the pure ZnO surface in Figure 3.2 when $\theta_{\text{H}} \leq \frac{1}{4}$ ML. Above this critical θ_{H} , E_{ad}^{H} suddenly increases to positive values, consistent with the proposed metal-semiconductor transition for ZnO surface. This interpretation is further confirmed by analyses of projected density of states (PDOS) of all four surface O atoms on (2×2) Al-doped ZnO surface in Figure 3.4. PDOS of O atoms with $\theta_{\text{H}} = 0$ ML case have strong peaks at the Fermi level. When Al-doped ZnO surfaces are covered by $\frac{1}{4}$ to 1 ML of H atoms, there are no peaks on the Fermi level, making these surfaces in semiconductor states. PDOS of all surface atoms, including all the O, Zn and adsorbed H atoms

on the topmost layer of Al-doped ZnO (000 $\bar{1}$) surface, are plotted in Figure 3.4 to confirm the above analyses. Similar to Figure 3.4, PDOS of all surface atoms for the case of $\theta_H = 0$ ML show strong peaks in the Fermi level, while PDOS of all surface atoms for the cases of $\theta_H = \frac{1}{4}$ ML and above exhibit semiconductor characteristics. PDOS of the Al atom, which is located at the third layer away from the (000 $\bar{1}$) O-term surface, under different H surface coverages is also plotted in Figure 3.4. As can be seen from the plot, there is no significant peak around the Fermi level for all the H surface coverages, showing that the bulk Al atom under different H surface coverages is also saturated in closed-shell electron configuration. Interestingly, PDOS of Al downshifts indicating a stronger bonding between Al and nearby O atoms as the H surface coverages increases.

If one Zn atom is replaced by one Ti or V atom in the (2×2) supercell, because both Ti and V have two or more valence electrons than Zn, all O atoms on (000 $\bar{1}$) surface are already saturated without any adsorbed H atoms. Therefore, both Ti-doped and V-doped ZnO surfaces have very weak H adsorption strengths with E_{ad}^H close to or above zero for all θ_H values in Figure 3.4. Meanwhile, if one Zn atom is replaced by one dopant atom with two valence electrons the same as Zn, such as beryllium (Be) or magnesium (Mg), the variations of E_{ad}^H with θ_H are almost the same as those on pure ZnO surface as shown in Figure 3.4, so the doped ZnO (000 $\bar{1}$) surfaces have strong H adsorption strength only when $\theta_H \leq \frac{1}{2}$ ML. If one Zn atom is replaced by a dopant atom with only one valence electron such as sodium (Na), the dopant can attract one electron from O atoms on (2×2) (000 $\bar{1}$) surface, so three H atoms are required to saturate all 4 O atoms in a (2×2) supercell. Correspondingly, this Na-doped ZnO (000 $\bar{1}$) surface has strong H adsorption strength when $\theta_H \leq \frac{3}{4}$ ML as shown in Figure 3.4.

Moreover, the dopant effects of elements with multiple common charge states are shown in Figure 3.4. Fe has both +2 and +3 charge states, so the Fe-doped ZnO

(000 $\bar{1}$) shows H adsorption strengths at the intermediate level between those on Mg-doped and Al-doped ZnO (000 $\bar{1}$) surfaces. It only demonstrates strong H adsorption strengths ($E_{\text{ad}}^{\text{H}} \ll 0$) only when $\theta_{\text{H}} \leq \frac{1}{2}$ ML, similar to the cases for Mg dopant, but the adsorption energy of the second H atom ($\theta_{\text{H}} = \frac{1}{2}$ ML) is much weaker than that of pure ZnO, similar to the cases for Al dopant. Meanwhile, Sn and Pb elements can have variant charge states ranging from +1 to +4, with +2 and +4 as the most common states[74]. Because of the +2 charge state, ZnO (000 $\bar{1}$) with either a Sn or Pb dopant atom show very weak H adsorption strengths ($E_{\text{ad}}^{\text{H}} \gg 0$) when $\theta_{\text{H}} > \frac{1}{2}$ ML, similar to the cases for Mg dopant. However, since each Sn or Pb atom can contribute more than 2 electrons to ZnO (000 $\bar{1}$) surface, H adsorption strengths are also significantly weakened when $\theta_{\text{H}} \leq \frac{1}{2}$ M. In addition, because the +3 charge state is not as stable as +2 or +4 states for Sn/Pb[74], E_{ad}^{H} of the first H atom ($\theta_{\text{H}} = \frac{1}{4}$ ML) is even weaker (more positive) than E_{ad}^{H} of the second H atom ($\theta_{\text{H}} = \frac{1}{2}$ ML).

3.5 Model Generalization for Other Polar Surfaces

According to Figure 3.6, in a (2 \times 2) supercell of ZnO (000 $\bar{1}$) surface, if one Zn atom is replaced by one metallic dopant atom with 1 (Na), 2 (Mg), 3 (Al) and 4 (Ti) valence electrons, the critical θ_{H} for the metal-semiconductor transition and the abrupt change of E_{ad}^{H} , denoted as $\theta_{\text{H}}^{\text{c}}$, is $\frac{3}{4}$, $\frac{1}{2}$, $\frac{1}{4}$ and 0 ML, respectively. $\theta_{\text{H}}^{\text{c}}$ is simply obtained by the requirement that all O atoms on the top surface layer should be fully saturated in closed-shell electron configuration according to the electron counting model. Thus, $\theta_{\text{H}}^{\text{c}}$ can be calculated for other (000 $\bar{1}$) surfaces of wurtzite structures, (111) surfaces of zincblende structures, and other semiconductor surfaces with two separate sublattices (one for cations and one for anions) and only the anions (O, N, S, etc.) on the top surface layer (*polar semiconductor surfaces*). Generally, with n_{dopant} types of dopant elements in bulk lattice, $\theta_{\text{H}}^{\text{c}}$ can be calculated in the unit of ML as

the following

$$\begin{aligned}\theta_H^c &= \left(\frac{8}{N_{\text{bond}}} - \frac{1}{N_{\text{bond}}} V_{\text{anion}} \right) \times 1.0 \text{ML} \\ &\quad - \sum_{i=1}^{n_{\text{dopant}}} \theta_{\text{dopant}}^i (V_{\text{dopant}}^i - V_{\text{cation}})\end{aligned}\tag{3.3}$$

Here V_{cation} , V_{anion} and V_{dopant}^i is the number of valence electrons for the cation element in bulk lattice, the anion element in bulk lattice and the dopant cation element i , respectively. N_{bond} is the number of bonds between one cation (anion) and its nearest anion (cation) neighbors in bulk lattice. θ_{dopant}^i is the concentration of the dopant element i per surface area (in unit of ML). For a Al-doped ZnO (000 $\bar{1}$) surface that has only one Al atom in a (2×2) supercell, $N_{\text{bond}} = 4$, $V_{\text{cation}} = 2$, $V_{\text{anion}} = 6$, $n_{\text{dopant}} = 1$, $V_{\text{dopant}}^1 = 3$ and $\theta_{\text{dopant}}^1 = \frac{1}{4}$ ML, so $\theta_H^c = \frac{1}{4}$ ML according to Equation 3.3, consistent with Al-doped result in Figure 3.4.

Equation 3.3 can be easily extended to the cases with multiple dopant elements ($n_{\text{dopant}} > 1$). For example, if two Zn atoms at bulk Zn substitutional sites are replaced by one Al dopant atom and one Ti dopant atom in a (2×3) supercell of ZnO (000 $\bar{1}$) surface, $n_{\text{dopant}} = 2$, $V_{\text{dopant}}^1 = 3$, $V_{\text{dopant}}^2 = 4$, and $\theta_{\text{dopant}}^1 = \theta_{\text{dopant}}^2 = \frac{1}{6}$ ML, so $\theta_H^c = 0$ ML according to Equation 3.3. This prediction is confirmed by our calculations of H adsorption strength on this Al-Ti-doped ZnO (000 $\bar{1}$) surface shown in Figure 3.5.

Equation 3.3 can also be easily extended to the cases of other defects such as vacancies. For example, recently it was reported that a stable ZnO (000 $\bar{1}$) surface configuration has $\frac{1}{3}$ ML Zn vacancies and 10 H atoms in a (3×3) (000 $\bar{1}$) surface unit cell[50]. Here the Zn vacancy can be regarded as a type of dopant cation with zero valence electron. Using the corresponding parameters ($N_{\text{bond}} = 4$, $V_{\text{anion}} = 6$, $n_{\text{dopant}} = 1$, $\theta_{\text{dopant}} = \frac{1}{3}$ ML, $V_{\text{dopant}} = 0$ and $V_{\text{cation}} = 2$), $\theta_H^c = \frac{7}{6}$ ML according to Equation 3.3, corresponding to 10.5 H atoms in a (3×3) ZnO (000 $\bar{1}$) surface unit cell. It means the adsorption of the 11th H atom in this unit cell would be too weak to occur under

normal environment conditions, consistent with the experimental observations and DFT calculations[50].

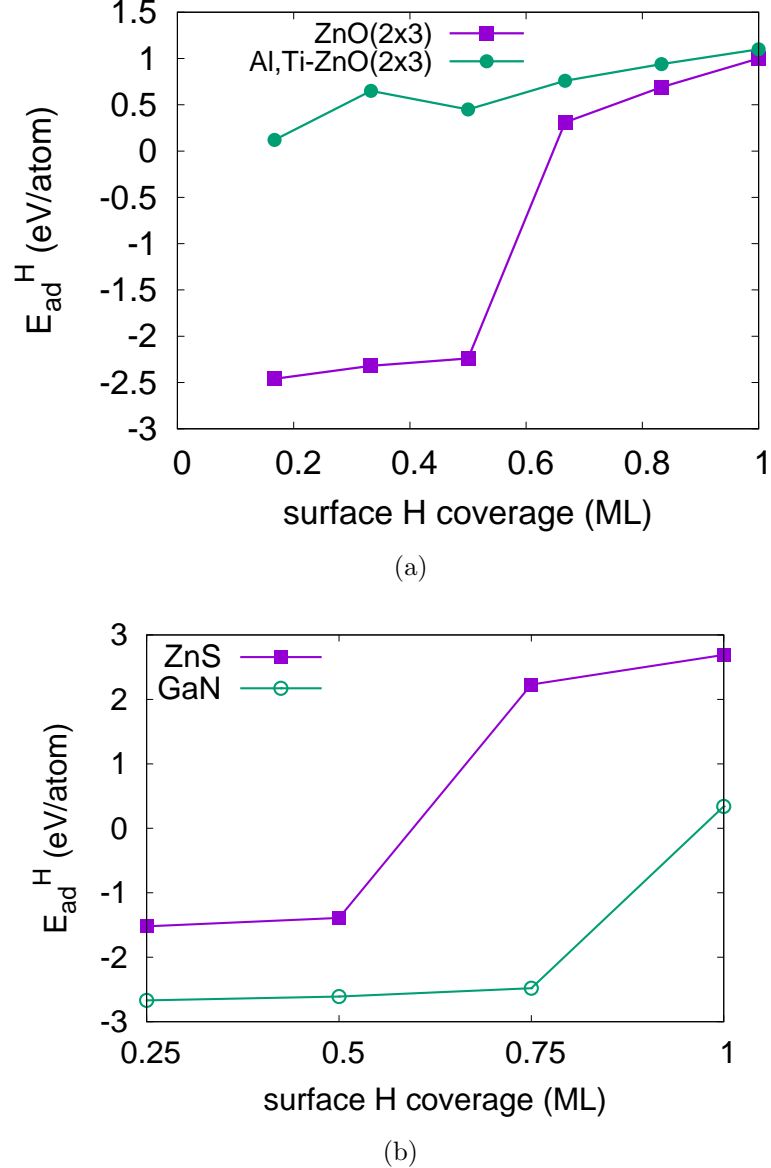


Figure 3.7: E_{ad}^H on (2×3) ZnO $(000\bar{1})$ surface with the co-existence of 1 Al substitutional dopant atom and 1 Ti substitutional dopant atom at bulk Zn sites. (a): E_{ad}^H on (2×2) zincblende ZnS $(\bar{1}\bar{1}\bar{1})$ and wurtzite GaN $(000\bar{1})$ surfaces with different θ_H .

The electron counting model and Equation 3.3 can be used to explain the H adsorption strength on other polar semiconductor surfaces. For example, sulfur(S)-terminated $(\bar{1}\bar{1}\bar{1})$ surface of zincblende ZnS have the similar atomistic structure and

valence electron configuration as those for wurtzite ZnO (000 $\bar{1}$). As shown in Figure 3.5, the dramatic decrease of H adsorption strength happens when θ_H increases from $\frac{1}{2}$ to $\frac{3}{4}$ ML, the same as ZnO in Figure 3.2. Moreover, for nitrogen(N)-terminated (000 $\bar{1}$) surface of wurtzite GaN, because each N atom has 5 valence electrons and 4 Ga-N bonds, $\frac{8-5}{4} = 0.75$ electron is required to saturate each N atom on (000 $\bar{1}$) surface once the GaN bulk lattice is chopped into two surfaces along [0001] direction. According to Equation 3.3, $N_{\text{bond}} = 4$, $V_{\text{anion}} = 5$, and $\theta_{\text{dopant}}^i = 0$ ML, so $\theta_H^c = \frac{3}{4}$ ML . Therefore, $\theta_H = \frac{3}{4}$ ML, equivalent to 3 hydrogen atoms in the supercell of a (2×2) GaN (000 $\bar{1}$) surface, can transform all 4 surface N atoms from metallic to semiconductor states. Correspondingly, the hydrogen adsorption strength decreases dramatically when θ_H increases from $\frac{3}{4}$ to 1 ML as shown in Figure 3.5.

3.6 Conclusions

The coverage-dependent adsorption of hydrogen atoms on O-terminated (000 $\bar{1}$) surface of wurtzite ZnO and other similar polar semiconductor surfaces behave differently than the counterparts on typical metal/alloy surfaces, where H adsorption strength usually decreases slightly and continuously (more positive values of E_{ad}^H in Figure 3.2) with increasing H surface coverage [36, 31]. The adsorption strength of individual H atom on these semiconductor surfaces strongly depends on hydrogen coverage and surface electronic structures. If the surface is in the metallic state, the hydrogen adsorption strength is so strong that the adsorption-dissociation reaction of a single H₂ molecule on this surface is highly exothermic at zero K ($E_{\text{ad}}^H < -2.0$ eV in Equation 3.1). If the surface is in semiconductor state, the hydrogen adsorption strength is so weak that the adsorption-dissociation reaction of a single H₂ molecule on this surface is endothermic at zero K ($E_{\text{ad}}^H > 0$ in Equation 3.1). The surface can be transformed from metallic to semiconductor state by either hydrogen adsorption on the surface or dopant elements in the bulk lattice to saturate unpaired electrons

of anion elements on the top surface layer. The critical H surface coverage θ_H^c to induce such metal-semiconductor transition, which is also the equilibrium H coverage at many experimental conditions [33, 47, 40], is determined by the classical electron counting model described in Equation 3.3 [51]. This model is confirmed by our investigations of H adsorption on $(000\bar{1})$ surfaces of ZnO with a series of doping elements (Na, Mg, Al, Ti, Fe, Sn, etc.). When doping elements (such as Be, Mg, Na) have equal or fewer valence electrons than Zn, the critical H coverage will remain unchanged or increase to higher coverages. When doping elements (such as Al, Ti, and V) have more valence electrons than Zn, the critical H coverage will decrease to lower coverages. When doping elements (such as Fe, Sn, and Pb) have multiple common charge states, the behavior of the critical H coverage will become sophisticated but still follows the general electron counting rule.

This simple electron counting model can be applied to determine and manipulate the equilibrium surface adsorption configurations for H and other adsorbates on different semiconductor polar surfaces with chemical dopant elements. It is different than the d-band model that is widely used to understand trends of H adsorption strengths on different transition metal surfaces [75, 76]. Since the driving force for surface reconstruction is also from the tendency to eliminate unpaired electrons and dangling bonds, the model can be used to identify the possible adsorbate and dopant configurations to obtain stable semiconductor surface structures [46, 51, 50]. It also suggests that the investigations of further adsorptions and depositions of other materials on these semiconductor surfaces should consider the coexistence of adsorbed H atoms at stable configurations. For example, in many optoelectronic applications, ZnO and other semiconductor oxides are used as the substrate materials for metallic thin films, whose adhesion strengths on these substrates can be reduced significantly because of adsorbed H on substrate surfaces, resulting in thin-film dewetting and the formation of the undesired discontinued islands [33, 34]. This study provides a critical

step to understand the substrate surface structures and adsorption characteristics for further investigations on thin-film qualities and optoelectronic properties. In the following chapter, Chapter IV, multiscale simulation efforts are made to improving the Ag thin-film quality during sputtering by changing substrate structures and chemistry based on our understanding of the H coverage on ZnO substrate.

CHAPTER IV

Grand Canonical Monte Carlo Simulations of Ag Thin Film Depositions

In this chapter, we utilize Grand Canonical Monte Carlo (GCMC) simulation to understand the possible reason why ZnO is the appropriate substrate for Ag thin film deposition. The quality of Ag thin film on the hexagonal surfaces of the substrate, like ZnO (000 $\bar{1}$), is robust to the variations of the substrate lattice constant and the Ag adsorption strength. GCMC simulations on these hexagonal surfaces usually yield Ag thin films that are in the fcc phase and {111} oriented. Besides, to achieve more continuous Ag thin films with less use of Ag, the doping elements, like Pd, Sb, Se, Sn, and Te, can be added as “anchor” sites on ZnO surfaces to bind incoming Ag atoms. With 0.05ML of “anchor” sites on the substrate, sufficient nuclei can be generated to achieve continuous ultra-thin films. We also search for alloying elements that can segregate in Ag grain boundaries to stabilize grain size during heat treatments. Current DFT calculation shows that tungsten (W) does not segregate to any investigated Ag grain boundaries. This result is inconsistent with the experimental fact that W can stabilize Ag grain boundaries during the heat treatment. The possible origin of such inconsistency can be resolved if more accurate and representative grain boundary structures in Ag alloys are constructed in future studies.

4.1 Introduction

Low-emission glasses are used for architectures widely. It is used to achieve better energy efficiency by minimizing the ultraviolet and infrared light that can pass through while not significantly compromising the amount of visible light. Multi-layer structures, as shown in Figure 4.1, are used for this purpose. Most of the multi-layer structures are repeating “dielectric layer/low-emission layer/dielectric layer” units.

Typical low-emission layers can be noble metals, e.g. Ag. The ability of a material to radiate energy is known as emissivity. In general, highly reflective materials, such as silver or aluminum, have a low emissivity. For example, untreated glass has an emissivity of 0.84, while silver has an emissivity of under 0.06[77]. Hence, reducing the emissivity of the window glass by coating Ag can improve the insulating property of architectural glasses. Dielectric layers are necessary to form an inferential filter that grants the reflection of the visible wavelengths to be reduced and consequently increases the light transmission. Another reason to utilize dielectric layers is that the reflected fraction in the visible results in as neutral a color as possible, and in particular so that the reflection does not lead to purple stains which are against human preferences. Moreover, the choice of dielectric layers or systems of dielectric layers is such that neutrality in reflection is realized for the broadest range of angles of incidence to the glazing. And oxides, e.g. ZnO, are usually great dielectric materials.

Multilayer Coating

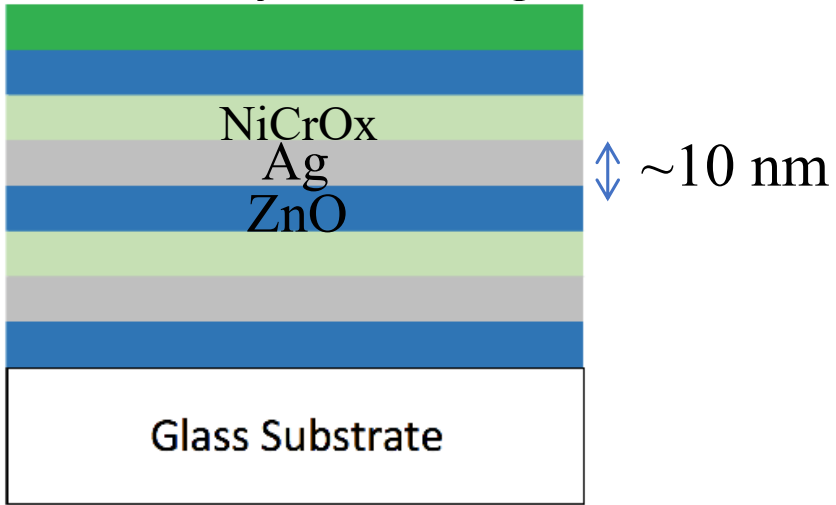


Figure 4.1: Illustration of multi-layer structures of architecture glass.

However, Ag/ZnO interface has weaker adhesion energy compared to many other metal/oxide interfaces. The strengths of adhesion between metals and oxides can largely affect the wetting behaviors and morphology of interfaces. On the other hand, defects, like islands forming, high surface roughness and high density of pinholes, will all reduce the glass quality, as shown in Liu's paper [78]. For industrial practices, Ag thin film deposited on ZnO layers is usually above 10 nm thickness so as to guarantee continuous thin film. Therefore, to achieve continuous thin film with thinner layers can improve the cost efficiency by reducing the amount of Ag needed.

In this chapter, attention was paid to mainly two parts: 1) the effect of substrate on the Ag thin film quality; 2) the effect of alloy segregation at Ag grain boundary on the Ag thin film stability. GCMC methods will be used to study the morphology of Ag thin film on different substrates with various substrate structures, lattice constant and bonding strength to Ag atoms. The goal of this study is to simulate the morphology after annealing, hence detailed kinetics, like bombardment effects, can be ignored. Therefore, GCMC simulation will be a suitable tool, because it is based on the thermodynamic driving force. We also search for alloying elements that

can segregate at Ag grain boundaries to stabilize grain size during heat treatments. Current DFT calculation shows that tungsten (W) does not segregate at any investigated Ag grain boundaries. This result is inconsistent with the experimental fact that W can stabilize Ag grain boundaries during the heat treatment. The possible origin of such inconsistency can be resolved if more accurate and representative grain boundary structures in Ag alloys are constructed in future studies.

4.2 Customized Empirical Potential and GCMC Simulation Setup for Deposition

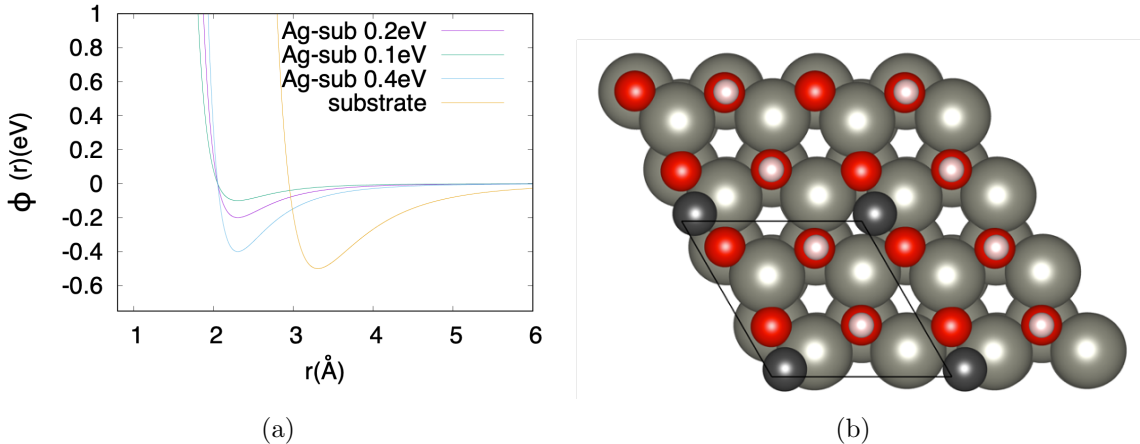


Figure 4.2: Lennard-Jones potential used to describe different bonding strength and bond length, and atomistic pictures of Ag adsorbed on ZnO surface with $\frac{1}{2}$ ML coverage. (a) L-J potential used to describe different bonding strength and bond length of Ag-substrate atoms, and substrate-substrate atoms. (b) illustration of Ag atom adsorbed on saturated ZnO (000 $\bar{1}$) with $\frac{1}{2}$ ML H.

In order to conduct GCMC simulations accurately for metal deposition, a reasonable potential must be used to describe the interaction between Ag adsorbates and substrate atoms. An embedded-atom (EAM) potential [79] is used to describe the interaction between Ag-Ag atoms, while the interactions between Ag and substrate atoms need to be able to tune for different bonding environments. As a result, we

applied simple L-J 12-6 potential [16] for Ag-substrate interaction and interactions between substrate-substrate atoms:

$$\Phi_{LJ} = 4\epsilon \left[\left(\frac{\sigma}{r} \right)^{12} - \left(\frac{\sigma}{r} \right)^6 \right] \quad (4.1)$$

where ϵ controls bonding strength and σ changes equilibrium bond lengths. As shown in Figure 4.2, purple, green and blue lines describes the interaction between Ag atom and regular, week, and strong bonding with substrates, respectively. The ϵ for normal bonding with substrates is fitted to match the DFT calculated results. In Figure 4.1 (b), we show the most stable Ag atom adsorption site on a fully saturated ZnO (0001) fully saturated surfaces with $\frac{1}{2}$ ML coverage of H. Here, a (2×2) surfaces is used, because this structure provides the identical $\frac{1}{2}$ ML H surface arrangement according to symmetry. If an isolated Ag atom is used as the reference state, the adsorption energy is -0.7 eV for the most stable Ag adsorption site. We fit the L-J potential to describe the Ag-substrate interactions so that the Ag adsorption energy on the substrate is equal to this value. And the equilibrium bond length is fitted for the bond distance between Ag and ZnO substrates at $\sim 2.3\text{\AA}$. And the yellow line corresponding to the substrate interactions itself, we set the bond length based on ZnO substrates lattice constant. And a strong potential well is used in order to simulate a more rigid substrate. The GCMC code we used is from J. Li's Group in MIT[80].

As we previously discussed in Chapter 2.2.3, the chemical potentials of elements of interest are used to decide the probability of accepting/rejecting a certain event. The Ag gas phase chemical potential is used, via:

$$\mu_{Ag(g)} = \mu_{Ag(bulk)} + k_B T \ln \frac{p}{p_0} \quad (4.2)$$

where, p_0 is the Ag evaporation pressure. Usually, the vacuum pressure of a sputtering

chamber is $\sim 1 \text{ Pa}$. So a chemical potential μ of -0.6 eV is used to simulate $p=1 \text{ Pa}$ Ag partial pressure at $300K$.

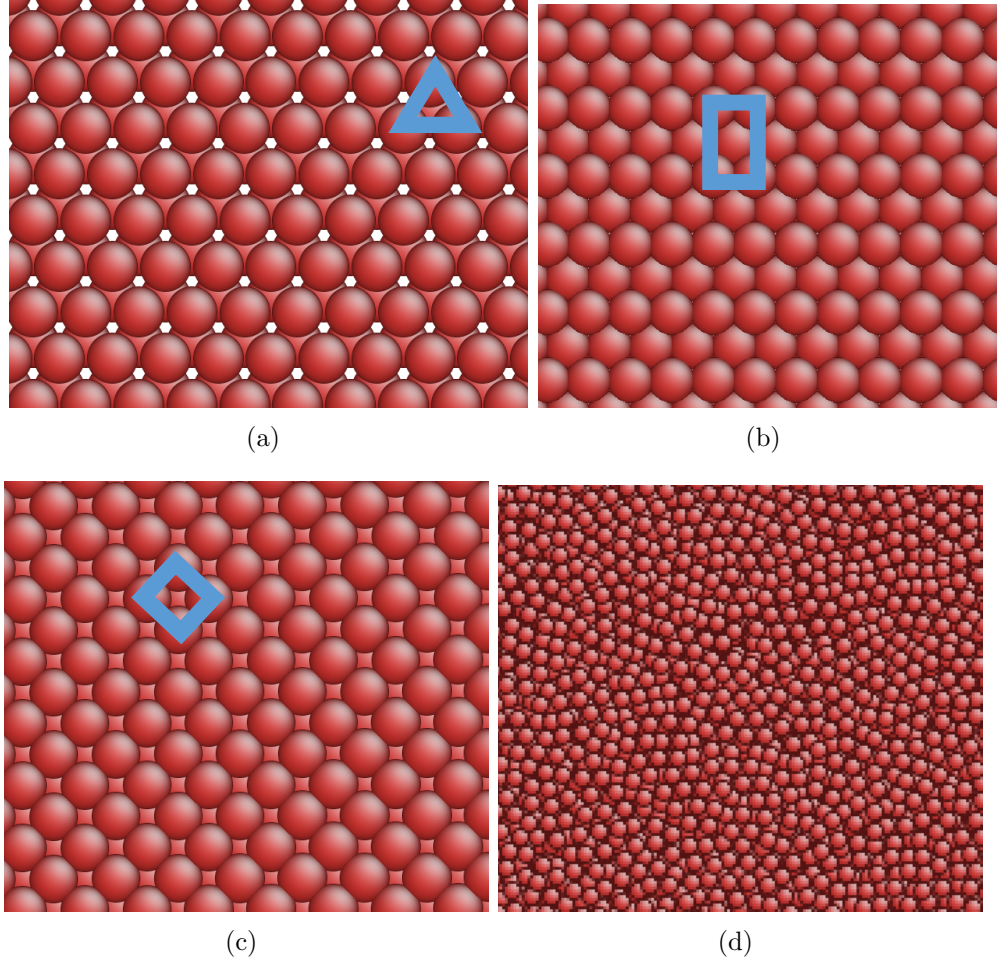


Figure 4.3: Four different substrate types for GCMC simulation. (a) hexagonal, (b) rectangular, (c) square like surface lattice, and (d) amorphous surface.

Four different substrate types are used in this simulation, as shown in Figure 4.3. Hexagonal surface unit, as shown in Figure 4.3 (a), corresponds to face-centered cubic (FCC) $\{111\}$ surfaces and hexagonal close-packed (HCP) $\{0001\}$ surfaces. Rectangular one, as shown in Figure 4.3 (b), corresponds to FCC $\{110\}$ surfaces and HCP $\{10\bar{1}0\}$ surfaces. Square one, as shown in Figure 4.3 (c), corresponds to FCC $\{100\}$ surfaces. Besides, an amorphous substrate, as shown in Figure 4.3 (d), is also created by quenching down from a high temperature. By combining different substrates

with tunable L-J potentials, different substrates with different lattice constants can be achieved. Because FCC and HCP structures have different ways to define lattice constant, we will use bond length in the following sections to avoid confusion. By using strong and weak bonding of Ag-substrate interactions together, one can also simulate “anchor” sites on a regular substrates which will be discussed in Subsection 4.4.

4.3 ZnO Substrate Yields the Best Ag Thin Film

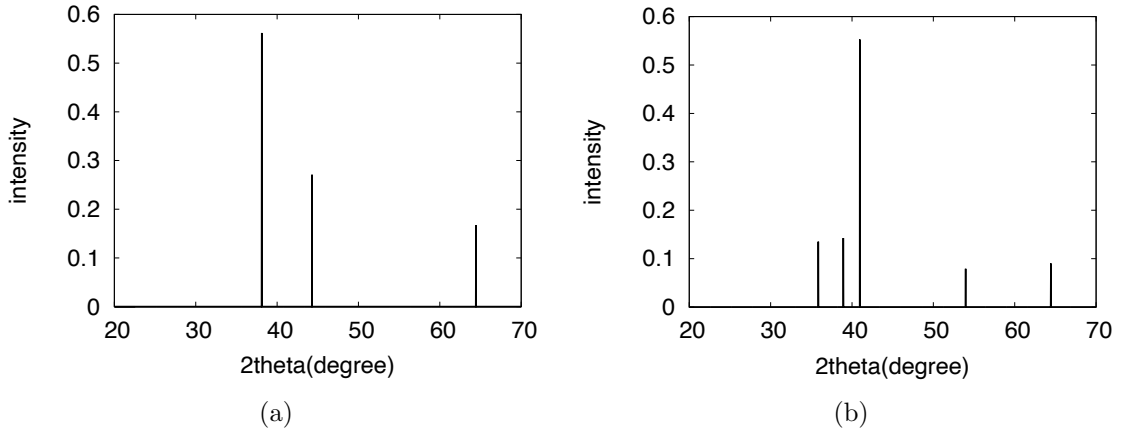


Figure 4.4: Simulated XRD plots of FCC and HCP Ag. (a) Simulated XRD results for FCC Ag. (b) Simulated XRD results for HCP Ag.

In this section, we will answer the question that which substrate type is best for Ag thin film deposition. Three different bond lengths will be used: 3.3Å, 2.9Å, 2.3Å. 3.3Å is equivalent to the ZnO lattice constant. 2.9Å is for Ag bond length, which means this substrate has a zero misfit for Ag thin film. At last, 2.3Å is selected for simulating a negative lattice mismatch factor, where lattice mismatch factor($f_{mismatch}$) is defined via:

$$f_{mismatch} = \frac{a_{substrate} - a_{film}}{a_{substrate}} \quad (4.3)$$

Where $a_{substrate}$ and a_{film} are the lattice constant of substrate and thin film, respectively. And the bond strength is fitted to match the Ag adsorption energy on fully-saturated ZnO substrates as we mentioned in Section 3.2.

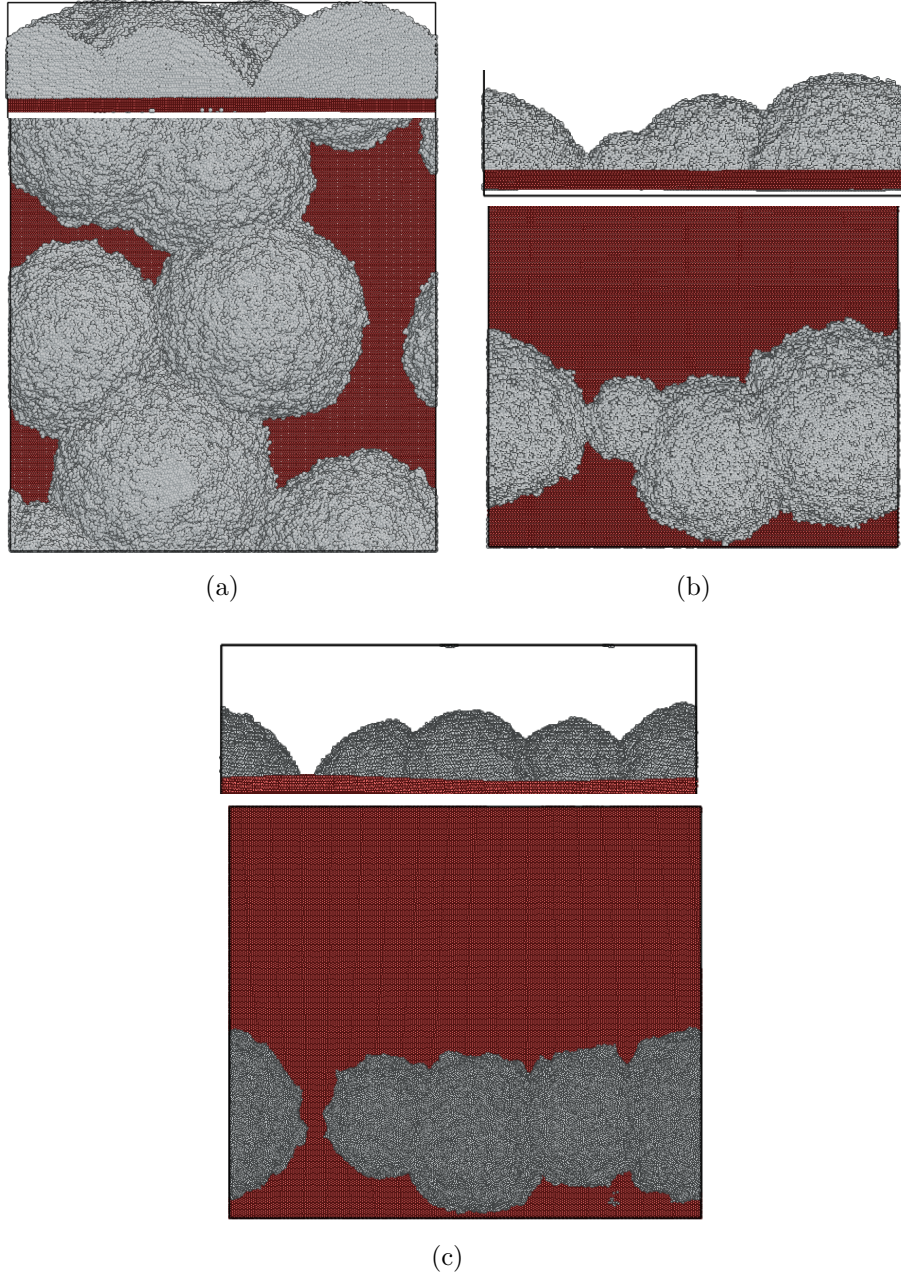


Figure 4.5: GCMC simulated Ag thin film morphology on hexagonal substrates with bond length of (a) 2.3\AA , (b) 2.9\AA , and (c) 3.3\AA . Top sub-figures are side views of 40 ML atoms and bottom sub-figures are top views.

In order to characterize the orientation of thin films, simulated XRD will be evaluated. From experimental XRD plot, Ag 111 orientation will have a strong peak around 38° from JCPDS No 04-0783 [81]. We also simulated XRD results for HCP Ag in order to characterize the crystalline quality of Ag thin films. And we can see if Ag is in HCP structure, there will be strong peaks around 35.86° , 38.95° , and 40.96° .

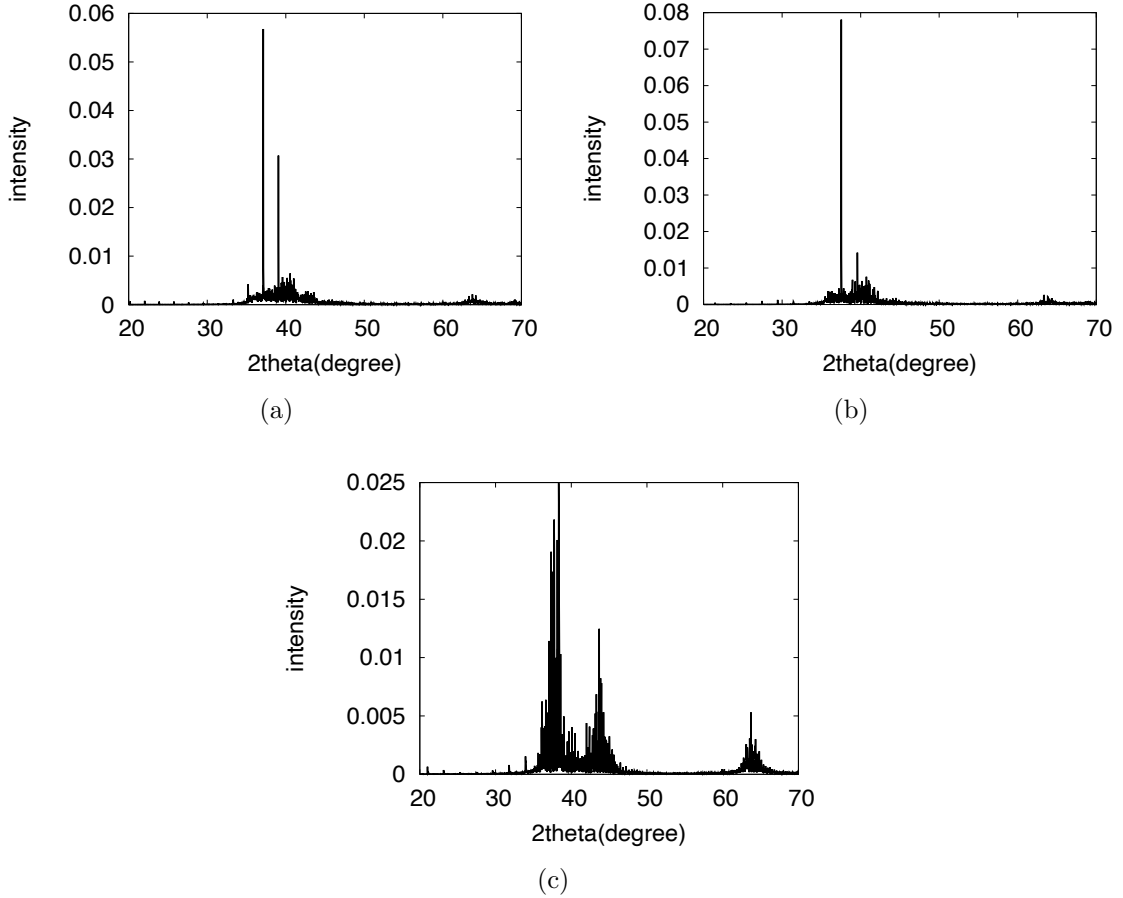
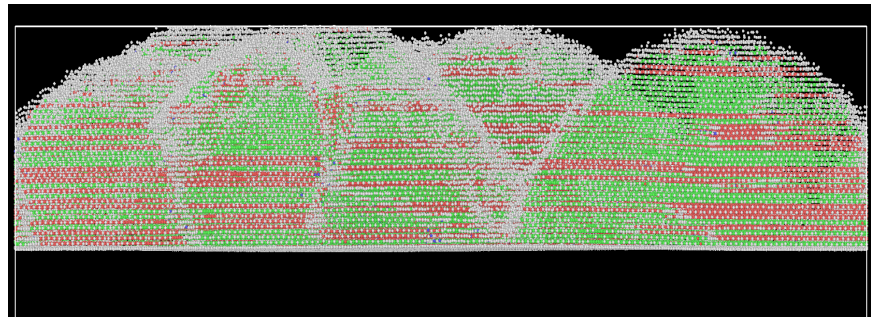


Figure 4.6: Simulated XRD results of Ag thin film on hexagonal substrates with different bond length. Bond length of (a) 2.3\AA , (b) 2.9\AA , and (c) 3.3\AA . The substrate with 2.9\AA bondlength (similar to Ag deposition on Ag (111) substrate) shows best Ag {111} orientation.

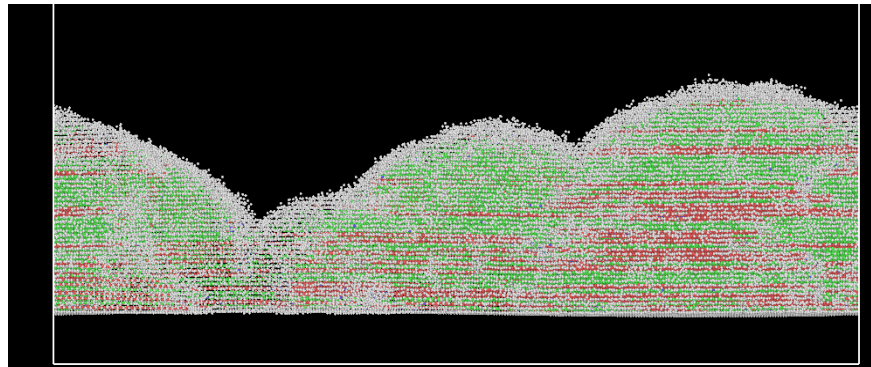
We first investigated the results of the hexagonal substrate with 3 different bond lengths, as shown in Figure 4.5. A $50\text{\AA} \times 50\text{\AA}$ substrate is used for Ag deposition. Assuming Ag thin films all follow 111 orientation, there will be $\sim 50,000$ Ag atoms/layer. We deposit 2,000,000 Ag atoms, which is equivalent to a ~ 40 MLs (~ 10 nm thick-

ness) of Ag atoms, then observed the morphology of thin films on different substrates. As shown in Figure 4.5, the left sub-figure is for 2.3\AA bond length, the middle one for 2.9\AA , and the right one for 3.3\AA . Ag thin film follows an island-like growth pattern with all three lattice constants/bond lengths. Note that the middle one, with a bond length of 2.9\AA , which is similar to the situation of Ag on Ag(111) island growth pattern [82]. For ZnO lattice constant (3.3\AA), still, island-like growth was observed for 10 nm thickness. Possible reasons could be: 1) a Ag chemical potential corresponding to ~ 1 Pa is used, and this could be orders of magnitude higher in the industrial-level sputtering chamber; 2) the substrate in the simulation is the perfect crystal, which does not consider the polycrystalline and surface defects. Those defect sites can have stronger binding to Ag adsorbates, thus they may increase the chance of surface nucleation; 3) detailed surface diffusion kinetics are ignored during GCMC simulations.

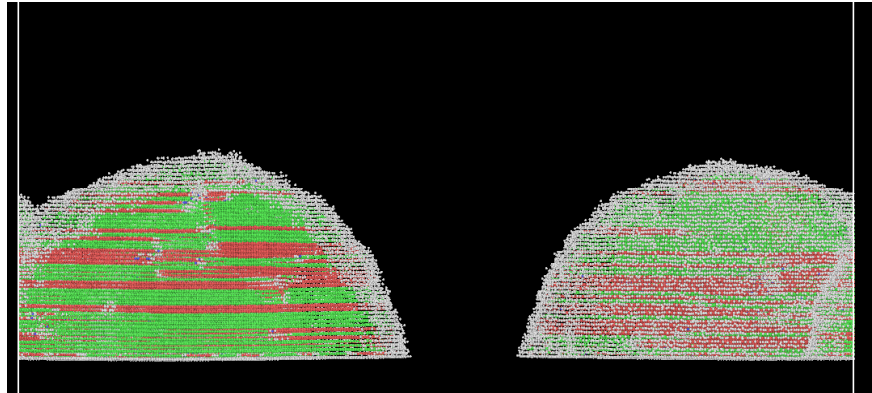
Simulated XRD results of hexagonal substrates are also plotted in Figure 4.6. The middle figure (similar to Ag deposition on Ag (111) substrate) shows best $\{111\}$ orientation. For larger and smaller lattice constant, 111 orientation still persist but with broadened peaks and other peaks for $\{200\}$ and $\{220\}$, as shown in Figure 4.3. Besides, common neighbor analysis (CNA) [83] is also applied, to identify internal defects. All three lattice constant have similar amount of layered defects (like stacking faults or twin boundaries) as noted as HCP layers in FCC structures in Figure 4.7.



(a)



(b)



(c)

Figure 4.7: CNA plots of Ag thin film on hexagonal substrates with different bond length. Bond length of (a) 2.3\AA , (b) 2.9\AA , and (c) 3.3\AA . Green, red, and grey atoms indicate FCC, HCP structure and structure cannot be identified (Usually due to lack of neighboring atoms, e.g. surface or interface atoms, or amorphous-like atoms), respectively.

Next, we investigated Ag thin film morphology and qualities on rectangular-shaped substrates. As shown in Figure 4.8, only Ag bond length substrate yields

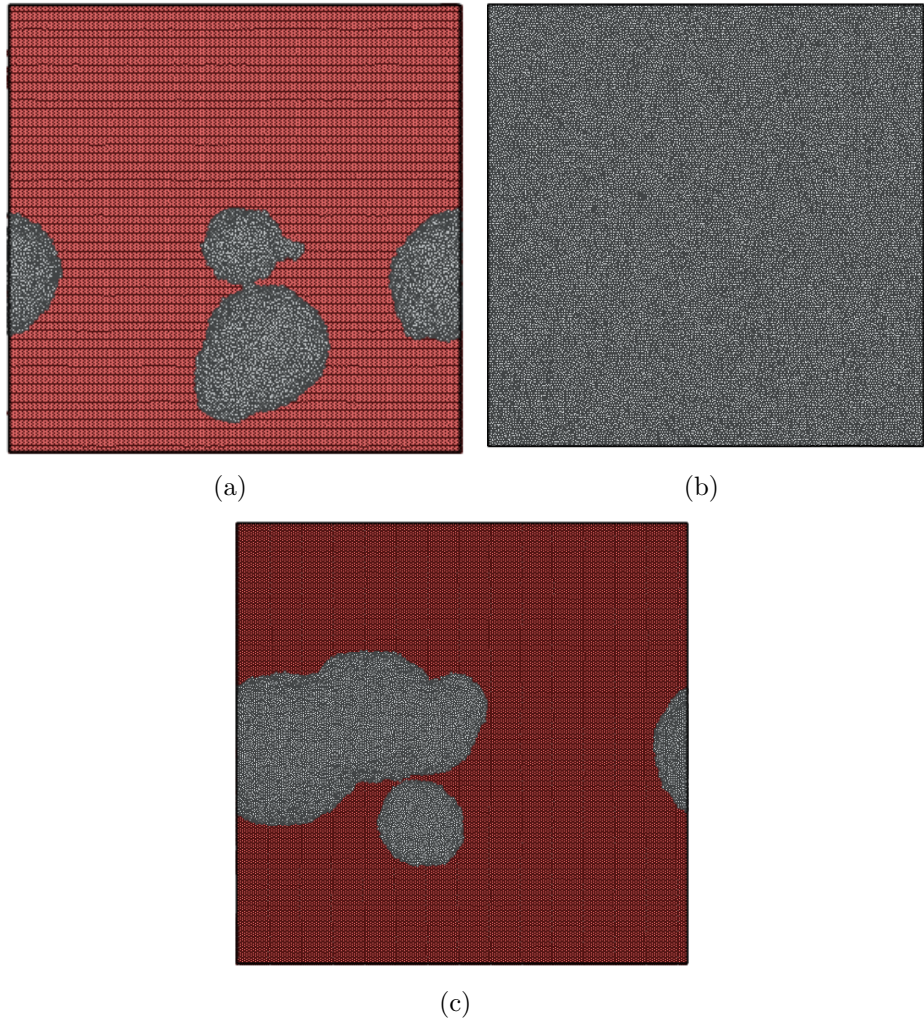


Figure 4.8: GCMC simulation results of Ag thin film morphology on rectangular substrates. Top-view of GCMC simulated Ag thin film morphology on rectangular substrates with bond length of (a) 2.3\AA , (b) 2.9\AA , and (c) 3.3\AA .

a continuous Ag thin film. Both higher and lower bond length substrates grow 3-D islands. Besides, from XRD results, Ag grown on substrates with lower bond length are amorphous, which will greatly affect Ag thin film quality. Strong HCP peaks are observed with a substrate of higher bond length. In Figure 4.3 and 4.3, CNA analysis is conducted for Ag thin film deposited on substrate with bond length of 2.9\AA and 3.3\AA . The majority of the thin film is HCP phase with a small amount of vertically layered defects. Besides, centrosymmetric analysis is conducted for 3.3\AA substrate, as shown in Figure 4.3. Vertical-oriented misfit dislocations are generated

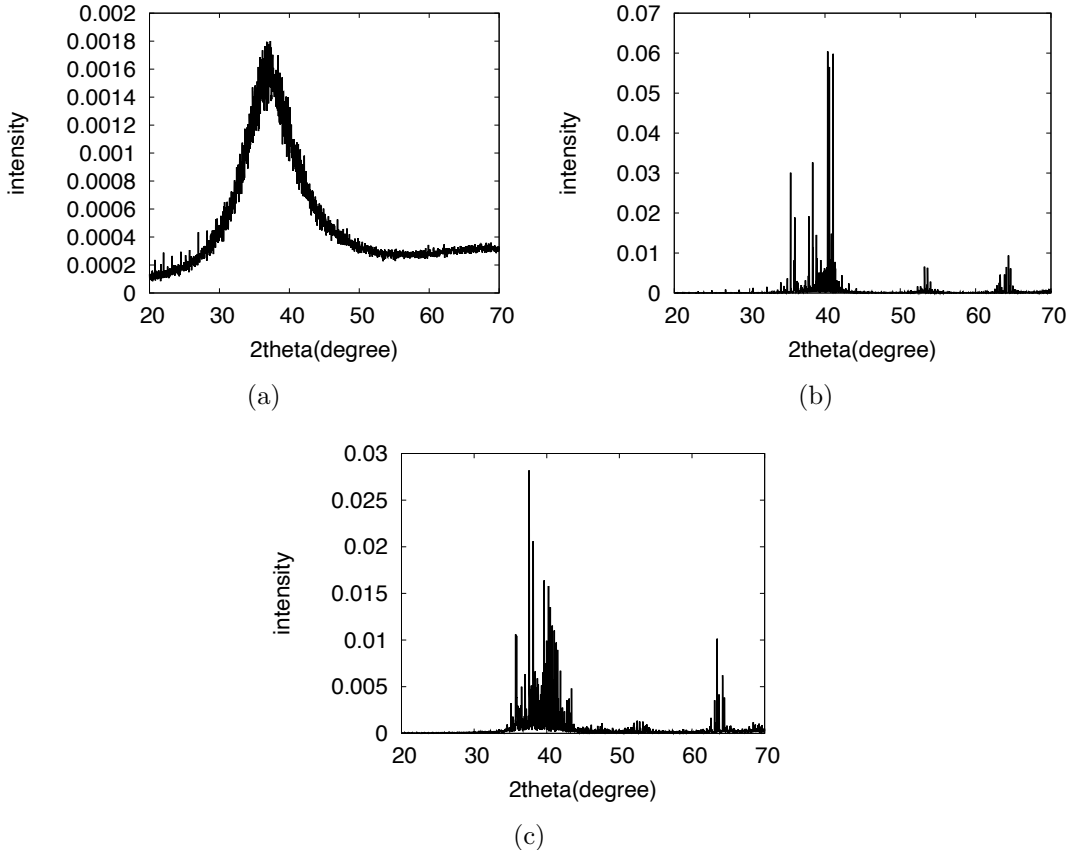


Figure 4.9: Simulated XRD results of Ag thin film morphology on rectangular substrates. Simulated XRD results of three Ag thin film deposited on substrates with bond length of (a) 2.3\AA , (b) 2.9\AA , and (c) 3.3\AA .

to release strain energy from lattice mismatch. Based on the above observation, Ag thin film quality on rectangular lattice substrates is sensitive to substrate lattice constant change. A similar conclusion also applies to square lattice substrates. As shown in Figure 4.3, amorphous phase comes out with decreasing lattice constant. When the substrate lattice constant increases, several nm of body-centered cubic (BCC) layers appear at the interface.

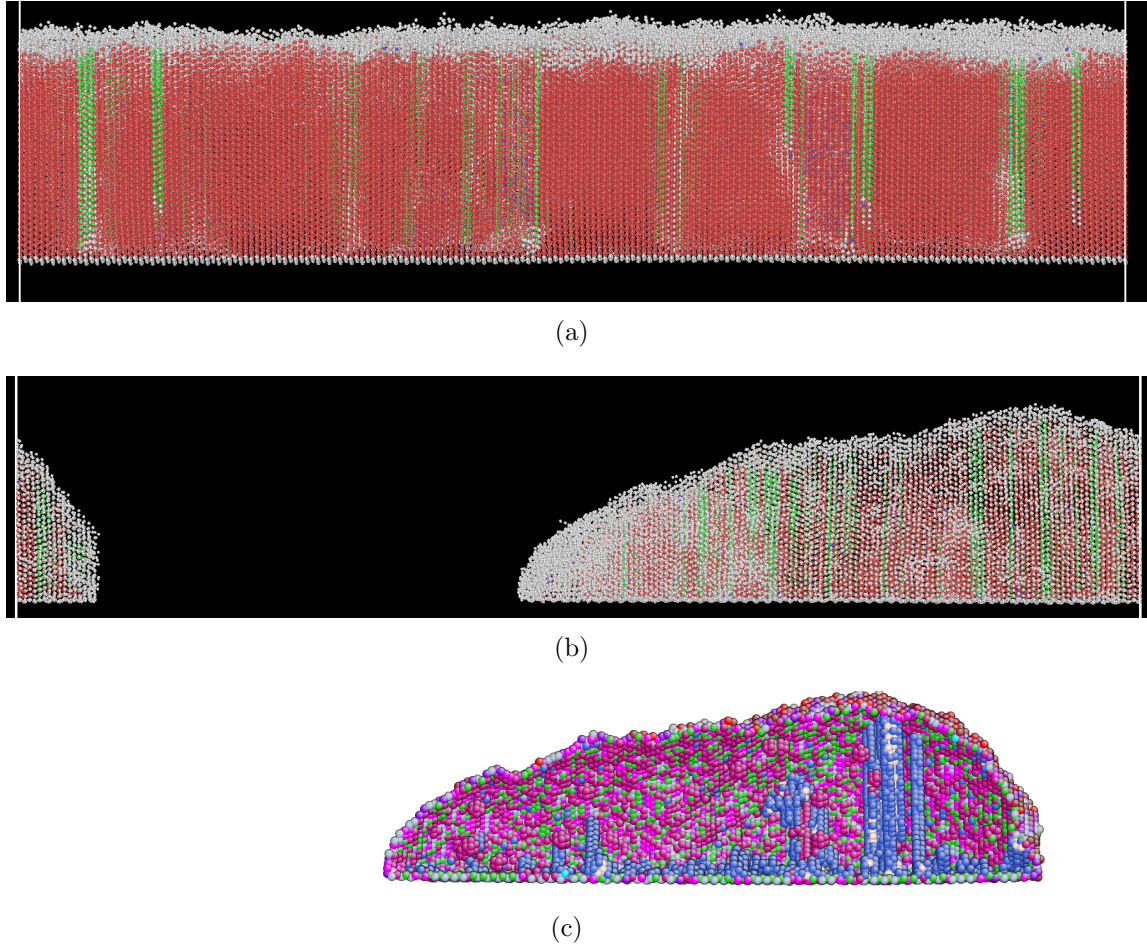


Figure 4.10: CNA and centro-symmetry analysis for Ag thin film quality on rectangular substrates. (a) CNA for Ag thin film deposited on substrate with bond length of 2.9\AA . (b) common neighbor analysis for Ag thin film deposited on substrate with bond length of 3.3\AA . (c) centro-symmetry analysis for Ag thin film deposited on substrate with bond length of 3.3\AA . Lines formed by blue atoms indicating misfit dislocations.

At last, Ag thin film is also deposited on an amorphous substrate during GCMC simulation. As shown in Figure 4.3, the thin film is more continuous compared to other ordered lattice substrate structures, because of amorphous substrates containing more surface defects acting as a trap site for Ag adsorbates. However, the quality of Ag thin film is not desirable for industry use, as the thin film shows an amorphous structure from the XRD.

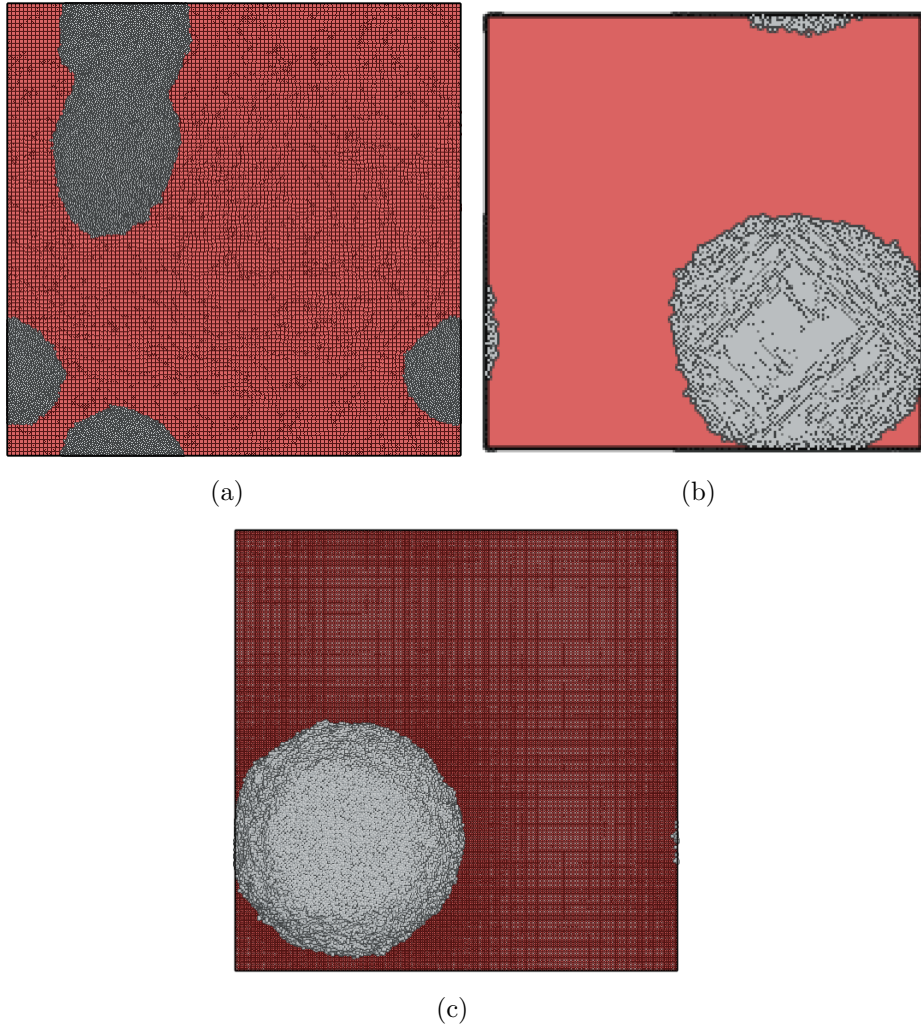


Figure 4.11: GCMC simulation results of Ag thin film morphology on square substrates. Top-view of GCMC simulated Ag thin film morphology on square substrates with bond length of (a) 2.3Å, (b) 2.9Å, and (c) 3.3Å.

4.4 Substrate “Anchor” Sites for Continuous Thin Film Morphology

As we mentioned before, random surface defects may have a positive effect on forming a continuous thin film. This may come from strong interactions between surface defect sites and Ag atoms. In this section, we will investigate the possibility of using the surface “anchor” site to improve the thin film continuity. A similar idea was initially proposed by Chambers et al. [84]. They considered the situation of

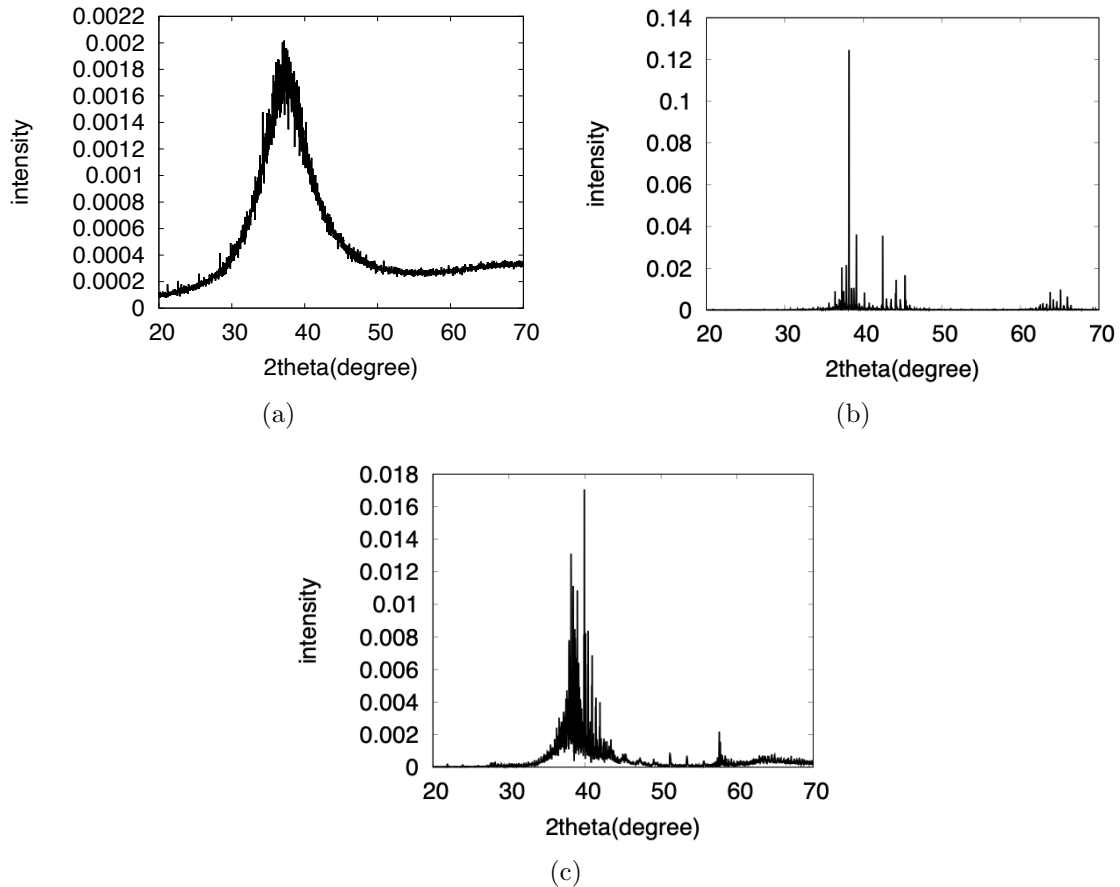


Figure 4.12: Simulated XRD results of Ag thin film morphology on square substrates. Bond length of (a) 2.3\AA , (b) 2.9\AA , and (c) 3.3\AA .

transition metal getting oxidized and immobilized by the ZnO substrate. This is true when experiments are done in ultrahigh vacuum (UHV). But sputtering, especially industry-level sputtering usually happens in high vacuum (HV) conditions and the main source of oxygen is the residual gas which consists of water vapor as majorities as pointed out by Anders et al. [85] in 2006. In this section, a new criterion is proposed to search for stable anchor sites that can stand with water vapor and H_2 attacks.

Therefore, we propose three criteria that are important for surface anchor elements: i) they can survive the attacks of water vapor(H_2O) and H_2 ; ii) they have high diffusion barriers on saturated ZnO substrates; iii) they have strong bonding

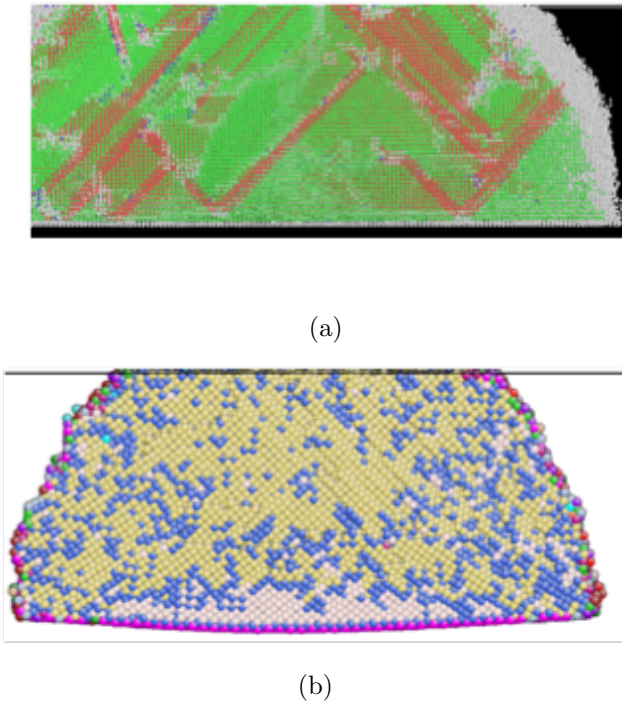
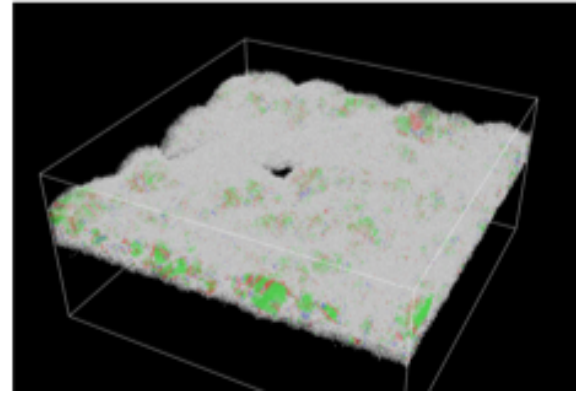


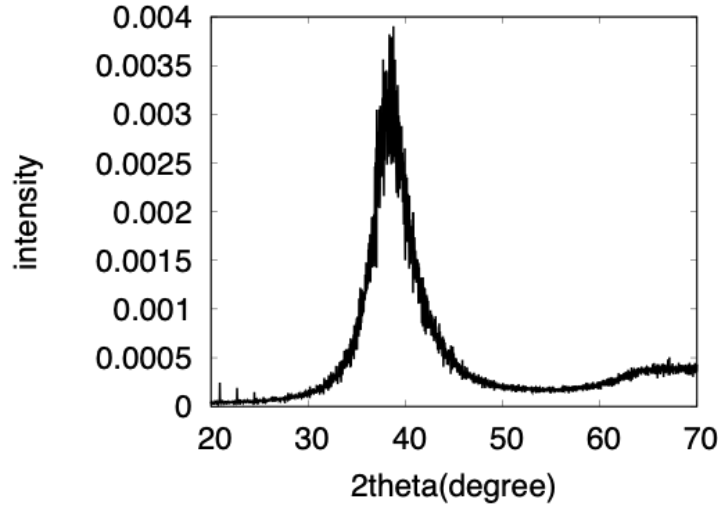
Figure 4.13: Side-view of GCMC simulated Ag thin film morphology on square substrates. (a) CNA for Ag thin film deposited on substrate with bond length of 2.9 Å. (b) coordination number of Ag thin film deposited on substrate with bond length of 3.3 Å. Yellow, blue and pink color are atoms with coordination numbers of 12, 11, 14 (second nearest neighbors included).

strength with Ag atoms.

For the first criterion, four different reactions are considered. The first two correspond to the two possible water (H_2O) dissociation reactions on the ZnO substrate with one “anchor” site, as shown in Figure 4.4. The upper reaction represents an incoming water molecule dissolve to one OH group attached to the “anchor” site and one H atom at a remote “anchor” site. The lower plot of Figure 4.4, represents the reaction of an incoming water molecule dissolve to one OH group attached to the “anchor” site and one H atom at a nearby O atom top. The third and fourth reaction corresponds to the two possible H_2 dissociation reactions on the ZnO substrate with



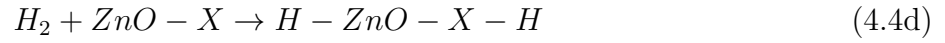
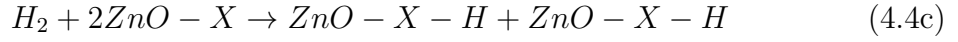
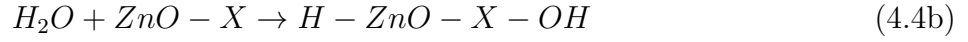
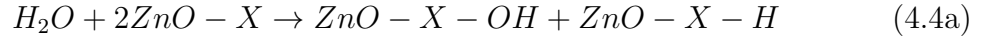
(a)



(b)

Figure 4.14: CNA and Simulated XRD results of Ag thin film morphology on an amorphous substrate. (a) CNA and (b) Simulated XRD results of Ag thin film morphology on an amorphous substrate.

one “anchor” site, as shown in Figure 4.4. We summarize the 4 reactions as below:



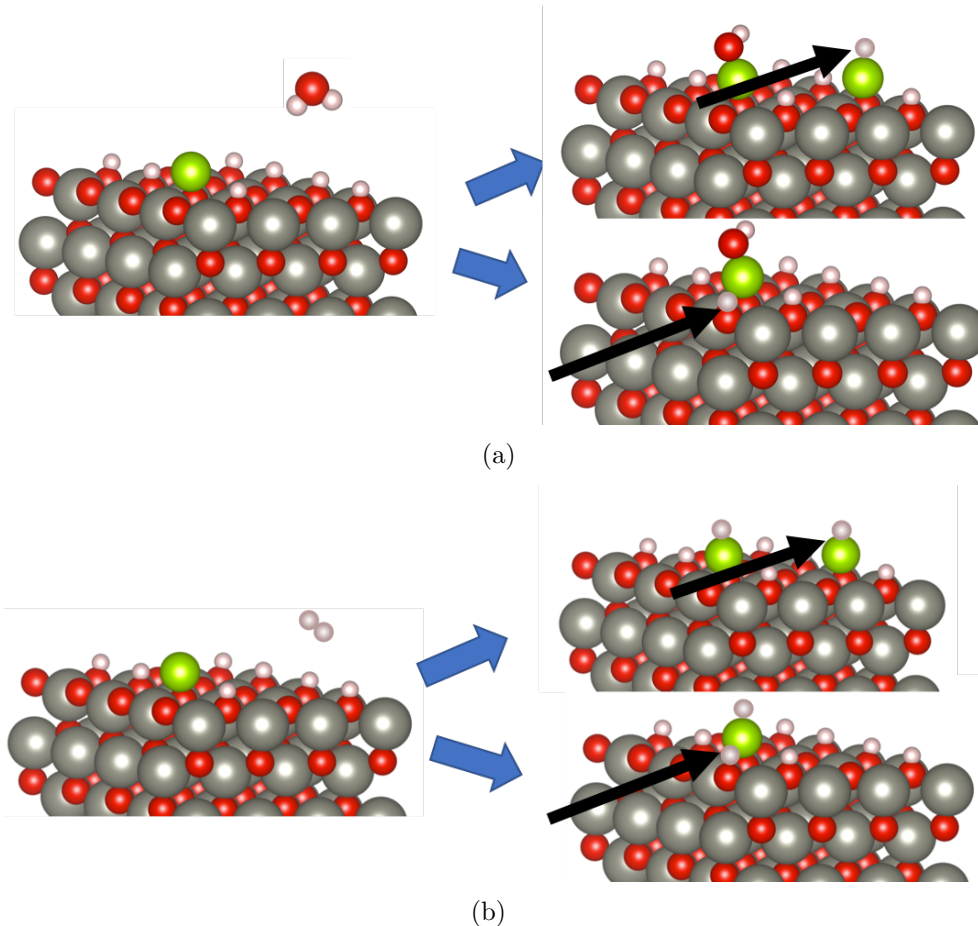


Figure 4.15: Possible water and H_2 dissociation reactions on ZnO substrate with one “anchor” site. (a) Two possible water (H_2O) dissociation reactions on ZnO substrate with anchor sites. (b) Two possible H_2 dissociation reactions on ZnO substrate with anchor sites. Red and grey atoms are O and Zn atoms, respectively. Green atoms represent the “anchor” element on ZnO substrate surfaces. Pink ones are H atoms.

In order to have the “anchor” elements staying reactive on ZnO substrates, all the four equations need to yield positive enthalpies. After screening the first criterion, as shown in Figure 4.16, Pd, Sb, Se, Sn, Cd, and Te can survive the environment of water and H. Cd is eliminated as it is an extremely toxic industrial and environmental pollutant.

For the second and third criteria, all the 5 elements have orders of magnitude higher diffusion barriers compared to Ag atoms on fully-saturated ZnO substrates, as shown in Table 4.1. Moreover, as we can see from Table 4.2, all the 5 elements have

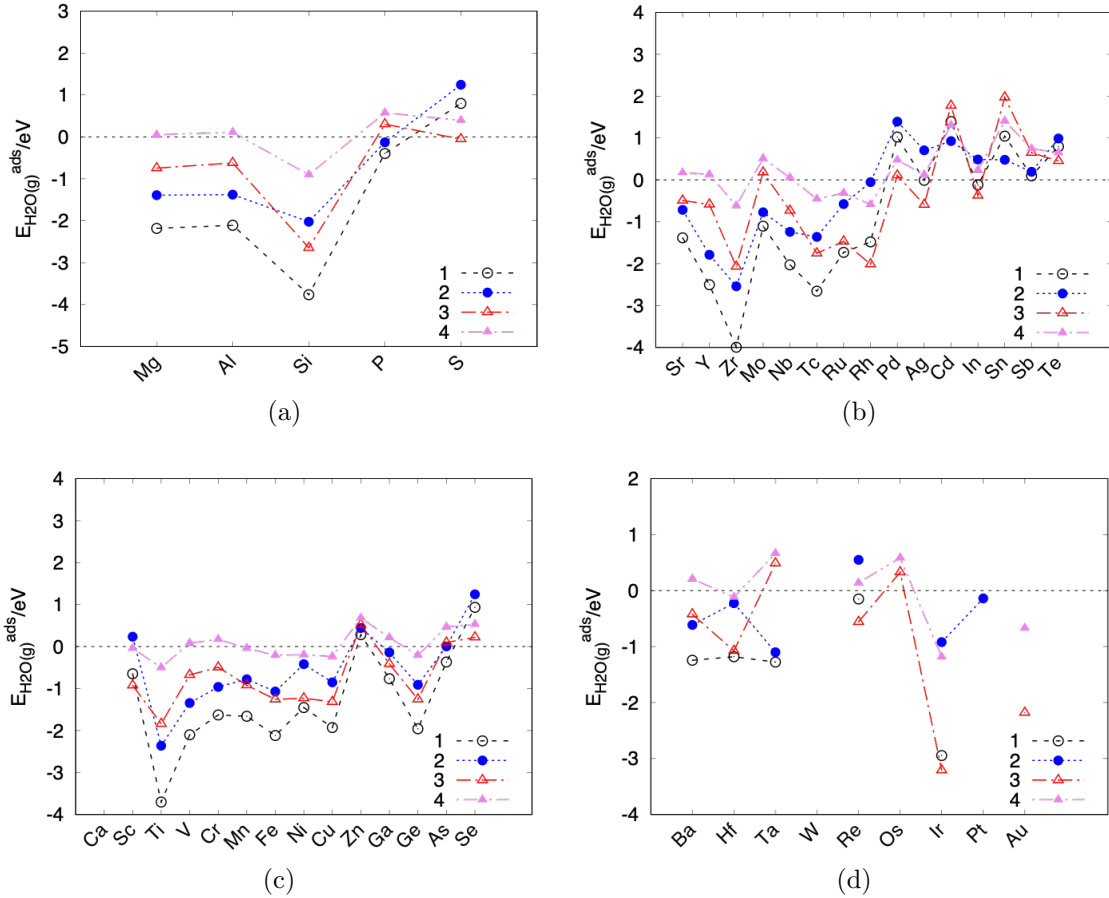


Figure 4.16: Water and H_2 dissociation reactions energies on ZnO substrate with “anchor” sites. Reaction 1 and 2 corresponds to 2 possible water dissociation reactions in Figure 4.15 (a), respectively. Reaction 3 and 4 corresponds to 2 possible H_2 dissociation reactions in Figure 4.15 (b), respectively.

Table 4.1: “Anchor” elements diffusion barriers on ZnO saturated with $\frac{1}{2}$ ML H.

| Substrate | Diffusion barrier on ZnO saturated with $\frac{1}{2}$ ML H [eV] |
|-----------|--|
| Ag | 0.077 |
| Pd | 0.275 |
| Sb | 0.111 |
| Se | 1.338 |
| Sn | 0.341 |
| Te | 0.999 |

much stronger bonding strengths to an Ag atom compared to bare ZnO substrates as well.

Table 4.2: Ag adsorption on saturated ZnO substrate with “anchor” sites.

| Substrate | Adsorption energy(eV) |
|---------------------------|-----------------------|
| ZnO with $\frac{1}{2}$ ML | -0.716 |
| Pd | -1.716 |
| Sb | -2.242 |
| Se | -2.055 |
| Sn | -2.284 |
| Te | -1.931 |

In order to demonstrate the effect of surface “anchor” sites on Ag thin film morphology, GCMC simulations are conducted. 0.05ML of substrate atoms are randomly changed to “anchor” site atoms which has a stronger binding to Ag. Then 10ML of Ag atoms are deposited. In Figure 4.17, a much more continuous Ag thin film can be seen with 0.05ML of “anchor” sites. With randomly distributed “anchor” sites, more nuclei can be achieved, hence more continuous ultra-thin film. The number of anchor sites added on ZnO substrates is limited, so there will not be a great change of Ag/ZnO interfacial energies globally. But the anchor sites might increase the interfacial energies locally. And the mechanisms of anchor sites to increase Ag wettability are from two aspects: 1) increasing adsorption energies of individual Ag atoms on ZnO saturated surfaces; 2) increase Ag surface diffusion barriers.

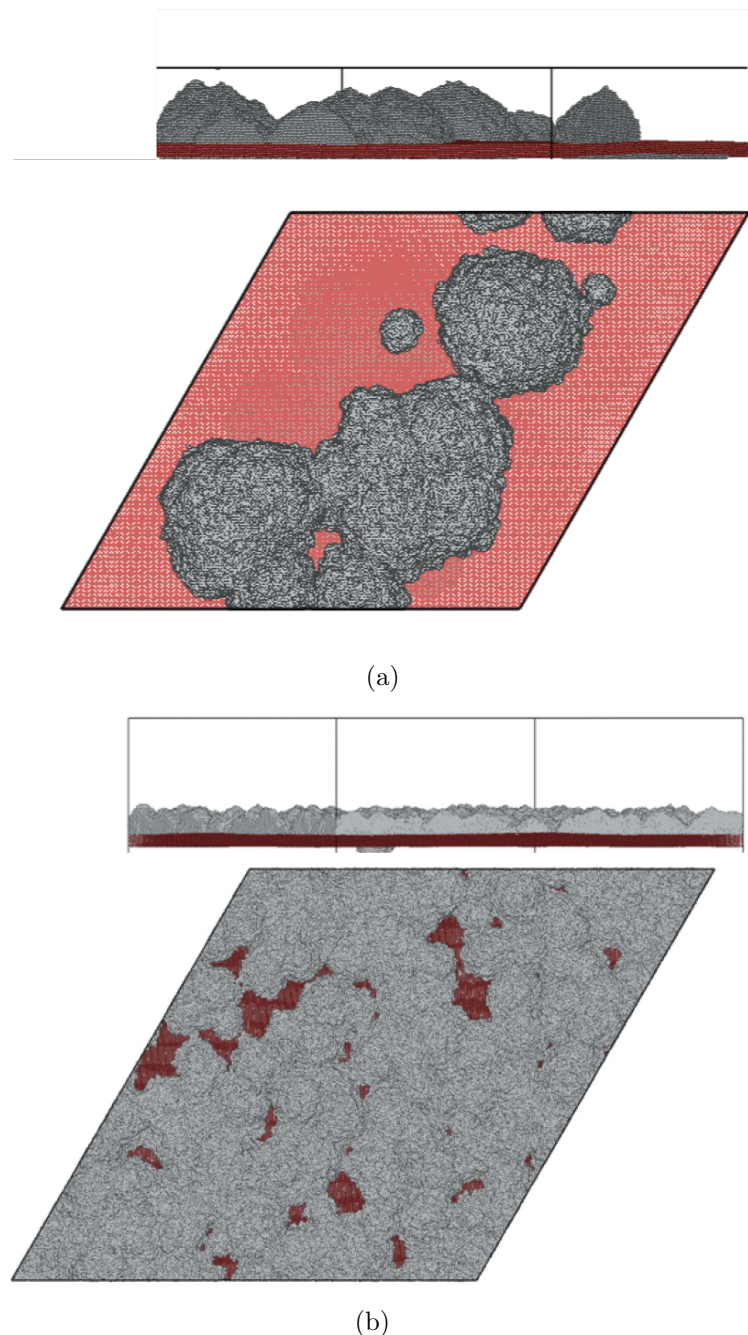


Figure 4.17: GCMC simulation results for 10ML Ag deposition on ZnO with and without 0.05ML surface “anchor” sites. (a) Ag island growth pattern on ZnO without surface “anchor” sites. (b) Ag island growth pattern on ZnO with 0.05ML surface “anchor” sites.

4.5 Alloy Segregation at Grain Boundary to Stabilize Poly-crystalline Thin Film

During the heat treatment of multi-layer coating structures, quality problems like discontinuous thin films, change of colors can happen. The grain boundary grooving effect, as shown in Figure 4.18, results in those voids and discontinuous films that degrade the quality of thin films[86, 87]. This grain boundary grooving effect will increase with larger grain sizes[88]. Therefore, we can try to stabilize grain sizes of nanocrystalline alloys by doping during heat treatment[89, 90].

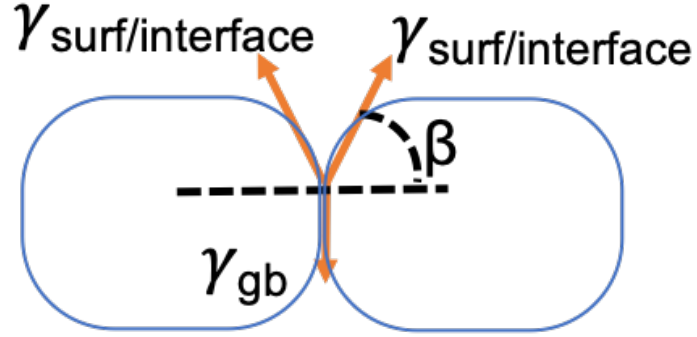


Figure 4.18: Illustration of grain boundary grooving between two grains. The blue solid circle-like shape indicates two connected grains. $\gamma_{\text{surf/interface}}$, γ_{gb} are the surface/interface energy and grain boundary energy, respectively. β is the dihedral angle between horizon and the $\gamma_{\text{surf/interface}}$ direction.

Solute atoms, whether they are added voluntarily for specific needs, inevitably remained as impurities after the synthesis, or introduced during the service of the material, can affect various properties of alloys by changing the stability and mobility of crystalline defects, like grain boundaries. In this section, we tried to add trace amounts of alloying elements to stabilize grain boundaries. From experiments and phenomenological modelling, W should segregate at Ag grain boundaries[89, 90]. We used DFT to search for potential candidates. Simple grain boundaries like $\Sigma 5$ (310),

$\Sigma 3$ (112) and $\Sigma 3$ (111) are used. We defined the segregation energy E_{seg} via,

$$E_{seg} = E_{XnearGB} - E_{XawayfromGB} \quad (4.5)$$

where $E_{XnearGB}$ and $E_{XawayfromGB}$ are energy when solute atoms are located close to and away from the grain boundary, respectively, for example, as shown in Figure 4.19.

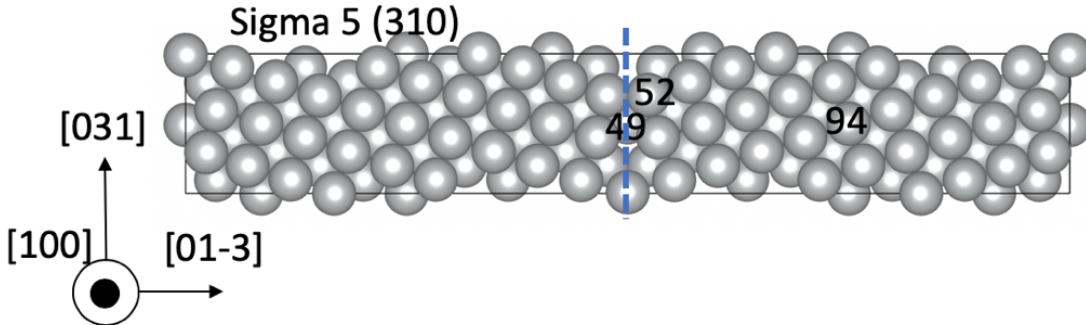


Figure 4.19: Atomistic structure of $\Sigma 5$ (310) Ag grain boundary. The blue vertical line indicates where the grain boundary is. Because of a periodic boundary condition is used, there is another grain boundary at the end of the simulation box. Atom labeled with #49, #51 and #94 are two atoms close to the grain boundary and far away from grain boundary, respectively.

All-electron projector augmented wave (PAW) potentials were employed for the elemental constituents with the GGA of Perdew-Burke-Ernzerhof (PBE) for the exchange-correlation energy functional, μ_{xc} , and the interpolation formula of Vosko et al. [91]. Using plane-wave cutoff energy of 450.0 eV, the total energy for all models of initial and final images was converged to 10^{-7} eV/cell. The reciprocal space of bulk supercells was sampled with $(2 \times 1 \times 5)$, $(10 \times 1 \times 4)$, and $(5 \times 3 \times 1)$ k-point grids for atomic structures of $\Sigma 5$ (310), $\Sigma 3$ (112) and $\Sigma 3$ (111). Each grid was generated using the Gamma scheme.

A double grain boundary periodic supercell was used for constructing a $\Sigma 5$ (310)

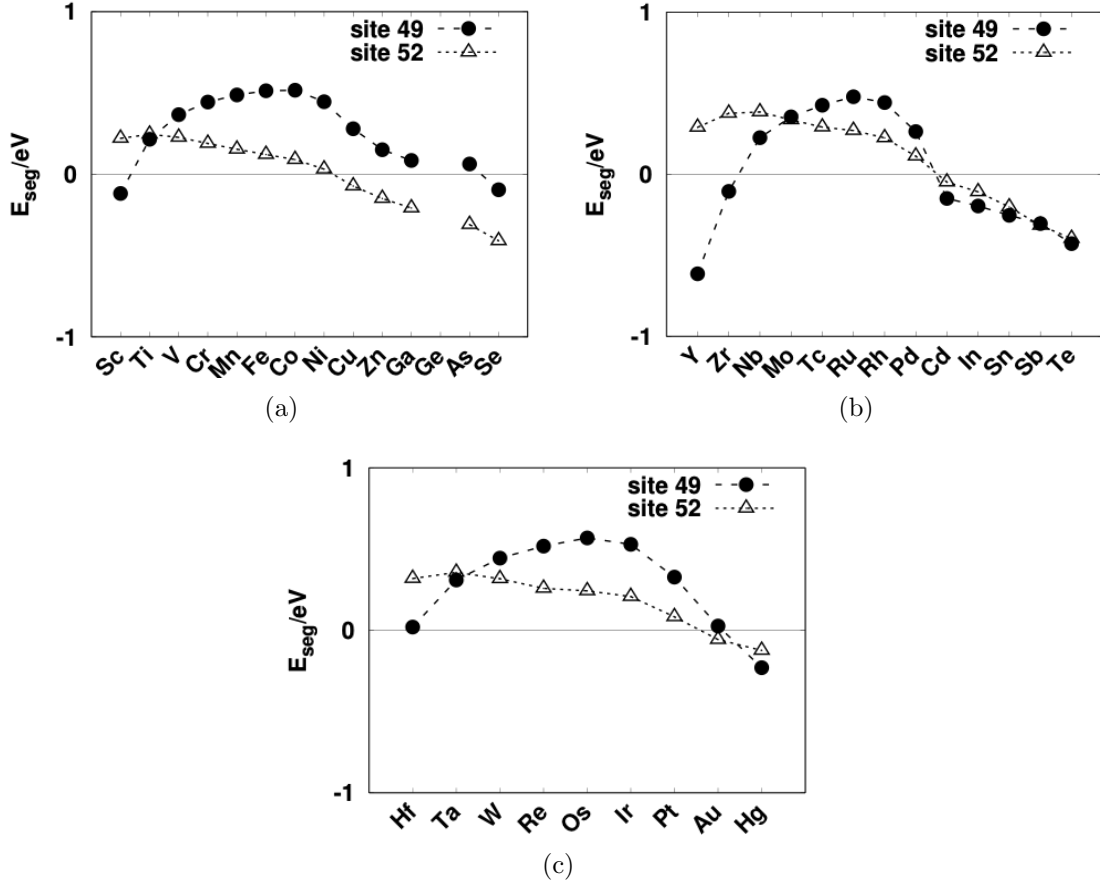


Figure 4.20: Segregation energies of different elements at $\Sigma 5$ (310) grain boundary. The solid circles are for elements segregated at location #49 in Figure 4.19. And the open triangles are for elements segregated at location #52 in Figure 4.19. Sub-figure (a), (b), and (c) show d-elements and some p-elements in fourth, fifth, and sixth periods, respectively.

grain boundary, as shown in Figure 4.19. Atom #49, #52 were chosen to be atoms close to the grain boundary. And atom #94 was chosen to be the atom far away from grain boundary. We calculated the grain boundary segregation energies for different elements in Figure 4.20. Their segregation across the period shows a consistent trend, which is that the segregation energy increases at first and then drops. A naive explanation would be the competition between the d-electron orbital filling and the effects of the volume as atomic size increases. However, these results are contradictory to the experimental values in terms of the element tungsten(W) [89, 90]. In Figure 4.21 and 4.22, other grain boundaries like $\Sigma 3$ (112) and $\Sigma 3$ (111), are also investigated using

DFT, and no case show W will segregate at either of those types of grain boundaries, despite a similar trend holds true for all of the three simple grain boundaries.

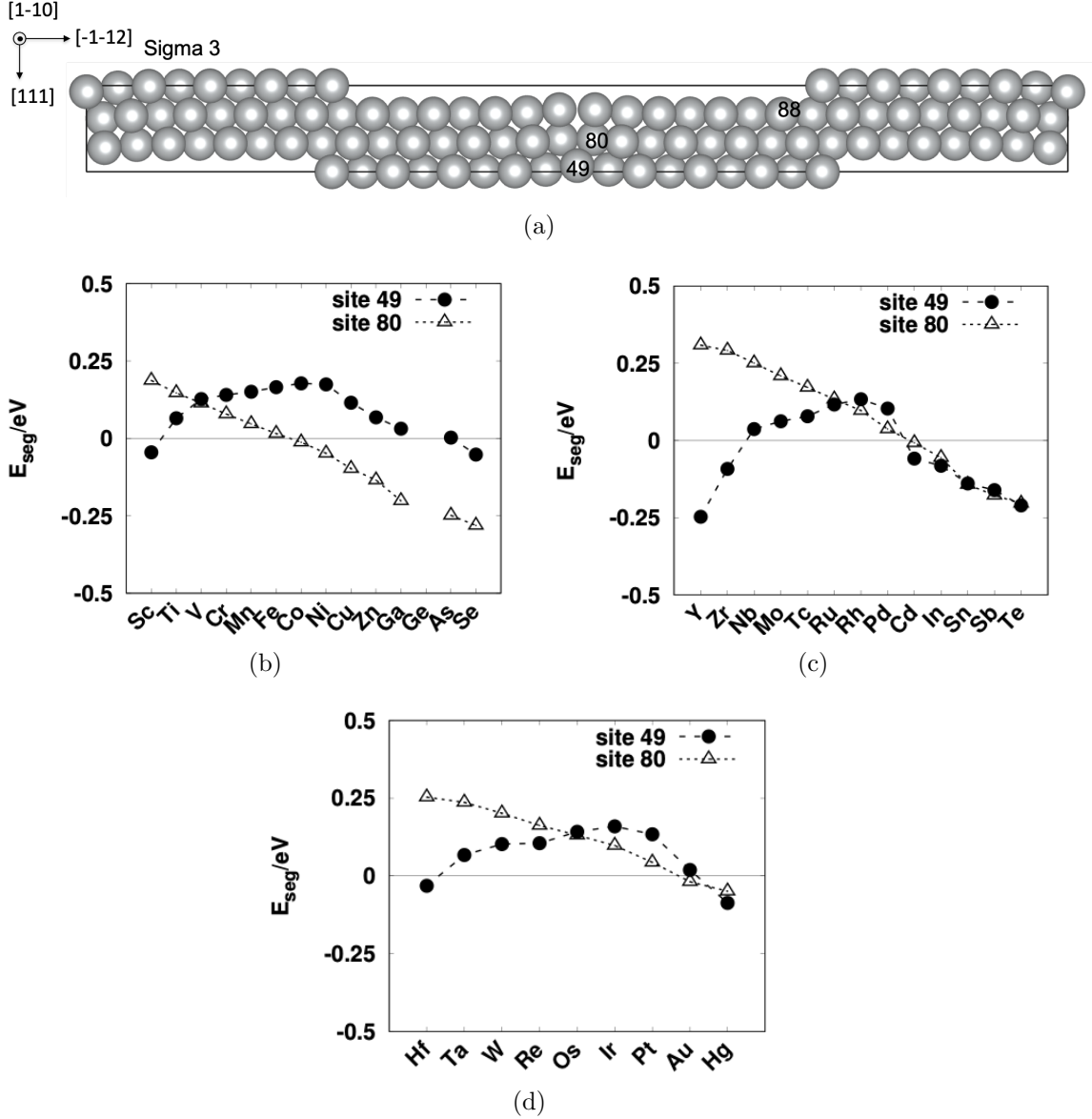


Figure 4.21: Segregation energies of different elements at $\Sigma 3$ (112) grain boundary. The solid circles are for elements segregated at location #49 in (a). And the open triangles are for elements segregated at location #80. Sub-figure (b), (c), and (d) show d-elements and some p-elements in fourth, fifth, and sixth periods, respectively.

A more complicated grain boundary, $\Sigma 29$ (520), from literature [92] as shown in Figure 4.23, was also studied, and it still shows repulsive interactions for W. In Table

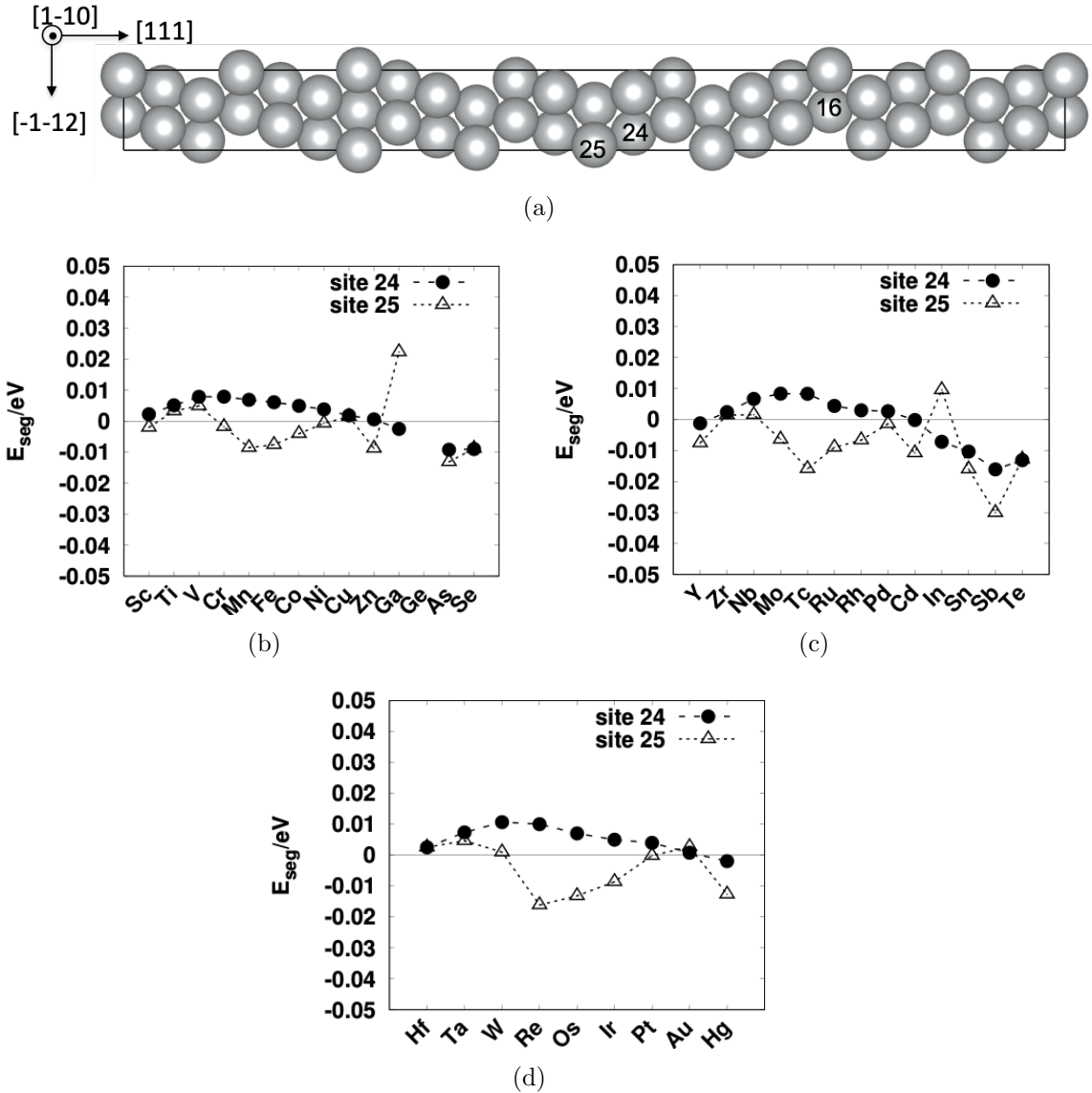


Figure 4.22: Segregation energies of different elements at Σ_3 (111) grain boundary. The solid circles are for elements segregated at location #24 in (a). And the open triangles are for elements segregated at location #25. Sub-figure (b), (c), and (d) show d-elements and some p-elements in fourth, fifth, and sixth periods, respectively.

4.3, W segregation energy at different sites was listed. All of them show positive values except site #196. However, when W atom was placed at that site, large distortion was observed across the grain boundary. And it was not a fair comparison to see W will segregate at that specific site #196. Traditionally, researchers first obtained relaxed grain boundary structures from pure metals and then substitute

dilute atoms to calculate alloy segregation effects. One possibility of the discrepancy we observed could be that alloying elements can not only change the chemistry of the grain boundaries but also change the atomistic structure of grain boundaries in alloys. Besides, in reality, more complicated grain boundaries, like grain boundary complexions, exist[93]. Therefore, more complicated grain boundary structures need to be obtained by global optimization methods, e.g. evolutionary algorithm [2], to investigate the alloy segregation effects.

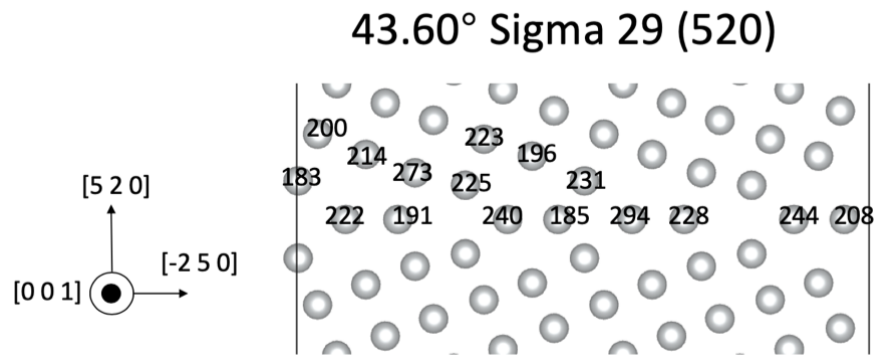


Figure 4.23: Atomistic structure of $\Sigma 29$ (520) Ag grain boundary. The blue vertical line indicates where the grain boundary is.

Table 4.3: Tungsten segregation energy E_{seg} at different sites of $\Sigma 29$ (520) Ag grain boundary. The segregation energy E_{seg} was calculated via Equation 4.5.

| site | E_{seg} eV/Atom | site | E_{seg} eV/Atom |
|------|-------------------|------|-------------------|
| 183 | .17150937 | 223 | .12724989 |
| 185 | .39017180 | 225 | .26205663 |
| 191 | .33935043 | 228 | .38927174 |
| 196 | -.01991584 | 231 | .11203458 |
| 200 | .10469391 | 240 | .51875226 |
| 208 | .45059809 | 244 | .55923929 |
| 214 | .02440580 | 273 | .18312458 |
| 222 | .42554973 | 294 | .42944364 |

4.6 Conclusions

In this chapter, we studied the effect of substrate on Ag thin film morphology by using GCMC and empirical potentials. This method is expandable to other metal thin films as well as other substrates, like MgO. It only requires customized parameters to match certain properties of the interaction between metal layers and substrates. Most of the metal side can use existing empirical potentials and other interactions can be tuned by L-J potential using the method described in this chapter.

GCMC simulations on these hexagonal surfaces usually yield Ag thin films that are in the fcc phase and {111} oriented. Therefore, Ag thin film quality (improve texture and reduce internal defects) can be improved by increasing ZnO substrate quality.

To achieve more continuous Ag thin films with less Ag, some elements can be added as “anchor” sites to incoming Ag atoms. Pd, Sb, Se, Sn, and Te can be good candidates as “anchor” sites on the ZnO substrate. With trace amount (0.05ML) of “anchor” sites on the substrate, more nuclei can be achieved, hence more continuous ultra-thin film.

We also search for alloying elements that can segregate in Ag grain boundaries to stabilize grain size during heat treatments. Current DFT calculation shows that tungsten (W) does not segregate to any investigated Ag grain boundaries. This result is inconsistent with the experimental fact that W can stabilize Ag grain boundaries during the heat treatment. The possible origin of such inconsistency can be resolved if more accurate and representative grain boundary structures in Ag alloys are constructed in future studies.

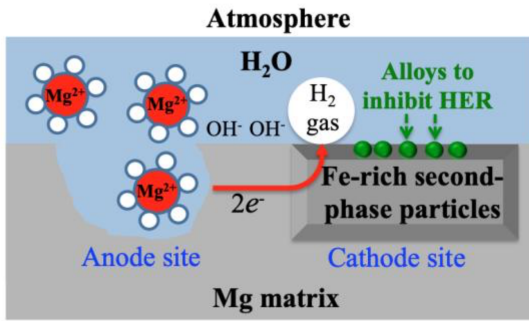
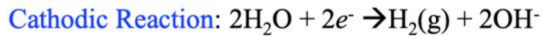
CHAPTER V

Using Alloy to Enhance Corrosion Resistance of Mg Alloy with Transition Metal Impurities

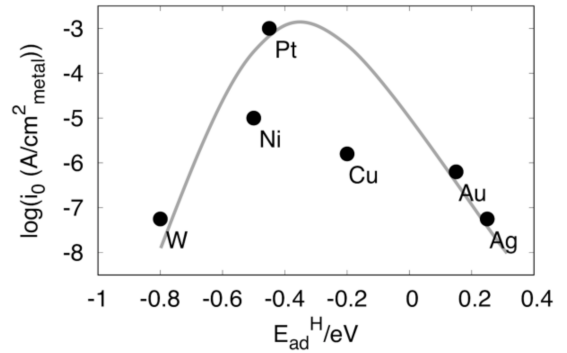
In this chapter, we focus on the Mg alloy corrosion due to impurities from casting processing and create a build-in corrosion-resistant mechanism by high-throughput first-principles calculations. A significant challenge for applications of Mg alloys is their poor corrosion resistance and hence Mg alloys designs with built-in corrosion resistance are of significant interest. Corrosion can result from the coupling of anodic dissolution of Mg and cathodic reduction of water on impurities such as Iron (Fe)-rich second-phase particles. Experiments have shown that small quantities of Arsenic (As) or Germanium (Ge) can inhibit Mg corrosion, possibly slowing the HER as the cathodic reaction on Fe surfaces. Since a broader experimental search across the periodic table for other Mg corrosion inhibiting elements is unavailable, we designed thermodynamic and HER criteria and used high-throughput computations to search a pool of 68 elements including As and Ge that can segregate from bulk Mg to surfaces of Fe particles and impede HER there. Our computational procedure predicts that six p-block elements meet these criteria, and they rank according to their ability to reduce H adsorption energies and the HER rate as follows: As > Ge > Si > Ga > P \approx Al. Results for As, the most effective corrosion-inhibiting element, and Ge are in qualitative accord with recent experiments. While none of the 68 elements was

found to enhance H adsorption, the six p-block elements reduce H adsorption via strong orbital overlap (Pauli repulsion) between their outer-shell orbitals and the s orbitals of H adsorbates. These p-block elements are also found to have the potential to reduce HER on surfaces of Ni second-phase particles in Mg according to the same criteria, but not on surfaces of Cu second-phase particles.

5.1 Introduction



(a)



(b)

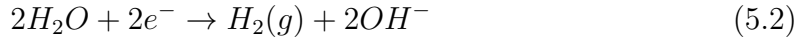
Figure 5.1: Illustration of corrosion reaction mechanism on Mg and the alloying strategy to inhibit HER. (a) Illustration of corrosion reaction mechanism on Mg and the alloying strategy to inhibit the HER as the cathodic reaction. The anodic reaction occurs to Mg matrix by dissolving one Mg atom to produce a Mg^{2+} cation into the electrolyte and two electrons for HER as the cathodic reaction, which occurs on surfaces of second-phase particles, usually rich in Fe and other transition metal elements, to produce a H_2 gas molecule. A possible strategy to reduce HER rate is to change the H adsorption energy on the surfaces of second-phase particles by proper alloying. (b) Exchange current density of HER, $\log(i_0(A/cm^2_{metal}))$, measured in experiments under pH=12 vs. H adsorption energy E_{ad}^H defined by Equation 5.6 from DFT calculations. This figure is adapted from the data of Sheng et al.[94]. A higher exchange current density corresponds to a faster HER and a higher corrosion rate. The volcano-shaped solid curve line is plotted only for an illustration the relation between $\log(i_0)$ and E_{ad}^H without quantitative accuracy.

Magnesium alloys are potential candidates for lightweight structural components

in transportation industries and other applications due to their low density and high specific strength. Substantial effort has been focused on exploring cast and wrought magnesium (Mg) alloys for application in vehicle propulsion systems and body structures, for example, as part of light-weighting strategies [95, 96, 97, 98, 99]. However, corrosion in aqueous and atmospheric environments is one of two significant challenges facing a broader implementation of current Mg alloys in vehicles. The other challenge is poor room temperature formability of Mg sheet alloys in stamping, a consequence of the anisotropy in plasticity response associated with the various dislocation slip systems in the HCP structure [100]. Post-forming surface treatments can be applied to mitigate Mg corrosion [101]. In an aqueous environment, the coupling between regions of anodic dissolution of Mg and cathodic reduction of water drives galvanic corrosion leading to the removal of Mg and the formation of pits surrounding second-phase particles as cathode sites [102, 103]. Magnesium has a highly negative standard electrode potential of -2.37 V relative to the standard hydrogen electrode (SHE), making it a very active anode (all electrode potential values are relative to the SHE in this paper). Anodic dissolution of Mg via



couples with the cathodic reaction, which is the reduction of water in an alkaline electrolyte

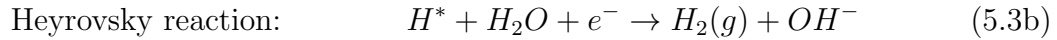
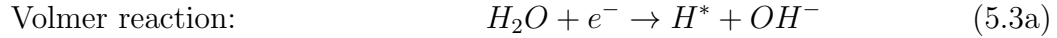


Equation 5.2 is the HER with a standard electrode potential of -0.828 V relative to SHE. The overall reaction mechanism is illustrated in Figure 5.1 (a).

Corrosion on Mg proceeds without any limitation for pH < 11 since oxygen is not involved and no passivating surface layer forms [104, 105]. Previously, it was found

that Fe, Cu, Co, and Ni accelerate Mg corrosion in aqueous environments containing chlorides [106, 107]. Even though Fe (an impurity often introduced during alloy processing [108, 109]) has a very low solubility limit in Mg [107], Fe particles in BCC structure have been identified as cathode sites. This was demonstrated by Taub et al. [110] with experiments involving powdered Mg and Fe in chloride solutions. The cathodic reaction in Mg alloys typically occurs at submicron and micron-scale Fe (and Fe-rich) second-phase particles positioned at the metal-aqueous solution interface [108, 111]. The detailed roles of Fe-rich particles as cathodic reaction sites can vary according to corrosion potentials (such as the negative difference effect (NDE)) and the populations/sizes of Fe-rich particles [112, 113]; the cathodic reaction rates should also depend on the surface configurations of Mg, which typically contain mixtures of porous Mg hydroxides and oxides (e.g. aluminum oxide). Hence, the accurate locations of Fe-rich particles relative to these mixtures can result in changes in corrosion rates [114, 115]. Song and Atrens provided an overview of galvanic as well as other corrosion mechanisms of Mg with some useful insights [116]. Esmaily et al. presented a comprehensive summary of the recent progress of studies in Mg-alloy corrosion [117].

There is significant interest in designing Mg alloys that have a “built-in” corrosion inhibition mechanism [111]. A possible strategy is to slow down the HER rates on cathode sites such as Fe particles in BCC phase. The HER can be completed through either the Volmer-Heyrovsky mechanism or the Volmer-Tafel mechanism [118, 119]. The associated reactions are



Here * means the corresponding atom/molecule is adsorbed on cathode surface sites. The Volmer-Heyrovsky mechanism proceeds first via Equation 5.3a followed by Equation 5.3b. The Volmer-Tafel mechanism involves Equation 5.3a twice followed by Equation 5.3c. The equilibrium potentials of Equation 5.3a, 5.3b and 5.3c depend on the free energies of hydrogen atoms adsorbed on cathode surface sites.

The slowing down of the HER as the cathodic reaction requires the reduction of reaction rates via the Volmer-Heyrovsky mechanism and the Volmer-Tafel mechanism. Regarding the Volmer reaction in Equation 5.3a, its fast kinetics favors the strong adsorption of an H atom on a cathode surface site to increase its thermodynamic driving force since H^* is its reaction product. However, the fast kinetics of the Heyrovsky and Tafel reactions in Equation 5.3b and 5.3c, respectively, require the weak adsorption of an H atom since H^* is the reactant on the left side of each equation. Thus, the adsorption strength of H atoms on a cathode surface must be at an intermediate-range to reach the maximum HER rate: this is the Sabatier principle [120]. Figure 5.1 (b) shows the exchange-current density of the HER vs. H adsorption energy, E_{ad}^H , in alkaline electrolytes [94]: the highest values of $\log(i_0)$ corresponding to the fastest HER rate appear for the intermediate E_{ad}^H . Similar plots of HER rate in acid electrolyte vs. E_{ad}^H have been explored on different metals, even though the detailed reaction mechanisms in the HER differ from those in an acid electrolyte. Therefore, to slow down the overall HER rate on cathode sites, either the adsorption strength of H must be strongly enhanced, so that the rate of the Heyrovsky and Tafel reactions is largely decreased, or the adsorption of H must be significantly weakened thereby reducing the rate of the Volmer reaction.

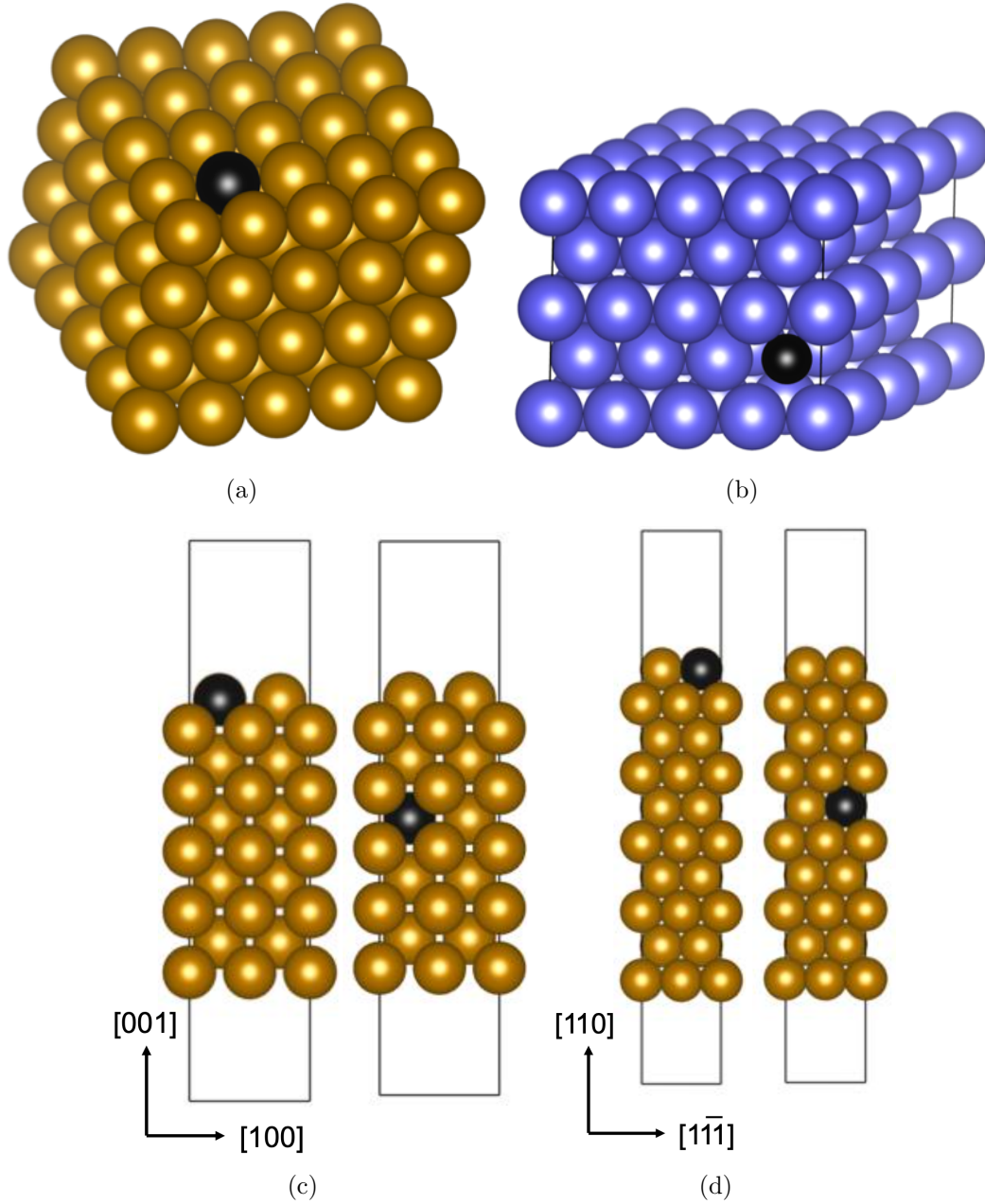


Figure 5.2: Perspective and side views of a generic alloying element in the simulation.

(a) and (b): Perspective view of a generic alloying element (black) in (a) bulk Fe (gold) and (b) bulk Mg (blue) lattice. (c)/(d): Side views of a generic alloying element (black) positioning in (2×2) Fe (100) (c) /Fe (110) (d) surface slab (the left sub-figure) at a substitutional site in the top surface layer and (the right sub-figure) at a substitutional site inside bulk Fe (5th layers from the top surface).

Experimentalists have identified Arsenic (As) and Germanium (Ge) as Mg corrosion inhibitors. These are thought to exert a form of “kinetic control” over Mg

corrosion, which is somewhat surprising from the standpoint that most elements tend to increase Mg corrosion rates [104]. Eaves et al. [111] were among the first to report that As is an effective corrosion inhibitor for commercially pure Mg with 280 ppm Fe in aqueous NaCl electrolyte. A subsequent report by Birbilis et al. [102] proposed that As effectively “poisons” Mg corrosion by acting as a barrier for hydrogen intermediate (H^*) recombination on surfaces of Fe particles (i.e. the cathode sites) thereby disrupting the formation of $H_2(g)$ and, consequently, the HER reaction. Noting that As is carcinogenic to humans, Liu et al. [104, 121] explored Ge and Ge-Zn metallurgically alloyed with pure Mg and found that Ge also interferes with cathode reactions. Other investigations have focused on adding rare earth elements to Mg [122, 123, 124]. New Mg-Li and Mg-Sn alloys were recently reported in which protective surface films form that prevent corrosion [125, 126]. While these studies have pointed to an effect of a few elemental additives on Mg corrosion, the experimental literature has not, to our knowledge, provided a more expansive study of Mg corrosion inhibiting elements, and it is essentially silent regarding the role of electronic structure and chemical bonding at surfaces of Fe particles especially with regards to possible disruption of the HER.

In this chapter, we use a high-throughput computational procedure based on DFT to search for potential Mg corrosion inhibiting elements. We first search for other elements that can effectively slow down/disrupt the HER by computing H adsorption energies on clean Fe surfaces with different alloying elements. Under realistic electrochemical conditions, there are other atoms/molecules and reaction intermediates, such as O atoms, OH groups and water molecules that affect the overall HER rate, and multiscale simulations would be required to output accurate electrochemical rates [31]. Alternatively, clean metallic surfaces have been widely used as effective model systems to quantitatively evaluate the relative changes of surface reaction rates, including those related to the HER on pure and doped Mg surfaces [79, 127]. In general,

the H adsorption energy on clean metallic surfaces has been proven to be an effective “descriptor” of HER rates on these surfaces [128].

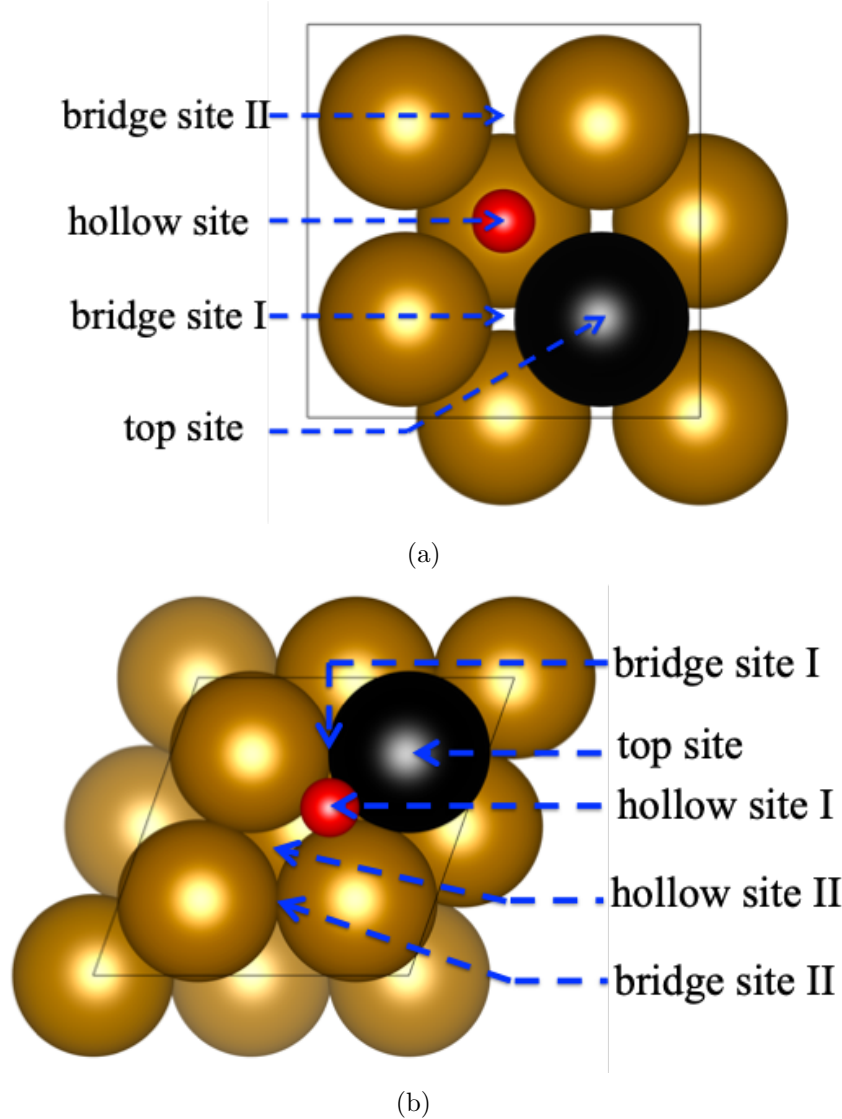


Figure 5.3: Top-down views of Fe surfaces with substitutional alloying elements and adsorbed H atoms. (a) The (2×2) Fe (100) slab with a generic alloying element substituting a Fe atom in the top surface layer and an adsorbed H atom at the hollow site. (b) The (2×2) Fe (110) slab with a generic alloying element substituting a Fe atom in the top surface layer and an adsorbed H atom at the hollow site I. The concentration of the adsorbed H and the substitutional alloying atom is $\frac{1}{4}$ ML for both Fe (100) and Fe (110).

5.2 Criteria to determine candidate elements to inhibit Mg corrosion

The following three criteria were applied to determine if an alloying element could potentially inhibit Mg corrosion by slowing down the HER as the cathodic reaction on surfaces of Fe-rich second-phase particles. (1) The alloying element must show a thermodynamic preference for bulk Fe over bulk Mg. (2) The alloying element must be thermodynamically more stable on Fe surfaces than in bulk Fe. (3) The adsorption energies of a lone H atom on Fe surfaces with an alloying element in their topmost layers should be significantly reduced (or enhanced) relative to the adsorption energies of a lone H atom on pure Fe surfaces, suggesting possible interference with $H_2(g)$ formation and a consequent decrease in the HER rate. Therefore, criterion 3 requires that a potential candidate significantly increase or reduce H adsorption strength on Fe particle surfaces.

The second and third criteria require the investigation of specific Fe surfaces. The Wulff plot shows (100) and (110) surfaces of a BCC Fe single crystal are the two-major low-index surfaces at equilibrium conditions; (100) and (110) occupy more than 50% of the BCC Fe surface area and have the lowest energies[129]. Other high-index surfaces are also combinations of these two surfaces with steps. Therefore, our high-throughput search was conducted on models constructed with either (100) or (110) surfaces of BCC Fe.

The first criterion requires that a Mg corrosion-inhibiting element must have a thermodynamic preference for bulk Fe over bulk Mg. Hence, models aimed at examining bulk segregation energetics were constructed. To simulate bulk Fe, we constructed a $4 \times 4 \times 4$ (64 atoms) supercell (each primitive cell consists of 1 Fe atom). To simulate bulk Mg, we constructed a $4 \times 4 \times 2$ supercell (64 atoms) with each primitive cell consisting of 2 Mg atoms. An element (e.g. As) was then placed at an Fe substi-

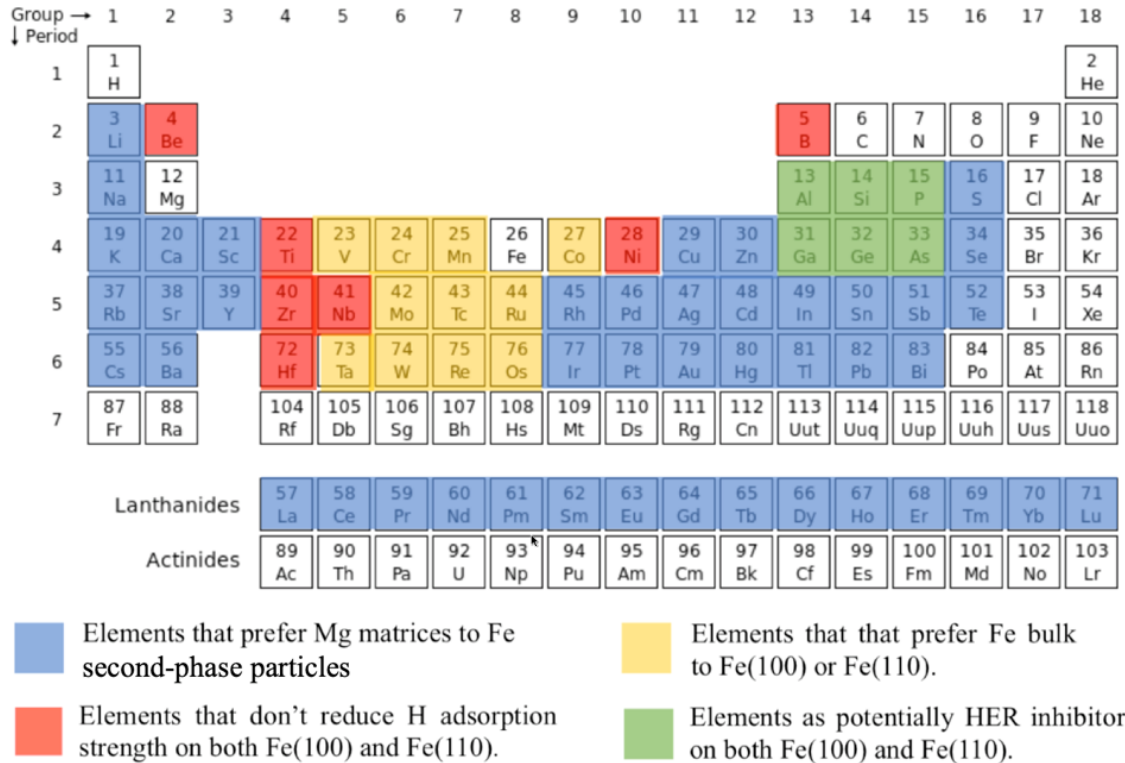


Figure 5.4: Summary of the high-throughput search for alloying elements that can inhibit HER on surfaces of Fe second-phase particles in Mg matrix. All investigated alloying elements are labeled in colors (blue, yellow, red and green). Different colors describe the search results for the corresponding alloying elements as explained in the figure legends. (White periodic table from Wikimedia Commons)

tutional site in the bulk Fe supercell and at a Mg substitutional site in the Mg bulk supercell, as shown in Figs. 2(a) and 2(b), respectively.

To address the second criterion (an element must have a thermodynamic preference for Fe (100) and Fe (110) surfaces rather than for bulk Fe), four models aimed at examining Fe surface segregation energetics were constructed. Each consisted of 40 atoms in the Fe (100) and Fe (110) slabs with 10 layers of 2×2 surface periodicity and a 12 Å vacuum. Two of the models contained an element placed at an Fe substitutional site in the top surface layers of Fe (100) and Fe (110) (i.e. where the HER is expected to occur). These models are shown in Figs. 2(c) and 2(d), respectively. For

the remaining two models, also shown in Figs. 2(c) and 2(d), an element (e.g. As) was placed at an Fe substitutional site five layers below the top surface.

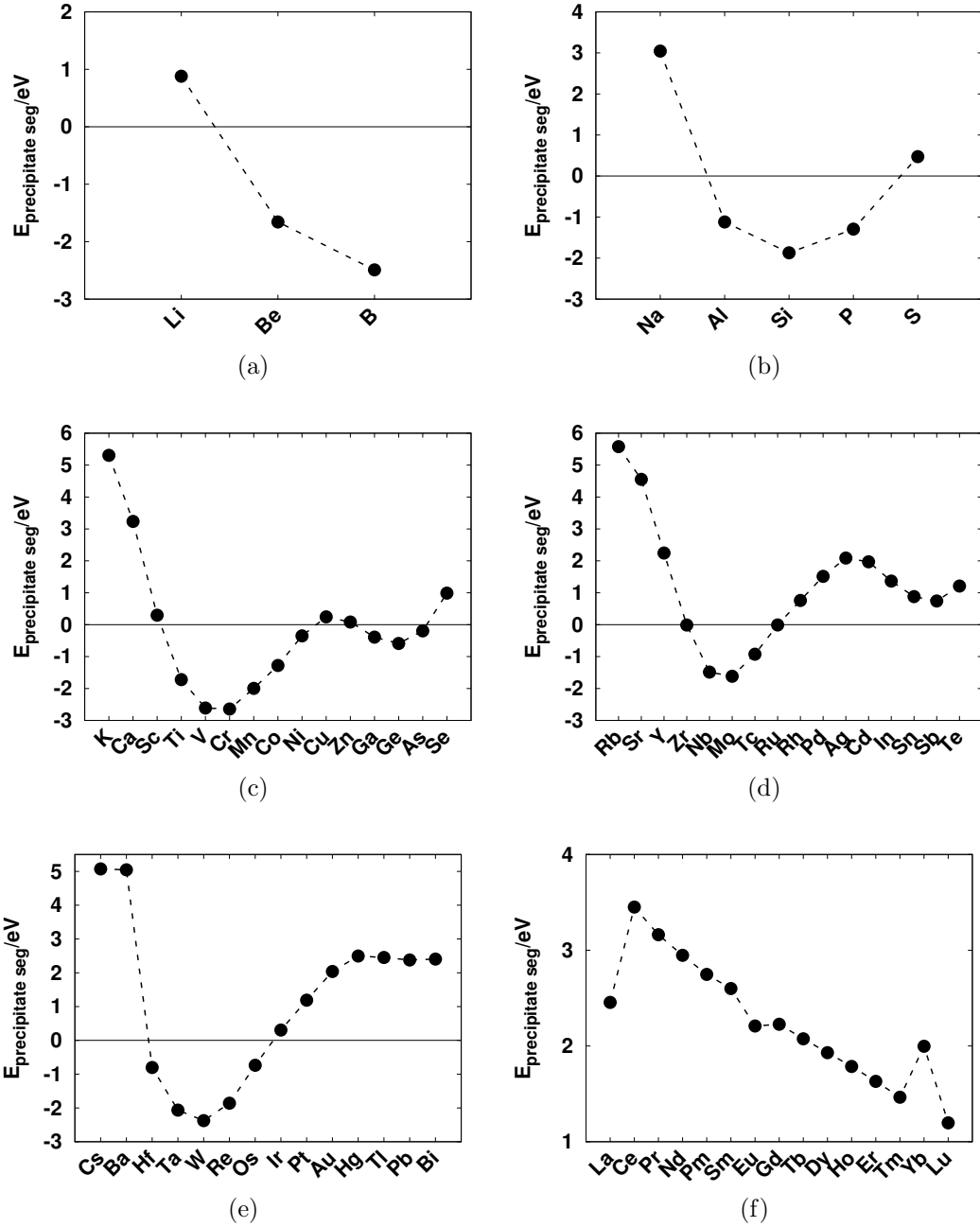


Figure 5.5: Segregation energies to bulk second-phase particles $E_{\text{particleseg}}$ defined in Equation 5.4 for the 68 potential alloying elements. Preference for a BCC Fe particle over the bulk HCP Mg requires that an alloying element should have a significantly negative value of $E_{\text{particleseg}}$. (a)-(e): Elements in Row 2, 3, 4, 5 and 6 of the periodic table, respectively. (f) Lanthanide Elements. Elements with negative $E_{\text{particleseg}}$ are narrowed to 24: Be, B, Al, Si, P, Ti, V, Cr, Mn, Co, Ni, Ga, Ge, As, Zr, Nb, Mo, Tc, Ru, Hf, Ta, W, Re and Os.

To address the third criterion that pertains to affecting H adsorption energies and possibly the HER rate, H adsorption energetics were investigated with both a single H atom adsorbed ($\frac{1}{4}$ ML) at different sites on Fe (100) and Fe (110) with (2×2) in-plane periodicity and an alloying element substituting a Fe atom in the top surface layer. On a (2×2) Fe (100) with a substitutional alloying atom in the top layer, there are four possible H adsorption sites as shown in Figure 5.3 (a): (1) a top site directly above 1 Fe atom or 1 alloying atom substituting for a Fe surface atom, (2) a bridge site I with 1 Fe atom and 1 alloying atom nearest neighbors (NNs), (3) a bridge site II with 2 Fe atoms as NNs, (4) a hollow site with 3 Fe atoms and 1 alloying atom NNs. On a (2×2) Fe (110) with a substitutional alloying atom in the top layer, there are five H adsorption sites of interest as shown in Figure 5.3 (b): (1) a top site directly above 1 Fe atom or 1 alloying atom, (2) a bridge site I with 1 Fe atom and 1 alloying atom as NNs, (3) a bridge site II with 2 Fe atoms as NNs, (4) a hollow site I with 2 Fe atoms and 1 alloying atom as NNs, (5) a hollow site II with 3 Fe atoms as NNs.

The computational engine that provided the energetics used to evaluate the three criteria for each of the 68 candidate alloying elements was the implementation of DFT in the VASP. Each model was spin-polarized to account for BCC Fe ferromagnetism. All-electron PAW potentials were employed for the elemental constituents with the GGA of PBE for the exchange-correlation energy functional, μ_{xc} , and the interpolation formula of Vosko et al.[91]. Using plane-wave cutoff energy of at 450.0 eV, the total energy for all models was converged to 10^{-7} eV/cell, and the force components on each atom were relaxed to less than 10^{-3} eV/Å. The reciprocal space of Fe (110), Fe (100) and bulk supercells were sampled with $(16\times 16\times 1)$, $(14\times 14\times 1)$, and $(8\times 8\times 8)$ k-point grids, respectively. Each grid was generated using the Monkhorst-Pack scheme [72]. A $20\text{\AA}\times 20\text{\AA}\times 20\text{\AA}$ supercell with a H_2 molecule in the middle was used for this calculation. The reciprocal space was sampled with a $(1\times 1\times 1)$ Gamma centered k-points grid. Using plane-wave cutoff energy of at 450.0 eV, the total energy

for all models was converged to 10^{-7} eV/cell.

Two successive structural optimizations (adapting basis vectors and computational grids to the cell parameters) were conducted on the bulk solids to ensure that the cell energies and structural parameters were fully converged. A VASP-optimized lattice parameter of 2.83 Å for BCC Fe was computed (the experimental room temperature value is 2.87 Å[130]) along with a $2.197 \mu B/atom$ spin moment. Our computed spin moment is in good agreement with the $2.2 \mu B/atom$ value from the DFT study of Tiago et al.[131]. For HCP Mg, the VASP-optimized lattice parameters are: $a=3.19$ Å, $c/a = 1.62$ (the room temperature experimental values are: $a=3.32$ Å, $c/a = 1.62$ [132]). DFT calculations predict Fe (110) to have the lowest surface energy ($2.40 J/m^2$) and Fe (100) to have the second-lowest surface energy ($2.45 J/m^2$), in accord with previous DFT studies of Fe surfaces[133]. Experiments, however, identify (100) as having the lowest surface energy[134]. Possible reasons for the disparity between DFT and experiments are provided by Hung et al.[133].

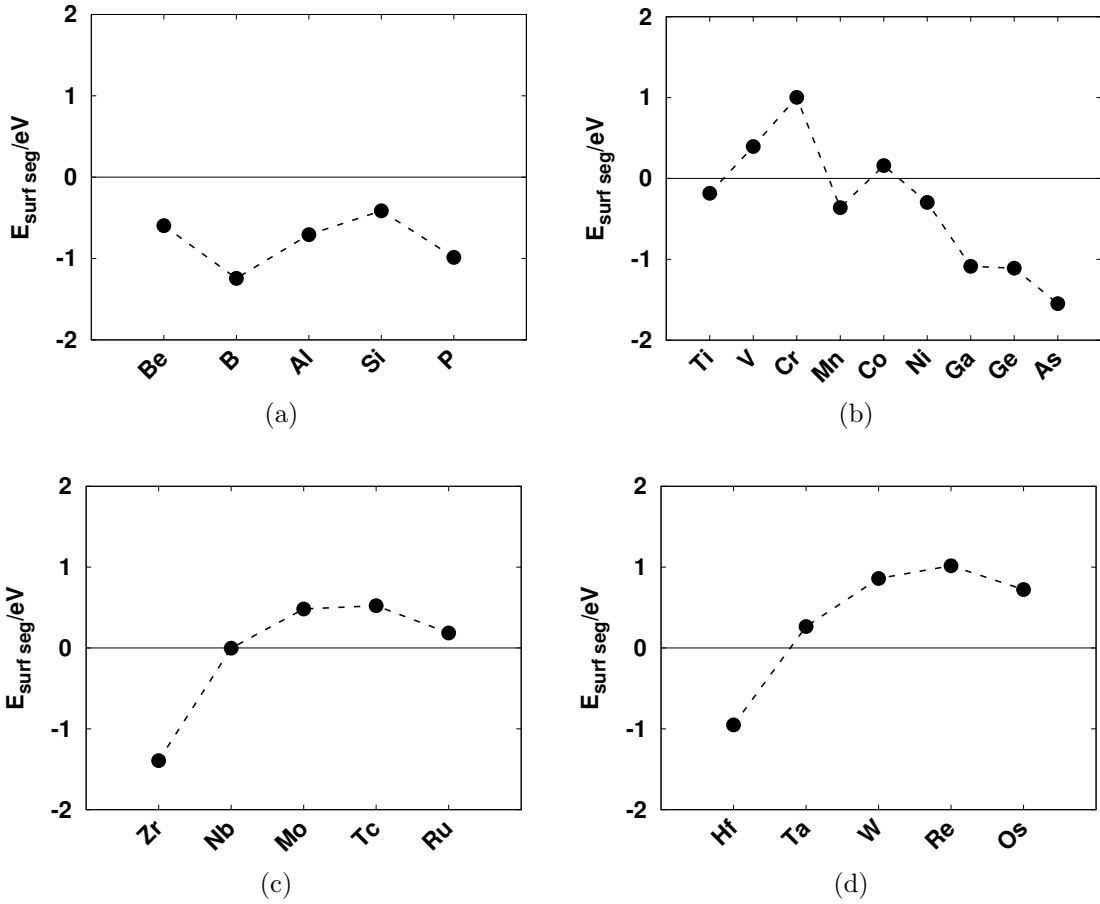


Figure 5.6: Segregation energies $E_{surfseg}$ defined in Equation 5.5 for Fe (100) of 24 alloying elements narrowed from the first screening round. A qualified alloy candidate should have a strongly negative value of $E_{surfseg}$. (a): Elements in Row 2 and 3 of the periodic table. (b) (d): Elements in Row 4, 5 and 6 of the periodic table, respectively.

Other than H adsorption energetics, there are two other criteria that are important as mentioned in Section 2.1: (1) an alloying element X should be more thermodynamically stable in bulk BCC Fe instead of bulk HCP Mg, (2) an alloying element X should segregate to an Fe surface rather than remaining in bulk Fe. Regarding the first criterion, we calculated the segregation energy to the second-phase particle, $E_{particleseg}$, via

$$E_{particleseg} = \left(\frac{63}{64} E_{Mg64} + E_{Fe63}X \right) - \left(E_{Mg63}X + \frac{63}{64} E_{Fe64} \right) \quad (5.4)$$

where E_{Mg64} , E_{Fe63X} , E_{Mg63X} , and E_{Fe64} are the total energies of 64-atom supercells for pure bulk HCP Mg, bulk BCC Fe with 1 substitutional X atom (see Figure 5.2 (a)), bulk HCP Mg with 1 substitutional X atom (see Figure 5.2 (b)), and pure bulk BCC Fe, respectively. A negative value of $E_{particlessig}$ for a given X means that it is energetically favorable for X to bind to bulk Fe instead of segregating to bulk Mg. The results show that a substitutional As atom has an energetic preference for bulk Fe over bulk Mg using the models shown in Figure 5.2 (a) and 5.2 (b), with a computed segregation energy of -0.19 eV.

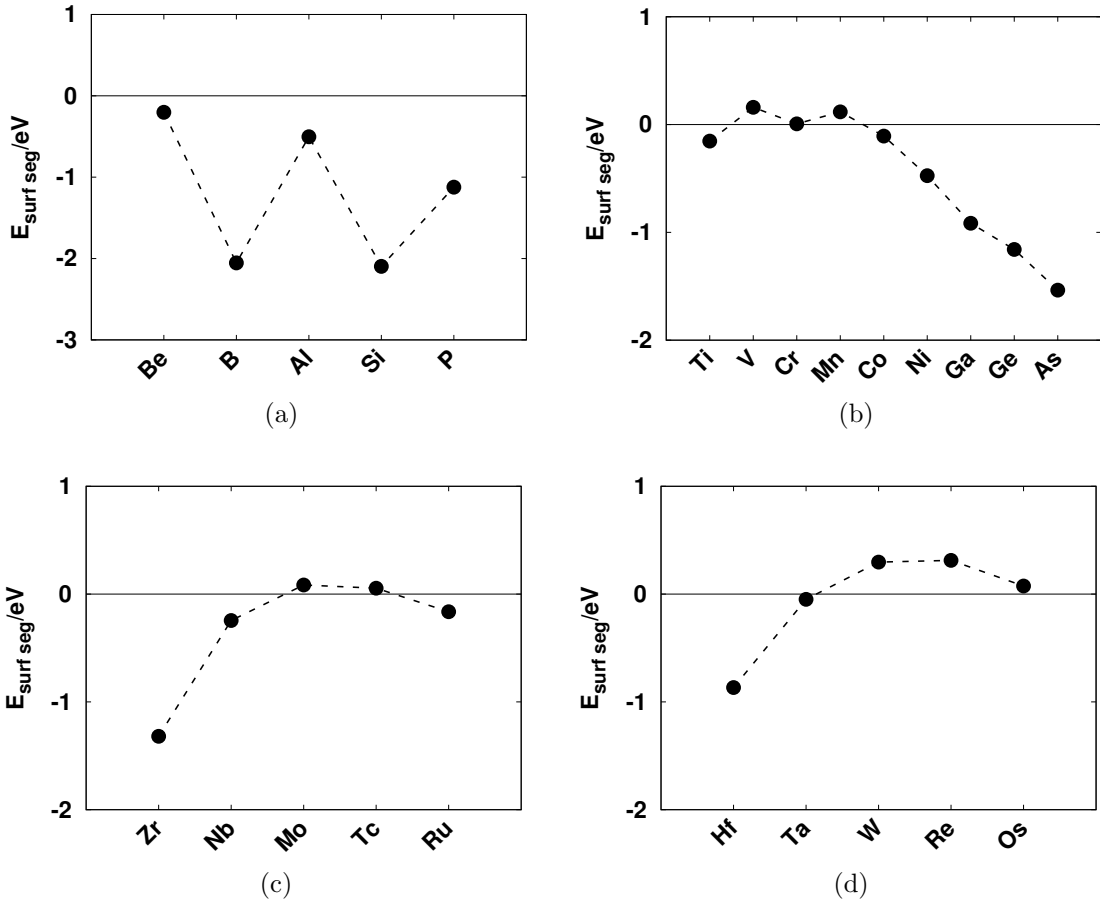


Figure 5.7: Segregation energies E_{surfseg} defined in Equation 5.5 for Fe (110) of 24 alloying elements narrowed from the first screening round. A qualified alloy candidate should have a strongly negative value of E_{surfseg} . (a): Elements in Row 2 and 3 of the periodic table. (b) (d): Elements in Row 4, 5 and 6 of the periodic table, respectively.

Regarding the second criterion, we calculated the surface segregation energy of a substitutional alloying atom, E_{surfseg} , via:

$$E_{\text{surfseg}} = E_{\text{surf}} - E_{\text{bulk}} \quad (5.5)$$

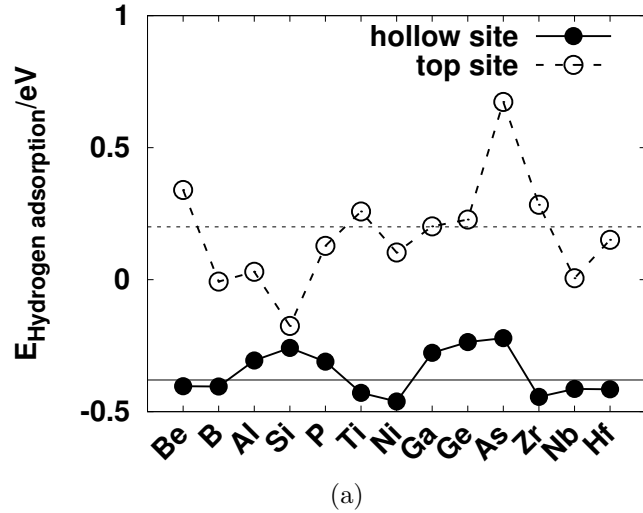
where E_{surf} and E_{bulk} are the DFT-computed energies of the corresponding surface slab with a substitutional alloying atom in the top surface layer (left figure in either Figure 5.2 (c) or 5.2 (d)) and the surface slab with a substitutional alloying atom inside the bulk (right figure in either Figure 5.2 (c) or 5.2 (d)), respectively). A

negative $E_{surfseg}$ suggests that an alloying element will preferentially occupy an Fe site in the top surface layer instead of a site within bulk Fe. The results show that As prefers Fe (100) and Fe (110) instead of bulk Fe with computed segregation energies of -1.55 eV and -1.54 eV, respectively. Similar computations based on Equation 5.4 and 5.5 were conducted for the other 67 elements noted in Figure 5.4 and detailed below.

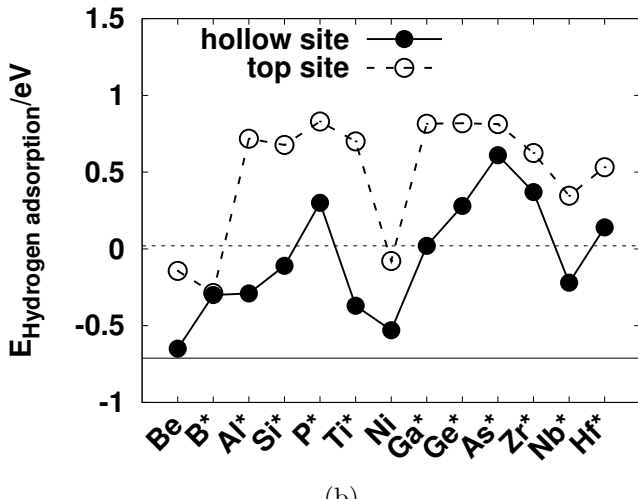
The H adsorption energy, E_{ad}^H , was computed from

$$E_{ad}^H = E_{H/slab} - E_{slab} - \frac{1}{2}E_{H_2}(g) \quad (5.6)$$

where $E_{H/slab}$ and E_{slab} are the total energies of supercells of an Fe surface slab with/without adsorbed H atoms, respectively. $H_2(g)$ is the energy of an isolated hydrogen gas molecule. Thus, the hydrogen adsorption strength is stronger with a more negative value of E_{ad}^H . The most stable H adsorption site on pure Fe (100) is the hollow site noted in Figure 5.3 (a) with $E_{ad}^H = -0.38$ eV. With an As atom substituting an Fe atom in the top surface layer of Fe (100), Table 5.1 shows that E_{ad}^H at the hollow site with an As NN in Figure 5.3 (a) changes to -0.22 eV/atom. If H is initially placed at the top site above the substitutional As atom in the top layer of Fe (100), an unfavorable $E_{ad}^H = 0.67$ eV is substantially different than the $E_{ad}^H = 0.20$ eV for H at the top site of pure Fe (100) as listed in Table 5.1. If H is initially placed at bridge site I in Figure 5.3 (a), it moves to the top site above the Fe NN during VASP optimization. E_{ad}^H at the bridge site II in Figure 5.3 (a) is very similar to E_{ad}^H at the bridge site of pure Fe (100) because there is no As as the NN.



(a)



(b)

Figure 5.8: H adsorption energies E_{ad}^H defined in Equation 5.6 on Fe (100) and Fe (110) with the 13 alloying elements that pass the second screening round. (a) H adsorption energies at the hollow site and the top site on Fe (100) with different alloying elements. Their surface geometry is shown in Figure 5.3 (a). The horizontal solid and dash lines are the hydrogen adsorption energy at the hollow site and top site of pure Fe (100), respectively. (b) H adsorption energies at the hollow site I and the top site on Fe (110) with different alloying elements. Their surface geometry is shown in Figure 5.3 (b). The horizontal solid and dash lines are the hydrogen adsorption energy at the hollow site I and top site on a pure Fe surface, respectively. H adsorption energies at the hollow site I on Fe (110) surfaces with B, Al, Si, P, Ti, Ga, Ge, As, Zr, Nb and Hf (marked with *) were computed by only allowing H and surface atoms to relax in the direction normal to the Fe (110).

5.3 High Throughput Screening Results

We next examined the remaining 67 elements identified in Figure 5.4 (all elements with colors in the periodic table) with high-throughput DFT computations. Three successive rounds of calculations, each aimed at addressing one of the three criteria listed in Section 2.1, were conducted to narrow down the broader pool of elements highlighted in Figure 5.4. In the first round, we examined Fe segregation energies to determine which of the remaining elements in Figure 5.4 prefers to segregate to bulk Fe rather than bulk Mg. This is the basis of the first criteria. In the second round, we determined which of those elements that passed the first round have favorable binding to Fe (100) and Fe (110) relative to bulk Fe. This is the basis of the second criterion. In the third and final round, we investigated which elements can either significantly weaken or strengthen H adsorption on Fe (110) and Fe (100).

For the first round, we calculated the second-phase particle segregation energy, $E_{particleseg}$, of all alloying elements X (except As, which was previously addressed) denoted with colors in Figure 5.4 using Equation 5.4. As shown in Figure 5.5, elements with negative $E_{particleseg}$ are narrowed to 24: Be, B (Figure 5.2), Al, Si, P (Figure 5.2), Ti, V, Cr, Mn, Co, Ni, Ga, Ge, As (Figure 5.5 (c)), Zr, Nb, Mo, Tc, Ru (Figure 5.5 (d)), Hf, Ta, W, Re and Os (Figure 5.5 (e)). No elements in the 7th row or lanthanide series passed the first screening round (Figure 5.5 (f)).

In the second round, we determined which of the 24 elements that passed the first screening round bind to Fe (100) and Fe (110) rather than to bulk Fe. The implication here is that potential slowing or even disruption of the HER can only occur if “X” preferentially binds to surfaces of Fe second-phase particles in an Mg alloy. We performed VASP calculations with the remaining 24 elements adsorbed on Fe (100) and (110) using the models in Figure 5.2 (c) and 5.2 (d), where there is one atom of alloying element X in the top surface layer or the bulk layer of a (2×2) periodic unit cell. We calculated the surface segregation energy, $E_{surfseg}$, of all 24

elements using Equation 5.5. According to Figure 5.6, only 13 elements from the pool of 24 from the second round were predicted to have favorable binding to Fe (100) ($E_{surfseg} < 0$): Be, B, Al, Si, P (Figure 5.6 (a)), Ti, Mn, Ni, Ga, Ge, As (Figure 5.6 (b)), Zr (Figure 5.6 (c)), and Hf (Figure 5.6 (d)). Figure 5.6 (c) suggests that Nb has no preference for either Fe (100) or bulk Fe. We passed Nb on, nevertheless, to the third screening round. Similarly, Figure 7 shows the same 13 candidates for Fe (110). Hence, Be, B, Al, Si, P, Ti, Ni, Ga, Ge, As, Zr, Nb, and Hf are passed to the third and final screening round.

Table 5.1: Summary of H adsorption energies (eV/atom) defined at Equation 5.6 at selected sites on (2×2) Fe (100) and Fe (110) surface slabs without/with one substitutional atom from one of the 13 alloying elements that pass the second screening round. H adsorption site is indicated at the top of each column and plotted in Figure 3(a) and 3(b). The “stability” at the top of the 5th column means that H stays at the hollow site I on Fe (110) with substitutional alloying atoms as Figure 3(b) after the H and surface atoms are fully relaxed by VASP optimization. Otherwise, the H adsorption energies at such hollow site I are calculated by only allowing the H and surface atoms to relax in the direction normal to the surface.

| | (100) top site | (100) hollow site | (110) top site | (110) hollow site I stability | (110) hollow site I |
|---------|-------------------|----------------------|-------------------|----------------------------------|------------------------|
| Pure Fe | 0.2 | -0.38 | 0.02 | Yes | -0.71 |
| Be | 0.34 | -0.4 | -0.14 | Yes | -0.65 |
| B | -0.01 | -0.4 | -0.29 | No | -0.3 |
| Al | 0.03 | -0.31 | 0.72 | No | -0.29 |
| Si | -0.18 | -0.26 | 0.68 | No | -0.11 |
| P | 0.13 | -0.31 | 0.83 | No | 0.3 |
| Ti | 0.26 | -0.43 | 0.7 | No | -0.37 |
| Ni | 0.1 | -0.46 | -0.08 | Yes | -0.53 |
| Ga | 0.2 | -0.28 | 0.82 | No | 0.02 |
| Ge | 0.23 | -0.24 | 0.82 | No | 0.28 |
| As | 0.67 | -0.22 | 0.81 | No | 0.61 |
| Zr | 0.28 | -0.44 | 0.62 | No | 0.37 |
| Nb | 0.01 | -0.41 | 0.35 | No | -0.22 |
| Hf | 0.15 | -0.42 | 0.53 | No | 0.14 |

In the third screening round, we investigated the H adsorption energies on both Fe (100) and Fe (110) with each of the 13 elements that passed the second screening

round. Results are shown in Figure 8 and Table 5.1. We used Equation 5.6 to calculate the H adsorption energies E_{ad}^H on the two Fe surfaces with 1 alloying element X substituting a surface Fe atom as shown in Figs. 5.3 (a) and 5.3 (b). Based upon our results for As, we limited the number of models for each Fe surface to two: H at the hollow site and at the top site of an alloying element X adsorbed on Fe (100) (Figure 5.3 (a)), H at the hollow site I and at the top site of an alloying element X adsorbed on Fe (110) (Figure 5.3 (b)). In the instance that an element X caused H to move from the hollow site I to the hollow site II on Fe (110), the same as the case for As, we only relaxed the H and the surface atoms along the direction normal to the surface to calculate E_{ad}^H . This decision was made after we fully relaxed all atoms on Fe (110) and determined which X causes H to move from its initial position. Whether to apply this restriction is summarized in Table 5.1, which uses the column of “(110) hollow site I stability” to indicate whether the H atom stays in the hollow site I (“Yes” in that column) or moves to another site (“No” in that column) after full relaxation.

Figure 5.8 shows H adsorption energies at hollow sites (the solid horizontal lines in both Figure 5.8 (a) and 5.8 (b)) and top sites (the dashed horizontal lines in both Figure 5.8 (a) and 5.8 (b)) on both pure Fe (100) and (110) surfaces, indicating that H prefers the hollow sites rather than the top sites. The same trend can be found for Fe surfaces with one of the 13 alloying element “X” as shown by the curved lines with open (for H at top sites) /solid (for H at hollow sites) circles in both Figure 5.8 (a) and 5.8 (b). The numerical values of the corresponding E_{ad}^H for each case are listed in Table 5.1. Thus, the hydrogen adsorption energy at the hollow site was used as a numerical criterion to determine whether an alloying element can increase or reduce the hydrogen adsorption strength on Fe surfaces. For the Fe (100) surface, 6 of the 13 remaining alloying elements (As, Ge, Ga, P, Si, Al) resulted in a significant reduction of hydrogen adsorption strength on the hollow site, all of which have E_{ad}^H values more positive than E_{ad}^H for H at the hollow site on pure Fe (100) as shown in Figure 5.8

(a). The other 7 alloying elements (Be, B, Ti, Ni, Zr, Nb, and Hf) resulted in almost no changes or even slightly increased the hydrogen adsorption strength.

On Fe (110), the addition of an element “X” may cause H to move, as was observed for As. This had the net result of moving the H from hollow site I to hollow site II in Figure 5.3 (b). Interestingly, Be and Ni were the notable exceptions in the pool of the 13 alloying elements X investigated in the third screening round since H remained at hollow site I in the presence of either element as indicated by the “Yes” in the column of “(110) hollow site I stability” of Table 5.1. Comparison of the pure Fe (110) H adsorption energy of -0.71 eV at hollow site I with H adsorption energies at the same site on Fe (110) with one of the 13 “X” implies that each of these elements weakens H adsorption strength on an Fe surface. Moreover, this comparison leads to the following rank ordering of the 13 elements starting with As, which causes the greatest weakening of H adsorption strength, and ending with Be that weakens H adsorption strength the least: As > Zr > Ge \approx P > Hf > Ga > Si > Nb > Al > B > Ti > Ni > Be.

Comparison of the H adsorption energies between the (100) hollow site and (110) hollow site identifies six elements that significantly weaken or destabilize H adsorption on both Fe (100) and Fe (110) are: Al, Si, P, Ga, Ge, As. The inference here is that they will reduce HER rates on both Fe surfaces by slowing the Volmer reaction in Equation 5.3c. Transition metal elements (Ti, Ni, Zr, Nb, and Hf) and B can have opposite effects on hydrogen adsorption strengths on Fe (100) and Fe (110) surfaces, and hence changes to the HER rate are likely to be quite small. Specifically, changes in hydrogen adsorption energies on Fe (100) with these transition metal elements are relatively minor, which are confirmed by further studies of Fe (100) with higher surface concentrations of substitutional alloying atoms in Sec. 4. Hence, these surfaces can still behave as active cathode sites with a fast HER rate, resulting in their elimination from the candidate list of potential corrosion inhibitors. Beryllium has the most favorable H adsorption energies at both the Fe (110) hollow site I (-0.65 eV/atom)

and the Fe (100) hollow site (-0.40 eV/atom) relative to corresponding H adsorption energies on the pure Fe surfaces (-0.71 eV atom for the Fe (110) hollow site I and -0.38 eV/atom at the Fe (100) hollow site), resulting in its elimination from the list.

Since all of the H adsorption energies on hollow sites of the alloyed Fe (100) (Figure 5.3 (a)) are obtained based on VASP relaxations with no ancillary restrictions, we expect that these adsorption energies can be used to rank the order the final six elements (Al, Si, P, Ga, Ge, As) based upon reduction and/or destabilization of H adsorption to the Fe surfaces. According to the results in Table 5.1, these H adsorption energies suggest the following rank ordering by reduction of H adsorption strengths, and consequently, HER rates as: As > Ge > Si > Ga > P \approx Al. These p-block elements, which are highlighted in green in Figure 5.4, are the final group of corrosion-inhibiting elements that resulted from the application of the three criteria discussed above in our high-throughput computations. Note that the high-throughput computations call out As and Ge as potentially the best corrosion inhibiting elements using the idealized models in Figure 5.2 and 5.3.

This result is in qualitative accord with experiments [104, 102]. A recent experimental study shows that microalloying additions of Ge, Sb, Pb, Sn, and Bi (group 14 and 15 elements) can reduce the cathodic kinetics upon Mg, and Mg-Ge alloys were demonstrated to have the highest corrosion resistance among them [121]. Another experimental study on corrosion behavior of biodegradable Mg-X (X = Sn, Ga, In) alloys shows a low amount (< 1 wt%) of Ga is the most effective among these three elements to improve the corrosion resistance of Mg alloys [135]. We didn't consider the effects of In, Sn, Sb, Pb or Bi in our studies because our VASP calculations suggest that these four elements prefer to stay in Mg matrix instead of Fe particles (Figure 5.4 and 5.5). In reality, even Sn, Sb, Pb and Bi may prefer to stay on the surfaces of Fe-rich particles relative to the Mg matrix due to surface segregation, and hence it possible that they reduce the cathodic kinetics to some extent.

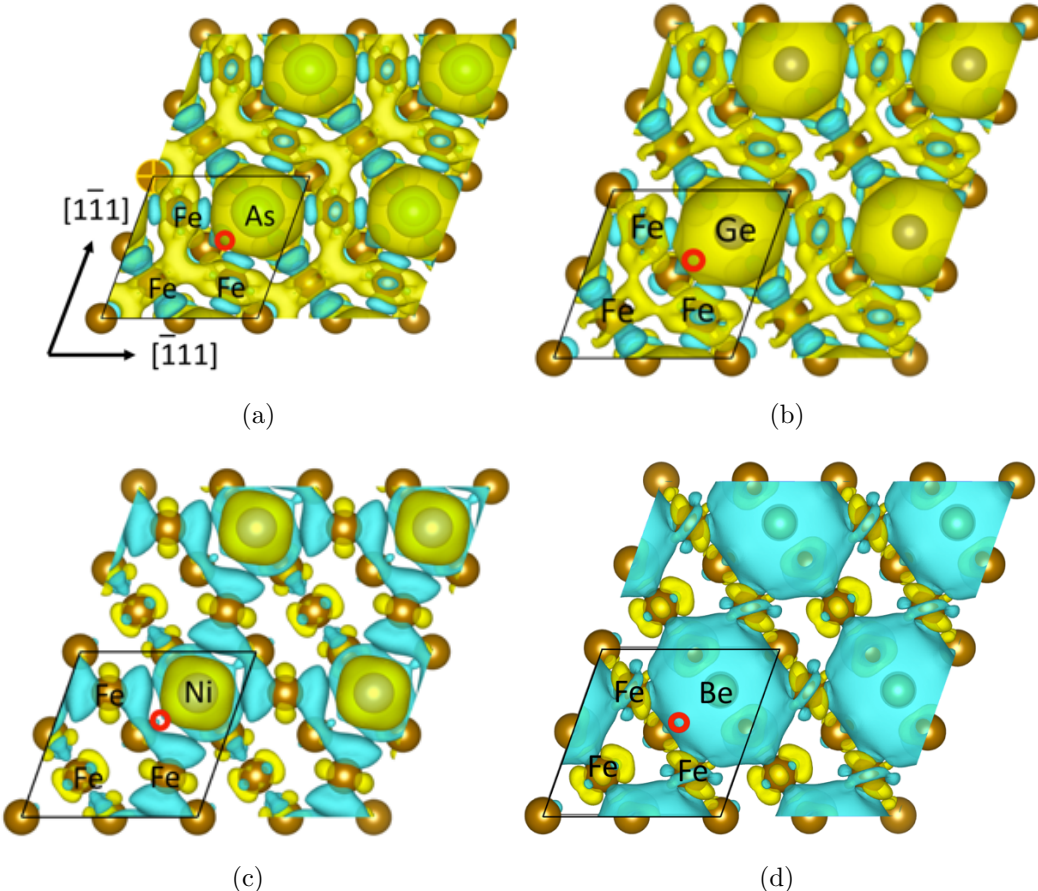


Figure 5.9: Top-down views of isosurfaces of electron density difference ($\Delta\rho$ defined in Equation 5.8) for (2×2) Fe (110) with one substitutional alloying atom in top surface layer. Surface Fe and alloy element “X” (X as As, Ge, Ni and Be in (a), (b), (c) and (d), respectively) are denoted. The open red circle is located at a hollow site I (Figure 5.3 (b)) for hydrogen adsorption. The black box indicates the periodicity of a (2×2) Fe (110). The yellowish isosurface is $1.5 \times 10^{-3} \frac{e}{bohr^3}$ corresponding to positive $\Delta\rho$ or electron accumulation after the substitutional alloying. The blue isosurface is $-1.5 \times 10^{-3} \frac{e}{bohr^3}$ corresponding to negative $\Delta\rho$ or electron depletion after the substitutional alloying.

5.4 Electronic Mechanism of Mg Corrosion Inhibition

In general, chemisorption on a transition metal surface is determined by two factors: a potential attractive energy term ($E_{attractive}$) related to the d-band center location relative to the Fermi level (i.e. so-called d-band center model), and a repulsive

energy term ($E_{repulsive}$) related to the orbital overlap between the adsorbate orbital and the orbitals of other surface atoms (so-called Pauli repulsion) [136, 137]:

$$E_{chemadsorption} \sim E_{attractive} + E_{repulsive} \quad (5.7)$$

We found that the effect of each of the 6 p-block elements identified as Mg corrosion inhibitors in Section 3c is negligible on the d-band center of Fe surface atoms. This was confirmed by computing and examining electronic density-of-states (Section S1 of the Supplementary Materials). Specifically, when one Fe atom in the top surface layer of (2×2) Fe (100) or (110) was substituted by an alloying atom from one of 6 p-block elements, the change of d-band center for all atoms in the top surface layer was always less than 0.2 eV. According to previous DFT studies of a series of transition metals, a change of ~ 1 eV in the d-band center of their surface atoms results in a change of ~ 0.5 eV in H adsorption energy [128]. Thus, it is not expected that such small changes in the d-band center for an Fe surface with p-block substitutional elements reported here can induce significant variations of hydrogen adsorption strengths.

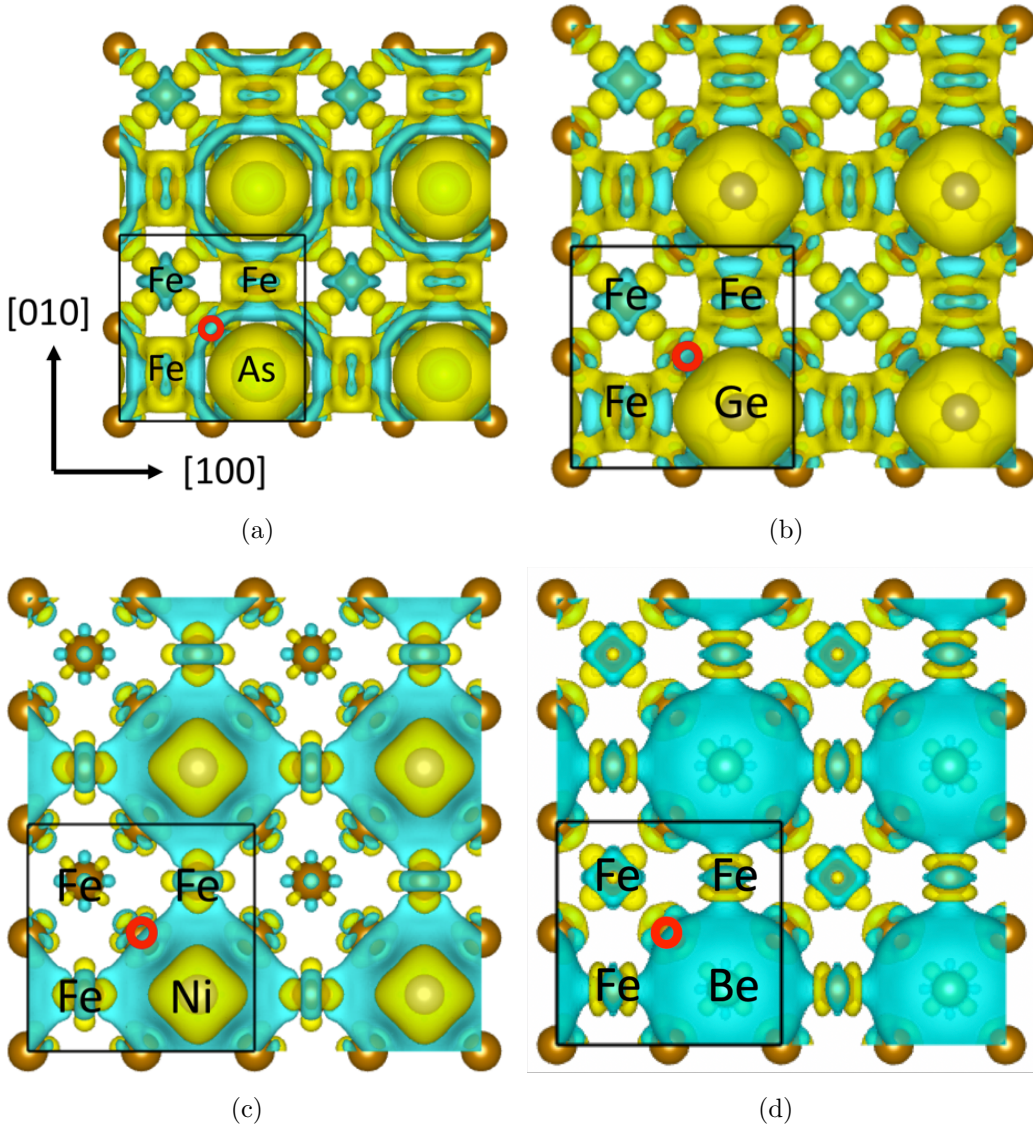


Figure 5.10: Top-down views of isosurfaces of electron density difference ($\Delta\rho$ defined in Equation 5.8) for (2×2) Fe (100) with one substitutional alloying atom in top surface layer. Surface Fe and alloy element X (X as As, Ge, Ni and Be in (a), (b), (c) and (d), respectively) are denoted. The open red circle is located at a hollow site I (Figure 5.3 (b)) for hydrogen adsorption. The black box indicates the periodicity of a (2×2) Fe (100). The yellowish isosurface is $1.0 \times 10^{-3} \frac{e}{bohr^3}$ corresponding to positive $\Delta\rho$ or electron accumulation after the substitutional alloying. The blue isosurface is $-1.0 \times 10^{-3} \frac{e}{bohr^3}$ corresponding to negative $\Delta\rho$ or electron depletion after the substitutional alloying.

We next examined surface charge redistribution by computing and displaying the difference, $\Delta\rho$, between the electron density of a pure (2×2) Fe (100)/(110) surface,

ρ_{Fe} , and the electron density of the same surface unit cell with a substitutional X atom in the top surface layer, ρ_{Fe+X} , via

$$\Delta\rho = \rho_{Fe+X} - \rho_{Fe} \quad (5.8)$$

Results are shown in Figure 5.9 and 5.10 for Fe (110) and Fe (100), respectively. Yellowish contours denote positive $\Delta\rho$ or regions of electron accumulation in the surface layer, while blue contours denote negative $\Delta\rho$ or electron depletion in the surface layer. Referring to Figure 5.9 (a), the yellowish contours surrounding the adsorbed As denote electron concentration in a shape resembling an s orbital with p-character. Figure 5.9 (a) also shows a network of electron accumulation that encircles the As atom and flows through Fe surface atoms. This is somewhat counter-intuitive since As has five valence electrons, which is less than the eight in Fe. This electron accumulation around the As atom suggests the enhancement of both the spatial extent and electron density of the s/p orbital for the As atom compared with the pure Fe surface. When a H atom is absorbed at the hollow site near the As atom, indicated by the red circle in Figure 5.9 (a), the electrons from the adsorbed H atom and those from the substitutional As atom should overlap, and quantum mechanics requires that they must be orthogonal to each other. This drives up the energy and leads to so-called Pauli repulsion as described by $E_{repulsive}$ in Equation 5.7. Therefore, the s/p orbital for an As atom adsorbed on Fe (110) results in larger Pauli repulsion of the nearby H atom, making the H adsorption energy weaker relative to adsorption on a pure Fe surface.

Similar effects were also predicted for adsorbed Ge on Fe (110), as shown in Figure 5.9 (b), as well as Al, Si, Ga, and P ($\Delta\rho$ contours not shown). Alternatively, the electron distribution is depleted around the adsorbed Ni atom in Figure 5.9 (c) (relative to As in Figure 5.9 (a)) and even more so around the adsorbed Be atom

in Figure 5.9 (d). This is consistent with the observation from our high-throughput computations that neither Ni nor Be repels an H adsorbate on Fe surfaces, and the H adsorption energy in both cases is close to that of pure Fe (110). Observations for alloying elements on Fe (110) also apply to Fe (100) as shown in Figure 5.10 (a) for As and Figure 5.10 (b) for Ge (as well as Al, whose $\Delta\rho$ contours not shown). All of these elements have electron accumulation that resembles that for As on Fe (110) in Figure 5.9 (a), and their corresponding H adsorption energies notably change from -0.4 eV/atom to \sim -0.2 eV/atom. Alternatively, Figure 5.10 (c) shows that Ni has only a small local electron accumulation in Fe (100) while electron density is severely depleted around Be in Figure 5.10 (d). This is consistent with the conclusion from our high-throughput computations that H adsorption in the presence of Be and Ni on Fe (100) is not weakened.

5.5 Sensitivity Analysis for H Adsorption Energy on Surface Alloying Coverage

All of the above evaluations are based on the three criteria in Section 2.1 with relatively simple but well-defined Fe surface structures with alloying elements. However, the quantitative predictions of alloying effects to Mg corrosion resistance require the accurate descriptions of surface and bulk structures of Fe-rich particles. As shown in Figure 5.1 (b), the overall alloying effect to reduce the HER rate depends on the hydrogen adsorption energies, which can change when the substitutional alloying concentrations vary. However, the highly negative segregation energies $E_{surf\ seg}$ for these six candidates calculated using one substitutional alloying atom in a (2×2) surface unit cell shown in Figure 5.6 and 5.7 suggest that there are substantial thermodynamic tendencies to have higher alloying element coverage on Fe surfaces. In addition, the reductions of hydrogen adsorption energies on Fe (100) surfaces due to $\frac{1}{4}$ ML alloy surface coverage for the six alloying candidates are not very large (0.2 ~ 0.4 eV per H atom), so the values of E_{ad}^H on these alloyed surfaces are still close to the region corresponding to the maximum exchange current density of HER indicated by Figure 5.1 (b). These E_{ad}^H values cannot strongly support the argument that such alloying elements can significantly reduce HER rates on Fe surfaces and inhibit the corrosion reactions on Mg alloys. For these reasons, we investigated the effects of higher substitutional alloying concentrations in the top layer of the two Fe surfaces.

The concentration effects of alloying elements can be addressed in three steps. First, the stability of alloying elements when their surface coverage is increased needs to be investigated based on DFT calculations. Second, the H adsorption energies on surfaces with different surface concentrations of alloy elements will be calculated. Third, the exchange current for hydrogen evolution reactions on surfaces with different concentrations of alloy elements can be estimated based on the H adsorption energies

(E_{ad}^H) in Figure 5.1 (b) and the kinetics model of HER [128, 138].

We first investigated whether it is possible to add a second substitutional alloying element in the top surface layer that already has one substitutional alloying element for a (2×2) Fe surface slab. Thus, we calculated the surface segregation energy $E_{surf\ seg}$ defined in Equation 5.5 for the second substitutional alloying element in the top layer of (2×2) Fe (100) and (110) surface slabs, where $E_{surf\ seg}$ for the first alloying element already has strong negative values as shown in Figure 5.6 and 5.7. In Equation 5.5, E_{bulk} is the energy of (2×2) surface slabs with one substitutional alloying element in the top surface layer and the other in the bulk far from the surface; E_{surf} is the energy of a (2×2) surface slab with two substitutional alloying elements in the top surface layer. As shown in Figure 5.11 (a) and 5.11 (b), there are two possible configurations of two substitutional alloying elements in a (2×2) Fe (100) surface slab. As shown in Figure 5.11 (c), the alloying configuration in Figure 5.11 (b) (“config 2”) always generates more negative $E_{surf\ seg}$ for the second substitutional element compared with their counterparts in Figure 5.11 (a) (“config 1”). Thus, it is energetically favorable for these elements to have the configuration shown in Figure 5.11 (b).

On these (2×2) Fe (100) surfaces, with two substitutional alloying elements in the top layer, there is at least one alloying element as the nearest neighbor for H atoms absorbed at all the hollow sites and bridge sites. Thus, the hydrogen adsorption energy should be very weak. The hydrogen adsorption energies on the hollow site in Figure 5.11 (b), the most favorable adsorption site on Fe (100), are indeed found to have very weak adsorption energy for the six p-block alloying element candidates. As shown in Figure 5.11 (d), E_{ad}^H of As, Ge, Ga, P, Si, and Al are positive values, with weaker hydrogen adsorption than that on the noble metal (Au, Ag) surfaces considered in Figure 5.1 (b). Such significant reductions of hydrogen adsorption energies suggest that the Volmer reaction in Equation 5.3c is indeed slow enough to

impede the HER rate on cathode sites. Alternatively, the (2×2) Fe (100) surface with 2 substitutional Zr atoms still has H adsorption energies comparable to those on pure Fe surfaces, suggesting higher surface concentrations of Zr (possibly for other similar transition metal elements like Hf) cannot result in noticeable changes in HER rates. Similar results apply to alloying Fe (110) surfaces.

The above DFT calculations suggest that one-half of a ML of alloying element X (As, Ge, Ga, etc.) can effectively inhibit the HER on Fe surfaces. Usually, the concentration of Fe impurities in Mg alloys is of the order of 100 ppm. Here, we assume all Fe impurities exist as second-phase particles in a nano-cube shape and each cube has 6 100 facets each with a length L of 10 or 100 nm. A simple analysis shows that \sim 10 ppm or \sim 1 ppm of alloying element X is enough to cover one-half of all Fe second-phase particle surfaces. Our calculations suggest that these alloying elements have a strong preference to segregate to Fe surfaces compared with the Mg or the Fe bulk lattice according to our DFT results, we conclude that \sim 10 ppm level of these alloying elements will be sufficient to show a noticeable effect on Mg corrosion resistance if there are no other phases/locations that can strongly attract these alloying elements. In reality, other stable occupation sites for these alloying elements could be on different precipitate phases and grain boundaries, so a higher concentration of alloying element X may be required to significantly enhance the corrosion resistance of Mg alloys.

5.6 Model Generalization on Other Precipitates

Finally, it is well known that Mg may contain other phases that can function as cathodic sites in Mg corrosion. Examples are the β -phase, $Mg_{17}Al_{12}$ [139], Cu [140] and Ni [106]. In fact, Song and Artens [116] claim that of the three types of second-phase particles that are rich in Ni, Fe, and Cu, respectively, Ni is the most detrimental with Fe intermediate to Ni and Cu. Thus, the high-throughput

computational strategy was applied to Cu and Ni particle cases by again following the three criteria in Section 2.1 to investigate whether the 6 p-block elements can inhibit HER on surfaces of these second-phase particles.

For the first criterion, we calculated the alloy segregation energy in the bulk of Cu and Ni particles when the alloying element X comes from the Mg matrix or bulk Fe particles via following Equation 5.4. For Cu, only Al and Si have a strong energetic preference (more negative than -0.5 eV) to stay in bulk Cu particles compared to bulk Mg as shown by closed black circles in Figure 5.12 (a). The segregation energies for P, Ga or Ge are between ± 0.1 eV, and As even has strong segregation (over +0.5eV) in Mg bulk matrix relative to bulk Cu particles. Therefore, As, Ge, Ga or P does not have a strong preference to be stable in Cu bulk. Besides, all the six p-block elements show thermodynamic preferences for bulk Fe particles over bulk Cu particles as shown by the open triangles in Figure 5.12 (a). Alternatively, Figure 5.12 (b) suggests that each of the six elements have a thermodynamic preference to stay in bulk Ni particles compared to the bulk Mg matrix, and all of these elements do not show a strong thermodynamic preference for bulk Fe particles over bulk Ni particles. Therefore, the ability of the six p-block alloying elements to inhibit HER on Cu particles is limited and out of the scope of further discussions, and we will only focus on Ni.

For the second criterion, the surface segregation energies of the six elements were calculated via Equation 5.5, which shows that all the six elements are also more stable on the clean Ni(111) surface compared to Ni bulk according to Figure 5.12 (c). For the calculations of H adsorption energies E_{ad}^H , defined in Equation 5.6, H adsorption energies at the FCC hollow site on Ni(111) surfaces were investigated by only allowing H and surface atoms to relax in the direction normal to the Ni(111) surface, following what was done for Fe (110) as described in Section 3c. Similar to their effects on the surfaces of Fe second-phase particle, all six p-block elements weaken H adsorption energies on Ni (111) surfaces as shown in Figure 5.12 (d). On (2 \times 2) pure Ni (111)

surfaces, the H adsorption energy is -0.56 eV for $\frac{1}{4}$ ML H coverage. Among the six elements, As, P and Ge alloyed surfaces show very weak H adsorption energies (to +0.42, +0.21 and +0.17 eV, respectively, comparable to E_{ad}^H on the noble metal (Au, Ag) surfaces in Figure 5.1 (b)). Germanium, Si, and Al can moderately weaken H adsorption energies (to -0.04, -0.10 and -0.29 eV). Hence, the six p-block elements that are effective on the two Fe surfaces are also effective on Ni(111).

5.7 Conclusions

In this chapter, we focus on the Mg alloy corrosion due to impurities from casting processing and create a build-in corrosion-resistant mechanism by high-throughput first-principles calculations. A strategy for increasing the corrosion resistance of Mg with Fe impurities that has gained significant traction in the experimental literature involves finding alloying elements that slow down or even inhibit the HER as the cathodic corrosion reaction on surfaces of Fe second-phase particles. The present study used a high-throughput DFT calculation strategy to search for such alloying elements based on three criteria. First, an element must show a thermodynamic preference for bulk BCC Fe over bulk HCP Mg; second, an element must be thermodynamically more stable on Fe (100) and Fe (110) than bulk Fe; third, the H adsorption energies on both Fe (100) and Fe (110) with an alloying element in their topmost layers should be significantly reduced or enhanced relative to the adsorption energies of a lone H atom on pure Fe (100) and (110), suggesting likely interference with the HER rate. The major conclusions of this study are as follows:

(1) Calculations show that As as an alloying element can satisfy the above three criteria. Depending on the As surface concentration, the hydrogen adsorption energies can be significantly reduced ($> \sim 10 k_B T$ at the room temperature $T \sim 300$ K), which can slow down the generation of adsorbed H atoms through water molecule dissociation (the Volmer reaction, Equation 5.3a) in the HER reaction mechanisms.

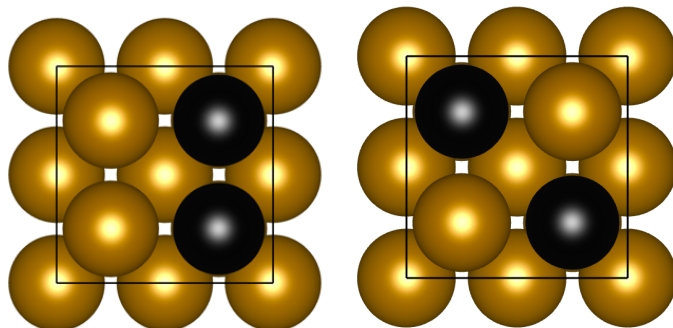
This is different than previous arguments where As can slow down the hydrogen recombination on Fe surfaces. The extent to which H adsorption energies are reduced depends on As concentration in the top surface layer of Fe. If one-half of the Fe atoms are substituted by As atoms in the top layer, which is thermodynamically favorable compared with As atoms in Fe bulk, then the H adsorption strength on such surface is predicted to reduce by ~ 1 eV per H atom, even weaker than H adsorption strength on Au surfaces, which is extremely inactive for HER.

(2) Of the 68 potential elements considered as possible corrosion inhibitors, the following six elements, rank-ordered by their ability to reduce (or destabilize) H adsorption on Fe surfaces, meet all three criteria: As > Ge > Si > Ga > P \approx Al. Each of the six identified elements likely inhibits the Volmer reaction (Equation 5.3a) necessary for the HER on Fe impurities that function as cathode surfaces. Identification of As and Ge as the best of all 68 elements examined is in qualitative accord with experiments. These p-block elements are also found to have the potential to reduce HER on Ni second-phase particles according to the same criteria. However, the ability of these p-block alloying elements to inhibit HER on Cu second-phase particles is limited because these elements do not show strong preferences to be stable in Cu particles relative to those in Mg matrix.

(3) Electron density difference contours show that excess electrons accumulate in the outer-shells (e.g. s and p orbitals) of each atom of the six elements replacing a Fe atom in both Fe (100) and Fe (110). This causes an enhancement to Pauli repulsion between an adsorbed H atom at an adjacent surface site and a substitutional alloying atom when orbitals of the latter overlap with the s-orbital of an H adsorbate. A significant reduction of H adsorption energy results (or destabilization of H binding) by increasing the repulsion.

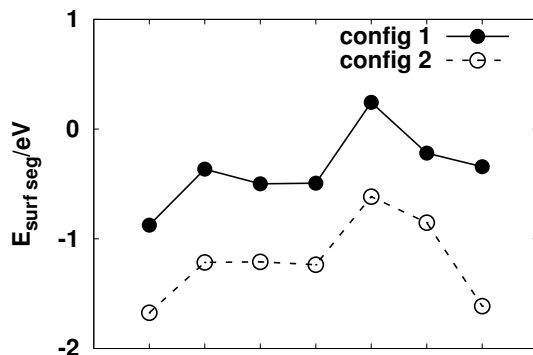
(4) Mg alloys may also contain other phases that can function as cathodic sites in Mg corrosion. Therefore, we extend our model to search the possible alloying

elements to impede HER on surfaces of other possible transition-metal impurities and precipitates in Mg alloys. These p-block elements are also found to have the potential to reduce HER on surfaces of Ni second-phase particles in Mg according to the same criteria, but not on surfaces of Cu second-phase particles.

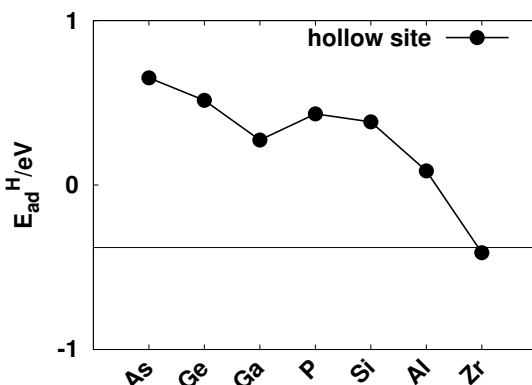


(a)

(b)



(c)



(d)

Figure 5.11: Effects of 6 p-block elements on higher surface alloying coverage. (a) and (b): two different configurations ((a) as “config 1” and (b) as “config 2”)) for (2×2) Fe (100) with two atoms of a generic alloying element substituting two Fe atoms in the top surface layer. (c) Segregation energies $E_{surfseg}$ defined in Eq. (7) for the second substitutional alloying atom in (2×2) Fe (100) with two substitutional atoms in different final configurations ((a) and (b)). (d) H adsorption energies E_{ad}^H defined in Eq. (8) on (2×2) Fe (100) with two substitutional alloying atoms in the top surface layer as “config 2” shown in (b).

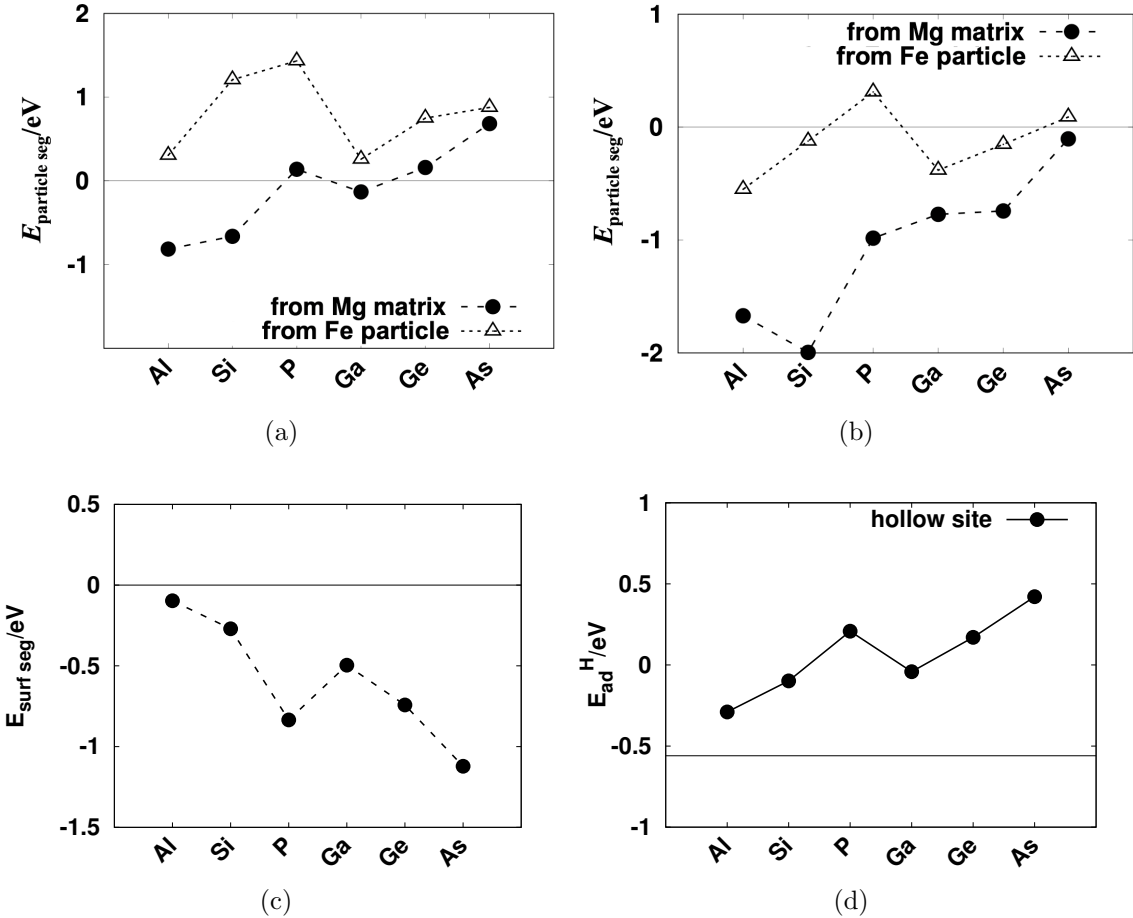


Figure 5.12: Effects of 6 p-block elements on other precipitates(Cu and Ni). (a) and (b): Bulk segregation energies $E_{\text{particleseg}}$ for 6 p-block alloying elements in bulk Cu (a) and Ni (b) second-phase particles in Mg matrix, respectively. The solid circles denote the segregation energies of alloying elements in bulk Cu/Ni particles over bulk Mg matrix, and the open triangles denote the segregation energies of alloying elements in bulk Cu/Ni particles over bulk Fe particles. The energy differences are defined in equations similar to Equation 5.4. Preference for a bulk Cu/Ni particle over the bulk Mg/Fe particles requires that an alloying element should have a significantly negative value of $E_{\text{particleseg}}$. (c) Surface segregation energies E_{surfseg} defined in Equation 5.5 for Ni (111) of 6 p-block alloying elements. A qualified alloy candidate should have a strongly negative value of $E_{\text{surf seg}}$. (d) H adsorption energies E_{ad}^{H} , which is defined in Equation 5.6, on (2×2) Ni (111) surfaces with $\frac{1}{4}$ ML alloying atom in the top surface layer. The horizontal line stands for the H adsorption energy of pure Ni (111) surface hollow site.

CHAPTER VI

Kinetic Monte Carlo Simulations of Solute Clustering in Multi-component Al Alloys

In this chapter, we focus on the methodology development on simulating the solute clustering kinetics in multicomponent Al alloys quantitatively. To slow down solute clustering at room temperatures (so-called natural aging) after the high-temperature solid-solution treatment is crucial to expand the time window for the mechanical forming of certain high-strength multicomponent Al alloys, such as 7000 series Al-Mg-Zn alloys. Since the clustering is achieved by solute diffusion based on vacancy migration, a neural network (NN) surrogate model based on the first-principles training data set is introduced to predict the vacancy migration barrier accurately. Then a kinetic Monte Carlo (kMC) simulation package based on NN model with advanced acceleration methods is introduced to simulate the solute clustering kinetics in multi-component Al alloys. The information on cluster compositions and structures lays the foundation for the studies of the clustering effects on the strengths and formability of multicomponent Al alloys in the future.

6.1 Introduction

7000 series Al alloys developed for aerospace applications have high specific strength in the peak-aged condition. Carmakers are exploring options for using stamped 7000 series sheets in structural applications in cars and trucks, from both the manufacturing perspective and the performance perspective. Their widespread implementation in the automotive industry for body and closure applications can achieve lightweight vehicle goals if the challenges of the component forming and fabrication can be overcome[141, 142, 143].

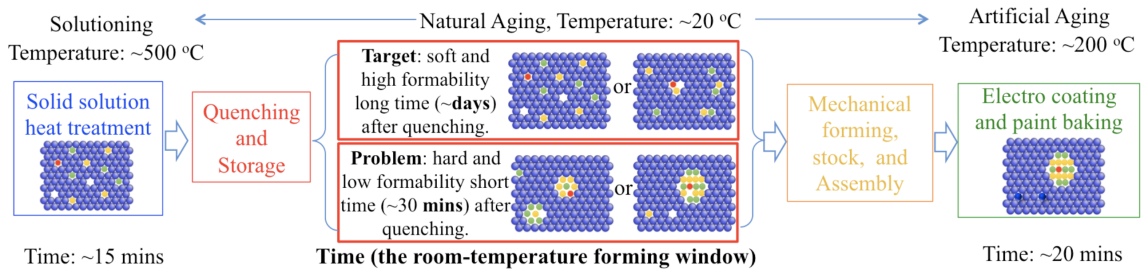


Figure 6.1: Schematics of the fabrication process of 7000 series Al sheet alloy parts in the automobile industry. The corresponding changes of illustrated structures of solute atoms (including clusters and precipitates) during this process are also plotted (blue: Al atoms, other colors: solutes).

As shown in Figure 6.1, conventional automotive mechanical forming processes, such as stamping and hemming, starts from solid solution heat treatment, then involve room temperature forming of Al sheet alloys in the as-quenched state when alloys have high ductility and formability, and finally followed by artificial aging during the paint bake operation. However, even during the natural aging at room temperatures, the transformation from solid solutions to solute clusters and early-stage precipitates can occur fast (often within 30 minutes after quenching) for current 7000 series Al alloys. As a result, the formability of these alloys decreases very rapidly and keeps changing as the aging time increases, necessitating costly steps such as warm stamping and coupled solutioning-quenching-stamping operations in a narrow time window[144,

145]. These variations of formability and other mechanical properties are all related to the evolution of atomistic structures of precipitates during the sheet processing procedures.

As a result, to understand and to control the nucleation and early stages of precipitation kinetics will have a great impact in automotive applications of age-hardened, light-weight alloys[146, 147, 148, 149]. The nucleation and growth of precipitates in Al-Zn-Mg-based alloys is currently understood to follow the following sequence: supersaturated solid solution (SSSS) → vacancy-rich clusters (VRC) → Guinier-Preston (GP) zones (nanoscale coherent Mg/Zn-rich clusters) → η' (semi-coherent Mg-Zn-Al precipitates with high Zn/Mg ratio) → η (incoherent MgZn₂)[150, 149, 151, 152]. During natural aging, the majority of precipitates are VRC and GP zones, even though η' can also be found in some cases[153]. Therefore, in this chapter, how to retard the nucleation and growth of VRC and GP zones in 7000 series Al alloys during natural aging without adversely affecting the precipitation kinetics during subsequent artificial aging will be focused on.

Beyond classical theory on the nucleation and early stages of growth of precipitates, atomistic simulations, especially kinetic Monte Carlo (kMC) simulations, have been applied to investigate the precipitation kinetics in Al alloys[154, 155, 156, 148, 157, 158, 159, 160, 161]. There simulations were usually conducted to simulate solute atom diffusion based on the vacancy migration in a coherent lattice of the matrix element. Such coherent lattice assumption is still acceptable in our studies of solute clusters and early-stage precipitates. In these kMC simulations, the key input is a potential function to describe the activation barrier/energy for the solute/vacancy migration at a particular local lattice occupation environment. For example, the vacancy migration barrier in the pure Al matrix should be different than its counterpart if there is a solute atom occupying the 1st-nearest-neighbor lattice site of the vacancy. Another specific example is shown in Figure 6.2, where the migration barriers for the

vacancy jumping to the site #1, #2, #3, and #4 should be different from each other because these migrations generate distinct change of lattice occupations in the 1st nearest neighbors of the vacancy.

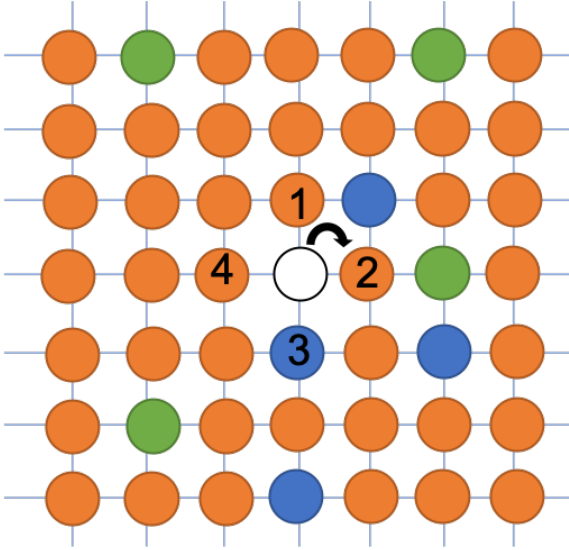


Figure 6.2: Illustration of a vacancy migration in a 2D lattice of a multicomponent system. The orange solid circles represent matrix atoms. Blue and green solid circles represent two different types of solute atoms. The white open circle represents a vacancy. The migration barriers for vacancy jumping to site #1, #2, #3, and #4 are different based on their 1st nearest neighbors local environment.

As we previously mentioned in Section 2.3, due to the simplicity of analytical formulas and costly DFT calculations, empirical potentials of the vacancy migration barrier usually focus on a limited number of energetic, structural and compositional features in the fitted material systems. As the number of chemical species included in the system increases, it is also getting more difficult to fit the desired empirical potential. For simple vacancy diffusion in bulk lattice or surface diffusion events, Bell–Evans–Polanyi (BEP) relationship [162, 163, 164] was commonly used for calculating the migration barriers of atoms and molecules:

$$E_a = a\Delta E + b \quad (6.1)$$

where a , b are weighting parameters from fitting, E_a and ΔE are the migration barrier and the corresponding total energy change due to this migration event, respectively. To further simply the calculations for diffusion in a bulk lattice, researchers used the bond counting model up to a certain cutoff to estimate the total energy change ΔE [156, 155]. More advanced methods to calculate ΔE in the coherent lattice include the cluster expansion (CE) formalism that can consider both pair and triple interactions between neighbors [161, 165, 166, 167, 168]. However, most of the CE methods only work efficiently for binary or ternary systems due to high computational costs[169]. Even though with some recent development[170], CE can predict energy accurately for quinary alloy systems, this method still oversimplified the contribution of atomistic local environments and elastic contributions. Besides, to achieve the same order of accuracy as the number of chemical species increases, the number of parameters needed to fit also increases dramatically[171], hence making the computation unaffordable for a long time kMC simulations.

Even with correction descriptions of ΔE , we found that the BEP relation as Equation 6.1 is not valid for the multicomponent alloy systems. As shown in Figure 6.3, the correlation between migration barriers (E_a) and energy differences (ΔE) for many vacancy migration events in Al-Mg-Zn systems is far from the linear relation. Here E_a and ΔE were calculated based on DFT calculations with climbing image nudged elastic band (CI-NEB)[172, 173] in ~ 1000 cases of vacancy migration in the $4 \times 4 \times 4$ supercells of Al fcc lattice with random occupations of Mg/Zn solute atoms. This deviation makes the prediction of accurate vacancy migration barriers very difficult. An inaccurate migration barrier could be fatal in kMC models, which is known as the "small-barrier" issue[174].

Thus, we use a machine learning method to predict accurate vacancy migration barriers for multi-component alloy systems in a coherent fcc lattice. Recently statistical machine learning and artificial intelligence techniques start to be used in many

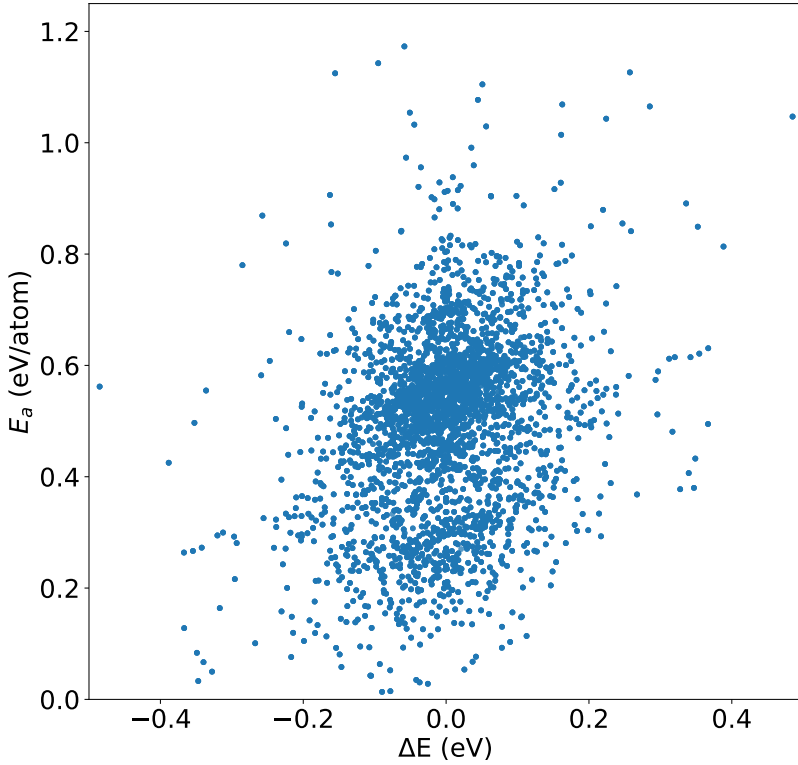


Figure 6.3: Correlation between migration barriers (E_a) and energy differences (ΔE) for many vacancy migration events in Al-Mg-Zn systems obtained from our DFT + CI-NEB calculations.

research fields, including materials science and engineering. A typical applications is to use machine learning to construct the numerical functions for the interatomic force fields [175, 176, 177, 20, 178, 179]. Compared with conventional interatomic potentials with fixed mathematical forms, the high flexibility of these machine-learning methods increase the possibility to fit complex potential energy landscapes with enough accuracy at the level needed. In this work, we develop a neural network (NN) model to predict vacancy migration barriers using the training data set of thousands of DFT calculated barriers for different alloy configurations.

Then, A kMC method based on this NN model is developed to study the early transition behavior from a supersaturated solid solution to solute clusters and Guinier-

Preston (GP) zones in Al-Mg-Zn alloys. A local super-basin method 6.3.2, together with LRU cache 6.3.3, is also implemented to accelerate kMC simulations. We also propose a pseudo-atoms approach to efficiently search the alloying strategy to slow down the solute clustering and the corresponding natural aging effects in Al 7000 series alloys. We also develop the quantitative analysis methods to describe the chemical and structural properties of clusters. At last, we propose a machine learning strategy based on the structural and chemical information of clusters and precipitates from kMC simulations to predict the cluster strengthening and natural aging effects in future studies.

6.2 Fitting Vacancy Migration Barriers using Neural Network work

The calculations that provided the energetics used to evaluate energy differences and activation barriers before and after vacancy jump in Al-Mg-Zn alloys were implemented by DFT together with climbing image nudged elastic band (CI-NEB) in the VASP software with VTST package from Henkelman's group[172, 173]. The nudged elastic band (NEB) is a general method for finding saddle points and minimum energy paths between the atomic configurations of the known initial and final states. This method works by optimizing a certain number of intermediate images along the reaction path. Each image finds the lowest possible energy while maintaining linear spline spacing to neighboring images. This is done by adding artificial spring forces along with the band between images and by projecting out the force component parallel to the band due to the interatomic potential. The CI-NEB method modifies the NEB method in a way that the highest-energy image is pushed up to the saddle point by trying to maximize its energy along with the band and minimize in all other directions. When the algorithm converges, the highest-energy image is at the

exact saddle point, so a smaller number of intermediate images is needed in CI-NEB than NEB. With this setup, we can use high-throughput calculations to extract forward/backward activation barriers by calculating the energy differences between the image of the highest energy and the initial/final image.

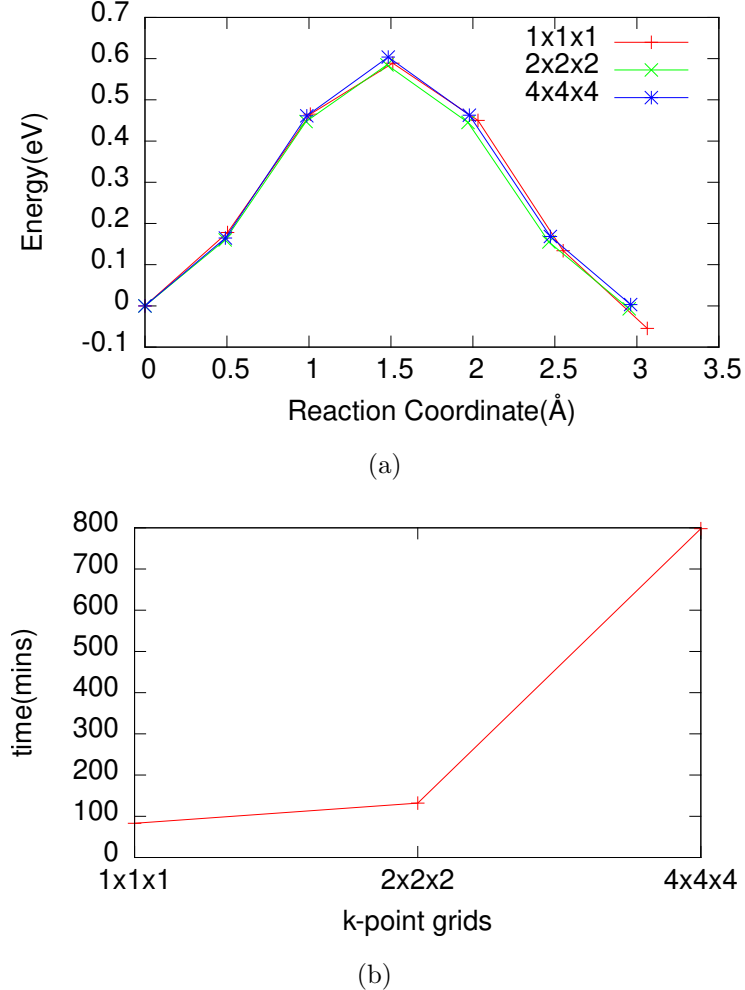


Figure 6.4: Plot of k-point grids convergence and efficiency test on vacancy migration barrier. (a) Vacancy migration barriers along reaction coordinates of $(1\times 1\times 1)$, $(2\times 2\times 2)$, and $(4\times 4\times 4)$ k-point grid setups are tested. (b) The total time elapsed using $(1\times 1\times 1)$, $(2\times 2\times 2)$, and $(4\times 4\times 4)$ k-point grid setups are plotted. A 256-atom randomly generated Al-Mg-Zn configuration is used for this test.

Pseudopotentials based on the PAW method were employed for the elemental constituents with the GGA of PBE for the exchange-correlation energy functional,

μ_{xc} , with the interpolation formula of Vosko et al. [91]. Using plane-wave cutoff energy of 450.0 eV, the total energy for all models of initial and final images was converged to 10^{-7} eV/cell. The reciprocal space of bulk supercells was sampled with $(2 \times 2 \times 2)$ k-point grids. Each grid was generated using the Monkhorst-Pack scheme [72]. In Figure 6.4, we plotted the vacancy migration barrier of a 256-atom randomly generated Al-Mg-Zn configuration using different k-point grids. In subplot (a), $(2 \times 2 \times 2)$ and $(4 \times 4 \times 4)$ k-point grids do not have a significant difference on reaction coordinates and migration barrier. However, running on a 120-core machine, $(4 \times 4 \times 4)$ k-point takes 5 times longer simulation time. Considering the efficiency, we choose $(2 \times 2 \times 2)$ k-points with almost no accuracy compromise. A $(4 \times 4 \times 4)$ conventional fcc supercell with a single vacancy embedded was used for these calculations. For activation barrier calculations, 5 images between relaxed initial and final images were used. A spring constant was set to 5 eV/ \AA^2 . The force convergence criteria for all models was set to be less than 0.05 eV/ \AA . The force-based quick-min optimizer was used to make NEB calculations stable for high local concentration cases[180].

We calculated lattice constant for Al-Mg-Zn alloys based on the chemical composition of 7075 Al alloy. A $(4 \times 4 \times 4)$ conventional supercell with 256 atoms was used to generate random lattice occupations by solute atoms using special quasi-random structures (SQSs) method [181]. The types of 256 atoms were chosen to be 244 Al atoms, 7 Mg atoms, and 5 Zn atoms, which is within the concentration range of Al 7075 alloy. The obtained lattice constant is 4.05838 \AA , which is roughly equal to the lattice constant of pure Al (4.041 \AA from the same DFT setup parameters) considering that Zn and Mg atomic weights are not high[182].

Our NN model training set contains mainly from the calculated vacancy migration barriers in two different types of supercells, as shown in Figure 6.5: 1) $(4 \times 4 \times 4)$ randomly generated solid-solution structures with different local concentrations around the jump pair, which is defined by the two lattice sites for the vacancy before and

after the migration event. 2) $(2 \times 2 \times 2)$ ordered structures embedded in $(4 \times 4 \times 4)$ pure Al. The first training set is good for simulating vacancy migration of a very early stage, during which Al alloy is still in the solid-solution state. The second training set is designed to accurately describe the behavior of vacancy migrations across/along the boundary between solid-solution Al and ordered clusters/precipitates, and moving inside the ordered phases. The atomic structures of ordered phases are randomly chosen from the proposed GP zone structures from [151] and low energy ordered L₁₀, L₁₂, L₁₀^{*}, W2, CH, L₁₂^{*}, Z1 structures of Au-Fe from [183] with random perturbations in lattice occupations. The atomic structures were generated using our in-house code KNN2[184].

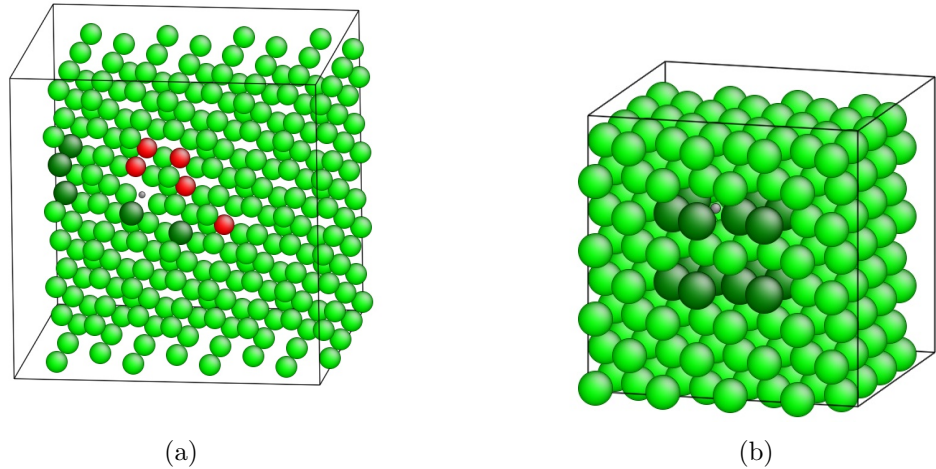


Figure 6.5: Atomistic pictures of $(4 \times 4 \times 4)$ supercells containing 256 atoms. (a) One typical $(4 \times 4 \times 4)$ randomly generated solid-solution structure. (b) One typical $(2 \times 2 \times 2)$ randomly chosen ordered structures embedded in $(4 \times 4 \times 4)$ pure Al. Light green, dark green, and red atoms are Al, Mg, and Zn, respectively. The small gray atom represents the location of vacancy.

Many different machine learning/deep learning models are widely used to study materials science problems[175, 176, 177, 20, 178, 179]. For our particular case, the feed-forward Artificial Neural Network (ANN) is chosen, as it provides a general frame to map non-linear input (atomic species of neighboring environment) to a continuous regressand (vacancy migration barrier). It is well known that a sufficiently large

number of hidden neurons can approximate any continuous multivariate function[185]. This property gives us the most expandability of this framework when the system needs to go even further complicated in terms of the number of species considered.

Table 6.1: Atom species encoding map for the neural network (NN) input layer. Here, “Vac” represents vacancies.

| Species | Encoding |
|---------|----------|
| Al | 1.0 |
| Mg | 2.0 |
| Zn | 3.0 |
| Vac | 4.0 |

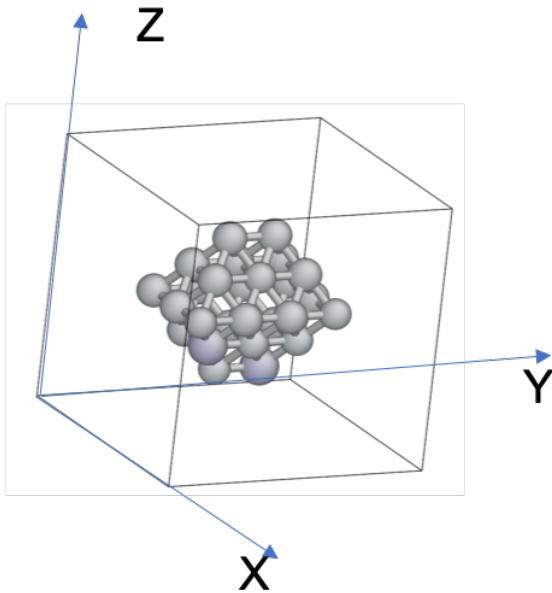


Figure 6.6: Illustration of atomic structures of the 1st and 2nd nearest neighbors surrounding the jumping pairs (the lattice sites of the vacancy before and after a migration event). The 26 neighboring atoms have 2-fold symmetry, mirror symmetry along Y-Z plane, and mirror symmetry along the X-Y plane.

The output layer of our NN model predicts vacancy migration barriers in a 1-D continuous space. Like the Ising model, the input layer was chosen to be 27 discrete numbers representing atom species that occupy all the 1st and 2nd-nearest-neighbor

lattice sites of the vacancy before and after the migration events (the jump pair), as shown in Table 6.1. Among the 27 numbers, the first one indicates the type of atom that will be swapped with the vacancy. The rest 26 numbers represent the neighboring atoms of the jump pair up to their 2nd nearest neighbors (each lattice site of the jump pair has 12 1st nearest neighbors and 6 2nd nearest neighbors. In addition, both of them share 10 neighbors in common. So $26 = (12 + 6) \times 2 - 10$). All these 26 atoms as shown in Figure 6.6, where the X, Y, and Z axes are defined as the following. In principle, X, Y, and Z directions can be any orthogonal vectors, as long as they are consistent during the training and serving stages of the simulation. Here, we choose Y as a $\langle 110 \rangle$ vector along the vacancy jumping direction; X is along another $\langle 1\bar{1}0 \rangle$ vector perpendicular to Y; Z is along the $\langle 001 \rangle$ vector perpendicular to both X and Y axes. Beside the first number for the swapped site for the vacancy jump, all the left 26 numbers are arranged in their geographical order, so their position will always respond to the same input neuron in the NN architecture. In addition, this cluster of 26 neighboring atoms also has 2-fold symmetry ($R_{2fold} = \begin{bmatrix} 1 & -1 & 0 \\ -1 & -1 & 0 \\ 0 & 0 & -1 \end{bmatrix}$), mirror symmetry along Y-Z plane ($R_{xmirror} = \begin{bmatrix} -1 & 1 & 0 \\ 1 & 1 & 0 \\ 0 & 0 & 1 \end{bmatrix}$), and mirror symmetry along the X-Y plane($R_{zmirror} = \begin{bmatrix} 1 & -1 & 0 \\ 1 & 1 & 0 \\ 0 & 0 & -1 \end{bmatrix}$). Therefore, for one jumping event, the vacancy migration barrier is taken as the average of the four symmetric configurations of the 26 neighboring atoms to have a rotation-invariant prediction. Details of this method is described in Algorithm 2. By using several layers of hidden neurons between 27 input and the final output, the contribution of pair-wise and triple-wise interactions

can be learned.

Algorithm 2 Jumping Pair Encoding Algorithm

1: set a reference matrix as a 3×3 identity matrix, $m_0 =$

$$\begin{bmatrix} 1 & -1 & 0 \\ 1 & 1 & 0 \\ 0 & 0 & 1 \end{bmatrix}$$

- 2: determine the jumping direction $v_0 = r_{atom} - r_{vac}$, where r is the coordinates of atom/vacancy. Noting that in the practice, atoms may need to be wrapped according to periodic boundary conditions.
 - 3: determine all the 26 neighboring atoms of the ghost atom at the vacancy site and the jumping atom within the 2^{nd} nearest neighbor distance cutoff.
 - 4: randomly pick one 2^{nd} nearest neighbor atom with coordinates r_1 of the vacancy atom, and calculate $v_1 = r_1 - r_{vac}$.
 - 5: calculate $v_2 = v_0 \cdot v_1$.
 - 6: concatenate matrix $m_1 = \begin{bmatrix} v_0 \\ v_1 \\ v_2 \end{bmatrix}$.
 - 7: calculate rotation matrix R for projecting m_1 to the reference coordinate m_0 .
 - 8: rotate coordinates of all the 26 atoms by applying the rotation matrix R to project all the atoms need to encode along the same reference directions. The new coordinates denotes as r' .
 - 9: encode atoms based on the preset mapping of type, and ascending order in X, Y, and Z coordinates accordingly.
 - 10: apply for the three rotational matrices, $R_{2fold} = \begin{bmatrix} 1 & -1 & 0 \\ -1 & -1 & 0 \\ 0 & 0 & -1 \end{bmatrix}$ $R_{xmirror} = \begin{bmatrix} -1 & 1 & 0 \\ 1 & 1 & 0 \\ 0 & 0 & 1 \end{bmatrix}$ $R_{zmirror} = \begin{bmatrix} 1 & -1 & 0 \\ 1 & 1 & 0 \\ 0 & 0 & -1 \end{bmatrix}$, to the coordinates r' and encode them use the same method mentioned above.
-

We implemented the NN model using Google's TensorFlow [186] with Keras [187]. TensorFlow is an open-source numerical computation framework using data flow

graphs with the ability to derive gradients automatically. Keras is a high-level neural networks API, written in Python and capable of running on top of TensorFlow. The optimized neural network structures were tuned by Talos [188]. The Adam optimizer [189] was used for optimizing weights in the neural network. Xavier uniform initializer [190] was used to generate the random weights and biases so as to break the symmetry of weighting parameters. The activation functions were chosen to be Rectified Linear Unit (ReLu) for all the hidden layers. The activation function for the output layer is chosen to be linear to predict vacancy migration barriers on a continuous scale. Normalization method has also been tested but is not helpful in improving accuracy, as vacancy migration barriers follow a very good normal distribution. The optimized NN architecture can be found in Table 6.2. Large neural nets trained on relatively small datasets can overfit the training data. So the dropout as a regularization method is applied to prevent overfitting. This introduces a new hyperparameter, the dropout probability, as listed in Table 6.2. Though more complicated restricted Boltzmann machine (RBM) and many other generative stochastic artificial neural networks can be used as a function approximator, their complexity slows down the kMC iterations significantly, so that they are not used here.

Table 6.2: Neural network architecture with activation functions and dropout probability of each layer.

| Layer | Shape | Activation | Dropout Probability |
|-------|-------|------------|---------------------|
| Dense | 256 | ReLU | 0.1 |
| Dense | 256 | ReLU | 0.2 |
| Dense | 128 | ReLU | 0.0 |
| Dense | 64 | ReLU | 0.05 |
| Dense | 64 | ReLU | 0.0 |
| Dense | 16 | ReLU | 0.0 |
| Dense | 1 | Linear | N.A. |

To train the NN, two different loss functions are used. The former one is the

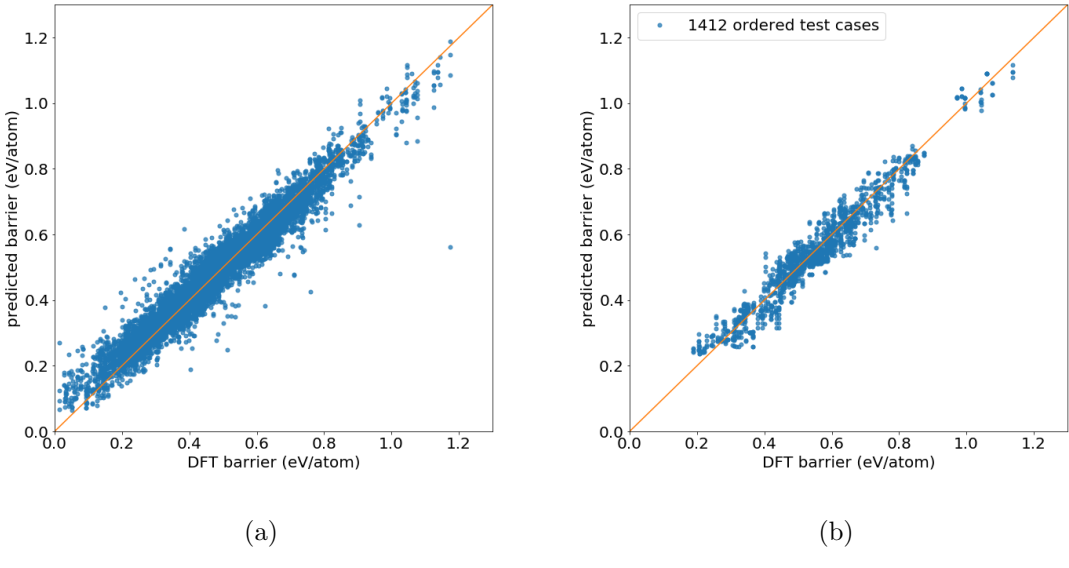


Figure 6.7: Predictions accuracy of vacancy migration barriers from neural network surrogate model, compared with DFT calculated results. During model training, Equation 6.2 was used as the loss function. The orange solid line indicates perfect fitting. Each blue solid dot represents one data point. (a) predictions of all the barriers from DFT training data set. (b) predictions of the barriers in certain ternary ordered structures as the testing data set.

common mean squared error (MSE) via:

$$MSE = \frac{1}{N} \sum_{i=1}^N (E_{ai}^{DFT} - E_{ai}^{NN})^2 \quad (6.2)$$

where N is the number of input data, which can be trained in batch or mini-batch, E_{ai}^{DFT} is the vacancy migration barrier of i^{th} data from DFT calculation, and E_{ai}^{NN} is from NN prediction. As shown in Figure 6.7, the model reached a root mean squared error (RMSE) of 0.04313 eV/atom for all the data points. The latter one is a customized loss function as:

$$Loss = \frac{1}{N} \sum_{i=1}^N (1.0 + \alpha(1.5 - E_{ai}^{DFT})(E_{ai}^{DFT} - E_{ai}^{NN})^2) \quad (6.3)$$

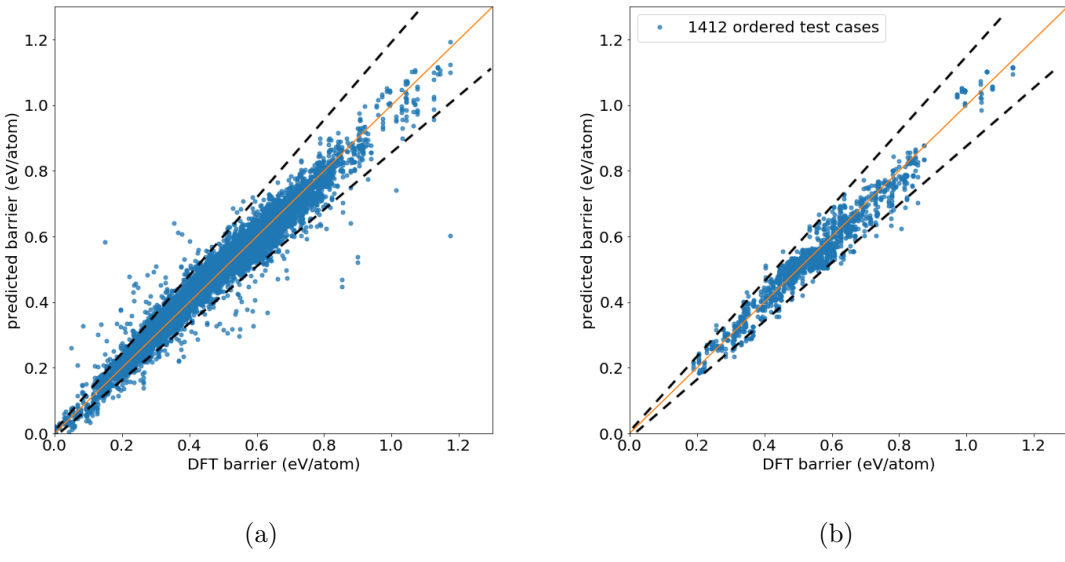


Figure 6.8: Predictions accuracy of vacancy migration barriers from neural network model using custom loss function, compared with DFT calculated results. During model training, Equation 6.3 was used to weigh more on low-energy barriers. The orange solid line indicates perfect fitting. Each blue solid dot represents one data point. The black dashed lines illustrate the confinement introduced by custom loss function with emphasis on low-energy-barrier data points. (a) predictions of all the barriers from DFT training data set. (b) predictions of the barriers in certain ternary ordered structures as the testing data set.

where α is a tunable knob. A larger α value will weigh more on vacancy migration barriers that are small. In this way, we are able to fit low-energy barriers more accurately, as they are the critical rate-determining steps in a kMC simulation. Using this custom loss function, the model reached a RMSE of 0.03785 eV/atom for all the data points. Noting that the model trained using the latter loss function is slightly more accurate than the former method because more data points are located far away from 1.5 eV. As we expected, low-energy barriers are predicted with higher accuracy, which can be seen from Figure 6.8.

6.3 Kinetic Monte Carlo Setup

The kMC code was written in C++17[184]. Our code has two dependent libraries. First, we used an open-source C++ module called “keras2cpp” to read the Keras model trained in python[191]. Second, we also applied another open-source numerical library, called Armadillo[192, 193], to do matrix multiplication for rotating current configurations to symmetry equivalent ones. As we mentioned above, all four symmetry equivalent structures needed to be calculated to evaluate vacancy migration barriers accurately, and both forward and backward vacancy migration barriers were required. Therefore, a total of 8 calculations were needed for one event. Therefore it becomes important to speed up calculations. We used message passing interface (MPI) to parallelize our kMC simulations. Two parts are benefited significantly from parallelism implementation: 1) building initial neighbor list of every atom; 2) kMC event rate calculations. Note that once the initial neighbor list is built, one can keep updating the neighbor list on the fly. Besides, vacancy migration barriers and event rates of 12 possible jumping events of one vacancy were distributed to different cores and collected afterward. We tested the scalability of the code, as shown in Figure 6.9. A $(30 \times 30 \times 30)$ supercell containing 108,000 atoms, was used for this testing. Calculations up to 80,000-steps were tested and benchmarked with the usage of different numbers of nodes. For very limited-steps cases, such as 10,000 steps, more cores showed more advantages, as the initial setup of the neighbor list takes a considerable amount of time. As the simulation goes on, the cost of communication between cores does not affect the scalability significantly.

6.3.1 kinetic Monte Carlo (kMC) Algorithm

Most parts of the kMC algorithm were implemented following the approach we discussed in Algorithm 1 of Chapter 2.4. In this implementation, several points are worth noticing: 1) Event list is determined on the fly. We consider the first

nearest neighbor exchange of vacancies. This yields a total of 12 times the total number of vacancies possible events. 2) Then, a NN potential is used, instead of traditional empirical potentials or analytical equations, to evaluate vacancy migration barriers. Noting that all the four symmetry equivalent structures are taken into consideration. 3) At each step, both the forward and backward vacancy migration barriers of executing the current jump are calculated to obtain the energy change of the current system, via:

$$\Delta E = E_a^{forward} - E_a^{backward} \quad (6.4)$$

where ΔE is the energy difference between initial and final state, $E_a^{forward}$ and $E_a^{backward}$, are the forward/backward vacancy migration barrier, respectively. And the overall energy change as time-evolving is cumulated. 4) In order to boost the system out of low-energy barrier trapping states, a local super-basin method is also implemented based on Fichthorn's method[194].

For the kMC simulations, ($30 \times 30 \times 30$) supercell containing 108,000 atoms were used. 3240 Mg atoms, 1700 Zn atoms and 1 vacancy atom were randomly chosen among 108,000 atoms. This setup corresponds to ~ 3 atom. % of Mg, ~ 2 atom. % of Zn and a vacancy concentration of $\sim 1 \times 10^{-5}$. The probability, p_i , of selecting an event i is calculated and the event k is chosen according to the typical kMC algorithm as the following:

$$p_i = r_i/R \quad (6.5a)$$

$$r_i = \mu_a * \exp(-E_a/k_B T) \quad (6.5b)$$

$$R = \sum_{j=1}^N r_j \quad (6.5c)$$

$$\sum_{k=1}^{i-1} p_k < rand < \sum_{k=1}^i p_k \quad (6.5d)$$

where μ_a is the pre-exponential factor, E_a is the vacancy migration barrier, k_B is the Boltzmann constant, T is the temperature, N is the total number of events, and $rand$ is a random number $\in [0, 1]$. In reality, the pre-exponential factor, AKA the attempt frequency, and the vacancy migration barrier depend on the specific configuration [195, 166, 196] and type of element which the vacancy jumps to[158]. We used NN to predict the vacancy migration barrier, E_a , based on local environments. However, the attempt frequency, μ_a , was chosen to use a Debye frequency of $1 \times 10^{13} Hz$ for all the jump pairs, regardless of their species and local environments. Usually, the pre-exponential factor can result in a 10 times difference[157]. This is still tolerable to predict the event accurately, considering that the difference introduced by the exponential term would be much larger.

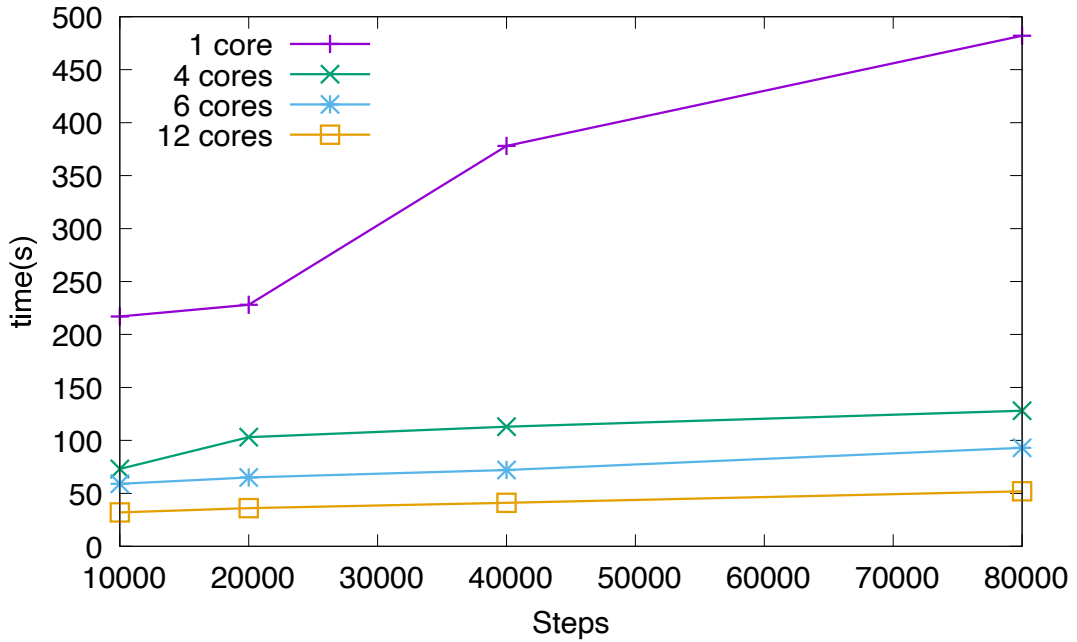


Figure 6.9: Scalability of KNN2 code for 108,000 atoms on Great Lakes HPC from the University of Michigan with 2x 3.0 GHz Intel Xeon Gold 6154 processors and InfiniBand HDR100 networking, capable of 100 Gb/s throughput.

6.3.2 Local Super-basin Kinetic Monte Carlo (LSKMC)

One effort we tried to make kMC simulation faster is to boost low-energy barrier events by using Local Super-basin Kinetic Monte Carlo (LSKMC) invented by Fichthorn et al[194]. The algorithm goes as shown in Algorithm 3. Even though the initial and final states of the vacancy are not next to each other in LSKMC steps, the corresponding energy change can also be calculated based on a depth-first search (DFS) method. Because if the NN function to predict the barrier is accurate enough, the energy differences along any path the vacancy takes from the initial site to the final site will be the same. We can do DFS to look for an available path and use the energy changes along the way to get the energy change between two states. However, the additional computational overhead is inevitable in this method as super-basin states require enumerating methods to explore.

Algorithm 3 Local Super-basin Kinetic Monte Carlo (LSKMC)

Algorithm from Fichthorn's method [194]

```

1: set  $epoch = 0$ ,  $step = 0$ ,  $time = 0$ 
2: while  $epoch < epoch_{Max}$  do
3:   perform a regular kMC step, get time increment  $t$ .
4:    $time += t$ 
5:   if  $t < t_{critical}$  then
6:      $step += 1$ 
7:   else
8:      $step = 0$ 
9:   end if
10:  if  $step == step_{critical}$  then
11:    A new super-basin is found.
12:    find transient and absorbing states based on preset
 $E_{critical}$ .
13:    compute the escape time  $t_{escape}$  and probability.
14:    decide the exiting state.
15:     $time += t_{escape}$ 
16:     $step = 0$ 
17:  end if
18: end while
```

Based on the description in Algorithm 3, there are mainly two hyperparameters,

$step_{critical}$ and $E_{critical}$. $step_{critical}$ means after these many steps, we have to involve a local “super-basin” step. And $E_{critical}$ is the energy cutoff we set to distinguish transient and absorbing states. If $E < E_{critical}$, then it is a transient state, and the vacancy does not end up in this state afterward. Otherwise, it is an absorbing state. We tested the effects of these two hyperparameters in Figure 6.10. As can be seen, when $step_{critical}$ were set very small and $E_{critical}$ were set very high, many local super-basin steps would be included, and the vacancy is pushed relatively farther away from the trapping sites. There was almost no flat area can be seen in the light blue line. This setup was a high slackness case. On the other hand, when $step_{critical}$ were set very large, and $E_{critical}$ were set very low, yellow or black line, less local super-basin steps are involved, and the vacancy is not pushed very far away. This was a low slackness case. When intermediate values were chosen, the LSKMC simulation behaves like regular kMC simulations, but needs much fewer steps to achieve the same simulated time and do not stick in low-energy barriers. Structures and concentrations of generated clusters were also compared to confirm LSKMC algorithm does not introduce new stochastic to the simulation results.

6.3.3 least recently used (LRU) Cache

In order to further speed up kMC simulations, a least recently used (LRU) cache, which evicts the least recently used entry, was implemented based on a hashmap and a doubly-linked list. The idea is based on memorizing the most recent entries. In this way, if the simulation was stuck in a local minimum, the repeated calculations can be ignored and directly obtained from memory. A similar idea was practiced by Mason et al.[197]. They used the “Zobrist” key to distinguish different binary alloy cluster structures. However, this method ignored detail local environment differences. Instead, we use the 27-digits encoding and store them in an array as the key. The hashmap holds the keys and the address of the nodes of the doubly-linked list. Each

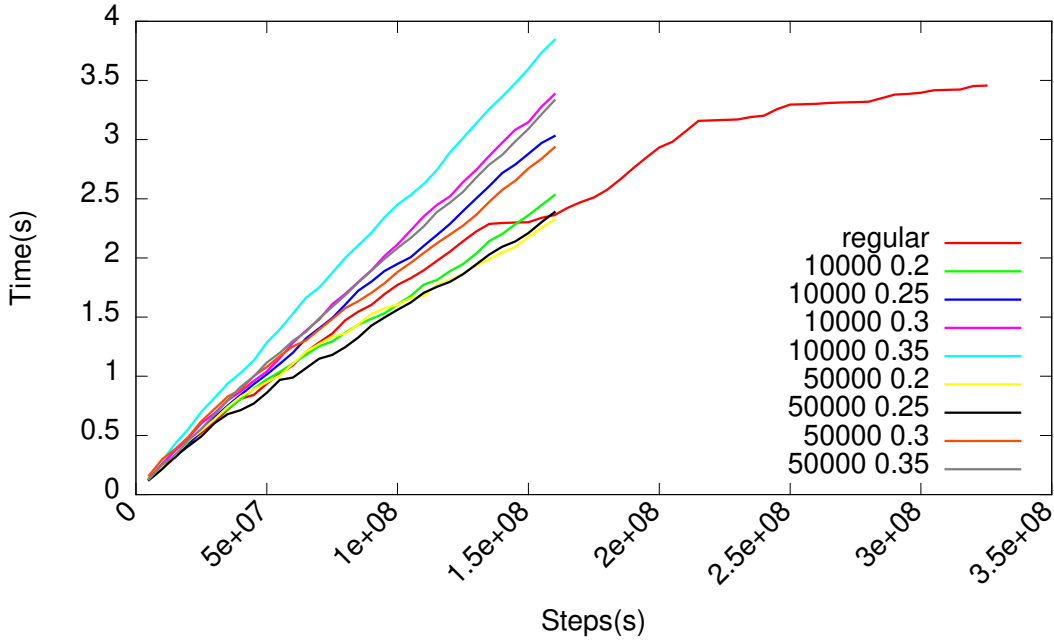


Figure 6.10: Comparison of different LSKMC parameters setup. The x axis shows the number of simulation steps, and the y axis show the corresponding evolution time of the investigated system. In the legend, “regular” means the regular kMC simulation without any local super-basin steps involved. Other than the “regular” label, the first and second numbers in each row of the figure legend correspond to the step count criteria $step_{critical}$ and energy criteria $E_{critical}$, respectively.

node of the doubly-linked list holds the value of the key, which represents the corresponding vacancy migration barrier. We remove elements from the bottom of the doubly-linked list and add new elements on top of the bottom of the doubly-linked list. When a new entry is accessed, it is moved to the top again, therefore most recently used entries are always on the top, and the least used ones are at the bottom of the list. However, by now, this implementation only supports single-core calculations. To make LRU Cache available for multiple cores, one way is to sync or share several most recent entries every several thousands of numbers of steps.

To hash on the key of encoding, we tried three different methods: 1) Hashing on a “long long” integer. The “long long” int data type of C++ for a 64-bit machine can store $2^{64} \sim 1 \times 10^{19}$ information. 27-digits encoding scheme with Al, Mg, Zn,

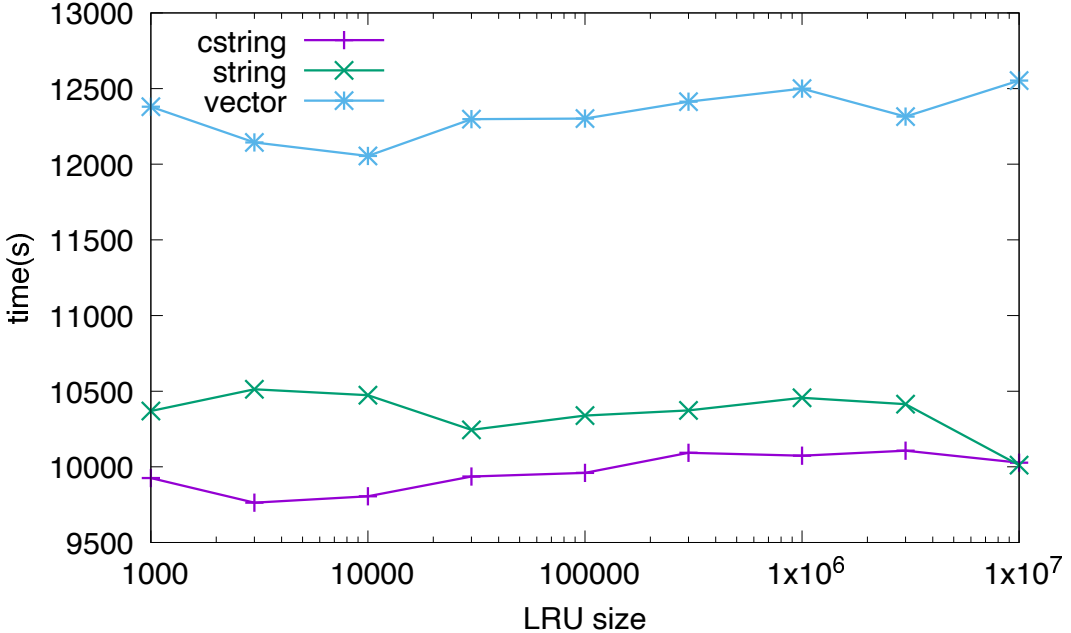
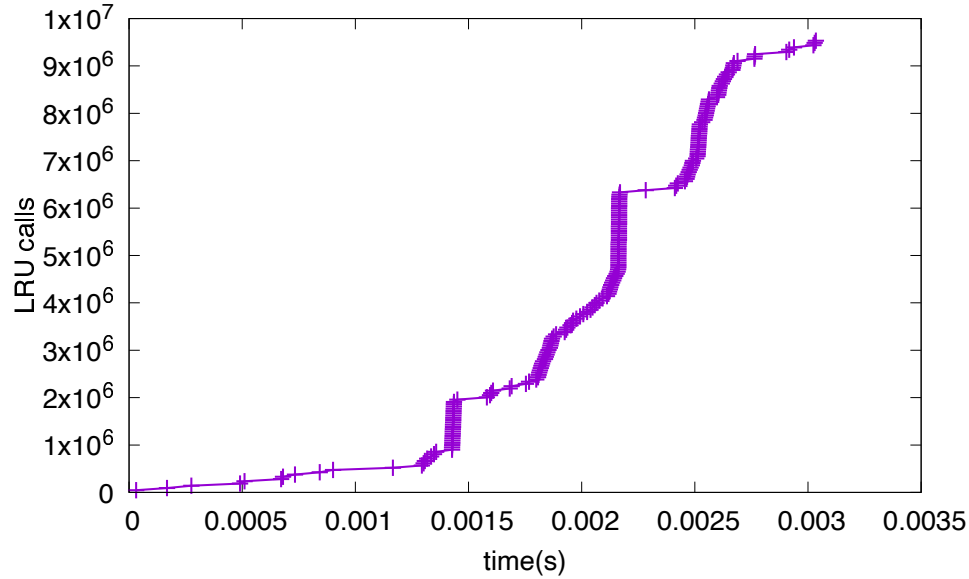


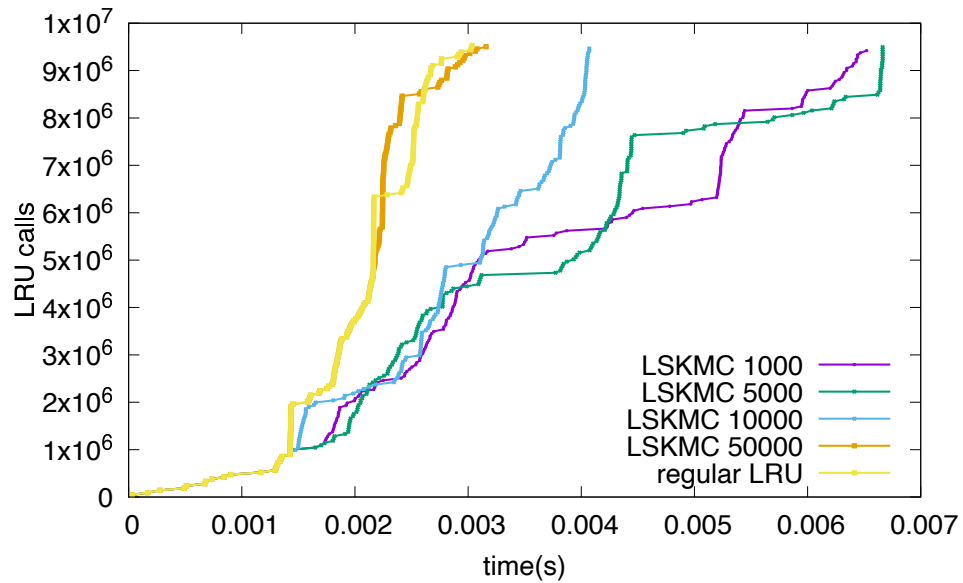
Figure 6.11: Comparison of LRU cache size effects on simulation speed for a 108,000-atom supercell system running 10,000,000 steps on TACC Stampede2 cluster. Without using LRU cache to memory recent encoding entries, it will take 55,135 seconds to run the simulation.

and Vac can take up to $4^{27} \sim 1 \times 10^{16}$. Therefore, we can simply convert an encoding array to a decimal integer and hash on the decimal integer. 2) Hashing on a string of C++. 3) Hashing on a C string, which is explicitly an array of char. It turned out that the best strategy would be the third one, directly hashing on a C string in C++ and the best size of LRU cache is between 3,000 and 10,000, as shown in Figure 6.11. Without using LRU cache to memory recent encoding entries, it takes 55,135 seconds to run the simulation. In general, the LRU cache method provides a 5 times speed-up. Generally speaking, in all the three methods, the speed initially drops and then increases slightly as we increase the size of the LRU cache storage capability. This can be explained by the size of the local minimum states. If the LRU cache size increase, it also takes a longer time to find the key and may also need more useless insertion operations to the cache.

In Figure 6.12 (a), we plot the number of LRU calls against the simulated time.



(a)



(b)

Figure 6.12: Number of calls of LRU cached results as time increases. A 3000-entries of LRU cache is used. (a) A single-core LRU cache for 10,000,000 steps. (b) Comparison of LRU with regular kMC and LSKMC of different local super-basin step involving criteria. Numbers in the legend indicates the value of $step_{critical}$. $E_{critical}$ was chosen to 0.3 eV for all LSKMC simulations in this plot.

Initially or during the early stage of simulation, only limited calls happened. Then the number of calls increase significantly around 0.0015, 0.00225, and 0.0025 seconds.

This indicates the existence of possible local trapping states. Around these timestamps, the encoding entries stored in the cache have a higher probability of being called. Once the system jumps out of the current low-energy barriers, the number of LRU calls becomes sparse again. In Figure 6.12 (b), we also tested LRU cache strategy together with LSKMC method. We chose a universal $E_{critical}$ of 0.3 eV and explored different $step_{critical}$ settings from 1,000 to 50,000. As can be seen from the plot, with very high $step_{critical}$, LRU calls invoked just like a regular kMC. But when we gradually tune this number lower, the curve becomes less steep and more stair-like. That can be explained by the fact that when LSKMC helps the vacancy getting out of the trapped state, less repeating visits happen. Interestingly, for a fixed number of simulation steps, even though with LSKMC, a much longer time is achieved, the number of LRU calls is on the same order (1×10^7). This is because LRU call happens when the event list is built but not during the moment when an event is executed.

6.4 Results and Discussion

In this section, we will first discuss how to distinguish and visualize clusters from the Al matrix. Then our benchmarks on key experimental value (Zn/Mg ratio, Al/(Mg+Zn) ratio) will be discussed. Next, we will study how to change cluster size distributions and chemical compositions by adding a small number of pseudo-atoms. At last, the viability of using cluster geometry and chemical composition to predict strength given a certain cluster will be briefly addressed.

6.4.1 Cluster Searching Algorithm

In order to better analyzing our results, we have to use a visualization method to characterize clusters. A cluster is a set of connected atoms, each of which is within the range of one or more other atoms from the same cluster. Thus, any two atoms from the same cluster are connected by a continuous path consisting of steps fulfilling

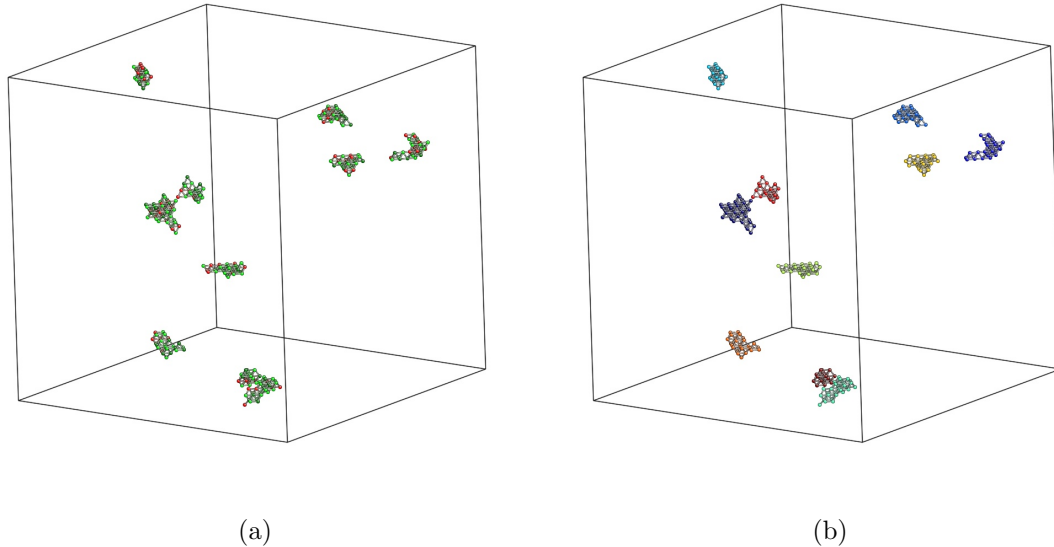


Figure 6.13: Atomistic pictures of the top 10 largest clusters by size via cluster searching algorithm from a snapshot during a kMC simulation. (a) Atomistic pictures of clusters coloring in atom species. Light green, dark green, and red atoms are Al, Mg, and Zn, respectively. (b) Atomistic pictures of clusters coloring in cluster id. The color mapping from dark blue to red is ranked by the cluster size in descending order. Small gray sticks are bonds between atoms.

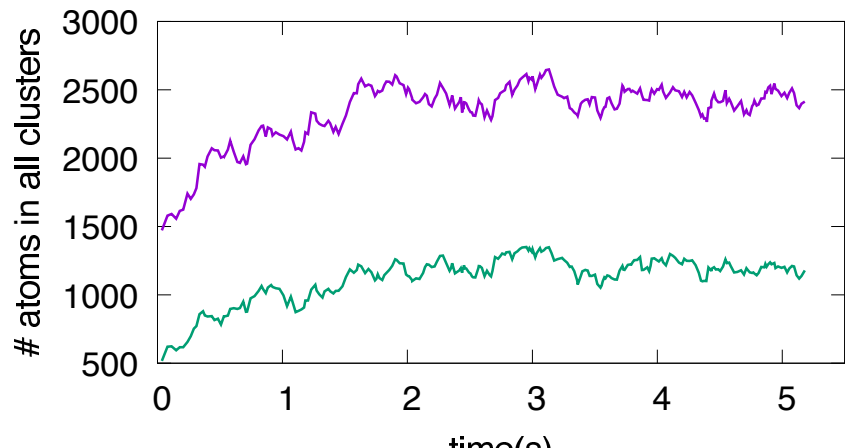
the selected neighboring criterion. Adversely, two atoms are not considered in the same cluster if there is no continuous path on the neighbor network leading from one particle to the other. We choose between the distance-based neighbor criterion, in which case two atoms are considered neighbors if they are within the neighbor list of each other. However, in our case, all the atoms are on the lattice, so the method described above does not work. It simply finds one huge cluster containing all the atoms. Therefore, we use the method described in Algorithm 4. We show one typical result in Figure 6.13 from a snapshot during a kMC simulation. To better visualize the details of clusters, only the top ten clusters are shown.

Algorithm 4 Cluster Searching Algorithm

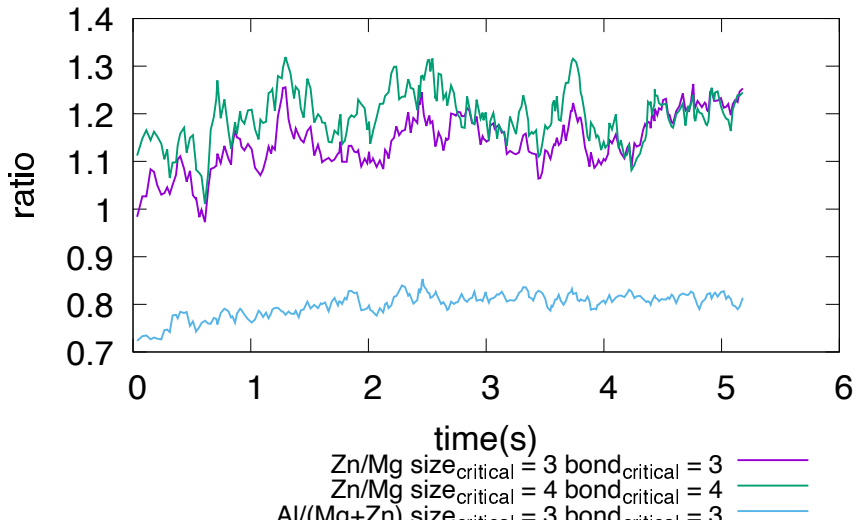
- 1: remove all the solvent atoms (Al for example).
- 2: assign an initial cluster id, ($cid = -1$), to all the atoms.
- 3: set $count = 0$.
- 4: **for** i in all the solute atoms **do**
- 5: **if** $cid_i = -1$ **then**
- 6: set $cid_i = count$.
- 7: breadth-first search (BFS) in the neighbor list of atom i to find other solute atoms if cluster size is greater than $size_{critical}$ and set their $cid = count$.
- 8: add their first nearest neighbor solvent atoms (Al for example) back if the solvent atom have more than $bond_{critical}$ solute first nearest neighbors and set their $cid = count$.
- 9: $count += 1$.
- 10: **end if**
- 11: **end for**
- 12: then clusters can be sorted according to any customized methods, by cluster size, element ratios for examples.

6.4.2 Benchmark of Al-Mg-Zn Clusters

For the kMC simulations, $(30 \times 30 \times 30)$ supercell containing 108,000 atoms were used. 3240 Mg atoms, 1700 Zn atoms, and 1 vacancy atom were randomly chosen among 108,000 atoms. This setup corresponds to ~ 3 atom. % of Mg, ~ 2 atom. % of Zn and a vacancy concentration of $\sim 1 \times 10^{-5}$. We used LSKMC algorithm to boost the simulation. After around ~ 5.5 seconds of simulation, clusters size and the ratio of Mg/Zn converged to a local minimum of a very initial stage of the multiple-stage clustering process. As shown in Figure 6.14 (a), the size of Al-Mg-Zn clusters are converging to a ~ 2400 atoms size using Algorithm 4 with $size_{critical}$ of 3 and $bond_{critical}$ of 3. If tighter criteria($size_{critical}$ of 4 and $bond_{critical}$ of 4) were used, much fewer atoms can be identified as forming clusters and number of atoms in clusters converges to a much smaller value of ~ 1000 . Although the tighter criteria offset cluster sizes by almost 1000, both two setups follow the same trend and converge after several seconds.



(a)



(b)

Figure 6.14: Size changes and ratio changes vs. time for ~ 5.5 seconds. Subplot (a) the change of cluster size including Al, Mg, and Zn atoms; (b) the change of $\text{Al}/(\text{Mg}+\text{Zn})$ and Zn/Mg ratio. The purple line uses $\text{size}_{\text{critical}}$ of 3 and $\text{bond}_{\text{critical}}$ of 3. The green line uses $\text{size}_{\text{critical}}$ of 4 and $\text{bond}_{\text{critical}}$ of 4. The change of cluster size and Zn/Mg ratio follow a similar trend and converge after around ~ 4 seconds.

And in Figure 6.14 (b), we plotted the ratio of Zn/Mg within identified clusters. Also, two different criteria were tested. When the bonding criterion ($\text{bond}_{\text{critical}}$) was set to 4, very little Al atoms are counted as clusters, resulting in a very low

$\text{Al}/(\text{Mg}+\text{Zn})$ ratio; therefore, we did not plot it here. Again, both setups trend similarly for Zn/Mg ratio and converge around 1.25. This ratio of Zn-rich clusters is comparable to the early stage solute clusters reported in [198]. Thus, in the following part of this chapter, $size_{critical}$ of 3 and $bond_{critical}$ of 3 were used for the cluster analyses.

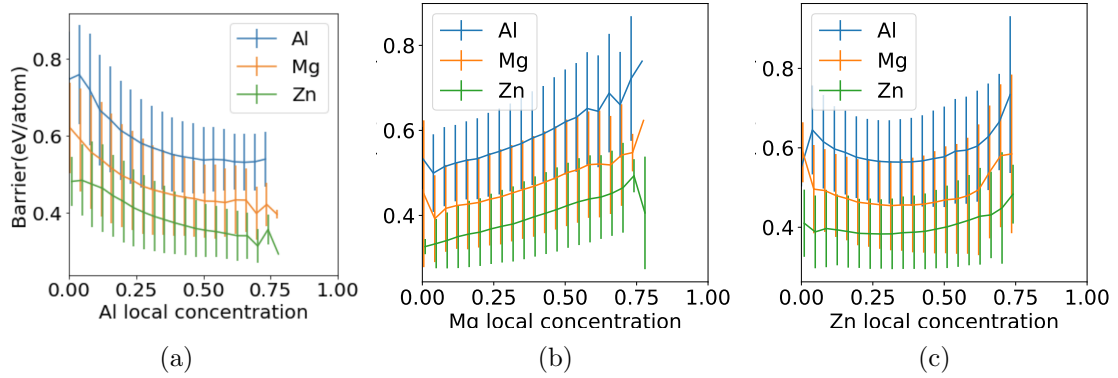
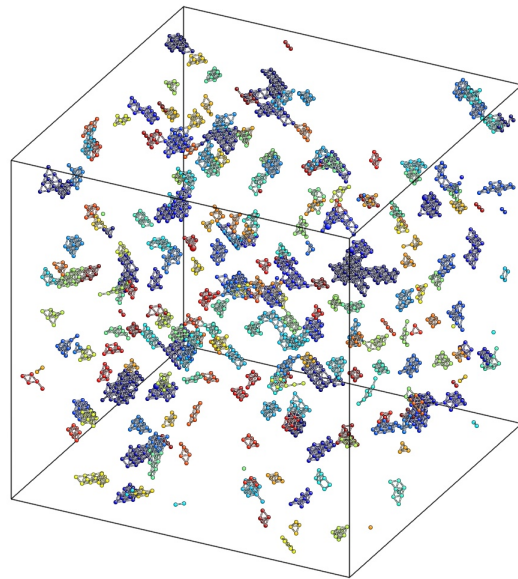


Figure 6.15: Vacancy migration barrier changes vs. different local environment concentrations. Vacancy migration barriers of a vacancy jumping to its adjacent lattice site that is occupied by Al, Mg, or Zn for different local environments are plotted. (a), (b), and (c) are local environments with concentration change of Al, Mg, and Zn, respectively. 500,000 different local environments are used to calculate this vacancy migration barrier distribution by a pre-trained neural network model. Blue, orange, and green lines are the migration barriers for a vacancy jumping to adjacent Al, Mg, and Zn, respectively. The X-axis is the local concentration of Al, Mg, and Zn defined by the lattice occupations on the first and second-nearest neighbors of the vacancy sites. The vertical line is the corresponding error bars. Concentration values of Mg and Zn are shifted by 0.001 to avoid error bars overlapping.

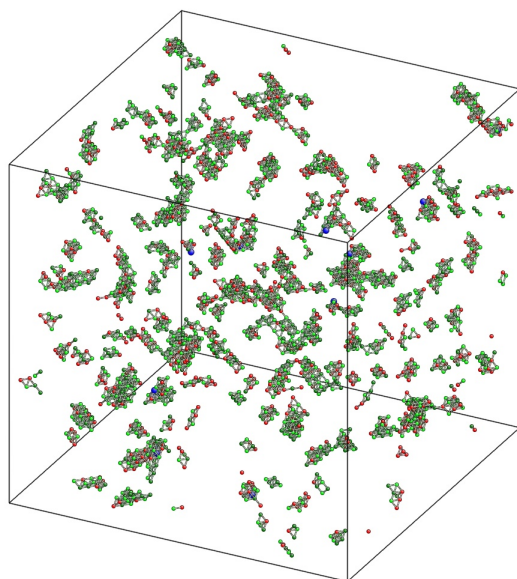
We would also like to explain why Zn-rich clusters are common during the early stage of clustering. Using the pre-trained neural network model, vacancy migration barriers can be studied under different amounts of local concentration change more systematically. As shown in Figure. 6.15, we plotted vacancy migration barriers of a vacancy jumping to its adjacent lattice site that is occupied by Al, Mg, or Zn for different local environments. We take advantage of our pre-trained neural network

model to randomly sample 500,000 different local environments. We found when Al local concentration is very low in Figure 6.15 (a), Zn and Mg mobility is much higher than Al since the migration barriers of the vacancy jumping to the adjacent Zn and Mg atoms are always lower than their counterpart for Al atoms. A local environment with very low Al concentration usually means Mg/Zn atoms are enriched. Highly mobile Zn and Mg atoms might provide the opportunity for Zn and Mg atoms to reorganize and form stable clusters under low Al concentration. In addition, lower barriers of the vacancy jumping to Zn compared with their counterparts of Mg could result in the slightly Zn-rich clusters during the early stage of clustering. As shown in Fig. 6.15 (b) and (c), the migration barriers of the vacancy jumping to the adjacent Zn, Mg, and Al atoms always rank in the order of $Zn < Mg < Al$ regardless of the local concentration, further suggesting the tendencies of high mobility of Zn atoms and the formation of Zn-rich clusters.

Atomistic pictures of those clusters can be found in Figure 6.16. In addition, the distribution of cluster sizes is provided in Figure 6.17. With cluster size frequencies, it becomes easier to identify how many clusters are stable. In Figure 6.17 (a) and (b) we compared the size distribution of a Al-Mg-Zn system evolving for 5 seconds and 22 seconds. Both configurations at 5 and 22 seconds follow a Poisson distribution pattern. In Figure 6.18, we also observed the number of Al, Mg, and Zn atoms in all identified clusters and the number of Mg-Zn bonds across the structure (both matrix and clusters) for the first 22 seconds. After the initial 1 or 2 seconds, these two descriptors became steady and oscillated around 2500 and 1200, respectively.



(a) cluster



(b) species

Figure 6.16: Atomistic pictures of 108,000 atoms for control group, corresponding to setup #0 in Table 6.3. Subplot. (a) is colored by cluster size. The color mapping from dark blue to red is ranked by the cluster size in descending order. Subplot. (b) is colored by atom species. Light green, dark green, red, and blue atoms are Al, Mg, Zn, and pseudo atoms respectively. Small gray sticks are bonds between atoms.

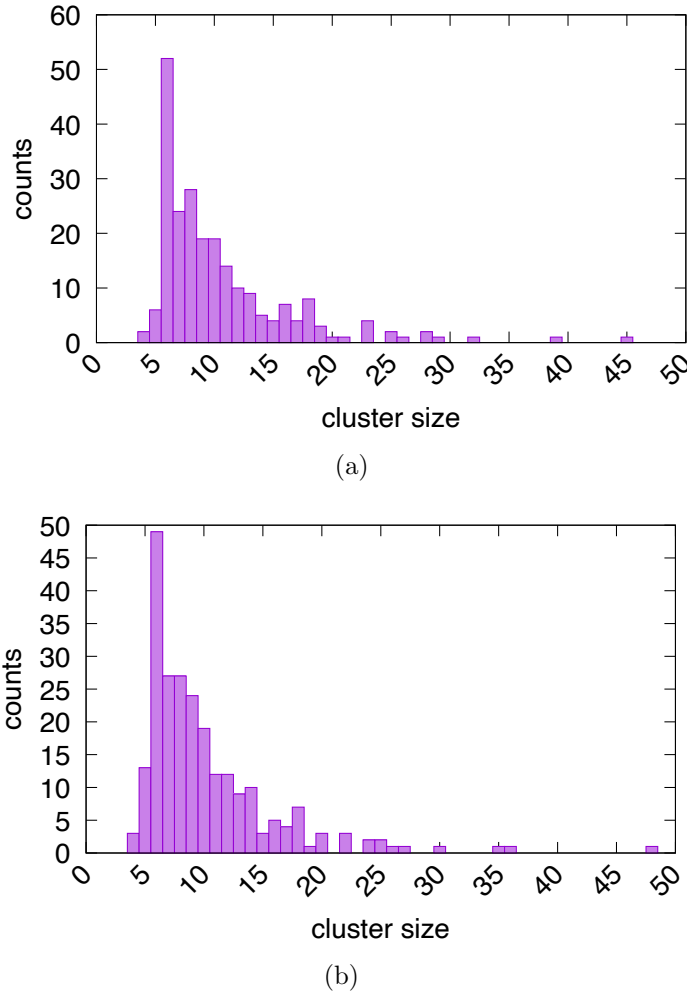


Figure 6.17: Size distribution of identified clusters at 5 and 22 seconds. Subplot (a) and (b) are for 5 seconds and 22 seconds, respectively.

6.4.3 Searching for Potential Elements that Can Slow Down Precipitate Hardening

Similar to the idea of searching “anchor” elements in Chapter 4.4, we will first use kMC simulation with some pseudo-atoms (denoted as “X”) to study their effects on the early stage clustering. In this study, we have Al atoms as solvent atoms, and Mg, Zn, and X atoms as solute atoms. For these simulations, $(30 \times 30 \times 30)$ supercell containing 108,000 atoms were used. 3240 Mg atoms, 1700 Zn atoms, 1080 X atoms, and 1 vacancy atom were randomly chosen among 108,000 atoms. This

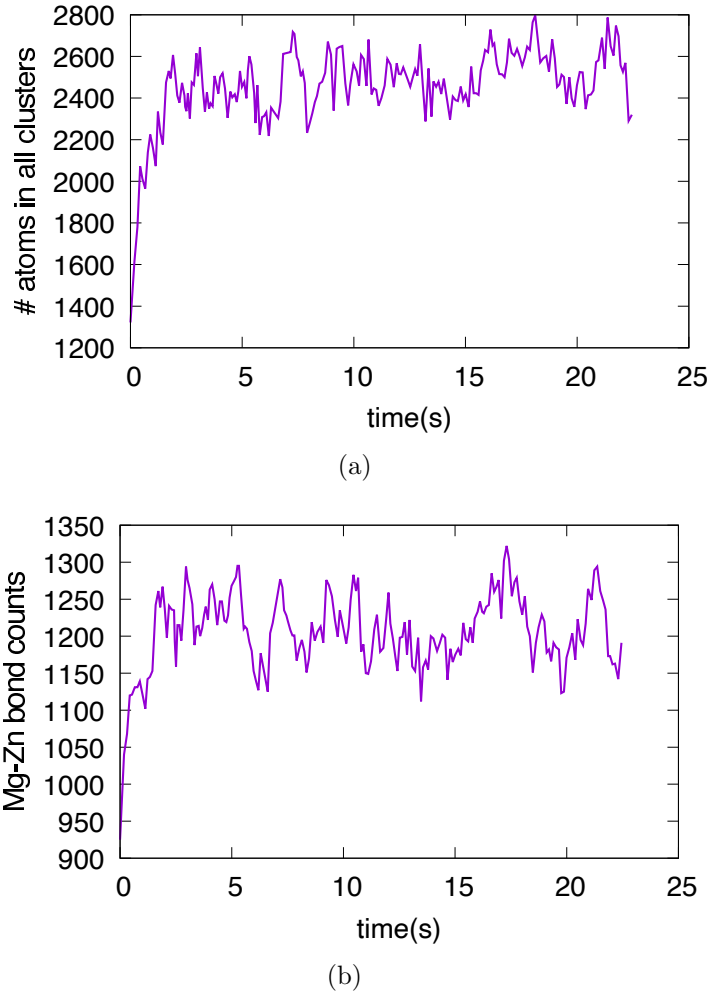


Figure 6.18: Cluster size and Mg-Zn bonds change for the first 22 seconds. Subplot (a) The number of Al, Mg, and Zn atoms in all identified clusters vs. time. Subplot (b) The number of Mg-Zn bonds across the structure (both matrix and clusters) vs. time.

setup corresponds to ~ 3 atom. % of Mg, ~ 2 atom. % of Zn, ~ 1 atom. % of X, and a vacancy concentration of $\sim 1 \times 10^{-5}$. Note that this concentration is set to conduct the sensitivity tests only. This ~ 1 atom. % is not a trace amount value, but it can help to boost the effects of pseudo-atoms. To tune the properties of pseudo atoms, we can change the effects of different elements on vacancy migration barriers to the pseudo-atoms, as well as barriers to other elements. We leverage this by adding an offset to the vacancy migration barrier calculated from NN model via Equation 6.6a. The amount of the offset is determined by counting first neighbor bonding of X-Al,

X-Mg, and X-Zn, via Equation 6.6b:

$$E_a^{actual} = E_a^{NN} + offset \quad (6.6a)$$

$$offset = \varepsilon_{i-X} * (n_{i-X}^{final} - n_{i-X}^{init}) \quad (6.6b)$$

where E_a^{NN} is the energy obtained by the neural network prediction of treating element “X” as the solvent element Al. i is the atomic type of the swapped atom that the vacancy would jump to, which can be Al, Mg, or Zn. ε_{i-X} quantify the pseduo-atom effects on the vacancy migration barrier $offset$ in Equation 6.6b by simple bond counting method. n_{i-X}^{init} and n_{i-X}^{final} are the number of $i - X$ bonds between the swapped atom i and the pseudo-atom X in its first nearest neighbor before and after the vacancy migration, respectively. For example, if $\varepsilon_{Al-X} = 0.01$ that means a new Al-X pair in the final state after the vacancy migration increases the vacancy migration barrier by a positive 0.01 eV.

The right-hand side of Equation 6.6a can be divided into two parts. The first part, which is NN potential part, can be seen as a more comprehensive bond counting model [156] base on the pair interactions of Al-Al, Al-Mg, Al-Zn, and Mg-Zn, plus cross interactions or higher-ordered angular contributions. The second part of the right-hand side can be seen as first-order bond counting of Al-X, Mg-X, and Zn-X. As a qualitative study, first order pair-wise interaction of the unknown pseudo-atoms should be sufficient. Then the target is to find an element “X” that can change the vacancy migration barrier of Vac-i by roughly the amount of ε_{i-X} to achieve the optimal effects to slow down the solute clustering during the natural aging in Al-Mg-Zn alloys. In the future, with the optimized ε_{i-X} values for slowing down solute clustering, we can use DFT with NEB to search for potential realistic chemical elements that can change the vacancy migration barriers according to Equations 6.6a and 6.6b with the optimized ε_{i-X} .

To setup the simulation for sensitivity tests, we use LSKMC method with $step_{critical}$ of 25,000 steps and $E_{critical}$ of 0.3 eV. After around 5 to 6 seconds simulations, we can already tell the differences of cluster size obviously. As discussed above, we tuned parameters of ε_{i-X} for $i \in Al, Mg, Zn$ in Equation 6.6b. Detailed setup is listed in Table 6.3. All the sensitivity tests can be divided into four groups: the control group with all $\varepsilon_{i-X} = 0$ (Setup #0 in Table 6.3), the Al group with only $\varepsilon_{Al-X} \neq 0$ (Setup #1 and #2 in Table 6.3), the Mg group with only $\varepsilon_{Mg-X} \neq 0$ (Setup #3 and #4 in Table 6.3), and the Zn group with only $\varepsilon_{Zn-X} \neq 0$ (Setup #5 and #6 in Table 6.3). Their corresponding final snapshots of clusters for the control group, Al group, Mg group, and Zn group can be found in Figure 6.16, 6.19, 6.20, and 6.21, respectively.

Table 6.3: Sensitivity analyses of different ε_{i-X} in Equation 6.6b. In the table, the number of different element types in all identified clusters are listed using $size_{critical}$ of 3(4) and $bond_{critical}$ of 3(4).

| setup | ε_{Al-X} | ε_{Mg-X} | ε_{Zn-X} | Al counts | Mg counts | Zn counts | pseudo counts |
|-------|----------------------|----------------------|----------------------|-----------|-----------|------------|---------------|
| 0 | 0.00 | 0.00 | 0.00 | 1078(230) | 588(421) | 737(524) | 11(4) |
| 1 | 0.05 | 0.00 | 0.00 | 1229(270) | 689(434) | 778(549) | 0(0) |
| 2 | -0.05 | 0.00 | 0.00 | 1407(312) | 922(753) | 1017(871) | 406(252) |
| 3 | 0.00 | 0.05 | 0.00 | 1442(353) | 1121(919) | 794(620) | 292(171) |
| 4 | 0.00 | -0.05 | 0.00 | 1012(215) | 588(407) | 638(463) | 5(1) |
| 5 | 0.00 | 0.00 | 0.05 | 1407(395) | 522(407) | 1325(1164) | 385(253) |
| 6 | 0.00 | 0.00 | -0.05 | 1042(222) | 590(363) | 730(489) | 3(0) |

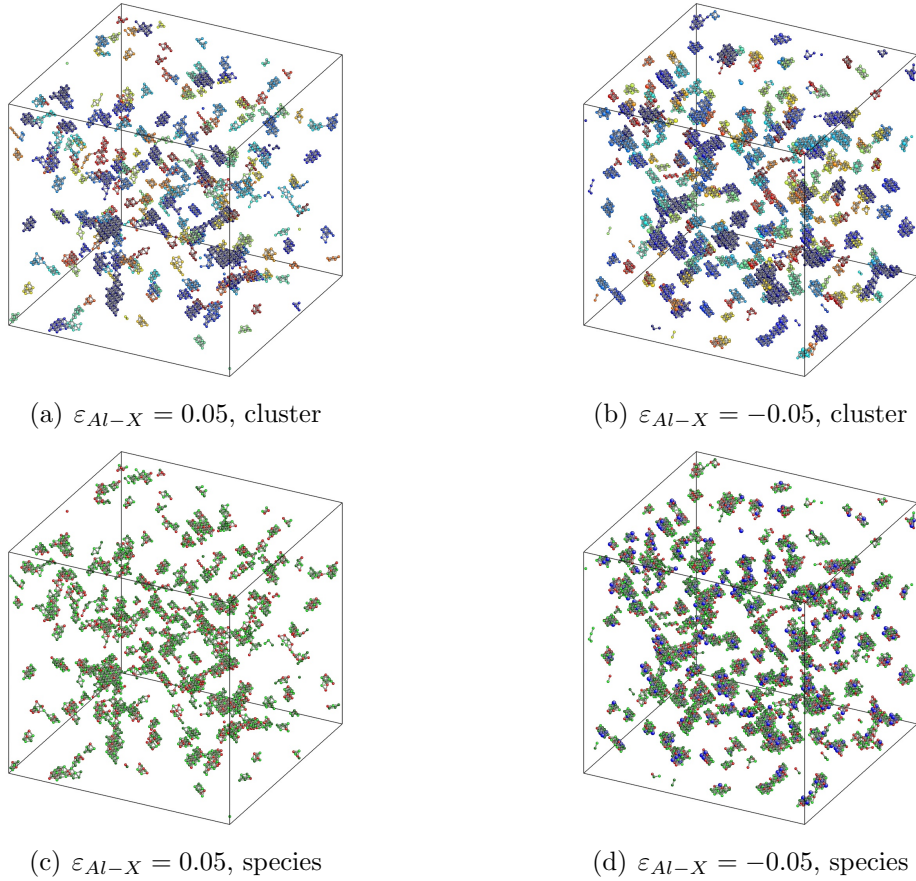


Figure 6.19: Atomistic pictures of 108,000 atoms for ε_{Al-X} sensitivity test using $size_{critical}$ of 3 and $bond_{critical}$ of 3. (a), (c) : $\varepsilon_{Al-X} = 0.05$, which is setup #1 in Table 6.3. (b), (d) : $\varepsilon_{Al-X} = -0.05$, which is setup #2 in Table 6.3. (a) and (c) are colored by cluster size. The color mapping from dark blue to red is ranked by the cluster size in descending order. (b) and (d) are colored by atom species. Light green, dark green, red, and blue atoms are Al, Mg, Zn, and pseudo atoms respectively. And small gray sticks are bonds between atoms.

In order to better visualize the change of structures and stoichiometry, we plotted the changes of the cluster sizes and the ratios between species in Figure 6.22 and 6.23. In Figure 6.22, cluster size change for the control group, Al group, Mg group, and Zn group are plotted. With and without considering pseudo-atoms in the clusters does not change the trend significantly. The purple line in Figure 6.22 represents the cluster size changes of the control group. Configurations with pseudo-atom having $\varepsilon_{Al-X} = -0.05$, $\varepsilon_{Zn-X} = 0.05$, and $\varepsilon_{Mg-X} = 0.05$ have the ability to make clusters to

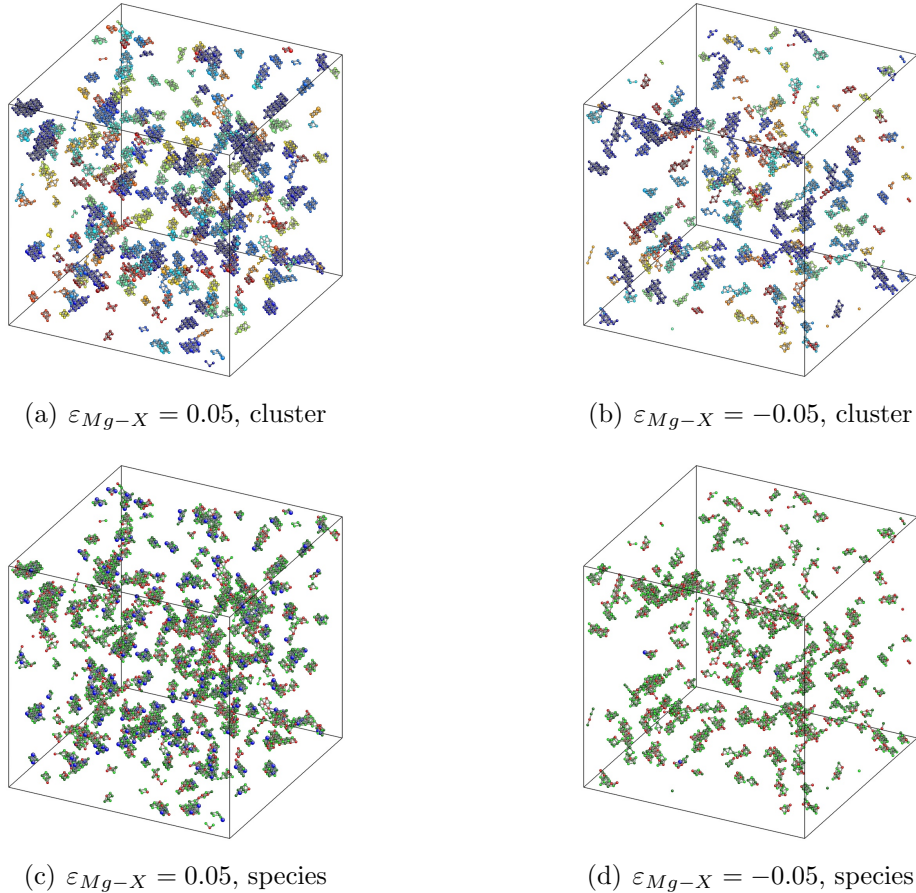


Figure 6.20: Atomistic pictures of 108,000 atoms for ε_{Mg-X} sensitivity test using $size_{critical}$ of 3 and $bond_{critical}$ of 3. (a), (c) : $\varepsilon_{Mg-X} = 0.05$, which is setup #3 in Table 6.3. (b), (d) : $\varepsilon_{Mg-X} = -0.05$, which is setup #4 in Table 6.3. (a) and (c) are colored by cluster size. The color mapping from dark blue to red is ranked by the cluster size in descending order. (b) and (d) are colored by atom species. Light green, dark green, red, and blue atoms are Al, Mg, Zn, and pseudo atoms respectively. And small gray sticks are bonds between atoms.

grow much larger after around 2 second. From Table 6.3, the number of Al, Mg, and Zn species in the identified clusters grow with the similar ratio relative to each other compared with those in the control group. However, their counterparts ($\varepsilon_{Al-X} = 0.05$, $\varepsilon_{Zn-X} = -0.05$, and $\varepsilon_{Mg-X} = -0.05$) cannot reduce the cluster size. Their curves behave similar to the control group.

To study the chemistry of solute clusters, we plotted the ratio of 1) solvent/solute atoms and 2) Zn/Mg in clusters in Figure 6.23. In Figure 6.23 (a), the Al/(Mg+Zn+X)

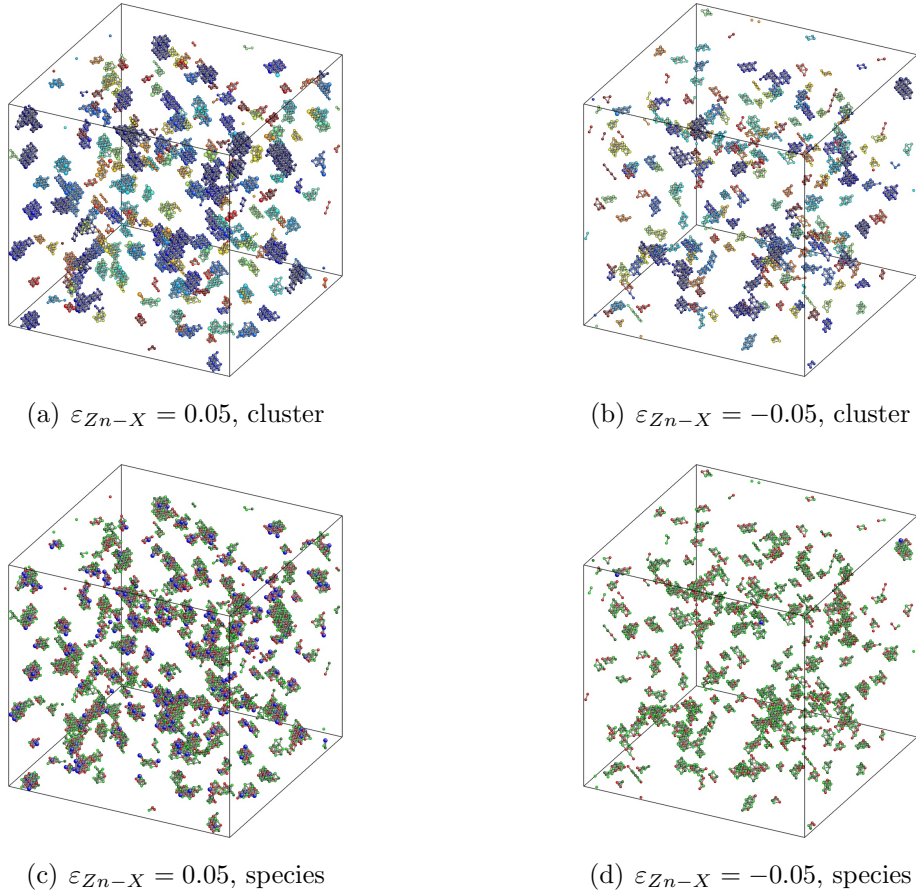
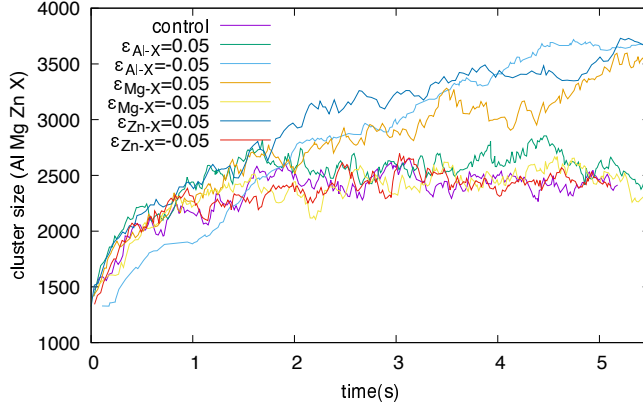
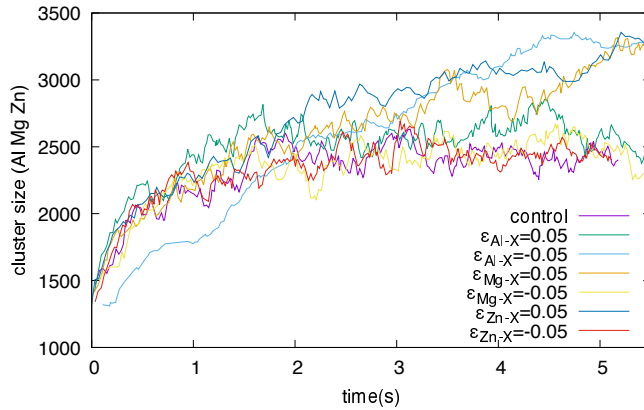


Figure 6.21: Atomistic pictures of 108,000 atoms for ε_{Zn-X} sensitivity test using $size_{critical}$ of 3 and $bond_{critical}$ of 3. (a), (c) : $\varepsilon_{Zn-X} = 0.05$, which is setup #5 in Table 6.3. (b), (d) : $\varepsilon_{Zn-X} = -0.05$, which is setup #6 in Table 6.3. (a) and (c) are colored by cluster size. The color mapping from dark blue to red is ranked by the cluster size in descending order. (b) and (d) are colored by atom species. Light green, dark green, red, and blue atoms are Al, Mg, Zn, and pseudo atoms respectively. And small gray sticks are bonds between atoms.

ratio in the clusters of those setups that generate larger cluster sizes drops significantly. The reason might be two folds: 1) the pseudo-atoms (X) inside the cluster increases in these setups. 2) the shapes of those clusters tend to be more blocky compared to the elongated structures. From Figure 6.20, and 6.21, we can see there is obvious more X atoms within the identified clusters. Also, in Figure 6.23 (b) we plotted the ratio of Al/(Mg+Zn). Without X atoms, the ratio only drops ~ 0.1 instead of ~ 0.2 . Therefore, configurations with pseudo-atom having $\varepsilon_{Al-X} = -0.05$,



(a) cluster size of Al Mg Zn X



(b) cluster size of Al Mg Zn

Figure 6.22: Size changes of different clusters vs. time using $size_{critical}$ of 3 and $bond_{critical}$ of 3. Subplot. (a) is for all the atoms including pseudo atoms. (b) is for Al, Mg, and Zn only.

$\varepsilon_{Zn-X} = 0.05$, and $\varepsilon_{Mg-X} = 0.05$ tended to have more pseudo atoms segregate into the cluster side, and their cluster shape might tend to be more blocky (less Mg, Zn coordinates for neighbor Al to be identified as within clusters).

In Figure 6.23 (c), we compared different pseudo-atoms alloying effects on changing Zn/Mg ratio. Most of the pseudo-atom setups did not change the ratio, and those configurations still form Zn-rich clusters with the ratio converging to a value of 1.2. However, more Zn-rich clusters or more Mg-rich clusters can be achieved by using $\varepsilon_{Zn-X} = 0.05$ and $\varepsilon_{Mg-X} = 0.05$. Zn/Mg ratio is more sensitive to diffusion barriers change of Zn bonds. This provides the opportunity to tune cluster local

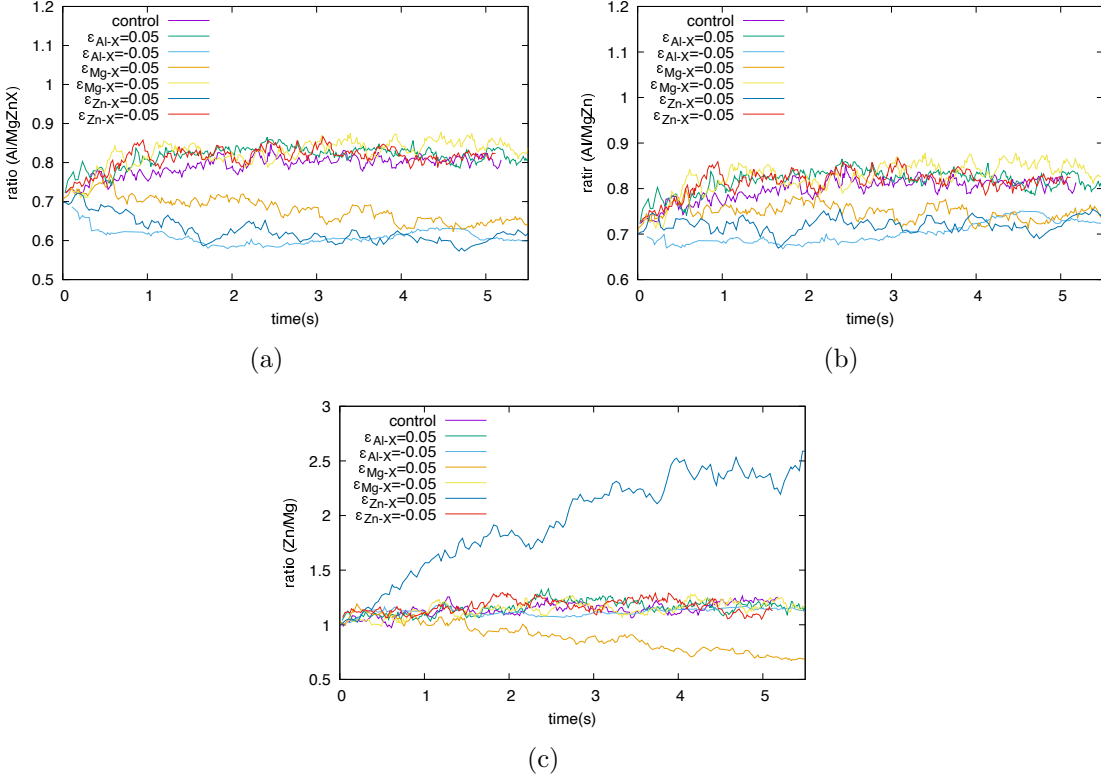


Figure 6.23: Ratio changes of different clusters vs. time using $size_{critical}$ of 3 and $bond_{critical}$ of 3. Subplot. (a) is for the ratio of all the Al atoms to the sum of Mg, Zn, and X atoms in the clusters. (b) is for the ratio of all the Al atoms to the sum of Mg and Zn atoms in the clusters. (c) is for Zn and Mg ratio in the clusters. X represents the pseudo-atom.

chemistry, hence enhancing/weakening the APB energy barriers. In Figure 6.24, detailed bond information was summarized by plotting changes of different bond counts against time for the entire environment(including both matrix and clusters). Counts of Al-Mg, Al-Zn, Mg-Zn, Al-X, Mg-X, and X-Zn bonds were plotted, respectively.

The ultimate provision of this study is to understand how clusters affect strengthening and how to manipulate it during natural aging in multicomponent Al alloys. To investigate the relationship between clusters and strength/hardness, many theories have been developed recently[100, 199, 200]. From a microscopic view, the hardening happens by clusters impeding dislocation motion. The effect of clusters on changing hardness can come from two sources: 1) the long-range effect, which

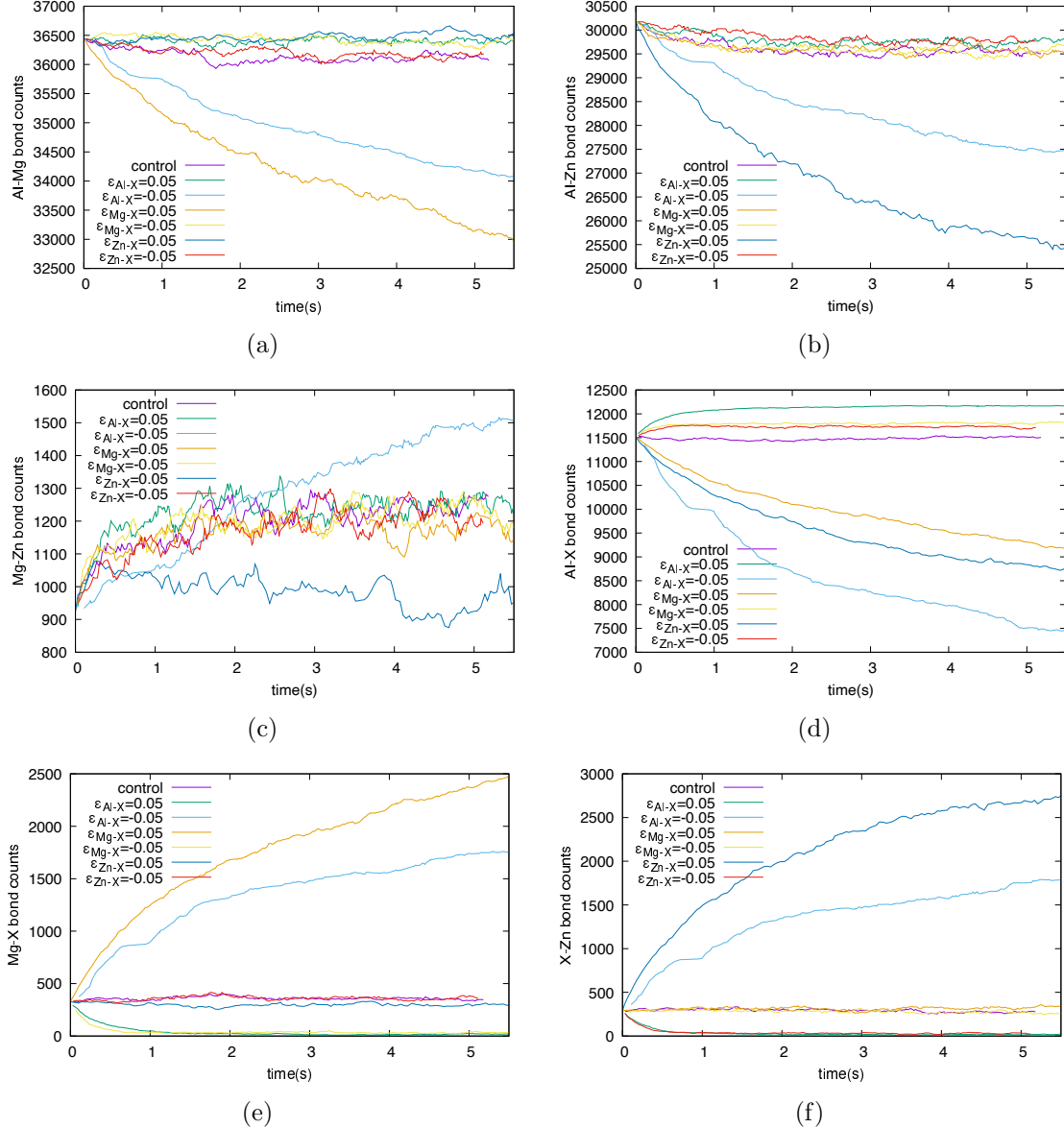


Figure 6.24: Bonds between different species vs. time using $size_{critical}$ of 3 and $bond_{critical}$ of 3. (a), (b), (c), (d), (e), and (f) are for numbers of Al-Mg, Al-Zn, Mg-Zn, Al-X, Mg-X, and X-Zn bonds, respectively. X represents pseudo-atom.

is the elastic interactions between the misfit strain field of clusters and dislocation strain fields (“strain misfit effects”); 2) the short-range effect, which is the change of stacking fault energies related to dislocation core behavior due to clusters(“chemical effects”)[100].

For the elastic strain effects, each cluster provides only a small amount of re-

sistance, but the very high density of clusters generates a high overall strain effect to impede the dislocation movement. This strain field is a function of cluster size, cluster distribution as well as chemical distribution across the matrix. For the short-range chemical effects, when dislocations cut through ordered solute clusters, only local bond changes is observed. Additional energy is required to create bond order changes, such as an anti-phase boundary (APB). The work needs to be done for movements of dislocations hampered by clusters equals the change in energy-related to the short-range order per unit area of slip planes. Hence it is then critical to figure out how the short-range order of clusters affects the hardness.

In multicomponent alloys, the elastic strain effects and chemical effects of solute clusters could couple together and become more complicated when the chemical compositions and structures of clusters become complex. First-principles calculations can be applied to obtain the parameters related to elastic strain and chemical effects of these clusters, similar to those for solid solution strengthening model[100]. Then these parameters are used in the classical continuum model to predict the overall cluster strengthening effects. Advanced machine learning models can be used to speed up the prediction based on first-principle data sets of the parameters of elastic strain effects and chemical effects of many clusters from kMC simulations. Then we can build a surrogate model to predict the natural aging hardening effects under the influence of various types of solute elements directly based on kMC simulation results.

6.5 Conclusion

In this chapter, Ag-Mg-Zn ternary alloy is used as a model system to simulate the solute clustering kinetics in Al 7000 series alloys. We first demonstrate that the Bell-Evans-Polanyi (BEP) relationship, which suggests a simple linear relation between the activation barrier and the reaction energy of one elementary reaction step, fails to provide quantitatively accurate migration barriers of vacancies in these

multi-component Al alloys. Then we develop a NN model to predict vacancy migration barriers using the training data set of thousands of DFT calculated barriers for different alloy configurations.

A kMC method based on this NN model is used to study the early transition behavior from a supersaturated solid solution to solute clusters and Guinier-Preston (GP) zones in Al-Mg-Zn alloys. A local super-basin method Section 6.3.2, together with LRU cache in Section 6.3.3, is also implemented to accelerate kMC simulations.

We also propose a pseudo-atoms approach to efficiently search the alloying strategy to slow down the solute clustering and the corresponding natural aging effects in Al 7000 series alloys. In this approach, a small number of pseudo-atoms with artificially designed ability to change vacancy migration barriers are added into the Al matrix, and the kMC simulations are performed to check their effects to clustering kinetics (so-called “sensitivity test”).

We also develop quantitative analysis methods to describe the chemical and structural properties of clusters. Using these quantitative analysis methods, we find that, 1) during the early stage of clustering, Zn-rich clusters appear first, and these clusters become stable very soon, only after 3 seconds; 2) for early-stage clusters, Zn/Mg ratio is converged to 1.2, which is consistent with experimental observations; 3) one possible reason for slightly Zn-rich early-stage clusters is the migration barriers for the vacancy to jump to the adjacent Zn atom is lower than their counterparts for Mg or Al.

At last, we propose a machine learning strategy based on the structural and chemical information of clusters and precipitates from kMC simulations to predict the cluster strengthening and natural aging effects in future studies.

CHAPTER VII

Summary and Future Work

7.1 Summary

The industrial-scale applications of metallic alloys with advanced structural and functional properties require the employment of efficient, low-cost, and environmental-friendly processing methods for industrial-scale manufacturing. However, there are many unsolved problems to achieve these alloy processing methods due to complex reactions, transformation, and deformation mechanisms in the commercially-available multicomponent alloys. In my dissertation, the thermodynamic driving force and kinetics of key reaction steps during relevant alloy processing procedures are studied systematically by theoretical/simulational tools at the atomistic scale. In Chapter III and IV, multiscale simulation efforts are made to improving the Ag thin-film quality during sputtering by changing substrate structures and chemistry. In Chapter V, we focus on the Mg alloy corrosion due to impurities from casting processing and create a build-in corrosion-resistant mechanism by high-throughput first-principles calculations. In Chapter VI, multiscale simulations are performed to search the methods to slow down solute cluster nucleation and growth in Al alloy during natural aging in order to avoid costly hot stamping procedures for 7000 series Al alloys. The main conclusions are summarized as the following.

In Chapter III, the thermodynamic driving force of H adsorption on anion-terminated

(000 $\bar{1}$) surfaces of pure and doped wurtzite ZnO, which is the dielectric substrate for Ag thin film deposition by sputtering, are investigated under varying H surface coverage conditions. A $\frac{1}{2}$ ML of adsorbed H changes the electronic structure of pure ZnO (000 $\bar{1}$) surface from metallic to semiconductor state by saturating unpaired electrons of surface oxygen atoms. This closed-shell electron configuration of ZnO (000 $\bar{1}$) surface significantly reduces the adsorption strengths of subsequent H atoms, making the dissociative adsorption of a hydrogen molecule endothermic. A simple electron counting model is applied to predict and tune the coverage-dependent H adsorption strengths on doped ZnO surfaces. The equilibrium H coverage, above which the dissociative adsorption of a hydrogen molecule is endothermic, will decrease when doping elements (such as Al, Ti, and V) have more valence electrons than Zn. We also expand the method of tuning H equilibrium coverage to other similar polar semiconductors, such as wurtzite GaN (000 $\bar{1}$), and zincblende ZnS ($\bar{1}\bar{1}\bar{1}$) surfaces. This method provides a general way to generate desired surface configurations of dielectric substrates before sputtering.

In Chapter IV, we utilize Grand Canonical Monte Carlo (GCMC) simulation to understand the possible reason why ZnO is the appropriate substrate for Ag thin film deposition. The quality of Ag thin film on the hexagonal surfaces of the substrate, like ZnO (000 $\bar{1}$), is robust to the variations of the substrate lattice constant and the Ag adsorption strength. GCMC simulations on these hexagonal surfaces usually yield Ag thin films that are in the fcc phase and {111} oriented. Besides, to achieve more continuous Ag thin films with less use of Ag, the doping elements, like Pd, Sb, Se, Sn, and Te, can be added as “anchor” sites on ZnO surfaces to bind incoming Ag atoms. With 0.05ML of “anchor” sites on the substrate, sufficient nuclei can be generated to achieve continuous ultra-thin films. We also search for alloying elements that can segregate in Ag grain boundaries to stabilize grain size during heat treatments. Current DFT calculation shows that tungsten (W) does not segregate to any investigated Ag

grain boundaries. This result is inconsistent with the experimental fact that W can stabilize Ag grain boundaries during the heat treatment. The possible origin of such inconsistency can be resolved if more accurate and representative grain boundary structures in Ag alloys are constructed in future studies.

In Chapter V, our computational procedure predicts that six p-block elements meet the thermodynamic criteria to slow down the hydrogen evolution reaction (HER) as the cathodic reaction on surfaces of Fe impurities and increase the build-in corrosion resistance of the cast Mg alloys. These six elements rank according to their ability to reduce H adsorption energies and the HER rate as follows: As > Ge > Si > Ga > P \approx Al. Results for As, the most effective corrosion-inhibiting element, and Ge are in qualitative accord with recent experiments. While none of the 68 investigated alloying elements was found to enhance H adsorption on Fe surfaces, the six p-block elements reduce H adsorption on Fe surface via strong orbital overlap (Pauli repulsion) between their outer-shell orbitals and the s orbitals of H adsorbates. We also extend our model to search the possible alloying elements to impede HER on surfaces of other possible transition-metal impurities and precipitates in Mg alloys.

In Chapter VI, Ag-Mg-Zn ternary alloy is used as a model system to simulate the solute clustering kinetics in Al 7000 series alloys. We first demonstrate that the Bell-Evans-Polanyi (BEP) relationship, which suggests a simple linear relation between the activation barrier and the reaction energy of one elementary reaction step, fails to provide quantitatively accurate migration barriers of vacancies in these multi-component Al alloys. Then we develop a NN model to predict vacancy migration barriers using the training data set of thousands of DFT calculated barriers for different alloy configurations. A kMC method based on this NN model is used to study the early transition behavior from a supersaturated solid solution to solute clusters and Guinier-Preston (GP) zones in Al-Mg-Zn alloys. A local super-basin method in Section 6.3.2, together with LRU cache in Section 6.3.3, is also implemented to

accelerate kMC simulations. We also propose a pseudo-atoms approach to efficiently search the alloying strategy to slow down the solute clustering and the corresponding natural aging effects in Al 7000 series alloys. In this approach, a small number of pseudo-atoms with artificially designed ability to change vacancy migration barriers are added into the Al matrix, and the kMC simulations are performed to check their effects to clustering kinetics (so-called “sensitivity test”). We also develop the quantitative analysis methods to describe the chemical and structural properties of clusters. Using these quantitative analysis methods, we find that: 1) during the early stage of clustering, Zn-rich clusters appear first, and these clusters become stable very soon, only after 3 seconds; 2) for early-stage clusters, Zn/Mg ratio is converged to 1.2, which is consistent with experimental observations; 3) one possible reason for slightly Zn-rich early-stage clusters is the migration barriers for the vacancy to jump to the adjacent Zn atom is lower than their counterparts for Mg or Al. At last, we propose a machine learning strategy based on the structural and chemical information of clusters and precipitates from kMC simulations to predict the cluster strengthening and natural aging effects in future studies.

7.2 Future Work

First, in Chapter V, we discuss the possibility of using six p-elements to “poison” surfaces of Fe precipitates in cast Mg alloys to slow down the Galvanic corrosion. However, for the top two most efficient elements, As is toxic, and Ge is still relatively expensive and less effective compared with As. It will be worthwhile to explore the combination of two alternative alloying elements that can achieve a similar or even improved effect to impede the cathodic reactions and the overall corrosion rates.

Second, in Section 4.5, efforts are made to search for potential elements that can stabilize Ag grain boundaries during heat treatment. Traditionally, the theoretical approach to study the alloy segregation effects is to first obtain relaxed grain boundary

structures from pure metals and then substitute the matrix atoms by solute atoms to calculate alloy segregation energies. One possible origin of the discrepancy between DFT calculations and experiments mentioned in Section 4.5 could be that alloying elements change not only the chemistry of the grain boundaries but also the atomistic structure of grain boundaries in alloys. Besides, in reality, more complicated grain boundaries, like grain boundary complexions, exist[93]. Therefore, more complicated grain boundary structures need to be obtained by global optimization methods, e.g., evolutionary algorithm [2], to investigate the alloy segregation effects.

Third, in Section 6.3, different approaches, such as LRU cache in Section 6.3.3, LSKMC in Section 6.3.2, parallel computing, are implemented to speed up the kMC simulations for a longer time. So far, the simulated time span that can be achieved is still at the level between \sim seconds to \sim minutes. This is still not sufficient enough to simulate the entire process of the solute clustering and GP zone formation during the natural aging. Further speedup of the kMC simulations could be achieved by the following methods.

1. One of the speed limitations of our current kMC simulation lies in the complexity of our NN architecture. If a smaller architecture with fewer weight parameters can be achieved, each prediction step will be more efficient during the simulations.
2. Our program is written in C++ with pure MPI, which means one MPI process on each core. The optimal efficiency can be achieved by using $12 * N$ cores. Here N is the number of vacancies in the kMC simulation supercell and 12 is the number of first-nearest-neighbor sites that a vacancy can jump to. In this parallel schema, one process(core) takes care of one possible jumping event, respectively. To speed up, we can combine MPI with OpenMP. OpenMP is a shared memory multiprocessing library[201]. In this hybrid schema, we can use

$12 * N * M$, where M is the number of threads per core. Then one event can be calculated by M threads.

3. LRU cache exhibits a significant speed-up effect by looking up existing keys of encoding swiftly. However, it only works in a serial version for now. One problem needs to be solved before multi-core LRU cache can be implemented. The problem lies in that different cores do not share the same memory. Thus each core can only store one specific event out of the 12 possible events for one vacancy migration. In the consecutive iterations, the probability of a core encounter with the same event is largely reduced. Thus the time of executing one step will be determined by the slowest one. One strategy is to share several most recently inserted data across all the cores once after a while. In this way, all the cores will cover all the 12 possible events of recent steps.

Fourth, the kMC simulation in this thesis ignores the effect of strain introduced by clustering or alloying. The strain effects on solute/vacancy migration barriers and clustering kinetics still remain unknown. The strain effect can be implemented by using regular on-lattice kMC with a continuum analytical function for the strain energetic contribution. The strain offsets could depend on the local concentration of the simulation cell, and the concentration of the simulation cell would be flexible and interchangeable with the external reservoir using a grand canonical ensemble mentioned in Section 2.2.

Fifth, we would like to continue to investigate the intrinsic mechanisms of the nucleation and growth kinetics for solute clusters and early-stage GP zones based on the sensitivity tests using pseudo atoms in Section 6.4.3. Once the requirements for the optimal pseudo atoms to slow down the cluster kinetics are identified, high-throughput DFT calculations will be performed to find the corresponding real alloy elements. To finally quantify the effects of these alloy elements in strengths and formability of Al alloys during natural aging, a cluster strengthening model will be constructed based

on chemical, structural, and energetic properties of the solute clusters obtained from kMC simulations discussed in the next paragraph.

Sixth, details about how clustering in Al alloy increases strength is still unclear. For typical solid solution strengthening model, the effects of individual solute atoms on both elastic interactions with dislocation strain fields (“strain misfit effects”) and the stacking fault energies related to dislocation core behavior (“chemical effects”) were considered to predict the solute strengthening effects based on first-principles calculations[100]. For the clustering strengthening model, there was a model that only considers the elastic strain effects of clusters[202]. In multicomponent alloys, the elastic strain effects and chemical effects of solute clusters could couple together and become more complicated when the chemical compositions and structures of clusters become complex. First-principles calculations can be applied to obtain the parameters related to elastic strain and chemical effects of these clusters, similar to those for solid solution strengthening model[100]. Then these parameters will be used in the classical continuum model to predict the overall cluster strengthening effects. Advanced machine learning models can be used to speed up the prediction based on first-principle data sets of the parameters of elastic strain effects and chemical effects of many clusters from kMC simulations. Then we can build a surrogate model to predict the natural aging hardening effects under the influence of various types of solute elements directly based on kMC simulation results.

According to previous studies, the chemical effect of clusters could be more important than the strain effects for the overall strengthening. For example, in the very latest research, Liu et al. [198] found that at room temperature, GP II zone clusters in Al-Zn-Mg alloys form very slowly. It will take a couple of weeks for the growth of GP zone clusters. However, the hardness of Al-Zn-Mg alloys still increases very quickly during natural aging. The authors claim that solute cluster hardening is accountable for the rapid hardening effect of the alloy. When dislocations cut through

an ordered solute cluster, only local bond changes will be observed. Additional energy is required to create an anti-phase boundary (APB). It is then critical to figure out how the short-range order of clusters affects the strengthening results. Such studies require analyses of chemical bonds and electronic structures based on first-principles calculations.

BIBLIOGRAPHY

BIBLIOGRAPHY

- [1] Mingfei Zhang and Liang Qi. Tuning hydrogen adsorption on pure and doped zno (000 $\bar{1}$) surfaces by a simple electron counting model. *Journal of Applied Physics*, 124(15):155302, 2018.
- [2] Chaoming Yang, Mingfei Zhang, and Liang Qi. Grain boundary structure search by using an evolutionary algorithm with effective mutation methods. *computational materials science*, submitted, 2020.
- [3] Mingfei Zhang, Louis G Hector Jr, Yang Guo, Ming Liu, and Liang Qi. First-principles search for alloying elements that increase corrosion resistance of mg with second-phase particles of transition metal impurities. *Computational Materials Science*, 165:154–166, 2019.
- [4] S Wilson. Electron correlation in molecules. clarendon. *Oxford Hohenberg P, Kohn W (1964) Inhomogeneous electron gas. Phys Rev*, 136:B864–B871, 1984.
- [5] Walter Kohn and Lu Jeu Sham. Self-consistent equations including exchange and correlation effects. *Physical review*, 140(4A):A1133, 1965.
- [6] John P Perdew and Alex Zunger. Self-interaction correction to density-functional approximations for many-electron systems. *Physical Review B*, 23(10):5048, 1981.
- [7] John P Perdew. Density-functional approximation for the correlation energy of the inhomogeneous electron gas. *Physical Review B*, 33(12):8822, 1986.
- [8] David M Ceperley and Berni J Alder. Ground state of the electron gas by a stochastic method. *Physical review letters*, 45(7):566, 1980.
- [9] John P Perdew and Yue Wang. Accurate and simple analytic representation of the electron-gas correlation energy. *Physical review B*, 45(23):13244, 1992.
- [10] John P Perdew, Kieron Burke, and Matthias Ernzerhof. Generalized gradient approximation made simple. *Physical Review Letters*, 77(18):3865, 1996.
- [11] John P Perdew, Adrienn Ruzsinszky, Gábor I Csonka, Oleg A Vydrov, Gustavo E Scuseria, Lucian A Constantin, Xiaolan Zhou, and Kieron Burke. Restoring the density-gradient expansion for exchange in solids and surfaces. *Physical review letters*, 100(13):136406, 2008.

- [12] Daan Frenkel and Berend Smit. *Understanding molecular simulation: from algorithms to applications*, volume 1. Elsevier, 2001.
- [13] Douglas Hubbard and Douglas A Samuelson. Modeling without measurements: How the decision analysis culture's lack of empiricism reduces its effectiveness. *OR/MS Today*, 36(5):26–31, 2009.
- [14] Alfred B Bortz, Malvin H Kalos, and Joel L Lebowitz. A new algorithm for monte carlo simulation of ising spin systems. *Journal of Computational Physics*, 17(1):10–18, 1975.
- [15] Ju Li. Atomeye: an efficient atomistic configuration viewer. *Modelling and Simulation in Materials Science and Engineering*, 11(2):173, 2003.
- [16] John Edward Jones. On the determination of molecular fields.—ii. from the equation of state of a gas. *Proceedings of the Royal Society of London. Series A, Containing Papers of a Mathematical and Physical Character*, 106(738):463–477, 1924.
- [17] Joao F Justo, Martin Z Bazant, Efthimios Kaxiras, Vasily V Bulatov, and Sidney Yip. Interatomic potential for silicon defects and disordered phases. *Physical review B*, 58(5):2539, 1998.
- [18] Wendy D Cornell, Piotr Cieplak, Christopher I Bayly, Ian R Gould, Kenneth M Merz, David M Ferguson, David C Spellmeyer, Thomas Fox, James W Caldwell, and Peter A Kollman. A second generation force field for the simulation of proteins, nucleic acids, and organic molecules. *Journal of the American Chemical Society*, 117(19):5179–5197, 1995.
- [19] Tao Liang, Tzu-Ray Shan, Yu-Ting Cheng, Bryce D Devine, Mark Noordhoek, Yangzhong Li, Zhize Lu, Simon R Phillipot, and Susan B Sinnott. Classical atomistic simulations of surfaces and heterogeneous interfaces with the charge-optimized many body (comb) potentials. *Materials Science and Engineering: R: Reports*, 74(9):255–279, 2013.
- [20] Nongnuch Artrith and Alexander Urban. An implementation of artificial neural-network potentials for atomistic materials simulations: Performance for tio₂. *Computational Materials Science*, 114:135–150, 2016.
- [21] Yong-Jie Hu, Ge Zhao, Baiyu Zhang, Chaoming Yang, Mingfei Zhang, Zi-Kui Liu, Xiaofeng Qian, and Liang Qi. Local electronic descriptors for solute-defect interactions in bcc refractory metals. *Nature communications*, 10(1):1–11, 2019.
- [22] Yong-Jie Hu, Ge Zhao, Mingfei Zhang, Bin Bin, Tyler Del Rose, Qian Zhao, Qun Zu, Yang Chen, Xuekun Sun, Maarten de Jong, et al. Predicting densities and elastic moduli of sio 2-based glasses by machine learning. *npj Computational Materials*, 6(1):1–13, 2020.

- [23] Andrew R Leach and Andrew R Leach. *Molecular modelling: principles and applications*. Pearson education, 2001.
- [24] SJ Pearton, F Ren, Yu-Lin Wang, BH Chu, KH Chen, CY Chang, Wantae Lim, Jenshan Lin, and DP Norton. Recent advances in wide bandgap semiconductor biological and gas sensors. *Progress in Materials Science*, 55(1):1–59, 2010.
- [25] RH Friend and AD Yoffe. Electronic properties of intercalation complexes of the transition metal dichalcogenides. *Advances in Physics*, 36(1):1–94, 1987.
- [26] Jin-Hong Lee, Kyung-Hee Ko, and Byung-Ok Park. Electrical and optical properties of zno transparent conducting films by the sol-gel method. *Journal of Crystal Growth*, 247(1):119–125, 2003.
- [27] S Major, Satyendra Kumar, M Bhatnagar, and KL Chopra. Effect of hydrogen plasma treatment on transparent conducting oxides. *Applied Physics Letters*, 49(7):394–396, 1986.
- [28] Yanwu Xie, Yasuyuki Hikita, Christopher Bell, and Harold Y Hwang. Control of electronic conduction at an oxide heterointerface using surface polar adsorbates. *Nature Communications*, 2:494, 2011.
- [29] Masatake Haruta, N Yamada, T Kobayashi, and S Iijima. Gold catalysts prepared by coprecipitation for low-temperature oxidation of hydrogen and of carbon monoxide. *Journal of Catalysis*, 115(2):301–309, 1989.
- [30] RB Levy and M Boudart. Platinum-like behavior of tungsten carbide in surface catalysis. *Science*, 181(4099):547–549, 1973.
- [31] Liang Qi and Ju Li. Adsorbate interactions on surface lead to a flattened sabatier volcano plot in reduction of oxygen. *Journal of Catalysis*, 295:59–69, 2012.
- [32] Anderson Janotti and Chris G Van de Walle. Fundamentals of zinc oxide as a semiconductor. *Reports on Progress in Physics*, 72(12):126501, 2009.
- [33] Zheshuai Lin and Paul D Bristowe. A density functional study of the effect of hydrogen on the strength of an epitaxial ag/zno interface. *Journal of Applied Physics*, 102(10):103513, 2007.
- [34] E Duriau, S Agouram, C Morhain, T Seldrum, R Sporken, and J Dumont. Growth of ag thin films on zno (000-1) investigated by aes and stm. *Applied Surface Science*, 253(2):549–554, 2006.
- [35] Spencer D. Miller and John R. Kitchin. Relating the coverage dependence of oxygen adsorption on au and pt fcc(111) surfaces through adsorbate-induced surface electronic structure effects. *Surface Science*, 603(5):794–801, 2009.

- [36] Venkataraman Pallassana, Matthew Neurock, Lars B Hansen, Bjørk Hammer, and Jens K Nørskov. Theoretical analysis of hydrogen chemisorption on pd (111), re (0001) and pdml/re (0001), reml/pd (111) pseudomorphic overlayers. *Physical Review B*, 60(8):6146, 1999.
- [37] P Benard and R Chahine. Determination of the adsorption isotherms of hydrogen on activated carbons above the critical temperature of the adsorbate over wide temperature and pressure ranges. *Langmuir*, 17(6):1950–1955, 2001.
- [38] Chris G Van de Walle and J. Neugebauer. First-principles surface phase diagram for hydrogen on gan surfaces. *Physical Review Letters*, 88:066103, 2002.
- [39] Y Wang, B Meyer, X Yin, M Kunat, D Langenberg, F Traeger, A Birkner, and Ch Wöll. Hydrogen induced metallicity on the zno (10-10) surface. *Physical Review Letters*, 95(26):266104, 2005.
- [40] Jeppe V Lauritsen, Soeren Porsgaard, Morten K Rasmussen, Mona CR Jensen, Ralf Bechstein, Kristoffer Meinander, Bjerne S Clausen, Stig Helveg, Roman Wahl, and Georg Kresse. Stabilization principles for polar surfaces of zno. *ACS Nano*, 5(7):5987–5994, 2011.
- [41] Walter A. Harrison. Theory of polar semiconductor surfaces. *Journal of Vacuum Science and Technology*, 16:1492, 1979.
- [42] Olga Dulub, Ulrike Diebold, and G Kresse. Novel stabilization mechanism on polar surfaces: Zno (0001)-zn. *Physical Review Letters*, 90(1):016102, 2003.
- [43] A Wander, F Schedin, P Steadman, A Norris, R McGrath, TS Turner, G Thornton, and NM Harrison. Stability of polar oxide surfaces. *Physical Review Letters*, 86(17):3811, 2001.
- [44] Matti Hellstrom and Jorg Behler. Surface phase diagram prediction from a minimal number of dft calculations: redox-active adsorbates on zinc oxide. *Physical Chemistry Chemical Physics*, 19(42):28731–28748, 2017.
- [45] Arrigo Calzolari, Mirco Bazzani, and Alessandra Catellani. Dipolar and charge transfer effects on the atomic stabilization of zno polar surfaces. *Surface Science*, 607:181–186, 2013.
- [46] E. Kaxiras, Y. Bar-Yam, J. D. Joannopoulos, and K. C. Pandey. Ab initio theory of polar semiconductor surfaces. i. methodology and the (2x2) reconstructions of gaas(111). *Physical Review B*, 35:9625, 1987.
- [47] B Meyer. First-principles study of the polar o-terminated zno surface in thermodynamic equilibrium with oxygen and hydrogen. *Physical Review B*, 69(4):045416, 2004.

- [48] Roman Wahl, Jeppe V Lauritsen, Flemming Besenbacher, and Georg Kresse. Stabilization mechanism for the polar zno (000-1)-o surface. *Physical Review B*, 87(8):085313, 2013.
- [49] Markus Valtiner, Mira Todorova, Guido Grundmeier, and Jörg Neugebauer. Temperature stabilized surface reconstructions at polar zno (0001). *Physical Review Letters*, 103(6):065502, 2009.
- [50] R. Jacobs, B. Zheng, B. Puchala, P. M. Voyles, A. B. Yankovich, and D. Morgan. Counterintuitive reconstruction of the polar o-terminated zno surface with zinc vacancies and hydrogen. *Journal of Physical Chemistry Letters*, 7:4483-4487, 2016.
- [51] MD Pashley. Electron counting model and its application to island structures on molecular-beam epitaxy grown gaas (001) and znse (001). *Physical Review B*, 40(15):10481, 1989.
- [52] Jason K Kawasaki, Abhishek Sharan, Linda IM Johansson, Martin Hjort, Rainer Timm, Balasubramanian Thiagarajan, Brian D Schultz, Anders Mikkelsen, Anderson Janotti, and Chris J Palmstrøm. A simple electron counting model for half-heusler surfaces. *Science advances*, 4(6):EAAR5832, 2018.
- [53] B Meyer and D Marx. Density-functional study of the structure and stability of zno surfaces. *Physical Review B*, 67(3), JAN 15 2003.
- [54] U Ozgur, YI Alivov, C Liu, A Teke, MA Reshchikov, S Dogan, V Avrutin, SJ Cho, and H Morkoc. A comprehensive review of zno materials and devices. *Journal of Applied Physics*, 98(4), AUG 15 2005.
- [55] C. Klingshirn. Zno: From basics towards applications. *Physica Status Solidi (b) Basic Solid State Physics*, 244(9):3027–3073, SEP 2007.
- [56] Zheshuai Lin and Paul D Bristowe. A first principles study of the properties of al: Zno and its adhesion to ag in an optical coating. *Journal of Applied Physics*, 106(1):013520, 2009.
- [57] Mohammed Ali Lahmer and Kamel Guergouri. Effect of hydrogen adsorption on the electronic and optical properties of the mg-doped o-terminated zno surface. *Surface Science*, 633:24–28, 2015.
- [58] F. Pan, C. Song, X. J. Liu, Y. C. Yang, and F. Zeng. Ferromagnetism and possible application in spintronics of transition-metal-doped zno films. *Materials Science & Engineering R: Reports*, 62(1):1–35, JUN 30 2008.
- [59] Reenamole Georgekutty, Michael K. Seery, and Suresh C. Pillai. A highly efficient ag-zno photocatalyst: synthesis, properties, and mechanism. *Journal of Physical Chemistry C*, 112(35):13563–13570, SEP 4 2008.

- [60] Yichuan Ling, Gongming Wang, Damon A. Wheeler, Jin Z. Zhang, and Yat Li. Sn-doped hematite nanostructures for photoelectrochemical water splitting. *Nano Letters*, 11(5):2119–2125, MAY 2011.
- [61] Raffaella Buonsanti, Anna Llordes, Shaul Aloni, Brett A. Helms, and Delia J. Milliron. Tunable infrared absorption and visible transparency of colloidal aluminum-doped zinc oxide nanocrystals. *Nano Letters*, 11(11):4706–4710, NOV 2011.
- [62] Hyo-Joong Kim and Jong-Heun Lee. Highly sensitive and selective gas sensors using p-type oxide semiconductors: overview. *Sensors and Actuators B: Chemical*, 192:607–627, MAR 2014.
- [63] Mu-Hsiang Hsu and Chi-Jung Chang. Ag-doped zno nanorods coated metal wire meshes as hierarchical photocatalysts with high visible-light driven photoactivity and photostability. *Journal of Hazardous Materials*, 278:444–453, AUG 15 2014.
- [64] Zhidong Lin, Na Li, Zhe Chen, and Ping Fu. The effect of ni doping concentration on the gas sensing properties of ni doped sno₂. *Sensors and Actuators B: Chemical*, 239:501–510, FEB 2017.
- [65] Christof Wöll. The chemistry and physics of zinc oxide surfaces. *Progress in Surface Science*, 82(2):55–120, 2007.
- [66] Georg Kresse and Jürgen Furthmüller. Efficient iterative schemes for ab initio total-energy calculations using a plane-wave basis set. *Physical Review B*, 54(16):11169, 1996.
- [67] Georg Kresse and D Joubert. From ultrasoft pseudopotentials to the projector augmented-wave method. *Physical Review B*, 59(3):1758, 1999.
- [68] Peter E Blöchl. Projector augmented-wave method. *Physical Review B*, 50(24):17953, 1994.
- [69] SL Dudarev, GA Botton, SY Savrasov, CJ Humphreys, and AP Sutton. Electron-energy-loss spectra and the structural stability of nickel oxide: an lsda+ u study. *Physical Review B*, 57(3):1505, 1998.
- [70] Gui-Yang Huang, Chong-Yu Wang, and Jian-Tao Wang. Detailed check of the lda+ u and gga+ u corrected method for defect calculations in wurtzite zno. *Computer Physics Communications*, 183(8):1749–1752, 2012.
- [71] Fumiyasu Oba, Minseok Choi, Atsushi Togo, Atsuto Seko, and Isao Tanaka. Native defects in oxide semiconductors: a density functional approach. *Journal of Physics: Condensed Matter*, 22(38):384211, 2010.
- [72] Hendrik J Monkhorst and James D Pack. Special points for brillouin-zone integrations. *Physical Review B*, 13(12):5188, 1976.

- [73] Zheshuai Lin and Paul D Bristowe. Microscopic characteristics of the ag (111)/ zno (0001) interface present in optical coatings. *Physical Review B*, 75(20):205423, 2007.
- [74] N Greenwood and A Earnshaw. *Chemistry of the Elements (2nd ed.)*. Butterworth-Heinemann, 1997.
- [75] B Hammer and JK Nørskov. Why gold is the noblest of all the metals. *Nature*, 376(6537):238–240, JUL 20 1995.
- [76] LA Kibler, AM El-Aziz, R Hoyer, and DM Kolb. Tuning reaction rates by lateral strain in a palladium monolayer. *Angewandte Chemie*, 44(14):2080–2084, 2005.
- [77] John W Salisbury and Dana M D’Aria. Emissivity of terrestrial materials in the 8–14 μm atmospheric window. *Remote Sens. Environ.*, 42(2):83–106, 1992.
- [78] Ruiyuan Liu, Fute Zhang, Celal Con, Bo Cui, and Baoquan Sun. Lithography-free fabrication of silicon nanowire and nanohole arrays by metal-assisted chemical etching. *Nanoscale research letters*, 8(1):1–8, 2013.
- [79] Kristen S Williams, Victor Rodriguez-Santiago, and Jan W Andzelm. Modeling reaction pathways for hydrogen evolution and water dissociation on magnesium. *Electrochimica Acta*, 210:261–270, 2016.
- [80] Sina Moeini. Mapp. <http://http://l17.mit.edu/> sina, 2017.
- [81] 2018 ICDD: Newtown Square, PA. No. 04-0783, 2017.
- [82] Maozhi Li, P-W Chung, E Cox, Cynthia J Jenks, Patricia A Thiel, and James W Evans. Exploration of complex multilayer film growth morphologies: Stm analysis and predictive atomistic modeling for ag on ag (111). *Physical Review B*, 77(3):033402, 2008.
- [83] Kenneth F Kelton. Crystal nucleation in liquids and glasses. In *Solid state physics*, volume 45, pages 75–177. Elsevier, 1991.
- [84] SA Chambers, T Droubay, Dr R Jennison, and TR Mattsson. Laminar growth of ultrathin metal films on metal oxides: Co on hydroxylated α -al₂o₃ (0001). *Science*, 297(5582):827–831, 2002.
- [85] André Anders, Eungsun Byon, Dong-Ho Kim, Kentaro Fukuda, and Sunnie HN Lim. Smoothing of ultrathin silver films by transition metal seeding. *Solid state communications*, 140(5):225–229, 2006.
- [86] William W Mullins. Theory of thermal grooving. *Journal of Applied Physics*, 28(3):333–339, 1957.
- [87] Nick J. Simrick, John A. Kilner, and Alan Atkinson. Thermal stability of silver thin films on zirconia substrates. *Thin Solid Films*, 520(7):2855–2867, 2012.

- [88] Paul A. Martin. Thermal grooving by surface diffusion: Mullins revisited and extended to multiple grooves. *Quarterly of applied mathematics*, 67(1):125–136, 2009.
- [89] Tongjai Chookajorn, Heather A Murdoch, and Christopher A Schuh. Design of stable nanocrystalline alloys. *Science*, 337(6097):951–954, 2012.
- [90] ZB Jiao and CA Schuh. Nanocrystalline ag-w alloys lose stability upon solute desegregation from grain boundaries. *Acta Materialia*, 161:194–206, 2018.
- [91] Seymour H Vosko, Leslie Wilk, and Marwan Nusair. Accurate spin-dependent electron liquid correlation energies for local spin density calculations: a critical analysis. *Canadian Journal of physics*, 58(8):1200–1211, 1980.
- [92] Qiang Zhu, Amit Samanta, Bingxi Li, Robert E Rudd, and Timofey Frolov. Predicting phase behavior of grain boundaries with evolutionary search and machine learning. *Nature communications*, 9(1):1–9, 2018.
- [93] Patrick R Cantwell, Ming Tang, Shen J Dillon, Jian Luo, Gregory S Rohrer, and Martin P Harmer. Grain boundary complexions. *Acta Materialia*, 62:1–48, 2014.
- [94] Wenchao Sheng, MyatNoeZin Myint, Jingguang G Chen, and Yushan Yan. Correlating the hydrogen evolution reaction activity in alkaline electrolytes with the hydrogen binding energy on monometallic surfaces. *Energy & Environmental Science*, 6(5):1509–1512, 2013.
- [95] Alan A Luo and Anil K Sachdev. Development of a moderate temperature bending process for magnesium alloy extrusions. In *Materials Science Forum*, volume 488, pages 477–482. Trans Tech Publ, 2005.
- [96] A Luo. Wrought magnesium research for automotive applications. *Magnesium Technology 2006*, pages 333–339, 2006.
- [97] Jon T Carter, Andres R Melo, Vesna Savic, Louis Gerard Hector Jr, and Paul E Krajewski. Structural evaluation of an experimental aluminum/magnesium decklid. *SAE International Journal of Materials and Manufacturing*, 4(1):166–174, 2011.
- [98] J Jekl, J Auld, C Sweet, Jon Carter, Steve Resch, A Klärner, J Brevick, and A Luo. Development of a thin-wall magnesium side door inner panel for automobiles. Technical report, General Motors LLC, 2015.
- [99] Alan A Luo. Magnesium casting technology for structural applications. *Journal of Magnesium and Alloys*, 1(1):2–22, 2013.
- [100] Joseph A Yasi, Louis G Hector Jr, and Dallas R Trinkle. First-principles data for solid-solution strengthening of magnesium: From geometry and chemistry to properties. *Acta Materialia*, 58(17):5704–5713, 2010.

- [101] Wenyue Zheng, C DeRushie, J Lo, and R Osborne. Corrosion protection of structural magnesium alloys: Recent development. Technical report, SAE Technical Paper, 2005.
- [102] Nick Birbilis, Andrew D King, Sebastian Thomas, Gerald S Frankel, and John R Scully. Evidence for enhanced catalytic activity of magnesium arising from anodic dissolution. *Electrochimica Acta*, 132:277–283, 2014.
- [103] Rong-chang Zeng, Jin Zhang, Wei-jiu Huang, W Dietzel, KU Kainer, C Blawert, and KE Wei. Review of studies on corrosion of magnesium alloys. *Transactions of Nonferrous Metals Society of China*, 16:s763–s771, 2006.
- [104] RL Liu, MF Hurley, A Kvryan, G Williams, JR Scully, and N Birbilis. Controlling the corrosion and cathodic activation of magnesium via microalloying additions of ge. *Scientific reports*, 6:28747, 2016.
- [105] Kevin Douglas Ralston, G Williams, and Nick Birbilis. Effect of ph on the grain size dependence of magnesium corrosion. *Corrosion*, 68(6):507–517, 2012.
- [106] JD Hanawalt, CE Nelson, JA Peloubet, et al. Corrosion studies of magnesium and its alloys. *trans. AIME*, 147:273–299, 1942.
- [107] RE McNulty and JD Hanawalt. Some corrosion characteristics of high purity magnesium alloys. *Transactions of The Electrochemical Society*, 81(1):423–433, 1942.
- [108] Lei Yang, Xiaorong Zhou, Michele Curioni, Surajkumar Pawar, Hong Liu, Zhongyun Fan, Geoff Scamans, and George Thompson. Corrosion behavior of pure magnesium with low iron content in 3.5 wt% nacl solution. *Journal of The Electrochemical Society*, 162(7):C362–C368, 2015.
- [109] Christiane Scharf and Andre Ditze. Iron pickup of az91 and as31 magnesium melts in steel crucibles. *Advanced Engineering Materials*, 9(7):566–571, 2007.
- [110] Irwin A Taub, Warren Roberts, Sebastian LaGambina, and Kenneth Kustin. Mechanism of dihydrogen formation in the magnesium- water reaction. *The Journal of Physical Chemistry A*, 106(35):8070–8078, 2002.
- [111] D Eaves, G Williams, and HN McMurray. Inhibition of self-corrosion in magnesium by poisoning hydrogen recombination on iron impurities. *Electrochimica Acta*, 79:1–7, 2012.
- [112] Daniel Höche, Carsten Blawert, Sviatlana V Lamaka, Nico Scharnagl, Chamini Mendis, and Mikhail L Zheludkevich. The effect of iron re-deposition on the corrosion of impurity-containing magnesium. *Physical Chemistry Chemical Physics*, 18(2):1279–1291, 2016.

- [113] Lei Yang, Guangkun Liu, Liangong Ma, Erlin Zhang, Xiaorong Zhou, and George Thompson. Effect of iron content on the corrosion of pure magnesium: Critical factor for iron tolerance limit. *Corrosion Science*, 139:421–429, 2018.
- [114] M Taheri, RC Phillips, JR Kish, and GA Botton. Analysis of the surface film formed on mg by exposure to water using a fib cross-section and stem–eds. *Corrosion Science*, 59:222–228, 2012.
- [115] Mehdi Taheri, JR Kish, Nick Birbilis, Mohsen Danaie, Elizabeth A McNally, and Joseph Robert McDermid. Towards a physical description for the origin of enhanced catalytic activity of corroding magnesium surfaces. *Electrochimica Acta*, 116:396–403, 2014.
- [116] Guangling Song and Andrej Atrens. Understanding magnesium corrosion—a framework for improved alloy performance. *Advanced engineering materials*, 5(12):837–858, 2003.
- [117] M Esmaily, JE Svensson, S Fajardo, N Birbilis, GS Frankel, S Virtanen, R Arrabal, S Thomas, and LG Johansson. Fundamentals and advances in magnesium alloy corrosion. *Progress in Materials Science*, 89:92–193, 2017.
- [118] Edward Ghali. *Corrosion resistance of aluminum and magnesium alloys: understanding, performance, and testing*, volume 12. John Wiley & Sons, 2010.
- [119] JF Walling. Electrochemical kinetics, theoretical and experimental aspects (veter, klaus j.), 1968.
- [120] Andrew J Medford, Aleksandra Vojvodic, Jens S Hummelshøj, Johannes Voss, Frank Abild-Pedersen, Felix Studt, Thomas Bligaard, Anders Nilsson, and Jens K Nørskov. From the sabatier principle to a predictive theory of transition-metal heterogeneous catalysis. *Journal of Catalysis*, 328:36–42, 2015.
- [121] RL Liu, ZR Zeng, JR Scully, G Williams, and N Birbilis. Simultaneously improving the corrosion resistance and strength of magnesium via low levels of zn and ge additions. *Corrosion Science*, 140:18–29, 2018.
- [122] Nick Birbilis, Mark A Easton, AD Sudholz, Su-Ming Zhu, and MA Gibson. On the corrosion of binary magnesium-rare earth alloys. *Corrosion Science*, 51(3):683–689, 2009.
- [123] Wenjuan Liu, Fahe Cao, Linrong Chang, Zhao Zhang, and Jianqing Zhang. Effect of rare earth element ce and la on corrosion behavior of am60 magnesium alloy. *Corrosion Science*, 51(6):1334–1343, 2009.
- [124] Zhiming Shi, Fuyong Cao, Guang-Ling Song, Ming Liu, and Andrej Atrens. Corrosion behaviour in salt spray and in 3.5% nacl solution saturated with mg (oh) 2 of as-cast and solution heat-treated binary mg–re alloys: Re= ce, la, nd, y, gd. *Corrosion Science*, 76:98–118, 2013.

- [125] Wanqiang Xu, Nick Birbilis, Gang Sha, Yu Wang, John E Daniels, Yang Xiao, and Michael Ferry. A high-specific-strength and corrosion-resistant magnesium alloy. *Nature materials*, 14(12):1229, 2015.
- [126] TW Cain, CF Glover, and JR Scully. The corrosion of solid solution mg-sn binary alloys in nacl solutions. *Electrochimica Acta*, 297:564–575, 2019.
- [127] Monica Pozzo and D Alfe. Hydrogen dissociation and diffusion on transition metal (= ti, zr, v, fe, ru, co, rh, ni, pd, cu, ag)-doped mg (0001) surfaces. *International journal of hydrogen energy*, 34(4):1922–1930, 2009.
- [128] Jeff Greeley, Thomas F Jaramillo, Jacob Bonde, IB Chorkendorff, and Jens K Nørskov. Computational high-throughput screening of electrocatalytic materials for hydrogen evolution. *Nature materials*, 5(11):909–913, 2006.
- [129] Richard Tran, Zihan Xu, Balachandran Radhakrishnan, Donald Winston, Wenhao Sun, Kristin A Persson, and Shyue Ping Ong. Surface energies of elemental crystals. *Scientific data*, 3(1):1–13, 2016.
- [130] R Kohlhaas, Ph Dunner, and PN Schmitz. The temperature-dependance of the lattice parameters of iron, cobalt, and nickel in the high temperature range. *Z Angew Physik*, 23(4), 1967.
- [131] Murilo L Tiago, Yunkai Zhou, MM G_ Alemany, Yousef Saad, and James R Chelikowsky. Evolution of magnetism in iron from the atom to the bulk. *Physical review letters*, 97(14):147201, 2006.
- [132] J Wrobel, LG Hector Jr, W Wolf, SL Shang, ZK Liu, and KJ Kurzydłowski. Thermodynamic and mechanical properties of lanthanum–magnesium phases from density functional theory. *Journal of alloys and compounds*, 512(1):296–310, 2012.
- [133] A Hung, I Yarovsky, J Muscat, S Russo, I Snook, and RO Watts. First-principles study of metallic iron interfaces. *Surface science*, 501(3):261–269, 2002.
- [134] WR Tyson and WA Miller. Surface free energies of solid metals: Estimation from liquid surface tension measurements. *Surface Science*, 62(1):267–276, 1977.
- [135] J Kubásek, D Vojtěch, J Lipov, and T Rumí. Structure, mechanical properties, corrosion behavior and cytotoxicity of biodegradable mg-x (x= sn, ga, in) alloys. *Materials Science and Engineering: C*, 33(4):2421–2432, 2013.
- [136] BJKN Hammer and JK Nørskov. Electronic factors determining the reactivity of metal surfaces. *Surface Science*, 343(3):211–220, 1995.
- [137] Bjørk Hammer and Jens K Norskov. Why gold is the noblest of all the metals. *Nature*, 376(6537):238–240, 1995.

- [138] Jens Kehlet Nørskov, Thomas Bligaard, Ashildur Logadottir, JR Kitchin, Jing-guang G Chen, S Pandelov, and U Stimming. Trends in the exchange current for hydrogen evolution. *Journal of The Electrochemical Society*, 152(3):J23–J26, 2005.
- [139] Lingling Guo and Jumei Zhang. Influence of the β -mg17al12 phase morphology on the corrosion properties of az91hp magnesium alloy. In *IOP Conference Series: Materials Science and Engineering*, volume 230, page 012009. IOP Publishing, 2017.
- [140] Hiroyuki Kawabata, Naohisa Nishino, Tsuyoshi Seguchi, and Yoshikazu Genma. Influence of aluminum content on corrosion resistance of mg-al alloys containing copper and zinc. In *Magnesium Technology 2012*, pages 277–280. Springer, 2012.
- [141] IN Fridlyander, VG Sister, OE Grushko, VV Berstenev, LM Sheveleva, and LA Ivanova. Aluminum alloys: promising materials in the automotive industry. *Metal science and heat treatment*, 44(9-10):365–370, 2002.
- [142] Jürgen Hirsch. Aluminium in innovative light-weight car design. *Materials Transactions*, 52(5):818–824, 2011.
- [143] Jürgen Hirsch. Recent development in aluminium for automotive applications. *Transactions of Nonferrous Metals Society of China*, 24(7):1995–2002, 2014.
- [144] J Daniel Bryant. The effects of preaging treatments on aging kinetics and mechanical properties in aa6111 aluminum autobody sheet. *Metallurgical and Materials Transactions A*, 30(8), 1999.
- [145] Daoming Li and Amit K Ghosh. Biaxial warm forming behavior of aluminum sheet alloys. *Journal of Materials Processing Technology*, 145(3):281–293, 2004.
- [146] A Deschamps and Y Brechet. Influence of predeformation and ageing of an al-zn-mg alloy—ii. modeling of precipitation kinetics and yield stress. *Acta Materialia*, 47(1):293–305, 1998.
- [147] John Banhart, Matthew DH Lay, CST Chang, and AJ Hill. Kinetics of natural aging in al-mg-si alloys studied by positron annihilation lifetime spectroscopy. *Physical Review B*, 83(1):014101, 2011.
- [148] Zequin Liang, Cynthia Sin Ting Chang, Christian Abromeit, John Banhart, and Jürgen Hirsch. The kinetics of clustering in al-mg-si alloys studied by monte carlo simulation. *International journal of materials research*, 103(8):980–986, 2012.
- [149] A Deschamps, F De Geuser, Zenji Horita, S Lee, and G Renou. Precipitation kinetics in a severely plastically deformed 7075 aluminium alloy. *Acta materialia*, 66:105–117, 2014.

- [150] Olivier Ragueneau, P Tréguer, A Leynaert, RF Anderson, MA Brzezinski, DJ DeMaster, RC Dugdale, J Dymond, G Fischer, R Francois, et al. A review of the si cycle in the modern ocean: recent progress and missing gaps in the application of biogenic opal as a paleoproductivity proxy. *Global and Planetary Change*, 26(4):317–365, 2000.
- [151] LK Berg, J Gjønnes, V Hansen, XZ Li, M Knutson-Wedel, D Schryvers, and LR Wallenberg. Gp-zones in al–zn–mg alloys and their role in artificial aging. *Acta materialia*, 49(17):3443–3451, 2001.
- [152] Tsai-Fu Chung, Yo-Lun Yang, Bo-Ming Huang, Zhusheng Shi, Jianguo Lin, Takahito Ohmura, and Jer-Ren Yang. Transmission electron microscopy investigation of separated nucleation and in-situ nucleation in aa7050 aluminium alloy. *Acta Materialia*, 149:377–387, 2018.
- [153] AK Mukhopadhyay. Guinier-preston zones in a high-purity al-zn-mg alloy. *Philosophical magazine letters*, 70(3):135–140, 1994.
- [154] Emmanuel Clouet, Céline Hin, Dominique Gendt, Maylise Nastar, and Frédéric Soisson. Kinetic monte carlo simulations of precipitation. *Advanced Engineering Materials*, 8(12):1210–1214, 2006.
- [155] Frédéric Soisson, CS Becquart, Nicolas Castin, Christophe Domain, Lorenzo Malerba, and Edwige Vincent. Atomistic kinetic monte carlo studies of microchemical evolutions driven by diffusion processes under irradiation. *Journal of Nuclear Materials*, 406(1):55–67, 2010.
- [156] F Soisson, A Barbu, and G Martin. Monte carlo simulations of copper precipitation in dilute iron-copper alloys during thermal ageing and under electron irradiation. *Acta Materialia*, 44(9):3789–3800, 1996.
- [157] G Sha and A Cerezo. Kinetic monte carlo simulation of clustering in an al–zn–mg–cu alloy (7050). *Acta materialia*, 53(4):907–917, 2005.
- [158] Emmanuel Clouet, Maylise Nastar, and Christophe Sigli. Nucleation of al 3 zr and al 3 sc in aluminum alloys: from kinetic monte carlo simulations to classical theory. *Physical Review B*, 69(6):064109, 2004.
- [159] E Vincent, CS Becquart, Cristelle Pareige, Philippe Pareige, and C Domain. Precipitation of the fecu system: A critical review of atomic kinetic monte carlo simulations. *Journal of Nuclear Materials*, 373(1-3):387–401, 2008.
- [160] Shoichi Hirosawa, Tatsuo Sato, Junichi Yokota, and Akihiko Kamio. Comparison between resistivity changes and monte carlo simulation for gp zone formation in al–cu base ternary alloys. *Materials Transactions, JIM*, 39(1):139–146, 1998.

- [161] Juan M Sanchez, Francois Ducastelle, and Denis Gratias. Generalized cluster description of multicomponent systems. *Physica A: Statistical Mechanics and its Applications*, 128(1-2):334–350, 1984.
- [162] JN Brönsted and Kai Pedersen. Die katalytische zersetzung des nitramids und ihre physikalisch-chemische bedeutung. *Zeitschrift für Physikalische Chemie*, 108(1):185–235, 1924.
- [163] MG Evans and M Polanyi. Further considerations on the thermodynamics of chemical equilibria and reaction rates. *Transactions of the Faraday Society*, 32:1333–1360, 1936.
- [164] Ronald Percy Bell. The theory of reactions involving proton transfers. *Proceedings of the Royal Society of London. Series A-Mathematical and Physical Sciences*, 154(882):414–429, 1936.
- [165] A Zunger, PEA Turchi, and A Gonis. Statics and dynamics of alloy phase transformations. *NATO ASI Series. Series B, Physics*, 319, 1994.
- [166] A Van der Ven, G Ceder, M Asta, and PD Tepesch. First-principles theory of ionic diffusion with nondilute carriers. *Physical Review B*, 64(18):184307, 2001.
- [167] K Persson and VA Sethuraman. Lj hardwick vet al. *J. Phys. Chem. Lett*, 1:1176–1180, 2010.
- [168] Anirudh Raju Natarajan, Ellen LS Solomon, Brian Puchala, Emmanuelle A Marquis, and Anton Van der Ven. On the early stages of precipitation in dilute mg–nd alloys. *Acta Materialia*, 108:367–379, 2016.
- [169] Qu Wu, Bing He, Tao Song, Jian Gao, and Siqi Shi. Cluster expansion method and its application in computational materials science. *Computational Materials Science*, 125:243–254, 2016.
- [170] Manh Cuong Nguyen, Lin Zhou, Wei Tang, Matthew J Kramer, Iver E Anderson, Cai-Zhuang Wang, and Kai-Ming Ho. Cluster-expansion model for complex quinary alloys: Application to alnico permanent magnets. *Physical Review Applied*, 8(5):054016, 2017.
- [171] Nicolas Castin, Roberto Pinheiro Domingos, and Lorenzo Malerba. Use of computational intelligence for the prediction of vacancy migration energies in atomistic kinetic monte carlo simulations. *International Journal of Computational Intelligence Systems*, 1(4):340–352, 2008.
- [172] Graeme Henkelman, Blas P Uberuaga, and Hannes Jónsson. A climbing image nudged elastic band method for finding saddle points and minimum energy paths. *The Journal of chemical physics*, 113(22):9901–9904, 2000.

- [173] Graeme Henkelman and Hannes Jónsson. Improved tangent estimate in the nudged elastic band method for finding minimum energy paths and saddle points. *The Journal of chemical physics*, 113(22):9978–9985, 2000.
- [174] Radu A Miron and Kristen A Fichthorn. Multiple-time scale accelerated molecular dynamics: addressing the small-barrier problem. *Physical review letters*, 93(12):128301, 2004.
- [175] Albert P Bartók, Mike C Payne, Risi Kondor, and Gábor Csányi. Gaussian approximation potentials: The accuracy of quantum mechanics, without the electrons. *Physical review letters*, 104(13):136403, 2010.
- [176] Jörg Behler. Atom-centered symmetry functions for constructing high-dimensional neural network potentials. *The Journal of chemical physics*, 134(7):074106, 2011.
- [177] Wojciech J Szlachta, Albert P Bartók, and Gábor Csányi. Accuracy and transferability of gaussian approximation potential models for tungsten. *Physical Review B*, 90(10):104108, 2014.
- [178] Pankaj Mehta and David J Schwab. An exact mapping between the variational renormalization group and deep learning. *arXiv preprint arXiv:1410.3831*, 2014.
- [179] Nongnuch Artrith, Alexander Urban, and Gerbrand Ceder. Efficient and accurate machine-learning interpolation of atomic energies in compositions with many species. *Physical Review B*, 96(1):014112, 2017.
- [180] Daniel Sheppard, Rye Terrell, and Graeme Henkelman. Optimization methods for finding minimum energy paths. *The Journal of chemical physics*, 128(13):134106, 2008.
- [181] Alex Zunger, S-H Wei, LG Ferreira, and James E Bernard. Special quasirandom structures. *Physical Review Letters*, 65(3):353, 1990.
- [182] Philipp Haas, Fabien Tran, and Peter Blaha. Calculation of the lattice constant of solids with semilocal functionals. *Physical Review B*, 79(8):085104, 2009.
- [183] IA Zhuravlev, SV Barabash, JM An, and KD Belashchenko. Phase stability, ordering tendencies, and magnetism in single-phase fcc au-fe nanoalloys. *Physical Review B*, 96(13):134109, 2017.
- [184] Mingfei Zhang and Zhucong Xi. Knn2. <http://github.com/1mingfei/KNN2>, 2020.
- [185] Kurt Hornik, Maxwell Stinchcombe, Halbert White, et al. Multilayer feed-forward networks are universal approximators. *Neural networks*, 2(5):359–366, 1989.

- [186] Martín Abadi, Ashish Agarwal, Paul Barham, Eugene Brevdo, Zhifeng Chen, Craig Citro, Greg S Corrado, Andy Davis, Jeffrey Dean, Matthieu Devin, et al. Tensorflow: Large-scale machine learning on heterogeneous distributed systems. *arXiv preprint arXiv:1603.04467*, 2016.
- [187] François Chollet et al. Keras. <https://github.com/fchollet/keras>, 2015.
- [188] Autonomio Talos. Talos software. <http://github.com/autonomio/talos>, 2019.
- [189] Diederik P Kingma and Jimmy Ba. Adam: A method for stochastic optimization. *arXiv preprint arXiv:1412.6980*, 2014.
- [190] Xavier Glorot and Yoshua Bengio. Understanding the difficulty of training deep feedforward neural networks. In *Proceedings of the thirteenth international conference on artificial intelligence and statistics*, pages 249–256, 2010.
- [191] Georgy Perevozchikov. Keras2cpp. <https://github.com/gosha20777/keras2cpp>, 2019.
- [192] Conrad Sanderson and Ryan Curtin. Armadillo: a template-based c++ library for linear algebra. *Journal of Open Source Software*, 1(2):26, 2016.
- [193] Conrad Sanderson and Ryan Curtin. A user-friendly hybrid sparse matrix class in c++. In *International Congress on Mathematical Software*, pages 422–430. Springer, 2018.
- [194] Kristen A Fichthorn and Yangzheng Lin. A local superbasin kinetic monte carlo method. *The Journal of chemical physics*, 138(16):164104, 2013.
- [195] E. Ma, M. Atzman, P. Bellon, and R. Trivedi. Phase transformations and systems driven far from equilibrium. *Materials Research Society Fall 1997 Meeting*, 12 1998.
- [196] Yann Le Bouar and Frédéric Soisson. Kinetic pathways from embedded-atom-method potentials: Influence of the activation barriers. *Physical review B*, 65(9):094103, 2002.
- [197] DR Mason, TS Hudson, and AP Sutton. Fast recall of state-history in kinetic monte carlo simulations utilizing the zobrist key. *Computer physics communications*, 165(1):37–48, 2005.
- [198] Jizi Liu, Rong Hu, Jialing Zheng, Yidong Zhang, Zhigang Ding, Wei Liu, Yun-tian Zhu, and Gang Sha. Formation of solute nanostructures in an al–zn–mg alloy during long-term natural aging. *Journal of Alloys and Compounds*, 821:153572, 2020.
- [199] MJ Starink and SC Wang. The thermodynamics of and strengthening due to co-clusters: general theory and application to the case of al–cu–mg alloys. *Acta Materialia*, 57(8):2376–2389, 2009.

- [200] William A Curtin, David L Olmsted, and Louis G Hector. A predictive mechanism for dynamic strain ageing in aluminium–magnesium alloys. *Nature materials*, 5(11):875–880, 2006.
- [201] Leonardo Dagum and Ramesh Menon. Openmp: an industry standard api for shared-memory programming. *IEEE computational science and engineering*, 5(1):46–55, 1998.
- [202] Qinglong Zhao. Cluster strengthening in aluminium alloys. *Scripta materialia*, 84:43–46, 2014.